New oxidation protective coatings for thermoelectric materials

Doctoral Dissertation
Doctoral Program in Material Science and Technology (32nd Cycle)

New oxidation protective coatings for thermoelectric materials

Fabiana D'Isanto
* * * * * *

Supervisors
Prof. Milena Salvo
Prof. Federico Smeacetto

Doctoral Examination Committee:

Dr.-Ing. Jochen Schilm, Referee, Fraunhofer-Institut für Keramische Technologien und Systeme IKTS- Dresden, Germany

Dr. Alessandra Sanson, Referee, CNR Istituto di Scienza e Tecnologia dei Materiali Ceramici – Faenza, Italy

Politecnico di Torino
June, 2020

I hereby declare that, the contents and organisation of this dissertation constitute my own original work and does not compromise in any way the rights of third parties, including those relating to the security of personal data.

…….....

Fabiana D'Isanto

Turin, June, 2020

Abstract

The increasing amounts of electricity consumed in everyday life and the well-known scarceness of fossil-fuel reserves is guiding research towards alternative energy sources and it represents one of the main challenges of the 21st century.

Today, most of the energy used in electrical power generation and transportation is lost in the form of heat. For example, around 60% of the energy obtained from power plants is lost as waste heat during the generation of domestic electric energy. Furthermore, around 40% of the energy generated in a car is wasted as heat and another 30% of the total is used for cooling the engine, making a total of 70% of wasted energy. In this scenario, thermoelectric materials (TEs) are of great interest among technologies aiming for clean energy generation with zero-emission technologies for direct thermal-to-electrical energy conversion.

Stability and oxidation resistance over time at high temperature is critical in the use of thermoelectric modules for waste heat recovery. In fact, most of the common thermoelectric materials are metal alloys and semiconductors which can be easily oxidized at high temperature. Consequently, the oxidation of the surface of the thermoelectric leads to the degradation of the generated power and significantly limits the efficiency of thermoelectric modules.

This PhD thesis is focused on the development and assessment of new oxidation protective coatings for different thermoelectric substrates: higher manganese silicide (HMS, MnSi1.74, p-type); magnesium silicide based material (Sb doped

$Mg_2(Si,Sn)$, $Mg_2Si_{0.487}Sn_{0.5}Sb_{0.013}$, n-type); titanium suboxide (TiO_x, n-type) and zinc doped tetrahedrite (Zn doped THD, $Cu_{11.5}Zn_{0.5}Sb_4S_{13}$, p-type).

In the case of HMS, Sb doped $Mg_2(Si,Sn)$ and TiO_x, a range of silica-based compositions were designed, produced and characterized and tested as glass-ceramic protective coatings for medium-high temperature range thermoelectric devices. The sinter-crystallization behaviour of each glass-ceramic was assessed in order to choose an appropriate coating thermal treatment. The coated samples produced were morphologically and thermo-mechanically characterized before and after oxidation tests. The thermoelectric properties of the coated and uncoated TEs were measured before and after oxidation tests, both aged and thermal cycled.

The higher manganese silicide was successfully coated in order to be used at temperature higher than 500°C. The thermal cycling stability (from room temperature to 600°C in air) of as-sintered and glass-ceramic coated HMS was studied, with respect to changes in their chemical composition and thermoelectric properties. The formation of a Si-deficient layer on the uncoated HMS, due to the reaction between HMS and oxygen at 600°C, led to a higher electrical resistivity as well as a reduced power factor. Glass-ceramic coated samples did not show variations in electrical properties compared to the as-sintered one, although they showed a lower electrical resistivity and a higher power factor in comparison with the uncoated ones. Furthermore, the glass-ceramic coating had self-healing properties at 600°C, thus enhancing the reliability and durability of the coated thermoelectric system.

In the case of Sb doped $Mg_2(Si,Sn)$, five new glass-based compositions were designed and characterized, and only one was found to be able to protect the thermoelectric substrate against oxidation up to 500°C. A very good compatibility between the substrate and the coating was demonstrated, with absence of cracks at the interface and within the thermoelectric and the glass-ceramic coating, also after the oxidation test at 500°C for 120 hrs in air.

In the case of titanium suboxide, a new silica-based glass-ceramic containing titanium oxide was produced in order to protect the substrate against oxidation up to 600°C and to match TiO_x thermal expansion (CTE ~ $8 \cdot 10^{-6} K^{-1}$). After sinter-crystallization treatment, the glass-ceramic coating was thermo-mechanically compatible with the substrate and had good wettability on TiO_x; its softening point was also found to be higher with respect to the parent glass. Preliminary oxidation tests at 800°C for 48 hrs on coated and uncoated samples are ongoing, therefore they will be published in a follow-up of this PhD thesis.

For Zn doped THD and $Mg_2Si_{0.487}Sn_{0.5}Sb_{0.013}$ the efficacy of commercial hybrid resins was estimated as protective coatings in oxidative atmospheres.

Two commercial hybrid coatings, cured at low temperature (<300°C), were tested and one of them - the water-based coating - was successfully used to protect a zinc doped tetrahedrite thermoelectric. The thermoelectric properties of the uncoated and coated Zn doped THD, measured after oxidations tests at 350°C and 400°C in air, demonstrated the hybrid coating effectiveness in preventing an increase in electrical resistivity and preserving the power factor for coated samples.

Acknowledgment

I would like to acknowledge all the people who helped and supported me during this research.

First of all, I would like sincerely to thank my supervisors Prof. Milena Salvo and Prof. Federico Smeacetto for their continuous support, motivation and knowledge they shared with me. It has been a pleasure to work with them.

Part of the experimental work was done in collaboration with other universities and research groups, as reported in detail in the thesis, thus I would like to thank:

- Nanoforce Technology Ltd, Queen Mary University of London, and in particular Prof. M.J. Reece and his research group (London, UK);
- Fraunhofer Institute for Ceramic Technologies, IKTS (Dresden, Germany), and in particular Dr.-Ing. Hans-Peter Martin and his collaborators;
- University of Hertfordshire (Hatfield, Hertfordshire, UK), and in particular Prof. Andreas Chrysanthou and his PhD students.

I would like to acknowledge all my colleagues of the Glance research group at Politecnico di Torino ("old and new entries"), for sharing with me parts of this path.

Finally, I would like to acknowledge all my friends, my parents and my partner for supporting me for all the last years, especially in the toughest periods.

Contents

List of Tables

List of Figures

Introduction and aim of the PhD thesis

Historically, the development and the use of energy always benefits the progress of human society and civilization. Continuous economic growth, industrial development and social stability are affected by the supply of energy, in particular fossil fuels[1]. Since they constitute the most important source of energy, actually fossil fuels are consumed quickly and they will be exhausted within 100 years if exploited at the current rate[2]. The depletion of natural energy sources, as well as negative environmental effects such as pollution, greenhouse gases emission and global warming have stimulated researchers to study advances renewable off- grid energy technologies: solar, wind, water and many others[3].

In October 2014, the European Union member countries signed the 2030 Climate and Energy Framework Agreement. This framework inevitably requests variations in the habitudes of consumers and energy producers, and opens new perspectives of research. In order to prevent dangerous climate change, three key targets have been proclaimed by the EU as a strategic priority to be achieved by 2030[4]:

- to reduce gas emissions in the EU territory by at least 40% (compared to 1990 levels)
- to bring the share of energy consumption satisfied by renewable sources to at least 27%
- an improvement of at least 27% in energy production efficiency

In the last decades, the thermoelectricity gained much interest in terms of sustainability and reliability on power generation technology. Research and development have been encouraged on thermoelectric (TE) modules which convert heat energy directly into electrical energy. These devices have the ability to either generate a voltage when exposed to a temperature gradient thanks to Seebeck effect, or produce a temperature gradient when supplied by electricity, thanks to Peltier effect [5].

About 70% of energy in the world is wasted as heat and it is released into the environment with a significant influence on global warming [6]. The waste heat produced in all the areas of daily life (e.g. in industry, homes and transport) is one of the most significant sources of clean, fuel-free, available and cheap energy. Thermoelectric generators (TEGs) can take advantage of this huge energy reservoir and transform it into a higher form of energy. In the last decade, thermoelectric generators have been used in an increasing number of fields to provide electrical

power in medical, military, and space applications, where combination of their interesting properties outweigh their high production cost. “Energy harvesting” with thermoelectric generators is based on the use of solid-state devices characterized by no moving parts, absence of noise, reliability and scalability [7], and is an ideal solution for small power generation [8]. Home heating, combustion exhausts, process exhausts, hot gases from drying ovens, cooling tower water and automotive exhaust all generate a huge amount of waste and unused heat [9] that can be converted into electricity by employing thermoelectric devices. Recent improvements are reported to replace the alternator in cars with a thermoelectric generator placed on the exhaust steam, aimed to increase the efficiency [10]. Other TE devices are employed in jet engines [11] or oil and gas pipelines[12].

Researchers and manufacturers are working to increase the efficiency of thermoelectric generators and to develop appropriate processes for mass production. The first thermoelectric materials were very expensive and could generate only a few watts. Actually available systems are able to produce up to 1000 watts. New materials and manufacturing methods enable greater temperature differences to be utilised, and therefore the power output will also continue to rise.

Motivation

The thermoelectric energy conversion system has great appeal in terms of silence, simplicity and reliability if compared to the traditional power generation and refrigeration. The last two decades have seen a significant increase in academic activities and industrial interests in thermoelectric materials. A crucial issue in the application of thermoelectric substrates in waste heat recovery is their stability and oxidation resistance over time at high temperatures. In fact, most of the high-performance TEs, such as tellurides and silicides, can be oxidized at high temperature in air [13]. Therefore, currently thermoelectric devices work at relatively low temperatures (<500°C) to avoid this degradation, but if they could be used at high temperatures, their efficiency would increase. There is an important number of publications that described the several attempts actuated to solve this critical aspect, such as employing vacuum- tight stainless steel containers or inert atmosphere, but obviously this increases considerably the cost of the building devices.

Glass and glass-ceramic based coatings are potential candidates for protecting thermoelectric substrates against oxidative atmosphere. As widely and subsequently discussed in the thesis, they are inexpensive and thermally stable, they have versatile compositions and therefore, their properties can be tailored to make them suitable for coating a large variety of metals and alloys. Although some glass-ceramic systems could be decisive in reducing oxidation, their effectiveness for maintaining transport and electric properties has not been reported yet. To the best of the author’s knowledge, silica-based glassy systems have been already studied in the past as protective coatings on tellurides and skutterudites, but not on silicides,

which are involved in this research. Furthermore, the majority of the research presented in literature focuses on the physical characterizations of the coatings, but only in a few, electrical properties of the substrate were measured, especially after oxidation or thermal cycling tests, as discussed in this thesis. Furthermore, the large amount of residual glassy phase belonged to these glass- based coatings could be beneficial by acting as a crack sealant and conferring self-sealing properties.

Preliminary experiments on the glass-ceramic oxidation protective systems developed during this thesis have shown promising results to reach high electrical performances. This is particularly important because thermoelectric modules that could operate at high temperature and therefore generate more energy per module are not yet available on the market.

Objective

The objective of this study has been the design and the development of innovative oxidation protective coatings for different types of thermoelectric substrates. Glasses and glass-ceramic coatings were produced to protect manganese- and magnesium- based silicide thermoelectrics, with the composition $MnSi_{1.74}$ and $Mg_2Si_{0.487}Sn_{0.5}Sb_{0.013}$, up to 600°C and 500°C respectively. Futhermore, a new silica-based glass ceramic was developed for the titanium suboxide (TiO_x), employed as both thermoelectric and electrode for high temperature (T > 600°C). Concerning the zinc doped tetrahedrite, the effectiveness of hybrid commercial coatings was investigated as oxidation protective systems ($Cu_{11.5}Zn_{0.5}Sb_4S_{13}$) working at 400°C.

In this perspective, the PhD thesis is organized in five chapters. **Chapter 1** gives an introducing overview on thermoelectricity and thermoelectric effects, the thermopower generation technology through the application of thermogenerators (TEGs) and the materials used to produce the thermoelectric substrates involved in this study. Particular attention is focused on their oxidation stability over time at high temperature.

Chapter 2 deals with the state of art of oxidation protective methods for thermoelectric power generation materials. The importance and the rising interest in new glass and glass-ceramic based coating technologies is underlined. Several solutions have been proposed and investigated in literature to solve the oxidation problem in this direction, but almost all of them didn't consider the effectiveness of an oxidation resistant coating respect to the thermoelectric properties.

In **Chapter 3,** the experimental approach used in the present thesis is summarized. The techniques and the instruments employed to design, produce and characterize both the oxidation protective coatings and the thermoelectric substrates are described. This chapter deals with the experimental procedures and methodology used in accomplishing this work.

In **Chapter 4,** the results and the discussions concerning the effectiveness of the using of oxidation protective coating (commercial hybrid resins or innovative glass-ceramics, depending on the thermoelectric substrate) are presented.

Research on oxidation protective coatings for thermoelectric materials is an important task, which helps to understand limitations and opportunities of this technology for future energy conversion systems. Many efforts in this field should be focused on the coating deposition technique, on the increasing of durability and efficiency as well as on the lowering of the production cost. These aspects are fundamental to transfer the production of reliable oxidation protective coatings from the laboratory scale to an industrial one.

The results, obtained and discussed in the present work, represent a promising solution to some critical issues in the thermoelectric devices technology. Useful information about the compatibility between different materials, in complex conditions, are collected and discussed constituting a precious contribute to the actual state of the art in this field. In the final part of the thesis the results are summarized and possible future perspective are discussed.

Chapter 1

Thermoelectricity: an overview

Thermoelectricity is a field of physics that concerns and studies the different phenomena of heat conversion into electricity and vice versa, correlating the heat flow passing through the materials to the electric current that flows through them. This can occur in particular conductive or semiconductor materials called “thermoelectric materials” where these phenomena become appreciable and exploitable.

This chapter represents an overview of the thermoelectric technologies developed since the discovery of the physical phenomena, related to the generation of thermoelectric energy and thermoelectric cooling, respectively the Seebeck and Peltier effects. In the past decades a fast increase in thermoelectric research occurred, followed by alternating periods of poor improvement up to the last years when, due to different technologies, social and environmental factors, the demand for new methods of energy production and management began to increase faster and faster. Thermoelectric effects refer to electronic and thermal properties of a system. For this reason, the objective of this paragraph is to provide an overview about the principles that give rise to the thermoelectric phenomena.

1.1 History of thermoelectricity and thermoelectric effects

The birth of thermoelectricity dates back to the late 1700s, when Alessandro Volta discovered the connection between heat and electricity observing how, by heating the ends of a metal arc, an "electrical voltage" was obtained which would disappear with its cooling [14].

During the 1800s thermoelectricity took on increasingly defined contours thanks to the discovery of its main effects, due to the studies of Thomas Johann Seebeck, Jean Charles Athanase Peltier and William Thomson (Lord Kelvin). These effects are explained by the phenomena of diffusion of charge carriers

(electrons and holes) due to the thermal effect in the conductors (or semiconductors), and in the phenomena of contact between the junctions connecting conductors of different material [15].
The first thermoelectric phenomenon studied was the Seebeck effect [16,17]. In 1821, during an experiment, the physicist T.J. Seebeck, noted that, in a circuit consisting of metal conductors or different semiconductors (copper and bismuth) but connected together, a temperature gradient generated a deviation of the magnetic needle of a compass. Seebeck thought that this phenomenon was correlated with terrestrial magnetism.
A few years later, the Danish physicist Hans Christian Ørsted, understood that the effect had electrical origin, officially decreeing the discovery of that known to us today as Seebeck effect. In fact, the experimental studies of Seebeck led to formulate a relation between heat and electricity. He considered a simple thermocouple junction (Figure 1.1-1) consisting of two dissimilar materials indicated as "A" and "B" electrically connected in series and thermally in parallel. The Seebeck effect is related to a voltage generated at the materials' edges indicated as "cold junction" which is kept at temperature T and "hot junction" which is at T+ ΔT, creating a temperature gradient ΔT.

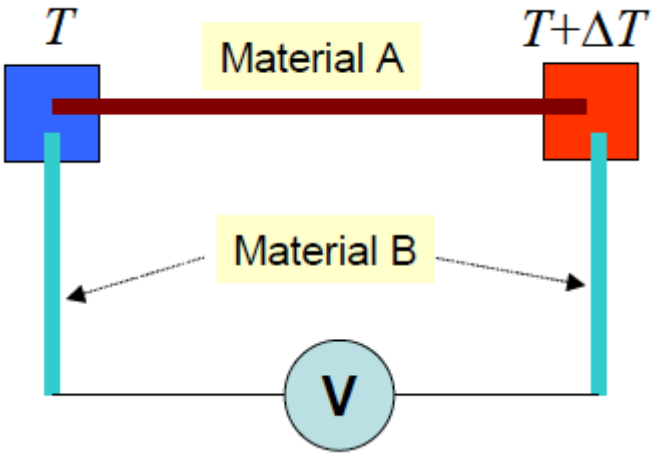

Figure 1.1-1: Diagram showing the Seebeck effect [18]

Under these conditions the electromotive force (ΔV, voltage difference) generated in the circuit is directly linked to ΔT by a proportionality coefficient α, which is an intrinsic property of the material and it is known as Seebeck coefficient or thermopower [18]. It is expressed in μVK^{-1} and is given by the equation *(1)*:

$$\Delta V = \alpha \Delta T \qquad (1)$$

The temperature difference causes the movement of the mobile charge carriers (electrons or holes) towards the cold junction, while the opposite immobile charged carriers remain behind the at the hot junction. Charge movement determines the increment of a thermoelectric voltage V, given by equation *(2)*:

$$V = (\alpha_A - \alpha_B) \Delta T \quad (2)$$

where α_A and α_B are the Seebeck coefficients of the materials A and B respectively, and ΔT is the temperature difference between the junctions.

In 1834 J. C. A. Peltier observed that an electric current flowing in a conductor consisting of two different metals generated a temperature difference that cannot be connected to the Joule effect, discovering the Peltier effect [19], [20].

Peltier effect is the opposite of the Seebeck effect. In fact, if an electrical current flows through the junction of two different materials, heat could be generated or absorbed, according to the current direction. This is an effect cause by the difference in the Fermi energies of the A and B materials.

The Peltier heat (Q), absorbed or generated by the junction is given by the following equation:

$$\frac{dQ}{dT} = (\Pi_A - \Pi_B) \quad (3)$$

where Π_A and Π_B are the Peltier coefficient of A and B materials respectively, and they represent the quantity of heat absorbed by the material when current I passes through it.

Finally, in 1851, the English physicist William Thomson demonstrated that the Seebeck and Peltier effects were closely correlated to each other [21]: an electric current flowing in the presence of a gradient of temperature gives rise to a heat flow proportional to both the current and the thermal gradient. The heat absorbed or emitted is called Thomson heat (Q) and it is expressed by the following equation:

$$Q = \rho J^2 - \mu^* J \frac{dT}{dx} \quad (4)$$

where ρ is the resistivity of the material and $\frac{dT}{dx}$ is the temperature gradient along the conductor, J is the current density and μ^* is the Thomson coefficient. The first term ρJ^2 is referred to as the Joule heating (irreversible) and the second part is the Thomson heating [22].

The fundamental difference between the Seebeck and Peltier effect separately considered and the Thomson effect is that the latter can manifest itself in a single material and therefore does not need of junctions to be detected.

The first applications of Thomson's theories came only after 1909 thanks to the German physicist Edmund Altenkirch [23], [24] who derived the maximum efficiency of a thermoelectric generator and of a cooler. In fact, based on the thermoelectric effects describes above, two different configuration of thermoelectric device can be produced: for power generation (Figure 1.1-2a) operating through the Seebeck effect and for cooling systems (Figure 1.1-2b), operating through the Peltier effect [18].

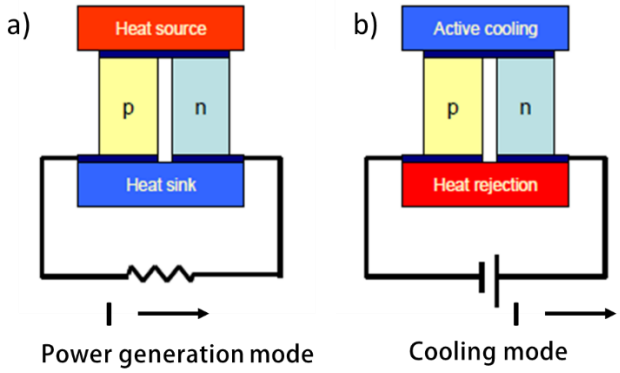

Figure 1.1-2: General operative configuration for (a) solid-state power generators and (b) solid- state refrigerators [18]

The development of thermoelectric applications began in the early 1930s, with the advent of semiconductor thermoelectric materials, mainly by the Russian school [25].

The absence of moving parts made these generators silent and reliable, ideal for military field devices or sensors; numerous applications have been developed essentially for the military and aerospace sector which are still strictly secret.

In the West, particularly in the U.S.A., the activity of research and development of thermoelectricity began immediately after the war, and was intense between 1950 and 1960, when numerous materials with rather interesting thermoelectric properties have been discovered. This is the case, for example, of the bismuth telluride (Bi_2Te_3), used in Peltier cells on the market (platelets refrigerants), or of the silicon and germanium (SiGe) alloys used for feeding the space probes in thermoelectric radioisotope generators (RTG), for example for Voyager, Galileo and Cassini Missions (Figure 1.1-3). Although until the early 1960s, over 100 companies were active in the thermoelectric sector, ten years later, thermoelectricity saw only a dozen companies involved, up to only two industries, Melcor and Marlow, active in the early 1990s.

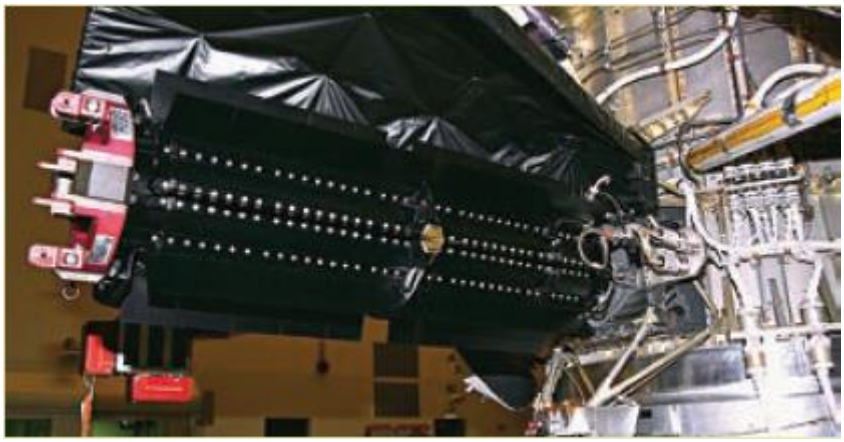

Figure 1.1-3: Third RTG installed in the Saturn probe Cassini. Source: Nasa

This progressive disengagement was motivated by the observation that, despite the discovery of new materials, the efficiency of thermoelectric generators invariably remained an order of magnitude lower than that was erroneously predicted in the late 1950s. In 1970 the "International Thermoelectric Society" was born, which brings together all the leading thermoelectric experts and promotes it, presenting all the technological innovations in an international meeting held annually since 1970 in the largest capitals of the world.

Since 1993, interest in thermoelectricity was revived [26] because the research activity was driven by a theoretical forecast: the efficiency of thermoelectric devices can be significantly increased through the use of low-dimensional systems, for example by using nano thermoelectric materials structured.
At the same time, the production cost of thermoelectric modules continued to fall both for physiological reasons of the market and thanks to academic studies, which led to the definition of new low-cost construction standards, and will make the use of this technology extremely advantageous in the direct conversion of heat into electricity.
Present-day applications, include space and automotive fields, both in cooling and electricity generation [25], but several example will be described in the following paragraph.

1.2 Thermoelectric generators (TEGs)

The increased interest in thermoelectric materials is due to the possibility of designing thermoelectric generators (TEGs). These are reliable and promising candidates as solid-state devices for converting the huge amount of industry and automobile exhausted waste heat into electricity, operating where the use of other technologies is not suitable.

The first thermoelectric devices were confined in military and aerospace industries, where reliability and quiet operation of the equipment were more important requests than high costs and energy efficiency. In this direction, efforts in the automotive market are already underway through the integration of TEGs into combustion engines. The goal is to replace the alternator in cars for enhancing the overall system efficiency using the exhaust steam heat recovery [27][28][29].

TEGs are ideal for small distributed power generation thanks to several advantages [7][30][31] respect to traditional energy sources:

- small size
- no rotating, vibration or moving parts
- noise absence
- high reliability and scalability
- environmentally- friendly
- selection of low cost materials
- gas emission free

Thermoelectric materials have the potential to revolutionize automotive heating, ventilation, and air-conditioning (HVAC) systems[32]. Improving

thermoelectric materials can enable the production of HVAC systems with the very desirable and unique features above mentioned.

Almost 70% of world energy is recognized to be waste heat that is dispersed into the atmosphere and is considered as one of the main causes leading to global warming [33].

Waste heat is produced in all the areas of daily life and in literature [34] is possible to find various sources that generate unused energy. They can be divided in three broad categories, depending upon the average temperature generated by them:

- low temperature sources (<250 °C): examples of sources in this range are condenser for air conditioning/refrigeration, ovens, air compressors, furnace doors and electric circuit;

- mid temperature sources (250–650 °C): for example steam boiler exhaust, gas turbine exhaust, drying and baking ovens, automotive exhaust;

- high temperature sources (>650 °C): include metal refining furnaces, steel heating furnace, hydrogen plants. The natural decay of the radio-isotopes (such as Pu238) is another example for this class of devices. They produce high temperature heat (800–1000°C) and TEGs utilizing these heat sources are known as radio-isotope thermoelectric power generators (RTG) [35], where the heat comes from the nuclear decay of a radioactive isotope which is an advantage because highly available, robust and compact.

TEGs have been mainly proposed for waste heat recovery in mid- and high-temperature applications because of the potential for appreciable power generation [9,36,37], and heat source temperatures and applications are shown in Table 1.2-1.

Table 1.2-1: Waste heat source temperatures provided for mid- and high- temperature TEGs applications [31]

Application	***Heat source temperature***	***Reference***
Automotive exhaust	400- 700°C	[38]
Diesel generator exhaust	~ 500°C	[39]
Primary aluminium Hall- Heroult cells	700- 900°C	[9,36]
Glass melting regenerative furnace	~ 450°C	[9,36]

A thermoelectric power generator module consists of several thermocouples electrically connected in series, each of them made of n- and p- type thermoelectric materials (Figure 1.2-1). Thermally these thermocouples are connected in parallel so that heat is able to flow through the TE materials. Electrical insulation on the hot and cold sides stabilizes the thermocouples arranged with this configuration.

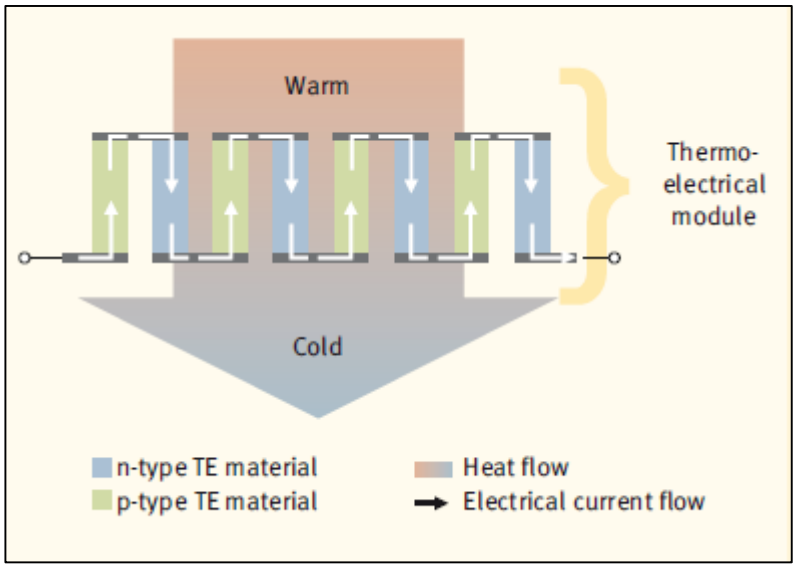

Figure 1.2-1: Design and operative scheme of a thermoelectric generator.

Source: Fraunhofer IPM

The p- and n- legs which constitute each thermocouple are joined by a metal interconnect and the series of legs are placed within a heat source and a heat sink. The typical and complete architecture of a single p-n thermoelectric couple showing electrical and thermal interfaces, is shown in the Figure 1.2-2.

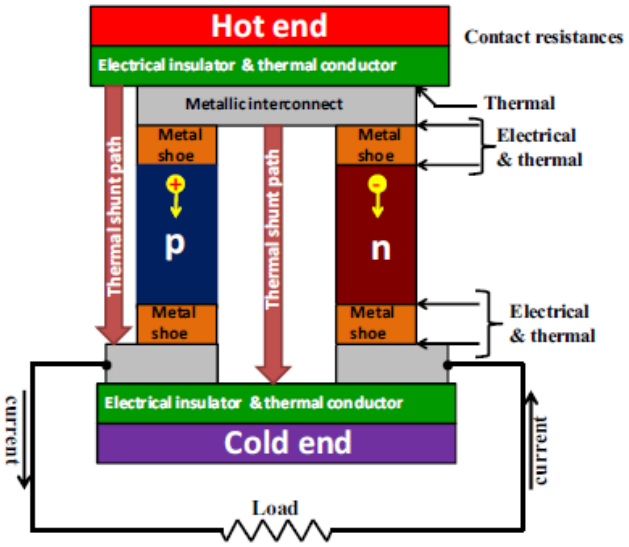

Figure 1.2-2: Scheme of the architecture of a single thermocouple [34]

TEG devices have a very complex structure and present many technical challenges and process implementation. For instance, a metallurgical bond should be guaranteed between the TE leg and the interconnects. These latter must be prepared in a specific and suitable size, in such a way to reduce the total electrical and thermal resistance, avoiding that a considerable proportion of the thermoelectrically generated energy is lost due to ohmic losses. The soldering /

brazing material must not diffuse into the thermoelectric material, in fact sometimes a barrier is required. The substrate must be electrically insulating but thermally conductive.

TEGs can operate at several different temperature ranges, so the application areas are many: communications, healthcare, aerospace, biomedical, military. Waste heat recovery is the main and also the more attractive because in this field TEGs can help to reduce the adverse effects of global warming. In fact, generating the electricity by harvesting waste heat which is a by-product of industries, automobile engines and solar power, TE devices can meet the environmental issues as already widely discussed in the introductory chapter. Other interesting areas are considering TEG as an alternative to their usual configuration.
For example the communication and health care body-mounted electronic devices require a portable and autonomous energy source having an electrical power between 5 μW and 1W with a life expectancy of ~ 5 years [40–42]. Nowadays these medical devices use batteries usually containing toxic substances (such as sulfuric acid, mercury, zinc, lithium, lead, nickel and cadmium) which are not human friendly and so, in some cases, TEGs represent a valid option. Furthermore, TEGs can be used as sensors (Figure 1.2-3), because of their ability to convert heat into electrical signals, such as cryogenic heat-flux sensors, water- condensation detectors, fluid-flow sensors, and infrared sensors[43,44]. However, concerning size and light weight, the most effective structure for thermoelectric sensors are based on thin-films [45].

Figure 1.2-3: Thermoelectric sensor. Source: Fraunhofer IPM, Kai- Uwe Wudtke

In space missions (from mars and beyond it), radio isotope thermoelectric generators (RTGs) have been used by the United States NASA to provide electrical power for spacecraft since 1961[46]. RTG technology has been used during the last four decades to convert the thermal power generated by a radioisotope heat source to electricity for many planetary exploration missions. The radioisotope thermoelectric generator can operate continuously and independently from the sun. That property suits well with the long time (7–10 years) missions which use either

a radioactive or a nuclear reactor heat source to provide a wide range of electrical power levels [35]. The last generator launched is the Radioisotope Thermoelectric Generator MMRTG [47], built in Mars Science Laboratory (Figure 1.2-4). It consisted of PbTe/TAGS TE materials, where the TAGS incorporates Tellurium (Te), Silver (Ag), Germanium (Ge) and Antimony (Sb), and with a mass of 45 Kg produced ~121W, with an efficiency of 6.0%.

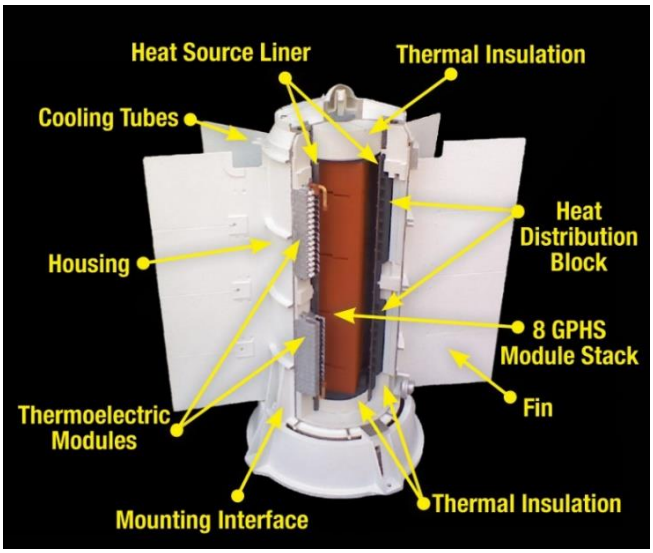

Figure 1.2-4: Multi-Mission Radioisotope Thermoelectric Generator [46]

The main markets are connected with cooling powers below 200 W: small refrigerator and beer tender [25], wine cabinets, ice cream makers, yogurt maker and others. There are today also many applications in the automotive sector, for example to keep drinks fresh in thermal cup holders (Figure 1.2-5), or for climate controlled seat (Figure 1.2-6).

Figure 1.2-5: Peltier elements can keep drinks fresh in thermal cup holders.

Source: Dometic Group

Figure 1.2-6: Cooler for the front seats of a car. Source: General Motors

More commonly, TEGS are used in electronic devices. Heat flux of microprocessor is gradually higher for the increasing of the microprocessor power and the reduction of the microprocessors sizes, with several difficulties related to cooling of the system. Hence, harvesting thermoelectric energy from the wasted heat leveraging on the temperature gradient between the processor surface and the environment (Figure 1.2-7), it is possible to meet the resolution of these issues [48].

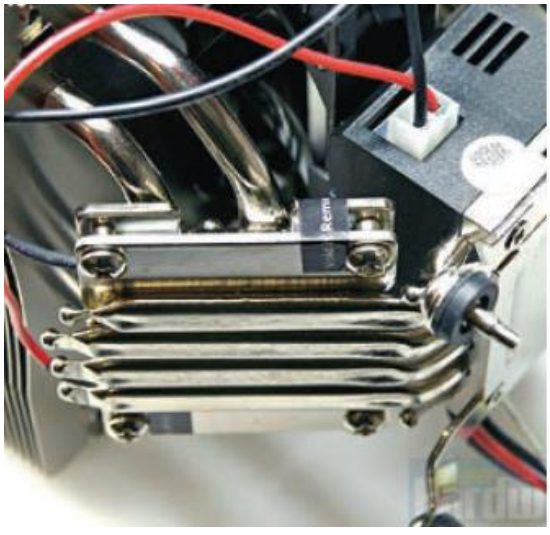

Figure 1.2-7: Peltier cooler in PC enable optimal processor performance.

Source: pcgameshardware

One of the interesting applications of TEGs is in producing electrical power from the heat generated by concentrating the solar energy in buildings and houses

heating and cooling systems [49–51]. In summer, utilizing the electrical power generated by photovoltaic/thermal modules, the TE device works as a cooler. In winter, the voltage applied on thermoelectric device is reversed. Thus, the thermoelectric device could release heat to increase the temperature of the room.

Automotive field needs to enhance the energy efficiency of vehicle engines in order to comply with severe CO_2 targets for 2020. Most of the energy is currently lost in the cooling and exhaust systems, and especially that contained in the hot exhaust gas can be transformed using TEGs into electrical energy in order to partially replace alternators and charge batteries (Figure 1.2-8). This is able to decrease the fuel consumption and consequently CO_2 emissions. Some years ago, different multinational car companies like BMW [52], Ford [53], Renault [54] and Honda [55] demonstrated their interest in exhaust heat recovery developing systems based on TEGs. Generally, the TEGs are placed on the exhaust pipe surface (shaped as a rectangle, hexagon, etc.) and they are cooled with cold blocks using engine coolant. This technology has not yet been installed in present production cars and is still in the concept stages. Most studies reported that converting unused waste heat would enable fuel savings of 3-5% [55–57], but more recently different number of project results showed that these values cannot be implemented, reaching in reality only ~1% of efficiency [58]. Therefore, more research is needed in particular towards materials, topological and electronic optimization in order to improve TEGs performances.

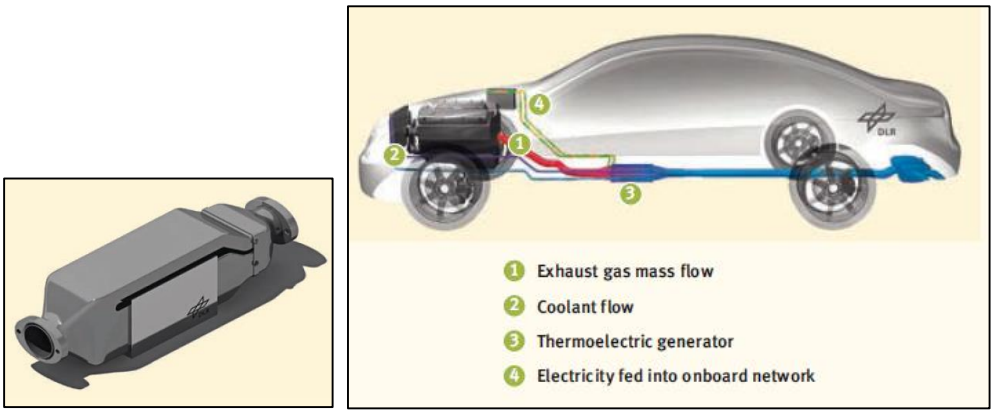

Figure 1.2-8: CAD model of a TEG component (on the left) for an integrated exhaust system of a combustion engine-powered vehicle (on the right). Source: DLR- FK

All the above applications are just some of the possible employments of thermoelectric modules and a lot of other perspectives still have to be studied and discovered.

1.2.1 Analysis of thermoelectric behaviour

1.2.1.1 Figure of Merit (zT) and thermoelectric efficiency (η)

In 1911, Altenkirch introduced the concept of the dimensionless unit called "Figure of Merit" to assess the performance of thermoelectric materials [59] and it is defined by the following equation:

$$zT = \frac{\alpha^2 \sigma T}{k} \qquad (5)$$

where:
α = Seebeck coefficient [μVK^{-1}]
σ = electrical conductivity [Sm^{-1}]
k = thermal conductivity [$Wm^{-1}K^{-1}$]

These three transport parameters α, σ e k depend on each other as a function of different factors such as the band structure and the carrier concentration. Figure 1.2-9 shows how the figure of merit varies depending on the three thermoelectric properties through carrier concentration tuning [7]. In particular, α and σ reciprocally vary, making improvements in the figure of merit more difficult. Furthermore, σ and α are inversely related, so it is not possible to rise the thermoelectric power factor upon an ideal value for a bulk material. However, a good thermoelectric material must have a high merit index. This implies that for a given temperature, the material would have very high values for both electrical conductivity (to allow the conduction of electricity which would create a potential difference across the sample) and Seebeck coefficient, but needs to have a very low thermal conductivity (to maintain the temperature gradient between the hot and the cold side). The high electrical conductivity decreases the joule heating and increases the thermoelectric voltage produced, on the other side the low thermal conductivity reduces the heat transfer between the junctions. Good performing thermoelectric materials are typically heavily doped semiconductors with a carrier concentration between 10^{19} and 10^{21} carriers per cm^3.

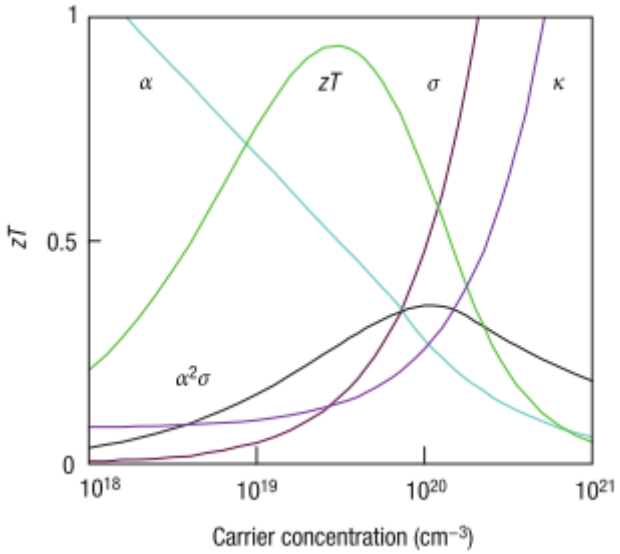

Figure 1.2-9: Figure of Merit maximization of a thermoelectric, which involves a compromise of thermal conductivity (k) and Seebeck coefficient (α) with electrical conductivity (σ) [7]

Since TE devices are constructed from several couples of p- type and n- type legs, the Figure of Merit of such devices is given by the equation *(6)*:

$$zT = \frac{(\alpha_p - \alpha_n)^2 T}{[(\rho_n k_n)^{1/2} + (\rho_p k_p)^{1/2}]^2} \quad (6)$$

where α_p, ρ_p, and k_p are the Seebeck coefficient, the resistivity, and the thermal conductivity of the p-type material, respectively, while α_n, ρ_n, and k_n are the Seebeck coefficient, the resistivity, and the thermal conductivity of the n-type material, respectively.

The equation (*7)* defines the device's efficiency[7,31,34,60]:

$$\eta = \frac{T_h - T_c}{T_h} \left(\frac{\sqrt{1 + zT_{avg}} - 1}{\sqrt{1 + zT_{avg}} + T_c/T_h} \right) \quad (7)$$

where T_C is the temperature in correspondence of the cold side, T_h is the hot side temperature and zT_{avg} is the average figure-of-merit for each thermoelement in the module temperature range. According to this relation, when zT is infinite, the efficiency is equal to the ideal Carnot. For this reason, thermoelectric generators can be considered Carnot hot engines [61].

In addition to the intrinsic properties of the TE materials, many factors determine the device efficiency. The efficiency of the TEG is much lower than the efficiency of the thermoelectric material itself since energy could also be required for the working operations of the system, for example in pumping the cooling fluid through the cold side of heat exchangers. Therefore, the net power of TEGs must take into account these parasitic power losses.

All the electrical contacts have to be characterized by the lowest value of contact resistance (i.e. the value of contact resistance should be far less than the bulk resistance of the thermoelement). Analogously, thermal contact should be as close to ideal value as possible, so that almost all the heat is able to flow through the thermoelements and the heat flowing through the shunt-path is nearly zero. Coefficient of thermal expansion (CTE) is another very important parameter to be considered especially in high temperature or thermal cycling conditions. TE legs are rigidly held in place by a solder joint to the electrical interconnect and substrate, so a CTE mismatch between the different materials, would determine stresses concentration causing cracks and efficiency lose. Certainly, this is an aspect which limits the choice of the set of materials involved.

Consequently, one of the main challenges in the power generation field through the application of thermoelectrics is certainly the choice of efficient materials. The selection standard to identify n- and p-type thermoelectric materials are the following:

- stable and high zT_{avg} in the temperature range of the application for several years. The stability of zT is linked to σ, α and k. Formation of voids, pores, cracks or sublimation (also partial) of the material and

chemical reactions of the thermoelectric with the metallic interconnects or with undesirable atmospheric gases could carry out to the thermoelement degradation.

- TE materials should be low cost and consisted of earth-abundant elements
- p- and n-type semiconductors should have zT_{avg} of nearly similar value at the operating temperature

Since the Figure of Merit is a temperature dependent parameter, using the same material in a broad range of temperature gradient is not possible. To make this technology more efficient, it is advised to utilize different materials, so that a thermoelectric element with high zT at high temperature is coupled with a material with high zT at low T.

However, a certain compatibility between the two materials involved in this large temperature range must be guaranteed. Compatibility is related to both heat and electricity which have to flow without difficulties in this two materials connected in series. For a specific material the compatibility factor "c" is calculated with the following equation [62,63]:

$$c = \frac{[(1 + zT)^2 - 1]}{\alpha\, T} \qquad (8)$$

This parameter should not differ more than 2, otherwise the segments will not function with the maximum efficiency and the overall power produced by the TEG will be lower than expected.

One of the most important requirements in order to have highly efficient TEG, is that p- and n-type thermoelements material should have high zT_{avg} of nearly similar value at the operating temperature. The maximum theoretical efficiency expected for TEG as a function of temperature difference between hot and cold sides (assuming the cold end is around 300 K) for materials having different zT_{avg} is shown in Figure 1.2-10.

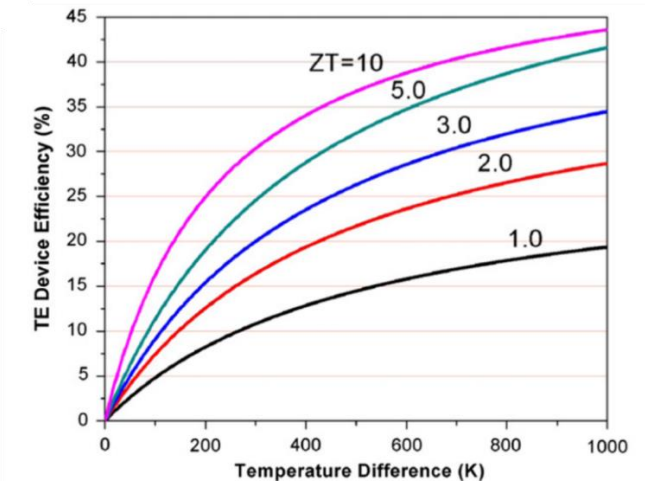

Figure 1.2-10: Thermoelectric energy conversion as a function of zT [64]

The commercial thermoelectric materials have a relatively low zT of ~1 and the average thermoelectric generators on the market have a conversion efficiency of approximately 5%. As it can be seen, there is a great potential to seek new materials with zT values of 2–3 to provide the desired conversion efficiencies in order to be competitive with traditional mechanical energy conversion systems [64]. Theoretically, for a material of zT_{avg} ~ 5 a conversion efficiency of ~ 30% with ΔT of 500 K can be reached. However, it is critical to synthesize thermoelectric materials with high zT with the aim to promote the practical applications of thermoelectric materials. In this direction, the major activities in thermoelectric materials have been focused on the increase of the Seebeck coefficient and the reduction of the thermal conductivity. Despite this, on the experimental side the situation for high zT materials is quite different. The temperature dependence of zT for various n- and p-type thermoelectric materials is shown in Figure 1.2-11 [7], where the highest zT of most of the materials is contained in the range of 0.8–1.2.

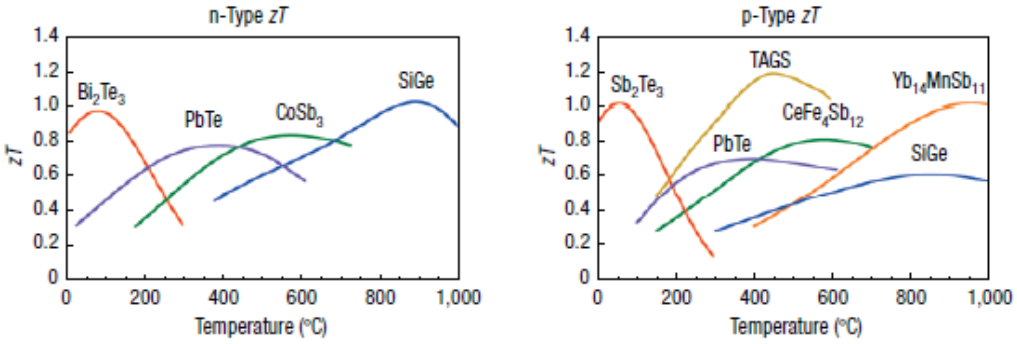

Figure 1.2-11: Figure of merit zT of commercial materials for thermoelectric power generation: n-type on the left and p-type on the right [7]

1.2.1.2 The Seebeck coefficient (α)

As reported in the 1.1 paragraph, the thermoelectric effect manifests when a temperature difference between two points in a conductor or semiconductor causes a voltage difference between these two points. In a different way, a temperature gradient in a conductor or semiconductor generates a built-in electric field [65]. The Seebeck coefficient, or also called thermopower, measures the magnitude of this effect and it is the ratio of the induced thermoelectric voltage to the temperature difference across the material. It expresses the thermoelectric voltage developed per unit of temperature difference in a semiconductor. Only the Seebeck voltage difference between different metals can be measured [18]. In effect, thermoelectric devices are able to act as electricity generators just through this effect.

The Seebeck coefficient is expressed in V/K or more commonly in μV/K and it is given by the equation *(9)*:

$$\alpha = \frac{8\pi^2 K_B^2}{3eh^2} m * T\left(\frac{\pi}{3n}\right)^{2/3} \qquad (9)$$

where K_B is the Boltzmann's constant, e is the electronic charge, h is the Plunck's constant, T is the temperature, m^* is the effective mass of the carrier and n is the

carrier concentration. The equation (*10)* shows that, at a specific temperature, Seebeck coefficient is proportional to the effective mass and to the inverse of the carrier concentration.

$$\alpha \propto \frac{m*}{n^{2/3}} \qquad (10)$$

Therefore, to have a large Seebeck coefficient, the material should have low carrier concentration and a high effective mass. This is the reason why semiconductors have higher thermopower than metals have.

The Seebeck coefficient for semiconductors materials, based on the band model for finely grained material, is given by the following equation [66]:

$$\alpha = \pm \frac{K_B}{e}[\ (2+ \mathrm{r}\ ) + \ln \frac{2(2\pi m^*_{p(n)} k_B)^{3/2}}{h^3 p(n)}] \qquad (11)$$

where *r* is the scattering factor, $m^*_{p(n)}$ is the effective mass of holes (electrons) and *p(n)* is the carrier concentration. From this equation, it can be deduced that Seebeck coefficient is inversely proportional to the carrier concentration, as explained before.

It was discovered that only the use of different materials, linked together in a so-called thermocouple, shows the Seebeck effect. For two legs of the same material, no Seebeck effect occurs, although both derivations intrinsically possess a Seebeck coefficient, for reasons of symmetry. However, it is present because the Seebeck effect is a mass property and depends neither on the specific arrangement of cables or material nor on the specific method of joining them [67].

Generally, most metals have Seebeck coefficients of 10 μV/K or less, but semiconductor materials are promising for thermocouple manufacturing because they have Seebeck coefficients higher than 100 μV/ K. It should be underlined that the relationship between the voltage of Seebeck and the temperature is linear only for small temperature changes (Hamid Elsheikh et al., 2014), because in the contrary case, this relationship becomes non-linear. Therefore, it is important to work the temperature at which the Seebeck coefficient is specified.

1.2.1.3 The electrical resistivity (ρ)

Electrical resistivity is the reciprocal of the electrical conductivity (σ), which represents the measure of the material's ability to conduct electric current, as given by equation *(12)*:

$$\sigma = \frac{1}{\rho} = ne\mu \qquad (12)$$

where μ is the mobility of the charge carriers, and it is obtained from the equation *(13)*:

$$\mu = \frac{e\tau}{m^*} \qquad (13)$$

where τ is the mean scattering time between the collisions for the carriers. It can be said that the electrical conductivity is directly proportional to the carrier concentration.

Electrical resistivity and conductivity are both important material– dependent properties that usually are function of temperature. In fact, the ρ value at room temperature indicates whether a material is an insulator (ρ is on the order of 10^6 Ω·m or more) or a metal (ρ is on the order of 10^{-6} Ω·m or less)[68]. The resistivity of a semiconductor material falls between the metal and insulator values. The optimum range of electrical resistivity for a thermoelectric material is in the range 10^{-3}- 10^{-2} Ω·m [69]. Eventual variations in the electrical resistivity depend on changes in the carrier concentration and the mean free path of the charge carriers. When the charge carriers reach the material are reflected/scattered by its surface[70]. In order to obtain a low electrical resistivity in semiconductors, the lattice should have almost infinite conductance at low temperatures, but in reality, the conductivity of semiconductors is very low at low temperatures due to the limited number of free electrons[68]. Information about the intrinsic properties of the materials involved can be acquired by the analysis of the temperature dependence of the electrical resistivity.

1.2.1.4 The thermal conductivity (k)

The thermal conductivity is the ability of the material to transfer heat under the effect of temperature gradient. It is given by the sum of two contributes , $k = k_e + k_L$, where k_e is related to electrons and holes transporting heat, while k_L is defined by phonons traveling across the lattice[66]. Therefore, the figure of merit can be optimized by maximizing the electrical conductivity and minimizing the thermal conductivity. Nevertheless, there is a relation between these two thermoelectric properties known as Wiedemann- Franz law and it is valid for electrons that obeys to degenerate and non- degenerate statistics:

$k_e = L_0 \sigma T$,

$L_0 = (\pi^2/3)(K_B/e)^2 = 2.44 \cdot 10^{-8}\ (K^2/V^2)$,

$L_0 = 2(K_B/e)^2 = 1.48 \cdot 10^{-8}\ (K^2/V^2)$

where L_0 is a constant called Lorentz's number and K_B is the Boltzman constant. Subsequently the increasing of the electrical conductivity, not only electronic thermal conductivity raises, but also decrease the thermopower. Therefore, zT optimization becomes a challenge, because while the power factor can in some cases be increased by changing the concentration of charge carriers, decreasing k and k_L is more difficult, especially for k_L, which depends on the structure, rigidity and other properties which characterize the lattice [71].

The ideal thermoelectric material would have regions of its structure composed of a high- mobility semiconductor, which supplies the electron- crystal electronic structure, crossed with a phonon glass. This last region would be ideal for hosting

dopants and disordered structure without damaging the carrier mobility in the electron- crystal region[72].

1.2.2 Thermoelectric materials

During last sixty years of research, numerous thermoelectric materials have been studied and employed. In order to identify the most efficient TE materials to be used in a specific application an appropriate analysis of costs and performances is necessary [65]. Elements not so abundant on earth could be utilized to make high-impact discoveries and obtain better understanding of materials trends [34], but when materials are employed for commercial application, scarcity is an important and decisive point to consider in design phase.

Presence in the nature, facility of transport, assembly and number of technologies using the same material are factor which influence the device cost that has to be considered.

In this section a brief overview on the most important categories of thermoelectric materials will be given [31,73–75], focusing on the state of art of the thermoelectric substrates involved in this research.

Chalcogenides, like Bi_2Te_3, Bi_2Se_3, PbTe, PbSe, SnTe, have a long history as thermoelectric materials especially bismuth telluride and lead telluride, which were investigated since the 1950s. They showed promising and potential characteristics for mid and low temperature application. Many new compounds derived from traditional tellurides, and their solid solutions with selenium and antimony are employed, for instance Se doped $HfTe_5$ and $ZrTe_5$. Since Tellurium is quite expensive due its low abundance in earth, a lot of companies working in photovoltaic area already considered a recovery and recycle program, so in most chalcogenides it has been replaced by S and Se.

New families have been studied following the concepts above mentioned, such as nanostructuring and looking for a PGEC (phonon glass electronic crystal) material[76]. New approaches have been investigated in TE materials such as clatherates, sulfides and selenides, oxides, half-Heuslers and skutterudites [77][78].

Sulfides and selenides, like SnSe, $AgCrSe_2$, $CuCrSe_2$, $TiSe_2$, $AgSbTe_2$, PbS, are the most used substitutes for Te-chalcogenides because the small variation in electronegativity between Se, S and Te makes possible to design and manifacture semiconductor with appropriate band gap for TE application over a wide range of T.

Half-Heuslers (HH) are intermetallic compounds showing very interesting thermoelectric properties in the mid and high T range. They are formulated as XYZ where X and Y are transition metals (X = Ti, Zr, Hf, V, Mn, Nb and Y = Fe, Co, Ni, Pt) and Z represents generally Sn or Sb.

The three filled sublattices are independently subject to chemical manipulation to optimize the thermoelectric properties of the compounds. They are promising for

commercial application for their easy synthesis, environmental friendly nature and low cost.

Moreover, they have high melting points of 1100–1300°C and a high chemical stability with essentially zero sublimation at temperatures near 1000°C.

Skutterudites The typical binary skutteridites are MX_3 families where M is a transition metal (M = Co, Rh, Ir) and X represents elements as P, As or Sb. These compounds are known for their high electron mobility, high Seebeck but also high lattice thermal conductivity. One successful chemical approach to correct this negative effect was to fill vacant space in the structure with many different elements including lanthanide, actinide, alkaline-earth, alkali, thallium, and Group IV elements [79]. Skutterudite antimonides possess the largest voids and are thus of interest for thermoelectric applications.

Clatherates represent another class of compounds which has open structures; they are able to host tetrahedrally coordinate bounded atoms, such as Al, Ga, Si, Ge, or Sn. Some examples are Sr_8Ga_{16} Ge_{30}, Ba_8 In_{16} Sn_{30}, $Ba_8Ga_{16}Ge_{30}$, $Ba_8Ga_{16}Si_{30}$, $Ba_8Ga_{16}Sn_{30}$, $Sr_8Ga_{16}Ge_{30}$.

This really complex structure leads to a very low thermal conductivity but is not enough to be suitable for TE application. Even if the power factor does not yet match that of bismuth telluride, at room T at 300 K equal to 0.34 for a Ge clatherate and it's sufficient.

Silicides are in general compounds that contain silicon and generate interest because of its abundance on the earth. In fact, although silicon is not a so good TE material, its high thermal conductivity, low cost and the possibility of enhancement of favourable TE properties, make compounds based on silicon some of the most common TE substrates.

Alloying Ge, already creates point defects sufficient to decrease sensibly the κ_t and gain a zT ~1. Furthermore, zT >>1 are achieved by nanostructuring approach with both p- and n-type $Si_{80}Ge_{20}$ compound. Ge can be replaced by another low-cost material, so other silicon compounds are actually under development.

Very promising results have been obtained with n-type magnesium silicide (Mg_2Si) compounds [80], which are low cost and non-toxic and p-type high manganese silicide ($Mn_{27}Si_{47}$) [81], both involved in this thesis.

Oxides are a related new class of materials in the thermoelectric field, because their properties have been investigated in detail since '90s [34]. Originally, their low carrier mobility made oxides poor thermoelectric materials, but they present lot of advantages because consisting of simple, abundant and harmless elements. They present a good stability at high T in air (a big issue for other TE materials were the need for coatings and protection systems).

Examples of good p-type thermoelectric oxides are the layered cobaltites $NaCo_2O_4$, $Ca_4Co_3O_9$ and $Bi_2Sr_2Co_2O_9$ with large Seebeck coefficients, low thermal conductivities. The most promising candidates for n-type oxide thermoelectric materials include perovskite-type as $SrTiO_3$ and $CaMnO_3$[82],[83] and titania based- materials[84].

Recently, certain **polymers**, have also exhibit thermoelectric properties at low temperatures. Especially conducting polymers, have shown various advantages

related to an easy and low cost of fabrication, light weight, and flexibility [61] [85]. Some examples [86] are polyacetylene, polypyrroles, polyanilines, polythiophenes, ethyl-enedioxythiophene, carbon fiber polymer-matrix structural composites.

In the following subparagraphs, the state of art of the TE substrates involved in this research is reported, with particular focus on the behaviour to oxidation.

1.2.2.1 Higher manganese silicide

Silicides are promising candidates for thermoelectric materials due to their abundance, chemical stability at operating temperatures and non- toxicity of the constituent elements. Since they fulfil these requirements are considered as a very promising class of material for power applications [87][88].

In particular, higher manganese silicide (HMS) represents a family of p-type thermoelectric with a generic composition $MnSi_{\gamma}$. They are semiconductors, and they are employed in the thermoelectric devices in mid temperature range with a zT value of ~0.6 at around 800 K[89–91].

Commonly HMSs are used in the thermoelectric module construction together their compatible n-type counterpart represented by $Mg_2Si_{1-x}Sn_x$. However, the difference of their related coefficient of thermal expansion (n-type silicides have CTE around $16\text{-}18\cdot10^{-6}$ K^{-1} whereas p-type HMS around $9\text{-}13\cdot10^{-6}$ K^{-1}) can lead to a stresses concentration resulting by the high temperature gradient between hot and cold side. Consequently, the overall degradation of the legs and a reduction of the efficiency of the device is inevitable.

The γ value can vary between 1.71-1.75. HMSs are the only known compounds in which the Si amounts (63-64 at. %) exceeds that of Mn. Synthesis of monophasic HMS is difficult due to the not very wide composition range in the phase diagram shown in Figure 1.2-12 [92].

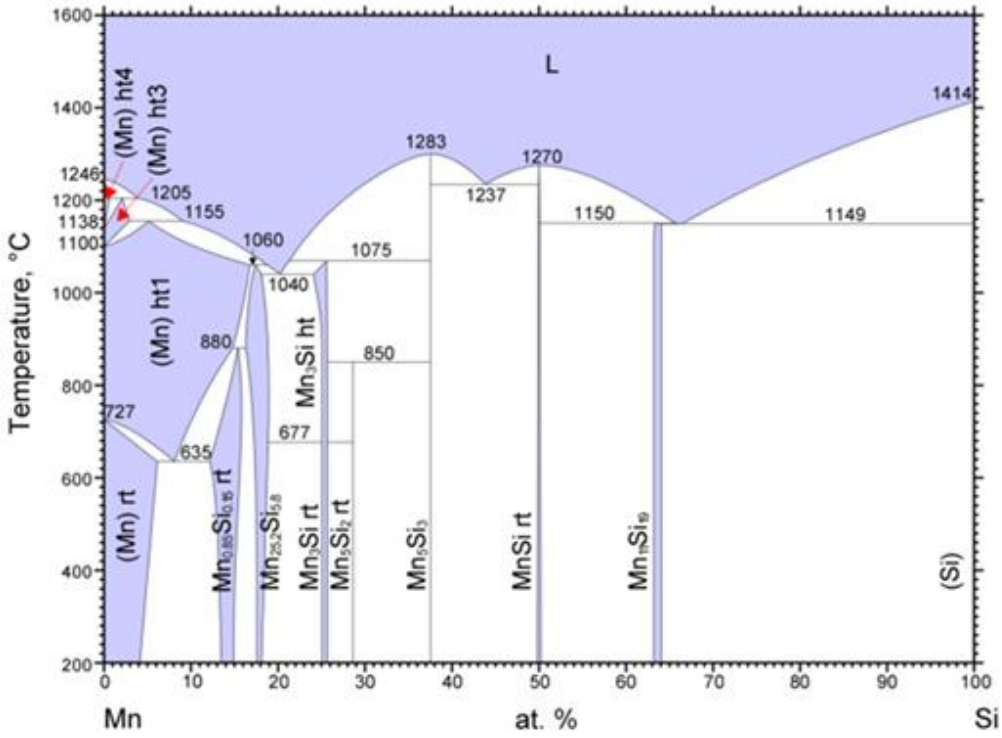

Figure 1.2-12: Mn-Si binary phase diagram [92]

Moreover, the possible evaporation of volatiles elements and the fact that solidification is not eutectical are reasons that make the synthesis process challenging. The undesired formation of MnSi during processes is the main negative effect that influences thermoelectric properties of HMS. MnSi is a good thermal conductor and it has a general negative effect on all the thermoelectric coefficient and properties[93]. The control of the amount in its bulk is a hot spot for researches.

Small variations in the composition determine similar phases such as $Mn_{11}Si_{19}$ ($MnSi_{1.72}$), $Mn_{15}Si_{26}$ ($MnSi_{1.73}$), $Mn_{27}Si_{47}$ ($MnSi_{1.74}$) and Mn_4Si_7 ($MnSi_{1.75}$). They are a series of crystallographically distinct phases referred to as the Nowtony Chimney Ladder phases which consist of a “chimney” subsystem of Si and a “ladder” subsystem of Mn.

All these crystal structures have tetragonal symmetry, as shown in Figure 1.2-13.

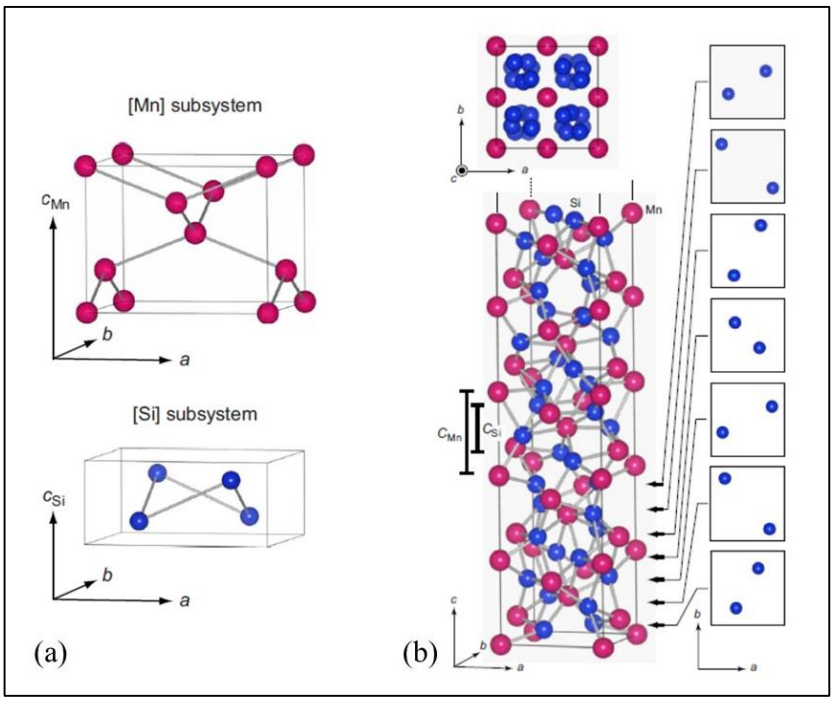

Figure 1.2-13: (a) Structural model for Mn and Si subsystem and (b) complete modulated structure for $MnSi_{\gamma}$ at 295K [94] .

Studies on electron diffraction[94] revealed that both these subsystems have nearly the same lattice parameter *a* (Figure 1.2- 13a) of ~5.5 Å but length of *c* axis is usually different. Miyazaki et al. [95] reported that γ represents the stoichiometry of the phase but also the c-axis ratio $\gamma = c_{Mn} / c_{Si}$. Figure 1.2- 13b shows the modulated structure of MnSiγ at 295 K. The upper right figure illustrates the c-axis projection to represent the helical arrangement of the chimney- Si atoms along the c-axis. The lower figure describes the atoms within 5 x c_{Mn} length.

This different atomic arrangement, and consequently the difference from one stoichiometry to another, affect the magnitude of the band gap (which usually is around 0.6 eV in undoped sample) and the density of state near the Fermi level, causing a small change in the thermoelectric properties.

A crucial aspect of the success of thermoelectric silicides is their stability over time and the oxidation resistance. Okada et al [96] studied the oxidation process of $Mn_{27}Si_{47}$ crystals in air, and found that the oxidation reaction initiated at about 760°C, producing MnSi, Mn_2O_3, and SiO_2. More recently, a silicide material, $Mn_3Si_4Al_2$, with good oxidation resistance, because thanks to a passive layer formed on its surface, was found to have constant electrical resistivity for 2 days at 600°C in air [97]. In the same work, thermoelectric modules developed from n-type $Mn_3Si_4Al_2$ and p-type $MnSi_{1.75}$ have achieved maximum power generation of 9.4 W with a heat-source temperature of 600°C in air.

The formation of a passive layer on higher manganese silicide when thermally treated up to 500°C in air was discussed by Funahashi et al.[98]. Furthermore, Ning et al.[13] demonstrated that at 600°C, HMS which is not protected, reacts with

oxygen, leading to the formation of a silica scale (of about 5 microns) on a Si-deficient layer (which is MnSi) formed on the top of the TE substrate.

The critical issue of the instability in HMS at high temperatures was investigated very recently by Ghodke et al. [99] using in situ x-ray diffraction, by which they observed a phase transformation above 500°C from $Mn_{27}Si_{47}$ to $Mn_{16}Si_{26}$ accompanied by a small amount of MnSi precipitation. This results are consistent with the earlier studies on HMS presented by Allam et al.[100] , who reported the same transformation at 800°C and that in the $Mn_{11}Si_{19}$ at 1000°C.

Although these silicide materials have good oxidation resistance, the output power of the modules decreases with time at temperatures higher than 500°C in air. Therefore, in order to use silicide modules over wide range of the temperatures this decrease in the output power must be overcome.

1.2.2.2 Sb doped $Mg_2(Si,Sn)$ based thermoelectric

Magnesium silicide is a n-type semiconductor belonging to the Mg_2X (X = Si, Ge, Sn and Pb) compounds. Its anti-fluorite structure allows to achieve an energy bandgap of 0.784 eV[101]. Commonly it can be doped in order to reach good thermoelectric properties as zT of 0.86 at around 870 K through Bi-doping[102] but it is quite limited because characterized by its relatively high thermal conductivity. N-type solid solutions of Mg_2Si with Mg_2Sn [103–106] and/or Mg_2Ge [107,108] have been investigated with the aim to reduce their thermal conductivity and consequently increase the thermoelectric performances. One of the best results in terms of figure of merit has been reported for $Mg_{2.08}Si_{0.364}Sn_{0.6}Sb_{0.036}$ with zT of 1.5 at 723 K[109].

The use of the magnesium silicide and its solid solutions is limited because of their behaviour inclined to oxidation above ~ 400 °C [110,111]. The first research worked on the oxidation of Mg_2Si-Mg_2Sn solid solutions reported similar results as for the pure compounds[112,113]. Although for $Mg_2Si_{0.4}Sn_{0.6}$, the oxidation starts at temperature of 400°C in air, materials with lower Sn content are reported to be more resistant towards catastrophic oxidation. Recent studies based on X-ray diffraction confirmed that $Mg_2Si_{1-x}Sn_x$ starts decomposing in air at 400°C producing MgO, Si, Sn and other $Mg_2Si_{1-x}Sn_x$ solid solutions [113].

Sondergard et al. [114] investigated the thermal stability in air of $Mg_2Si_{0.4}Sn_{0.6}$ and $Mg_2Si_{0.6}Sn_{0.4}$ up to 400 °C, reporting the formation of Sn-rich $Mg_2Si_{1-x}Sn_x$, as the major phase, and MgO for powders heated in air, while sintered pellets showed an higher stability. Skomedal et al. [115] studied the degradation of $Mg_2Si_{1-x}Sn_x$ with $0.1 < x < 0.6$, demonstrating a slow oxidation rate for temperatures below 430 °C, while in the temperature range between 430-500 °C, all of the alloys exhibited breakaway oxidation. This study explained that the breakaway behaviour was due to a combination of two main mechanisms: firstly, the depletion of Mg at the alloy-oxide interface leading to the decomposition of the Sn-rich phase forming liquid Sn, and secondly, stress build-up between alloy and oxide, causing cracks and non-protective oxide layers.

1.2.2.3 Titanium suboxide

Titanium oxides belong to a class of materials of specific interest in various applications such as tribology, photocatalysis, electrical and elettrochemical fields [116].

Titanium oxide can exist as different intermediate substoichiometries of the Ti-O binary system, they are called Magnéli phases and have compositions Ti_nO_{2n-1} with n >4 [117]. In particular, Magnéli phases are interesting because of their special structural complexity and unusual electrical and thermal properties[118]. Since titanium suboxide is able to reach high electrical conductivity, moderate Seebeck coefficient and low thermal conductivity, its application as thermoelectric materials can be advantageous[119]. Studies concerning the potential of titanium suboxide as TE material and for manufacturing of power generation modules were reported by an increasing number of publications[84], [120], [121–123].

Although TiO_x has not a very high Seebeck coefficient, its remarkable advantage is the unlimited availability and the low raw material as well as the manufacturing costs respect other TE materials. Since titanium suboxide is an ordinary ceramic compound, its synthesis can be carried out without difficulties. In fact, pressure- less sintering can be conducted easily, without important loss of thermoelectric performances. This makes its manufacturing economically competitive[123].

A drawback related to the use of this ceramic oxide is represented by its transformation into TiO_2 at temperatures >500°C. In order to avoid this reoxidation, oxidation resistant glass- based coating would help to overcome this negative aspect expanding the temperature range for titanium suboxides for high- temperature application [123].

1.2.2.4 Tetrahedrite

Tetrahedrite ($Cu_{12}Sb_4S_{13}$) is a sulphur semiconductor belonging to the ternary I-V-VI group, where I includes Cu and Ag, V represents P, As, Sb, Bi, and VI group involved S, Se, Te elements. It can be considered as ternary derivative structure from zincblende or wurtzite semiconductors[124]. CAS compound (Cu-Sb-S) attracted the interest of many researchers in last years, because of their intrinsically low lattice thermal conductivity[125]. One of the reason why tetrahedrite is considered a good thermoelectric material is related to its highly symmetric and complex crystal structure with a large number of atoms per unit cell, helpful in providing low thermal conductivity [126,127] and useful for improving the power factor [128]. It has a sphalerite-like structure with 58 atoms arranged in a cubic cell (*I43m*) crystalize in a cubic structure[129], as shown in Figure 1.2-14 (a), made of different polyhedrons as CuS_4 tetrahedra, CuS_3 triangles and SbS_3 pyramids [128]. This structure, with ione-pair electrons on Sb sites is the origin of the low lattice thermal conductivity[127], which is shared by other compounds in the Cu-Sb-S system [130] such as chalcostibite [131] ($CuSbS_2$), famatinite [132][133] (Cu_3SbS_4) and skinnerite (Cu_3SbS_3) [134].

Naturally, tetrahedrite occurs with the composition $Cu_{12-x}M_x(Sb,As)_4S_{13}$, which is a solid solution of As rich tennantite ($Cu_{12}As_4S_{13}$) and Sb rich tetrahedrite ($Cu_{12}Sb_4S_{13}$). It has characterized by high hole concentration (consequently it is a p- type semiconductor). Several elements have been proposed as dopants in THD. Their effects are linked mainly to the carrier concentration that influences the Seebeck coefficient and the electrical properties. Models can be used to predict the ideal dopant concentration range that is able to give a reasonable and useful zT value. The literature related to this thermoelectric substrate showed that the best thermoelectric properties are achieved by replacing Cu^{2+} atoms with Zn: for an un-doped sample zT is 0.6 at 400 °C, and increases up to 0.9 at around 450 °C with Zn substitution, due to a reduction of the thermal conductivity[135].

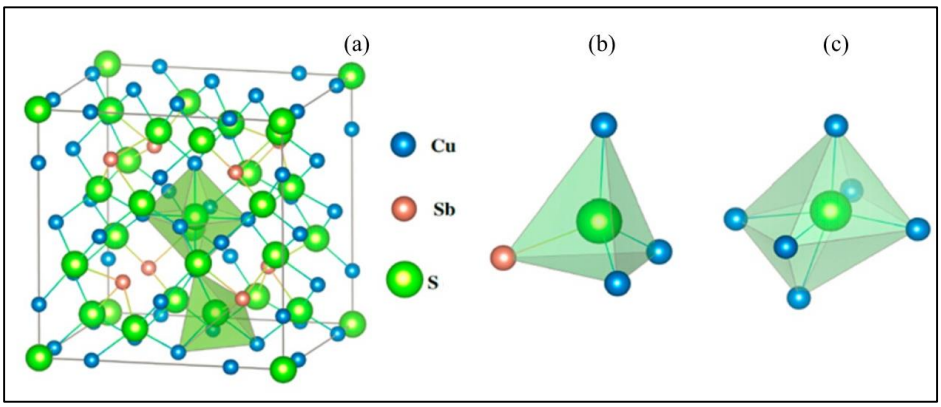

Figure 1.2-14: (a) Tetrahedrite crystal structure and polyhedrons with S atom at the center: (b) tetrahedral site and (c) octahedral site [129].

The tetrahedrite has limited thermal stability due to sulphur loss. For example, the decomposition of $Cu_{12}SbS_{13}$ into Cu_3SbS_3 at 522°C has been reported by Braga et al.[136]. Barbier et al. [137] observed the same phase transformation at 530°C and a weight loss due to sulphur volatilization. Furthermore, diffraction patterns recorded at different temperatures, showed that the main phase is $Cu_{12}Sb_4S_{13}$ below 410°C and Cu_3SbS_3 above 490°C. Between these two temperatures, the interpretation of the XRD patterns is reported to be quite difficult, but the authors suggested that the decomposition of the tetrahedrite into Cu_3SbS_3 can also lead to the formation of intermediate phases such as Cu_3SbS_2 and $Cu_{2-\delta}S$. Nevertheless, Chetty et al. [138] reported that tetrahedrite is usually stable only up to ~ 330°C , and that the overall stability may increase or decrease depending on the dopants. More recently the oxidation behaviour of a tetrahedrite was investigated by Pi et al.[139], reporting that when $Cu_{12}Sb_4S_{13}$ samples were exposed at temperatures higher than 450°C in air, the tetrahedrite decomposed into Cu-S binary sulfides ($Cu_{1.96}S$, Cu_2S, Cu_9S_8), SbO binary oxides (Sb_2O_3, SbO_2), and ternary compounds (Cu-Sb-S and Sb-S-O), with antimony oxides content increasing as the ageing time increased. Gonçalves et al. [140] showed that the formation of a $Cu_{2-x}S$ surface barrier, due to the tetrahedrite decomposition, decreased the corrosion rate at 275 °C acting as a weak passivation layer. However, this layer was not effective at 350 °C and 375 °C because of the simultaneous action of sulphur sublimation.

Impurities and second phases were found in all of the samples at the end of oxidation tests, evidencing the need of an efficient protective coating, but no studies have been performed to identify a suitable coating for this thermoelectric material.

Chapter 2

Oxidation protective coatings: state of art

A critical aspect for the success of TE materials in waste heat recovery is their stability and oxidation resistance over time at high temperature. In fact, most of the high- performance thermoelectrics, are metal alloys and semiconductors which can be easily oxidized at high temperature. For this reason, current devices usually working at relatively low temperatures (< 500°C), just to avoid degradation. However, if they would be used at high T, their efficiency could improve.

The oxidation of the surface of the thermoelectric degrades the power generation and significantly limits the long-term reliability and efficiency of TE modules. As reported by W. Park et al.[141], the performances of TE modules degrades with thermal cycling as the constituents materials and interfaces are exposed to broad temperature gradients. To develop practical thermoelectric modules that can be applied to various intermediate-temperature-range waste heat re-generation sites (e.g., steel industry, incinerators, auto- mobiles), anti-oxidation technology for thermoelectric modules is needed [142,143].

Several solutions have been proposed and evaluated to solve the oxidation problem in the intermediate temperature thermoelectric module.

2.1 Oxidation protective common methods

Recently, several studies of high performance thermoelectric materials reported high zT results, but all these preliminary researches were obtained under vacuum or under controlled, inert gas conditions due to severe oxidation problems. Since the operation temperature of an intermediate temperature thermoelectric module is very high (300–700 °C), all the components of the thermoelectric device are exposed to severe oxidizing conditions.

Already in 1975, C. E. Kelly had shown that a similar issue with SiGe unicouples used in RTGs had been dealt with by applying a thin Si_3N_4 coating for a few millimeters on legs nears the hot junction, typically at 1273 K[144]. More

recently, the suppression of the oxidation of an intermediate temperature thermoelectric module were investigated exploiting other ceramic- based coating[143]. Four different ceramic oxides (Al_2O_3, Y_2O_3, yttria-stabilized zirconia and samaria-doped ceria) were coated onto Mg_2Si thermoelectric leg surfaces (Figure 2.1-1) and their anti-oxidation characteristics were compared. While the first three oxide- based layers failed to prevent the progression of oxidation at 700 °C, YSZ showed potential oxidation suppression characteristics and therefore its reliability was investigated trough thermal cycling tests from room temperature to 600 °C. Even if a detailed investigation after 10 thermal cycles showed slight migration of oxygen into the Mg_2Si thermoelectric no massive oxygen penetration was detected (as for Al_2O_3, Y_2O_3, and samaria- doped ceria coatings).

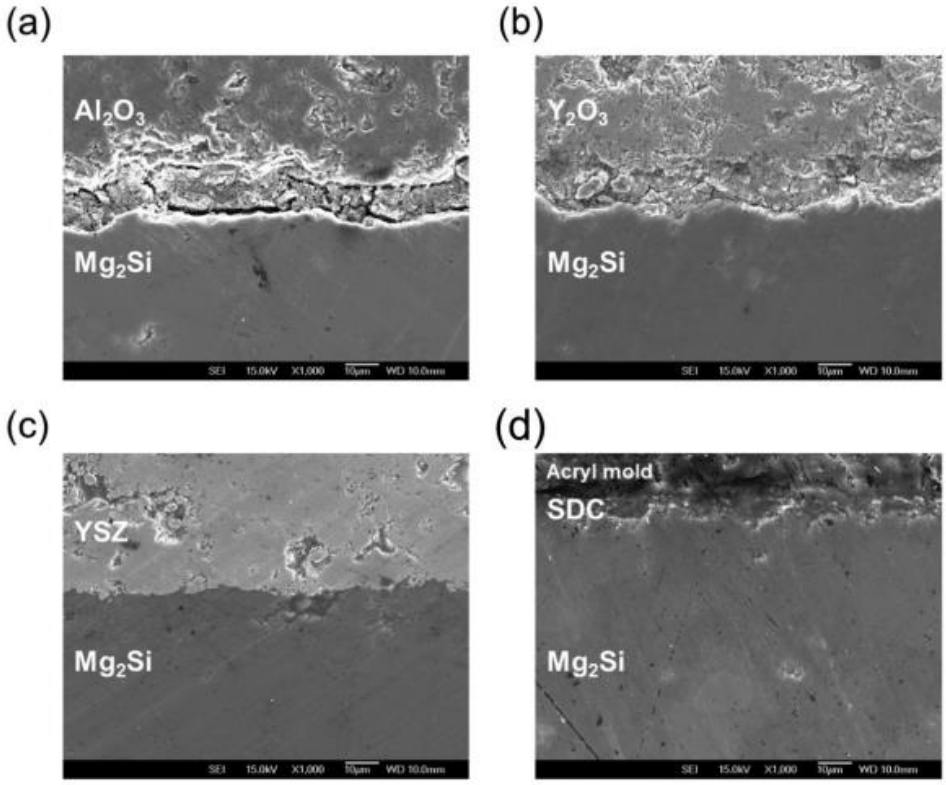

Figure 2.1-1: Cross-section SEM images of Mg2Si thermal treated for 1 hour and coated with: (a) alumina, (b) yittria, (c) YSZ, and (d) SDC (samaria-doped ceria) [143]

Other promising alternatives have been investigated as coating materials, especially for skutterudite based thermoelectrics, consisting for instance in metallic foils [145,146], metallic electrodes [147] or metallic films [148,149]. In the Saber et al. work [147], Ta, Ti, Mo and V- based material were tested as protective layers, resulting that increasing the coating thickness decreases the conversion efficiency but increases the load electrical power of the unicouple. Despite their high CTE, Ti or V coatings were best in terms of the effect on the unicouple performance. They caused the smallest decreases, while Ta or Mo coating with lower CTEs, resulted in the largest decreases in the conversion efficiency. With thin coatings, however, the effects on conversion efficiency and electrical power of the unicouple are

significantly smaller. Concluding, a Mo coating resulted the best since it has the smallest CTE and low vapour pressure.

Some researchers faced the challenge of oxidation phenomenon by using a hermetically sealing packaging. A metallic housing containing the module and keeping it under vacuum or immersed in inert gases such as argon [150] (Figure 2.1-2) or in aerogels[151–154] (Figure 2.1-3).

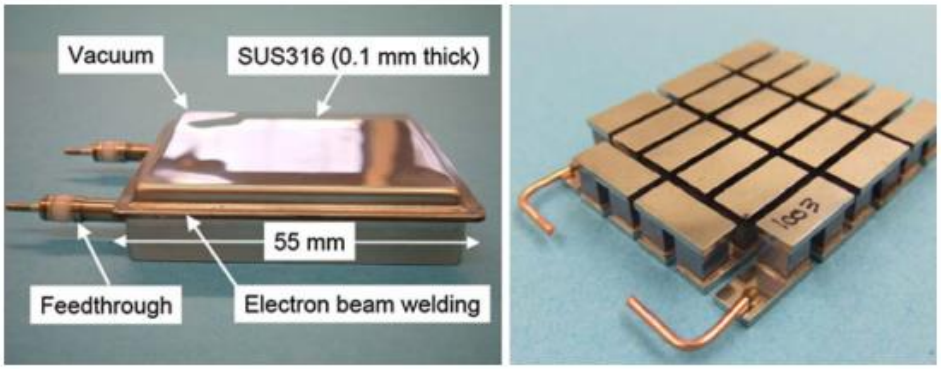

Figure 2.1-2: Encapsulated TE module (left) in which the SiGe module (right) is encased [150]

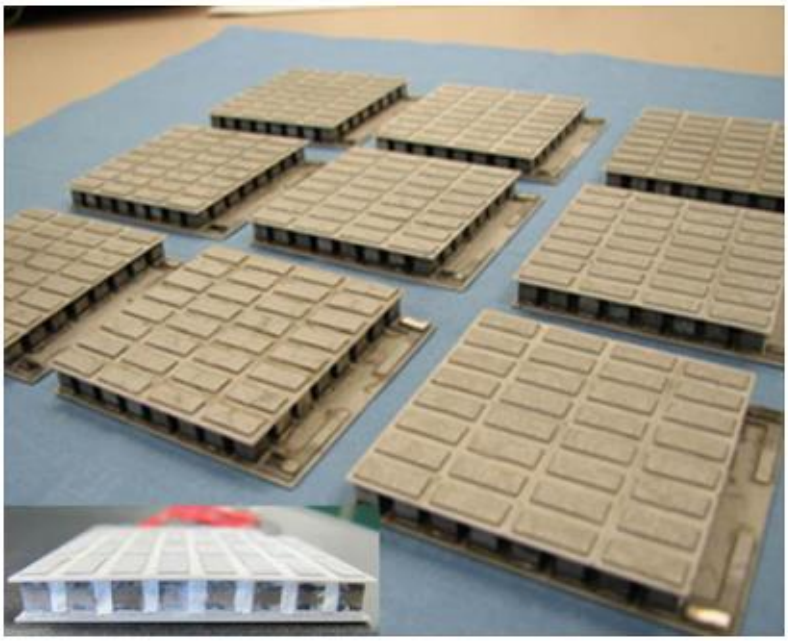

Figure 2.1-3: Skutterudite devices produced by Marlow Industries. The image in the lower left corner is a full-sized skutterudite module after encapsulation with aerogel [151]

Several researches at the Jet Propulsion Laboratory of Pasadina, CA, USA [155] identified aerogel as an effective sublimation barrier for a wide range of thermoelectric technologies based on SiGe, novel Skutterudites, TAGS, and PbTe. Aerogel typically consists of extremely porous (>99% porous) silicon dioxide, which has very low thermal and electrical conductivity. Since aerogel has interconnected pores, with size in the range of angstroms to tens of nanometers, the

path required for metal vapour to permeate in aerogel is extremely tortuous, thus significantly decreasing sublimation rates. This solution is suitable for mid temperature range (300°-700°C), but the significantly rising costs of these metallic housing structures and the additional reliability issues of sealing for the long term make this technology difficult to apply in practical waste-heat power regeneration sites. Also the selection of the filler, which in the Skutterudite-based thermoelectric modules [151] consisting in a casted ortho-organo-silicon- based sol mixture and condensed to form a silicon oxide gel, must be accurate to be stable during operating conditions. Filling the void space within the device could help the module to better resist to mechanical stresses and to be less affected by impacts. However, a reliability issue, related to the sealing for a long term application, could make this solution not so desirable to be applied in practice in waste-heat recovery devices. This skutterudite module solution sometimes is even not sufficient to prevent oxidation on the thermolegs surface, so it could be required a local solution that can also reduce the sublimation risk of Sb and to potentially increase the thermal conversion efficiency of the module by reducing radiative and convective heat losses from the TE legs. A schematic diagram showing how degradation can occur in a typical n- and p-power generation couple in a SKD-based materials TE device is represented in Figure 2.1-4 [156]. A typical couple consisting of n- and p-type legs connected on the hot side with an interconnect (Fig. 2.1-4a). After heating, n- and p-type legs shows air sensitive behaviour, leading to the substrates oxidation (Fig. 2.1-4b). It has been shown also by Garcia-Canadas J. et al. that the rapid degradation of thermoelectric modules consisting of n-type $Yb_xCo_4Sb_{12}$ and p-type $Ce_xCoFe_3Sb_{12}$ was due to oxidation from testing in air [157]. While heating a couple in an inert atmosphere can prevent oxidation and sublimation of species such as Sb from SKD [151] responsible for causing couple performance degradation (Fig. 2.1-4c). An enamel layer, used as suggested by Y. S. Park et al. [156] as protective coating, could prevent both oxidation and sublimation (Fig. 2.1-4d). It is about a silica-based enamel used in powder form consisting of silicon and sodium oxide (66at.% oxygen, 11at.% silicon, 11at.% sodium, 6at.% fluorine, 2at.% aluminium, 2at.% nitrogen, 1at.% barium, and 1at.% calcium) with which n-type $Ba_{0.05}Yb_{0.025}CoSb_3$ and p-type $Ce_{0.9}Co_{0.5}Fe_{3.5}Sb_{12}$ were successfully coated to prevent their oxidation up to 600 °C in air continuously for 8 days or thermally cycled for 20 cycles.

Thick enamel layers have been developed as oxidation inhibiting coating also by Zawadzka et al. [158] to protect $CoSb_3$ up to 600°C. In the case of ceramic coating technology, radio frequency magnetron sputtered silicide multilayers have been deposited to protect $CoSb_3$ [159] up to 500°C. Furthermore, also ceramic composite protective coatings were reported in literature as an anti- oxidation layer for skutterudite thermoelectric material thermally aged at 600°C. A coating slurry was obtained by Dong et al. mixing uniformly hybrid sol, glass frit (main chemical components: SnO and P_2O_5 small amount of ZnO and SiO2) or alumina particles and ethyl alcohol as solvent [142]. Later, a siloxane resin based- composite borosilicate glass consisting in a dispersion system of modified nano-silica aerogel

and micro glass powder was tested in air up to 550°C [160] showing good oxidation resistance.

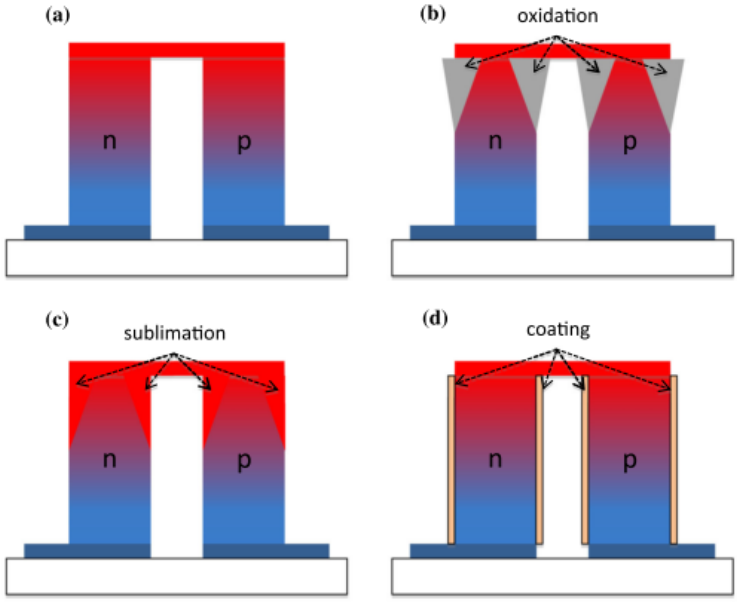

Figure 2.1-4: A schematic diagram showing how degradation can occur in a typical n/p power generation couple [156]

Scientific papers dedicated to protective coatings for silicides, two of the thermoelectric substrates involved in this PhD thesis, are not so many. To protect Mg_2Si, Tani et al. [161] suggested the development of oxidation-resistant iron silicide thin films (ß-$FeSi_2$), which possess excellent oxidation-resistance up to 800 °C. As alternative to iron silicide, Battiston et al. [162] investigated on $MoSi_2$, as an attractive material suitable to corrosion protection at high temperature due to its high melting point (2030 °C), excellent oxidation resistance and diffusion barrier characteristics.

Plasma sprayed yttria stabilized zirconia and atomic layer deposited (ALD) alumina have been proposed as oxidation barriers for pure magnesium silicides [143] and $Mg_2Si_{0.4}Sn_{0.6}$ [163] up to 550- 600°C.

2.2 Oxidation protective glass-ceramic and glass-based coatings

Glass-ceramic and glass-based coatings are potentially optimal candidates for protecting thermoelectrics against oxidation. Firstly, they soften and flow above glass softening temperature (T_s) at the interface for coating the TE substrate. Furthermore, they are easy to manufacture, inexpensive and thermally stable, with low electrical and thermal conductivity, and thanks to the versatility of compositions and properties, are excellent materials as low cost protective coatings. In fact, some of their characteristic properties can be tailored in order to make them suitable for coating different types of substrates and to satisfy the requirements in terms of thermo-chemical stability and thermo-mechanical compatibility with other materials. In particular, the coefficient of thermal expansion (CTE) must be as close as possible to that of the materials to be coated, thus avoiding residual stresses at the thermoelectric/glass-ceramic interface[164]. The development of oxidation-resistant glass-ceramics is an easy efficient method to overcome the main drawback of oxidation and could extend the temperature range for the thermoelectric materials.

Since the composition of the glass influences the properties of the glass-ceramic, it is really important to know the effect that the different constituents oxides have on the amorphous network. This is related to the cation coordination number and single bond strength; it also gives the possibility to predict the crystalline phases which will be present in the glass-ceramic and to predict some thermal (T_g, glass transition temperature) and thermo-mechanical properties (CTE).

A glass consists of three main components: network formers, network modifiers, and intermediate oxides, and additives as minor components. A schematic of a generic glass structure is shown in Figure 2.2-1 [165].

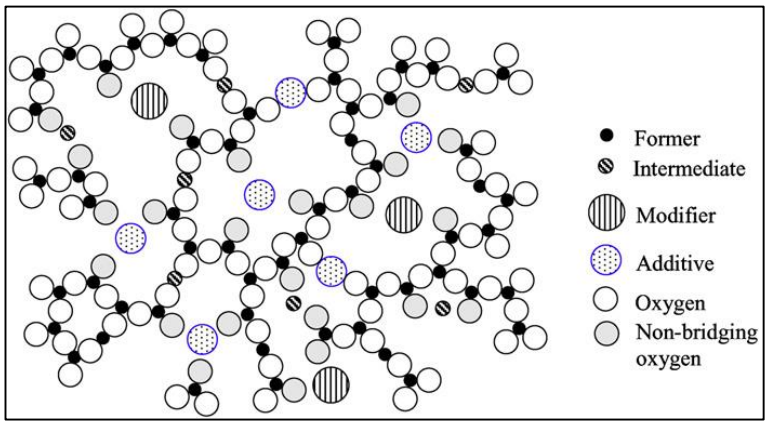

Figure 2.2-1: A scheme of glass structure showing network formers, intermediates, modifiers, additives, bridging and non-bridging oxygen [165]

Common glass formers are SiO_2 and B_2O_3, their coordination number is between 3 and 4 and have higher bond strength (80- 120 Kcals); they form an

amorphous network in which the cations act as the centres of glass polyhedral units (tetrahedra and triangles), which are connected each other. Alkali (Li_2O, Na_2O and K_2O) and alkaline-earth (BaO, SrO, CaO and MgO) oxides are network modifiers, with a coordination number between 6 and 12 and lower bond strength (10- 60 kcals). Since they occupy random positions in-between the polyhedral, they interrupt the network, generating non-bridging oxygen. Consequently, the glass transition temperature (T_g) and the softening point (T_s) decrease and the coefficient of thermal expansion increases. They also give additional oxygen ions in order to maintain the charge neutrality. Intermediate oxides like Al_2O_3 and Ga_2O_3, give cations that have higher valance and lower coordination number (between 4 and 6), with bond strength between the values of formers and modifiers They may or may not participate in the glass network. Usually they hinder devitrification and modify glass viscosity [165]. Additives tailor the desired glass properties although they are not necessary constituents. Some rare earth metal oxides, such as La_2O_3 and Nd_2O_3, and transition metal oxides, such as TiO_2, ZnO, and Y_2O_3, are some examples of additives in a glass. If the amount of an additive is $\leq$ 10 mol%, it is called nucleating agent, which can tailor glass properties by influencing its devitrification. Transition metal oxides such as ZnO, NiO, TiO_2, Cr_2O_3, and ZrO_2 are common nucleating agents. However, there is no strict distinction between additives and nucleating agents. Modifiers and additives create non-bridging oxygen species in order to maintain charge neutrality in a glass- structure. Different oxides used in common seal glasses for solid oxide fuel cells can be used to produce potential oxidation protective glass-ceramic coatings too, and their functions are shown in the Table 2.2-1.

Table 2.2-1: Functions of different oxides constituents a potential oxidation protective glass-based coating [165]

Glass constituent	Oxide	Function
Network former	SiO_2, B_2O_3	Form glass network Determine Tg and Ts Determine CTE Determine adhesion/wetting with other substrates
Network modifier	Li_2O, Na_2O, K_2O BaO, SrO, CaO, MgO	Maintain charge neutrality Create non-bridging oxygen species Modify Tg, Ts, and CTE
Intermediate	Al_2O_3 , Ga_2O_3	Hinder devitrification Modify glass viscosity
Additive	La_2O_3, Nd_2O_3, Y_2O_3	Modify glass viscosity Increase CTE
	ZnO, PbO	Improve glass flowability
	NiO, CuO, CoO, MnO, Cr_2O_3, V_2O_5	Improve glass adhesion to other substrates
	TiO_2, ZrO_2	Induce devitrification

In the glass-ceramic method, glasses can be used as pressure-less coatings for high temperature applications, because after their softening, they can crystallize to obtain stable and thermo-mechanically resistant glass-ceramic coatings.

The development of a glass-ceramic coating starts with the design, the production and the characterization of a glass. The transformation into a glass-ceramic occurs through the sinter-crystallization process of fine powdered glasses [164], which consists in a heat treatment carried out at temperatures around the softening point and in a partial crystallization of the amorphous microstructure.

Considering the whole process, sintering and crystallization phenomena can interact, and therefore affecting the final density of glass-ceramic materials. The specific order of the events in the sinter-crystallization process is a critical aspect which allows the production of dense glass-ceramic coatings, with desired thermo-mechanical properties and microstructure.

Glass-based coatings can be subjected to devitrification during the deposition thermal treatment. Typically, this is a desirable process; in fact, the formation of one or more crystalline phases improves the mechanical properties of the material and can help to tailor and adjust the thermo-mechanical behavior [166]. The design of the initial composition of the parent glass should take into account the properties of the material will change after crystallization; this is closely related to the nature and quantity of the crystalline phases formed. Table 2.2-2 shows some crystalline phases commonly observed in alkaline-earth containing glass ceramics with their CTE.

In some cases, glass-ceramic coating compositions can be designed to have an adequate amount of residual glass phase. In this way, the viscous flow of the glassy phase could provide self-healing effect [167,168], ie, glasses and glass-ceramics can be heated above their softening point temperature (T_s) to heal creaks produced during thermal cycling working conditions (Figure 2.2-2). At the same time, T_s should be higher than operating temperatures to avoid an excessive flow. Furthermore, it is also necessary to consider the possible chemical reactions of the coating components with the TE substrates in the relevant operating conditions as well as the stability of the coating in the oxidative atmospheres to which it will be exposed.

Table 2.2-2: Common crystalline phases produced during the devitrification of alkaline-earth containing silicate glasses and their CTEs [165]

Devitrified phases	Formula	CTE ($\times 10^{-6}\,°C^{-1}$)
Quartz	SiO_2	11.2–23.3
Enstatite	$MgSiO_3$	9.0–12.0
Clinoenstatite	$MgSiO_3$	7.8–13.5
Protoenstatite	$MgSiO_3$	9.8
Forsterite	Mg_2SiO_4	9.4
Wollastonite	$CaSiO_3$	9.4
Calcium orthosilicate	Ca_2SiO_4	10.8–14.4
Barium silicate	$BaSiO_3$	10.5–12.5
	$Ba_2Si_3O_8$	12.6
Barium borate	BaB_2O_4	$\alpha_a = 4.0$ $\alpha_c = 36.0$
Barium zirconate	$BaZrO_3$	7.9
Hexacelsian	$BaAl_2Si_2O_8$	6.6–8.0
Monocelsian	$BaAl_2Si_2O_8$	2.3
Orthorhombic celsian	$BaAl_2Si_2O_8$	4.5–7.1
Hexacelsian	$SrAl_2Si_2O_8$	7.5–11.1
Monocelsian	$SrAl_2Si_2O_8$	2.7
Orthorhombic celsian	$SrAl_2Si_2O_8$	5.4–7.6
Cordierite	$Mg_2Al_4Si_5O_{18}$	2.0

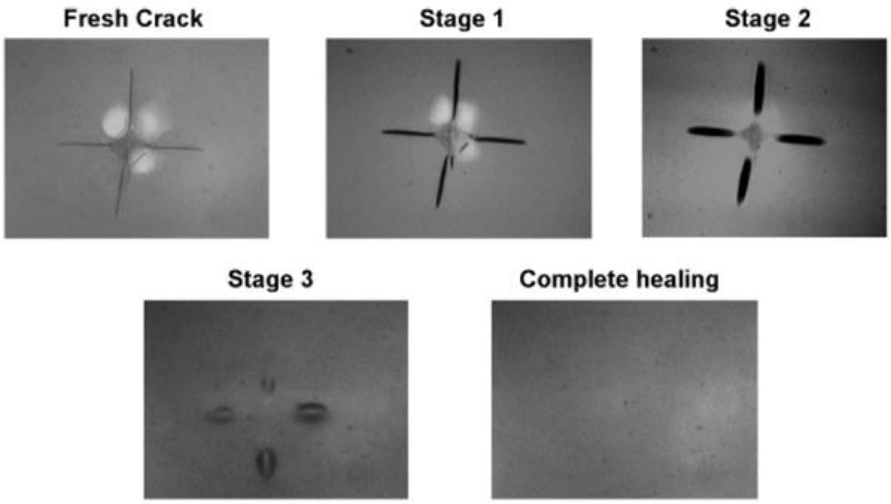

Figure **2.2-2:** Example of the complete self-healing of a glass sealant [167]

In this way, it is possible to produce coatings with unique features, changing their properties in function of the parent glass composition and of the different sinter-crystallization process. The development of glass-ceramic coating materials proves the positive effect of that can be found in one material

The possibility to produce glasses and glass-ceramics with several different compositions, and consequently of combining various properties (i. e. both glass and crystalline phases) is another important advantage [164].

Already twenty years ago, dense glass coatings for PbTe thermoelectrics were produced with SiO_2- PbO- BaO and SiO_2- Na_2O- B_2O_3- PbO- TeO_2 compositions [169], showing good oxidation resistance up to 500°C.

More recently, a silica-based glass-ceramic coatings was developed as protective barrier against humidity, oxygen and chemical agents to prevent degradation of Bi_2Te_3- based modules [170]. The porous glass composite coating [160] and the silica-based enamel [156] above mentioned were produced to protect skutterudite thermoelectric. In this latter work, a critical aspect is discussed concerning the mismatch between the coefficient of thermal expansion of the silica-based enamel and the substrate, which leads to the formation of high stresses and cracks in the coating.

In the case of substoichiometric titanium oxide thermoelectric (TiO_x), researchers at the Fraunhofer Institute reported crystalline glass material- based coating technology to inhibit oxidation of an intermediate temperature thermoelectric module up to 300°C [120] and subsequently, the effectiveness of another glass- based coating able to limit oxidation up to 600°C[122].

Recently, magnesium silicide samples were covered by dip-coating method with a silane-based amorphous coating (produced using sol- gel method) and then annealed in Ar gas atmosphere in various temperatures between 400–550 °C [171]. The oxidation protective coating resulted successful only up to 450°C, probably due to the differences in thermal expansion coefficients between the coating, the thermoelectric material and the oxidation products.

There is a growing number of researches that recognise the importance of this innovative oxidation protective method for both n- and p- type thermoelectric materials [13,156,160,172] but in some studies the effectiveness for maintaining their transport and electric properties has not been reported yet.

The above studies were carried out on oxidation protective glass- based coating focusing especially on tellurides and skutterudites; furthermore, no electrical properties of the substrates after the oxidation test were reported, but only physical characterization of the coatings were investigated.

In this PhD thesis the effectiveness of different oxidation protective technologies was investigated, employing different coatings for each thermoelectric substrate involved: the higher manganese silicide, (HSM, $MnSi_{1.74}$, p-type); magnesium silicide based material (Sb doped $Mg_2(Si,Sn)$, $Mg_2Si_{0.487}Sn_{0.5}Sb_{0.013}$, n-type); titanium suboxide (TiO_x, n-type) and zinc doped tetrahedrite (Zn doped THD, $Cu_{11.5}Zn_{0.5}Sb_4S_{13}$, p-type).

For HSM ($MnSi_{1.74}$), a silica-based glass-ceramic coating was developed to provide oxidation protection up to 600°C for 500 hrs and the thermal cycling stability (from room temperature to 600°C in air). Furthermore, it showed self-sealing properties when heated above its softening point. The efficacy of the coating concerning the variations of electrical and thermoelectric properties upon thermal cycling are discussed.

In the case of Sb doped $Mg_2(Si,Sn)$, new silica-based glass-ceramic coatings were designed and characterized, and only one was chosen as potential glass-ceramic able to protect the thermoelectric substrate against oxidation up to 500°C. In order to evaluate the effectiveness of this type of coating, the properties of $Mg_2Si_{0.487}Sn_{0.5}Sb_{0.013}$ as-sintered, with and without the coating, were tested after ageing in air.

As previously reported, glass-based coatings for TiO_x were already studied to resist up to 500°C, but in this work the development of a new silica-based glass-ceramic containing titanium oxide, to protect the substrate against oxidation for T up to 600°C (to be used both as thermoelectric and electrode at high temperatures) was carried out. In a follow- up of the study, the oxidation behaviour and the thermal cycling stability of coated and uncoated TiO_x will be investigated.

Since glass-ceramic coatings would require a deposition temperature too high for Zn doped THD ($Cu_{11.5}Zn_{0.5}Sb_4S_{13}$), two commercial hybrid resins with low curing temperature and with nominal temperature resistance up to 590°C, were employed as protective resistance coatings. After preliminary tests, the water-based silicone resin was identified as potential candidate to avoid oxidation of Zn doped tetrahedrite. Compositional changes in both the Zn doped THD substrate and the hybrid coating are described and discussed with respect to the electrical properties of the uncoated and coated Zn doped THD before and after ageing at 350 and 400°C in air.

Chapter 3

Experimental

In this chapter, the experimental procedure for the production and characterization of different compositions of oxidation protective coatings for n- and p-types TE materials is illustrated.

The glasses were produced by conventional melting technique and then milled in form of glass powders, which were thermally characterized, in order to identify their characteristic temperatures as well as the sintering and crystallization behaviour. On the basis of the results, the thermal treatment needed to obtain the glass-ceramic coating was chosen. The glass-ceramic coatings, obtained carrying out the thermal process, were studied under the point of view of their thermo-mechanical properties as well as their composition after the sinter-crystallization (by qualitative and semi-quantitative analyses).

Only for Zn doped tetrahedrite and Sb doped $Mg_2(Si,Sn)$, commercial hybrid coatings were used to protect them against oxidation.

Compositional changes in both the TE substrates and the coatings are described and discussed respect to the electrical properties of the uncoated and coated thermoelectrics before and after thermal cycling treatment (for HMS) and before and after thermal ageing (for Zn doped THD). In the case of Sb doped $Mg_2(Si,Sn)$ and titanium suboxide only the designing and the optimization of a suitable glass-ceramic coatings was carried out, while the thermoelectric tests will be a follow- up of this PhD work.

Part of the work described in this chapter has been already published during the PhD period [173,174].

Figure 3.0-1 shows a schematic representation of the experimental procedure, concerning the glass-ceramic production and the coated thermoelectric materials studied here.

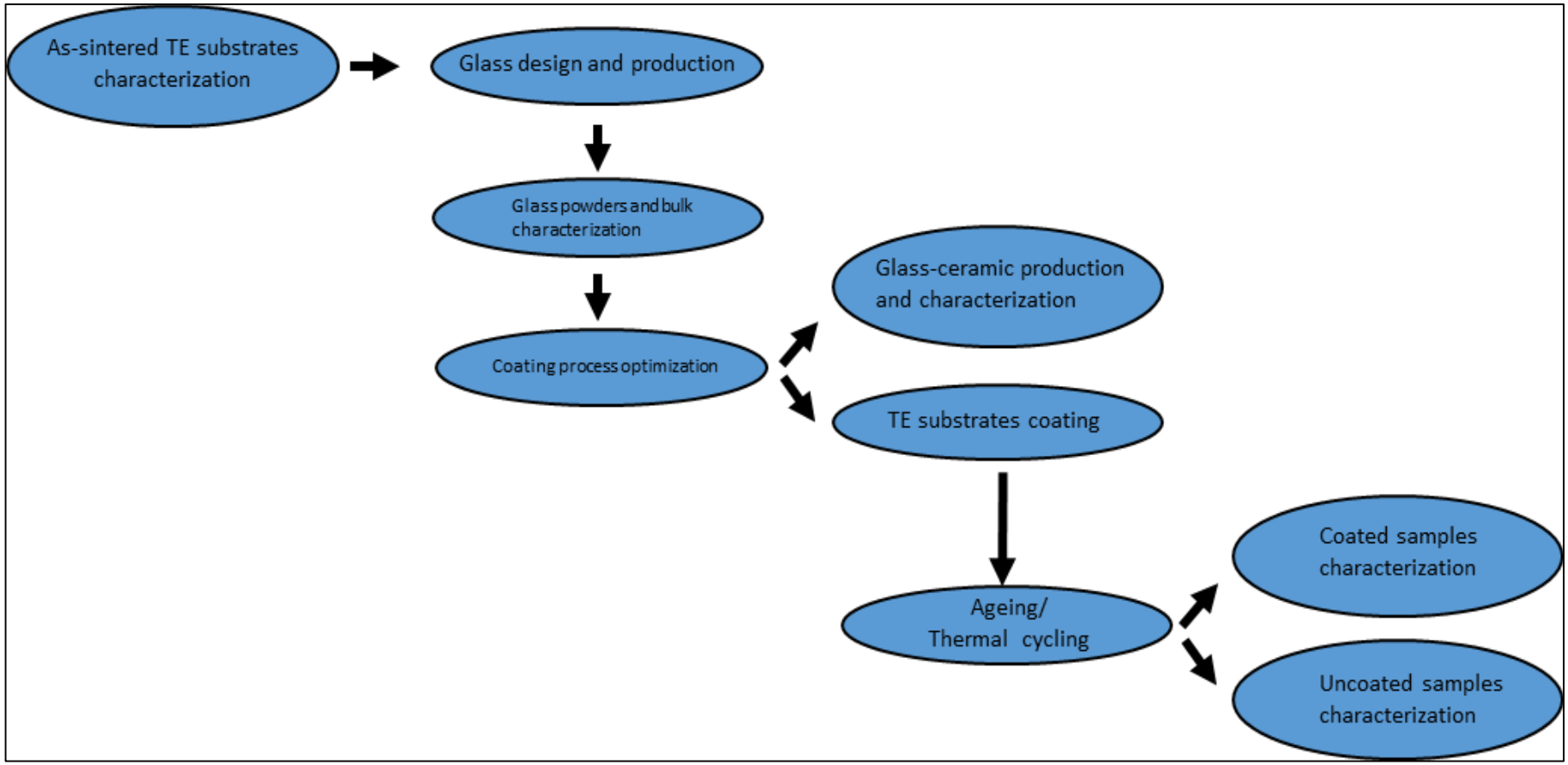

Figure 3.0-1: Schematic illustration of the experimental process carried out during the PhD work

3.1 TE Substrates synthesis and characterization

Three of the the thermoelectric substrates involved in this research were synthesised by solid-state reaction and densified with a spark plasma sintering (SPS) furnace (HPD- 25/1, FCT Systeme GmbH, Rauenstein, Germany) at Nanoforce Technology Ltd., at Queen Mary University of London. SPS is a low voltage (typically below 10V), direct high current (DC) (from 1 to 10 kA), pressure-assisted (50-250 kN) technique belonging to the group of Electrical Current Assisted/Activated Sintering (ECAS) techniques (process with discharge time more than 0.1 second). Even if the field of quicker techniques based on capacitive discharge directly through the sample (ultrafast ECAS) is still under development, SPS is now well-optimized[175]. In fact, since the 90's, SPS is gradually replacing the traditional Hot Press technique[176]. It is used both to synthetize and densify new compound in one step.

The operating principle consisting in a combination of conduction and Joule heating[177]: if the sample is conductive, energy is dissipated directly within sample and other conductive parts; otherwise electrically conductive tools are used and the heat produced by Joule heating is transmitted to the sample by conduction.

The higher manganese silicide (HMS) with composition $MnSi_{1.74}$ was produced with sintering conditions of 1000°C/ 50 MPa/ 3 min as previously reported [87]. $Mg_2Si_{0.487}Sn_{0.5}Sb_{0.013}$ (Sb doped $Mg_2(Si,Sn)$) powders were prepared by ball-milling (P5 Fritsch, FRITSCH GmbH, Idar-Oberstein, Germany) and they were sintered into 15 mm diameter discs using the SPS furnace at a temperature of 720°C, with a heating and cooling rate of 100° C/min, a dwell time of 5 min and a pressure of 50 MPa.

The thermoelectric material $Cu_{11.5}Zn_{0.5}Sb_4S_{13}$ (Zn doped THD) was prepared starting from single elements powders: Cu (Alpha Aesar,150 mesh, purity 99.5%), Sb (Alpha Aesar, 100 mesh, purity 99.5%), S (Sigma Aldrich, 100 mesh, purity reagent grade) and Zn (Sigma Aldrich, ≥ 99%). They were weighted in the appropriate stoichiometry and sealed in a stainless steel jar in an argon filled glove box, treated in a ball milling machine (QM-3SP2, Nanjiing University, China) employing stainless steel balls at 360 rpm for 96 h, with a ball to powder ratio of 30:1. Powders were then sintered into 10 mm diameter discs using SPS at a temperature of 400° C with a heating and cooling rate of 50°C/min, a dwell time of 5 min and a pressure of 50 MPa.

The titanium suboxide involved in this research labelled as TiO_x can be employed both as thermoelectric material and electrode for high temperature application.

This substrate was synthesized at Fraunhofer Institute for Ceramic Technologies and Systems IKTS, starting from the following materials:

- TiO_2 Kronos 3025 powder
- TiC STD-120 A (H.C.Starck)

The powder preparation was milling of TiO_2 and TiC powder in a ball mill for 4 hrs. Subsequently the synthesis of Titanium suboxide powder at 1200°C under argon atmosphere was carried out. Then, ball milling of the TiO_x powder with 50

mol % TiO_2 powder (Crenox 8602) and adding of pressing aids (5.5 mol%) acrylate and wax. Shaping by dry pressing of the powder granulates with 150 MPa by isostatic pressure was induced. After that, the pyrolysis (debindering) of the pressing aids followed at 1000°C / 1h / 3K/min under argon.
Finally sintering at 1300°C under nitrogen flow, with a heating rate of 5 K/min and dwell time 2 hrs.

Field emission scanning electron microscope (FE-SEM, Merlin electron microscope, ZEISS, Oberkochen, Germany) was used to morphologically characterise both powders and pellets. The latter were polished using SiC papers (grits 600/800/1000/1200/2500/4000) in the first polishing steps and diamond pastes (MetaDi, monocrystal diamond suspension of 1 μm by Buehler, Lake Bluff, Illinois, USA) for the finishing. The HMS samples were coated with gold, while the other thermoelectric substrates with chromium, in order to achieve the necessary electrical conductivity on the surface for performing the analysis. The energy dispersive X-ray spectroscopy (EDS, Zeiss Supra TM 40, Oberkochen, Germany) was carried out in order to chemically characterise all samples.

The density of some as-sintered samples was measured through the Archimede' s method in deionized water.

XRD pattern of powders after milling and as-sintered samples of the Sb doped $Mg_2(Si,Sn)$ and Zn doped THD were collected in the range 20- 70°, while XRD analysis on HMS as-sintered pellets were carried in the range 20- 60°, using a X'Pert Pro MRD diffractometer with Cu Kα radiation (PANalytical X'Pert Pro, Philips, Almelo, The Netherlands), with the aid of the X-Pert HighScore software. The crystalline phases were identified with JCPDS data base provided by ICDD (International Centre for Diffraction Data, Newton Square, Pennsylvania, USA).

Dilatometry (DIL) was chosen to investigate the thermo-mechanical properties of the as-sintered Sb doped $Mg_2(Si,Sn)$, of all the glasses and glass-ceramic oxidation resistant coatings involved in this work.

The dilatometric analysis is a thermo-mechanical investigation method that is based on the high precision measurement of the dimensional variations of a sample placed in a furnace, heated at controlled rate, with a programmed temperature variation and a minimum voltage applied to the sample. From this analysis the thermal expansion coefficient (CTE) and the characteristic temperatures of the sample T_g (glass transition temperature) and T_d (dilatometric softening point) are obtained.
The measurements were carried out in a dilatometer (DIL 402 PC/4, Netzsch, Selb, Gemany) equipped with an alumina sample holder. The description of the analysis carried out on the glassy compositions will be discussed later in this chapter. The Sb doped $Mg_2(Si,Sn)$ substrate was shaped in order to obtain a bar with 5 mm height. The measurements were conducted with 5 K/min as heating temperature, applying a constant compressive force, between the sample and the piston, of 25 cN. The instrument was set for stopping at 350°C, to avoid the starting of degradation of the material inside the furnace.

In the next two paragraphs, two different approaches in order to protect the thermoelectric materials against the degradation caused by oxidative atmosphere

will be described. The first method involves the protective coating through the development of glass (for Sb doped $Mg_2(Si,Sn)$) and glass-ceramic materials (for HMS and TiO_x), while the second one consists in the utilize of commercial resins deposited on the thermoelectric substrate and cured according to the manufacturer's instructions (for Sb doped $Mg_2(Si,Sn)$ and Zn doped THD).

3.2 Glass production and coating deposition thermal treatment

The glass coating used for higher manganese silicide, named G11, has the composition reported in the table 3.2-1. It was previously designed by F. Smeacetto et al. [178] to develop a glass-ceramic coating with high durability and good thermo-mechanical compatibility with that of a foam glass substrate. The G11 composition derive from a soda-lime glass with network modifier oxides (Li_2O, Na_2O, K_2O, B_2O_3, BaO). It was designed to obtain a lead-free and low cost glass with characteristic temperatures suitable to be applied by slurry deposition and direct heating on the HMS substrate. The glass-ceramic, obtained from the heat treatment of G11 glass, was chosen as coating for higher manganese silicide because of its coefficient of thermal expansion ($10.7 \cdot 10^{-6}$ K^{-1}, 200-400°C), which well matches to that of this type of silicide ($11.5 \cdot 10^{-6}$ K^{-1}, from room temperature to 700°C) [13]. In order to keep fixed the formers/modifiers ratio and the thermo-mechanical properties, no variations of the glass were investigated and taken in account. The objective was to avoid the crystallization of crystalline phases not thermo-mechanically compatible with the thermoelectric substrate, maintaining a residual glassy phase in order to the self-sealing of the glass-ceramic system, as it will be discussed later.

Table 3.2-1: Composition in wt and molar% of G11 glass

Composition of G11 glass		
OXIDES	**Weight %**	**Mol %**
SiO_2	66.3	75.24
BaO	15.9	7.07
K_2O	9.8	7.09
Na_2O	2.7	2.97
LiO_2	2.3	5.25
Al_2O_3	1.8	1.2
B_2O_3	1.2	1.18

Five different glasses compositions were designed, characterized and tested for $Mg_2Si_{0.487}Sn_{0.5}Sb_{0.013}$, and they were labelled from M1 to M5. These compositions (Table 3.2-2) were designed with the help of the SciGlass® software (Science Serve GmbH, Sciglass 6.6 software, Newton, Massachusetts, USA), using Priven-98 model, in order to obtain the desired characteristic temperatures in the glass, especially the glass transition temperature (T_g), and a coefficient of thermal expansion (CTE) of the glass-ceramic as close as possible to that of the TE substrate, which is very high. In order to increase the CTE, all the glass compositions included high contents of alkaline oxides like K_2O and Na_2O, and the addition of MgO to reduce the Mg diffusion from the TE substrate. Additionally, a T_g lower than 500 °C was the target in order to ensure an adequate viscosity of the glass during the coating process that could not exceed 720°C (the TE sintering temperature). Therefore, different variables were taken into account during the design step. Furthermore, the composition of each glass belonging to M serie was based on the results obtained on the previously glasses (as discussed in chapter 4). The main idea tailoring the following compositions was to reach to best performances in term of adhesion between substrate and protective coating, with the absence of cracks at the interface, in the Sb doped $Mg_2(Si,Sn)$ thermoelectric and in the glass-ceramic. This can be achieved when the thermoelectric material and the coating are thermo-mechanically compatible (CTE match), thus avoiding the formation of residual stresses and tensions.

The T1 glass coating designed to protect TiO_x in oxidative atmosphere up to high temperatures (600-800°C) has the composition reported in the table 3.2-3. It was developed with the support of the SciGlass® software modifying the composition of a resistant glass coating for gas turbine engine components, previously reported by Datta et al. in order to obtain thermal shock and oxidation resistance up to 1000°C [179].

Table 3.2-2: Composition in wt and mol% of M glasses

Chemical composition										
Oxides	M1		M2		M3		M4		M5	
	Wt%	Mol%	Wt%	Mol%	Wt%	Mol%	Wt%	Mol%	Wt%	Mol%
SiO_2	49.26	54.4	51.05	54.99	44.05	49.4	47.90	53.4	45.86	51.4
K_2O	25.86	18.22	22.56	15.5	24.07	17.22	22.81	16.22	24..9	17.22
Na_2O	14.78	15.82	11.7	12.22	13.63	14.82	10.94	11.82	11.80	12.82
CaO	4.31	5.1	7.06	8.15	3.41	4.1	3.43	4.1	3.41	4.1
MgO	2.71	4.46	4.44	7.13	1.47	2.46	1.48	2.46	1.47	2.46
Al_2O_3	3.08	2	3.18	2.02	3.03	2	3.04	2	3.03	2
B_2O_3	-	-	-	-	10.33	10	10.39	10	10.34	10

The objective in this research was to produce a glass-ceramic coating with high durability and good thermo-mechanical compatibility with the substrate, which has a CTE between 7 and $9 \cdot 10^{-6}$ K^{-1} [123]. TiO_2 and Y_2O_3 oxides were added in order to obtain a glass-ceramic materials containing $Y_2Ti_2O_7$, a crystalline phase with thermo-mechanical properties (CTE matching) similar to TiO_x. Furthermore, the formation of this phase at the interface between the coating and the TE could increase the adhesion, as it will be discussed later.

Table 3.2-3: Composition in wt and molar% of T1 glass

Composition of T1 glass		
OXIDES	**Weight %**	**Mol %**
SiO_2	30.91	41.48
Al_2O_3	20.60	16.29
TiO_2	20.60	20.79
Y_2O_3	15.45	5.52
CaO	5.15	7.40
K_2O	2.13	1.82
Na_2O	5.15	6.70

All the glasses were produced by conventional melting and casting method, starting from high purity grade raw materials (Table 3.2-4).

Table 3.2-4: Precursors, brands and purity of the raw materials

OXIDE	PRECURSOR	BRAND	PURITY(%)
SiO_2	-	Sigma Aldrich	99.5
BaO	$BaCO_3$	Alfa Aesar	99.8
K_2O	K_2CO_3	Sigma Aldrich	99.5
Na_2O	Na_2CO_3	Sigma Aldrich	99.5
Li_2O	Li_2CO_3	Alfa Aesar	99
Al_2O_3	-	Alfa Aesar	99.9
B_2O_3	H_3BO_3	Sigma Aldrich	99.99
CaO	$CaCO_3$	Sigma Aldrich	99
MgO	$MgCO_3$	Sigma Aldrich	99.9
TiO_2	-	Sigma Aldrich	≥ 99
Y_2O_3	-	Sigma Aldrich	99.99

Before the melting process, the oxides and carbonates raw materials powders were mixed in the proper ratios for 24 h. The melting was carried out with a heating

rate of 10°C/min using a Pt-Rh crucible, which was put into the furnace when the maximum temperature was reached and:

- G11 glass was melted in an electric furnace (HTF 18/ 4, Carbolite, Hope Valley, UK) in air at 1450- 1500 °C for 1 h;
- M glasses were melted in an electric furnace (Nabertherm LHT418PN2, Lilienthal/ Bremen, Germany) in air at 1200 °C for 1 h; in the covered crucible and then the lid was removed and the temperature increased to 1250°C for 30 minutes
- T1 glass was melted in an electric furnace (Nabertherm LHT418PN2, Lilienthal/ Bremen, Germany) in air at 1500 °C for 1h in the covered crucible and then the lid was removed and the temperature increased to 1550°C for 30 minutes.

The melted glass was cast onto a brass plate in order to obtain a full amorphous material. Subsequently it was milled in a ZrO_2 ball mill and was sieved into particle size ≤ 38 μm in a stainless steel sieve. In the case of G11 glass, the obtained powders were used for the production of the glass-ceramic and for the preparation of the slurry to deposit on the TE substrate, because the characteristic temperatures, as well as the thermal expansion coefficient and the sintering behaviour of the glass-based coating were already reported by previously works [13,178].

In the case of M series and T1 glasses, the glassy powders obtained after the sieving, were before characterized by mean of differential thermal analyses (DTA) and heating stage microscopy (HSM), which were carried out with heating and cooling rates of 10°C/min, while one bulk of glass was used for the dilatometric measurement, recorded with a heating rate of 5°C/min.

The DTA analysis is a thermoanalytic technique in which the difference of temperature between the sample and an inert reference material is recorded in function of time or temperature, while the temperature of the sample, in a specified atmosphere, is programmed. It is an analysis enable of providing qualitative information on the chemical-physical processes that take place in a sample, like the nature and temperature at which a particular thermal event occurs (exo or endothermic).

The DTA analyses (DTA 404 PC, Netzsch, Selb, Germany) were carried out by using Al_2O_3 powders (Alfa Aesar, 99,99% purity) as the reference. The same amount (about 100 mg) of sample and reference was used in Pt crucibles. The analyses were conducted from room temperature to 1000 °C/ 1400°C for M glasses/ T1 glass, respectively, with 10°C/min as heating rate, on glass powders sized ≤ 38 μm. From each DTA thermogram, glass transition temperature (T_g), crystallization onset temperature (T_x) and crystallization peak temperature (T_p) were extrapolated. The T_g was evaluated as the onset of the endothermic transformation related to the glass transition in the DTA curves, while T_x and T_p are, respectively, the onset and the peak of the crystallization exotherm [180].

The sintering behaviour of the glasses powders (≤ 38 μm) was investigated by using hot stage microscopy (HSM). This is a thermal analysis through which it is possible to visually follow the change in shape of a sample subjected to a precise

heat treatment, so as to obtain information on the shrinkage and the surface tension of the material.
The sample for HSM (EM 301, Hesse Instruments, Harzgerode, Germany) was a cylindrical pellet (3 mm diameter and 3 mm height) obtained by uniaxially pressing the glass powders with some drops of ethanol. The measurements were conducted placing the sample on an alumina support. For all the glasses, the thermal parameters of the HSM analyses were the same: the measurements started from room temperature, with a heating rate of 10 °C/min, until the instrument automatically detected the melting of the sample. On the basis of the shapes and dimensions assumed by the samples during the heat treatment, the instrument automatically recorded some characteristic temperatures: first shrinkage temperature (T_{FS}), maximum shrinkage temperature (T_{MS}) deformation temperature (DT), sphere temperature (ST), half-sphere temperature (HT), flow temperature (FT).

The deposition thermal treatments (coating processes) were chosen for all the glasses, starting from glass powders with size ≤ 38 μm on the basis of the results of DTA and HSM analyses carried out at 10°C/min:

- for higher manganese silicide:
  - G11: 1h at 700°C under flowing Ar (as reported in the previous work [13])

- for Sb doped $Mg_2(Si,Sn)$:
  - M1, M2: 1h at 650 °C under flowing Ar;
  - M3: 1 h at 550 °C under flowing Ar;
  - M4, M5: 1h at 600°C under flowing Ar

- for titanium suboxide:
  - T1: 10 min at 1300°C + 30 min at 855°C under flowing Ar in a tubular furnace

A small quantity of slurry paste composed of ethanol (70 wt %) and glass powder (30 wt %), was manually deposited with a spatula onto the thermoelectric substrate and let dry for a few minutes. All these deposition treatments were carried out in a tubular furnace (STF 16/ 180, Carbolite Gero, Hope Valley, UK) under a continuous flowing Ar, with 10°C/min as heating rate, and they were used also to produce glass-ceramic samples with the same composition of the glass-ceramic coatings. The latter were produced starting from glass powders (≤ 38 μm) pellets, obtained by uniaxial pressing (100 bar) for 15 seconds.

3.3 Glass-ceramic and glass coatings

The studies on the glass-ceramic and glass-based coatings were carried out at the same time of the deposition treatment which was performed at different temperatures. In particular, the analyses had the main objective to identify the crystalline phases eventually formed during the thermal treatments. Furthermore, where the comparing between the glass and the glass-ceramic was possible, the effect of the crystallization on the thermo-mechanical properties of the glass-ceramics was evaluated.

Concerning the higher manganese silicide (HMS), as mentioned in the 3.2 paragraph, the G11 glass-ceramic was previously characterized by F. Smeacetto et al. [178] and used for an oxidation test on the same thermoelectric substrate at 600°C for 500 hrs [13]. In this work the differential scanning calorimetry (DSC 404 F3 Pegasus®, Netzsch, Selb, Germany) was performed from room temperature up to 1000°C with a heating rate of 10°C/min, to confirm the characteristic temperatures of the coating material as-cast and after the deposition treatment. Furthermore, the self-healing properties of the G11 glass-ceramic system were evaluated both by manually engraving a scratch on its surface with a diamond tip, and performing an indentation with a Vickers indentator; subsequently the coated thermoelectric was fired at 600°C for 30 minutes under flowing Ar, with a 10°C/ min heating rate.

In order to identify the crystalline phases formed in the glass-ceramic derived from each glass, X-ray diffraction analyses were performed in the range 10- 70°, also on the coating after the oxidation tests. The X-ray diffraction patterns were collected on powders obtained by milling the glass-ceramic bulks.

As earlier reported, the dilatometry was performed to evaluate the thermo-mechanical properties, in particular the coefficient of thermal expansion (CTE) of the glass-based materials studied in this work. For all the compositions the analyses were carried out on the as-cast glass and on the glass-ceramic coating (obtained after the coating deposition heat treatment). The glass sample was obtained starting from the as-cast glass. It was shaped in order to obtain cylinders with 5 mm height and around 10 mm of diameter. On the other side, after the coating thermal treatment, the glass or glass-ceramic material was shaped by polishing with SiC grinding papers, obtaining the same dimensions of the glassy pellets. In the case of Sb doped $Mg_2(Si,Sn)$ the behaviour of the glass-based coating was investigated also after t. The measurements were conducted with 5°C/min as heating temperature for all the samples, applying a constant compressive force, between the sample and the piston, of 25 cN. The instrument was set for detecting automatically the dilatometric softening point when a contraction higher than 0.13 % was detected at temperatures above 350 °C.

In order to study the suitability of the glasses and glass-ceramics as oxidation protective coatings for thermoelectrics, glasses/glass-ceramics coated thermoelectrics were processed and characterized, obtaining morphological and

chemical information about the devitrification of the glass and its compatibility with the thermoelectric substrate after the coating process.

In order to demonstrate the effectiveness of these glass and glass-ceramic coatings against oxidation, coated and uncoated samples of higher manganese silicide, Sb doped $Mg_2(Si,Sn)$ and titanium suboxide were subjected to the following oxidation tests:

- HMS: thermal cycling with 10 cycles from room temperature up to 600°C, dwelling time 1h (heating/ cooling rate of 1000°C/h)
- Sb doped $Mg_2(Si,Sn)$: ageing test at 500°C for 120 hrs
- TiO_x: ageing test at 600°C for 120 hrs (tests in progress)

FE-SEM and EDS were performed using the above mentioned microscope. Before and after the thermal cycling, the microstructure morphology and chemical composition of uncoated and coated samples were analysed. Their surface was polished using SiC papers (grits 600/800/1000/1200/2500/4000) and then they were coated with gold (HSM) or with chromium (Sb doped $Mg_2(Si,Sn)$ and TiO_x), in order to achieve the necessary electrical conductivity on the surface for performing the analyses.

X-ray diffraction analyses were carried out on coated and uncoated samples after the thermal cycling (in the case of HMS) and after the oxidation test (in case of Sb doped $Mg_2(Si,Sn)$ and TiO_x); the surface coating was removed to reveal the thermoelectric substrate.

The HMS electrical properties were carried out at Nanoforce Technology Ltd, on the as-sintered thermoelectrics, on the coated and uncoated samples after the oxidation tests. The Seebeck coefficient and electrical resistivity were measured in vacuum with the thermoelectric system in Figure 3.3-1 (ZEM- 3, Ulvac, Methuen, Massachusetts, USA). The functioning principle provide that the sample is set in a vertical position between the upper and lower blocks in a furnace. While the sample is heated, and held, at a specified temperature, it is heated by the heater in the lower block to guarantee a temperature gradient. Seebeck coefficient is obtained by measuring the upper and lower temperatures T1 and T2 with the thermocouples pressed against the side of the sample, followed by measurement of thermal electromotive force dE between the same wires on one side of the thermocouple. Electric resistance is measured by the dc four-terminal method, in which a constant current I is applied to both ends of the sample to measure and determine voltage drop dV between the same wires of the thermocouple by subtracting the thermo-electromotive force between leads.

In order to calculate the figure of merit of HMS samples, the thermal conductivity (k) was determined using the equation $k = \lambda \cdot C_p \cdot d$, where λ is the thermal diffusivity, C_p is the heat specific and d the density. The thermal diffusivity was measured using a laser-flash method in a flowing Ar atmosphere (LFA- 457

MicroFlash, Netzsch, Selb, Germany); the specific heat capacity was calculated using the Dulong-Petit law to avoid the large uncertainty in the differential scanning calorimetry method, and the density was obtained using the Archimede's method. For all the electrical measurements, the outer layers of both coated and uncoated samples were gently removed to allow electrical contacts to take place.

Further experimental activities will focus on the electrical characterization on the glass coated Sb doped $Mg_2(Si,Sn)$ after the ageing tests at 500°C for 120 hrs, (at Nanoforce Technology Ltd) and on T1 glass-ceramic coated TiO_x after the oxidation test (at Fraunhofer Institute for Ceramic Technologies and Systems IKTS).

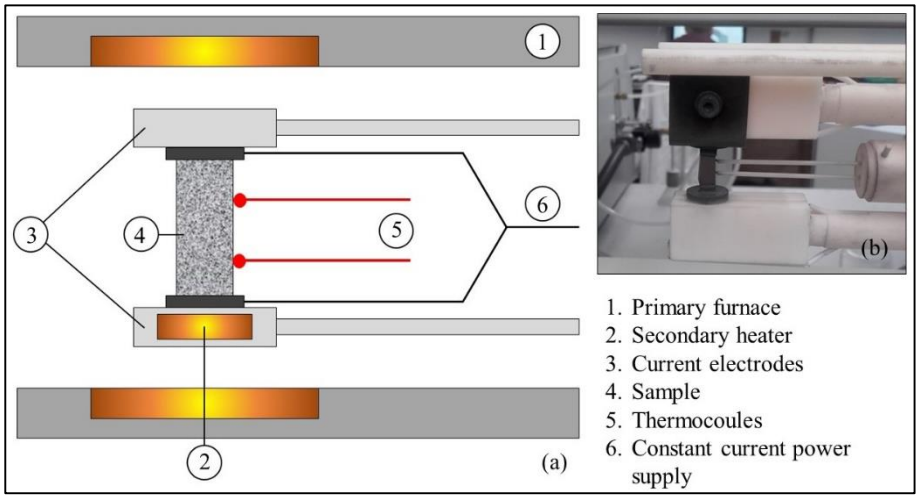

Figure 3.3-1: Functioning diagram of instrument for Seebeck coefficient measure (a) and experimental set-up of QMUL instrument (b)

3.4 Hybrid commercial coatings

An alternative route to glass-ceramic materials, could be represented by the use of a commercial hybrid coating, which would be a promise candidate to avoid the oxidation of TE materials, and consequently the degradation of their electrical properties.

For Sb doped $Mg_2(Si,Sn)$ a commercial electrical insulation paste (Ceramacoat™ 512-N, with composition reported in the Table 3.4-1) purchased from AREMCO SCIENTIFIC COMPANY (Los Angeles, USA), with low curing temperature and nominal temperature resistance up to 1316°C, was chosen as oxidation protective coating as previously reported by Gucci et al. [174] for a different hybrid commercial resin. It was applied using a foam brush and then cured in air in a muffle oven (CWF 13/ 5, Carbolite, Hope Valley, UK) with a heating and cooling rate of 2° C/min at subsequent steps of temperature, as indicated from the company:

- at a temperature of 93°C for 4 hrs,
- at a temperature of 177°C for 2 hrs,
- at a temperature of 260°C for 1h

Table 3.4-1: Composition in vol% of Ceramacoat™ 512-N

COMPONENTS	*CONCENTRATION (vol%)*
Silicate solution	10- 20
Silica, Crystalline	40- 60
Alumina- Silica fiber	5- 10
Alumino-Silicate	5- 10
water	25- 35

After the deposition of Ceramacoat™ 512-N on the $Mg_2Si_{0.487}Sn_{0.5}Sb_{0.013}$ substrate, the cross-section of a sample was polished using SiC paper and then it was coated with chromium, in order to make the surface conductive for performing the morphological analyses. Field emission scanning electron microscope (FE-SEM) and X-ray electron dispersion spectroscopy (EDS) were performed using the same Merlin microscope by ZEISS before mentioned.

After the completely deposition of Ceramacoat™ 512-N on all the faces of the $Mg_2Si_{0.487}Sn_{0.5}Sb_{0.013}$ substrate, an ageing test was performed, in a muffle oven (Manfredi OVMAT 2009, Pinerolo, Italy) in air at a temperature of 500°C for 120 hrs with a heating rate of 2° C/min. Since this hybrid commercial coating demonstrated not to be able to protect the Sb doped $Mg_2(Si,Sn)$ up to 120hrs (as discussed in the next chapter) no other characterization was carried out.

Since glass-ceramic coating would require a deposition temperature too high for the zinc doped tetrahedrite, other two commercial hybrid resins purchased from the same company were tested: a water-based resin (Corr- Paint CP4040) and a solvent-based resin (Corr- Paint CP4040- S1). Both of them are characterised by low curing temperature and nominal temperature resistance up to 590°C. Their compositions are reported in the Table 3.4-2. The two resins were characterised by means XRD after the curing treatment at 250°C for 45 minutes, and after curing followed by the ageing at 580°C for 4hrs in order to evaluate their high temperature reliability with a preliminary testing. They were applied on the Zn doped THD substrate using a foam brush and subsequently cured under flowing Ar in a tubular furnace (STF 16/ 180, Carbolite Gero, Hope Valley, UK) for 45 min at 250°C with a heating and cooling rate of 1.6° C/min.

Table 3.4-2: Composition in vol% of CP4040 and CP4040-S1 hybrid resins

COMPONENTS	*CP4040 (vol%)*	*CP4040- S1 (vol%)*
Silicone emulsion	30-50	20- 30
Methoxy Propyl Acetate	-	30- 40
Zinc oxide	< 1	< 1
Trizinc bis (Orthophosphate)	< 4	< 4
Titanium Dioxide	1.0-5.0	1- 5
Magnesium Silicate Hydrate	1.0-5.0	1.0-5.0
Mica	5-10	1- 5
Aluminium hydroxide	-	1- 10
Water	20- 30	-

FE-SEM and EDS analyses were used to morphologically and chemically characterise the cross- section of CP4040 and CP4040-S1 coated Zn doped THD, which were polished and metallized with chromium.

On the base of the above mentioned preliminary tests, only the water-based resin was chosen as oxidation protective coating for the Zn doped tetrahedrite. Two different aging tests were performed on the completely coated samples, in a muffle oven (OVMAT 2009, Manfredi, Pinerolo, Italy) in air:

- at a temperature of 350°C for 48 hrs with a heating rate of 1.2° C/min.
- at a temperature of 400°C for 120 hrs with a heating rate of 1.2° C/min.

X- ray diffraction, FE-SEM and EDS analyses were carried out. to characterize the microstructure morphology and the chemical composition of uncoated and coated samples after ageing treatments. The measurements of the electrical properties, in this case the Seebeck coefficient and the electrical resistivity, were carried out using a Linseis LSR-3 thermoelectric measurement system (Linseis Messgeraete GmbH, Selb, Germany) with Pt thermocouples and electrodes. The surface coating of the aged samples was manually removed before carrying out XRD and before measuring electric properties.

Chapter 4

Results and discussion

In this section, the results concerning new oxidation protective coatings for four different thermoelectric materials are presented and discussed in terms of their thermal and thermo-mechanical characterization, their compatibility with the substrates as well as their efficiency in different relevant conditions (thermal ageing or thermal cycling).

The following text, data and images concerning higher manganese silicide (HMS) are an adaptation of the results that were submitted during the PhD period in the article:

*Salvo M., Smeacetto F., **D'Isanto F.**, Viola G., Demitri P., Gucci F. and Reece M. J., Glass-ceramic oxidation protection of higher manganese silicide, J. Eur. Ceram. Soc. 39 (2019) 66-71.*

The following text, data and images concerning zinc doped tetrahedrite (Zn doped THD), reproduced in this section with the incorporation of more results and some modifications, were published in:

*Gucci F., **D'Isanto F.**, Zhang R., Reece M. J., Smeacetto F. and Salvo M., Oxidation Protective Hybrid Coating for Thermoelectrics Materials, Materials 12 (2019) 573.*

4.1 G11 glass-ceramic coated HMS

4.1.1 HMS characterization

The higher manganese silicide powders synthesised by a high-temperature calcination method are shown in Figure 4.1-1a, b; they are regular and spherical particles with a size ranging from 10 to 50 µm. The polish surface of a sample densified by Spark Plasma Sintering (1000 °C/50 MPa/3 min, under vacuum) is reported in Figure 4.1-1c, d. The EDS analysis shown in Figure 4.1-1e reveals that the sintering with SPS produces nearly fully dense samples with a HMS matrix ($MnSi_{1.74}$) and with the presence of brighter areas dispersed in this matrix, which correspond to MnSi phase.

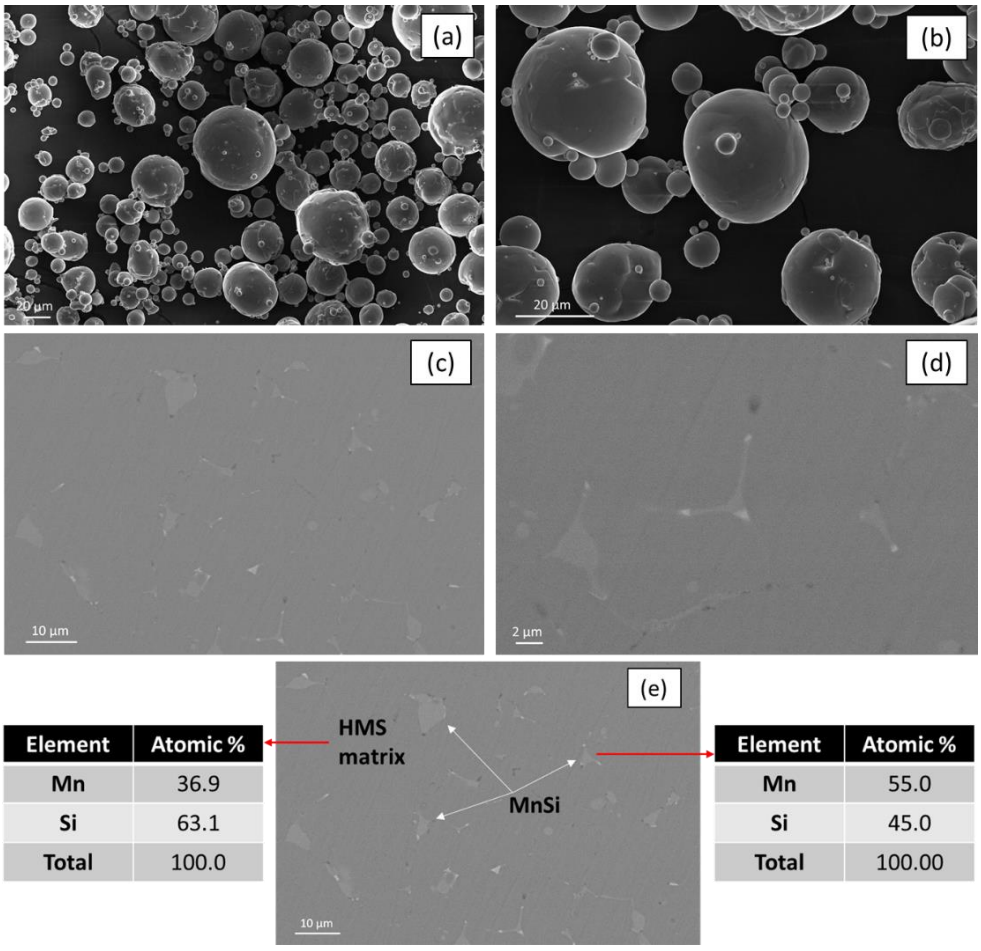

Element	Atomic %
Mn	36.9
Si	63.1
Total	100.0

Element	Atomic %
Mn	55.0
Si	45.0
Total	100.00

Figure 4.1-1: SEM images of (a, b) HMS powder synthesised by solid-state reaction and (c, d) polished surfaces of a HMS pellet sintered by SPS; (e) EDS analysis of the HMS matrix and MnSi phases

The density of five sintered HMS pellets was measured by means of the Archimede's method, resulting to have an average of 5.16 g/ cm^3 (Table 4.1-1), which corresponds to 99.2% of the theoretical density of $MnSi_{1.74}$. The density can

be considered as an index of the quality of the SPS process and, in this case, a density similar to other values reported in literature was measured [81,181].

Table 4.1-1: Density of sintered HMS samples

Samples	Density (g/cm^3)
1	5.167
2	5.158
3	5.157
4	5.162
5	5.165
Average	**5.162**

The XRD pattern of the as-sintered HMS is presented in Figure 4.1-2a; it confirmed that the main phase is the tetragonal $MnSi_{1.74}$ phase, identified by the PDF card n. 00- 026- 1251 (Figure 4.1-2d), while the second phase MnSi, identified by the PDF card n. 01-081-0484, is present in very small quantity.

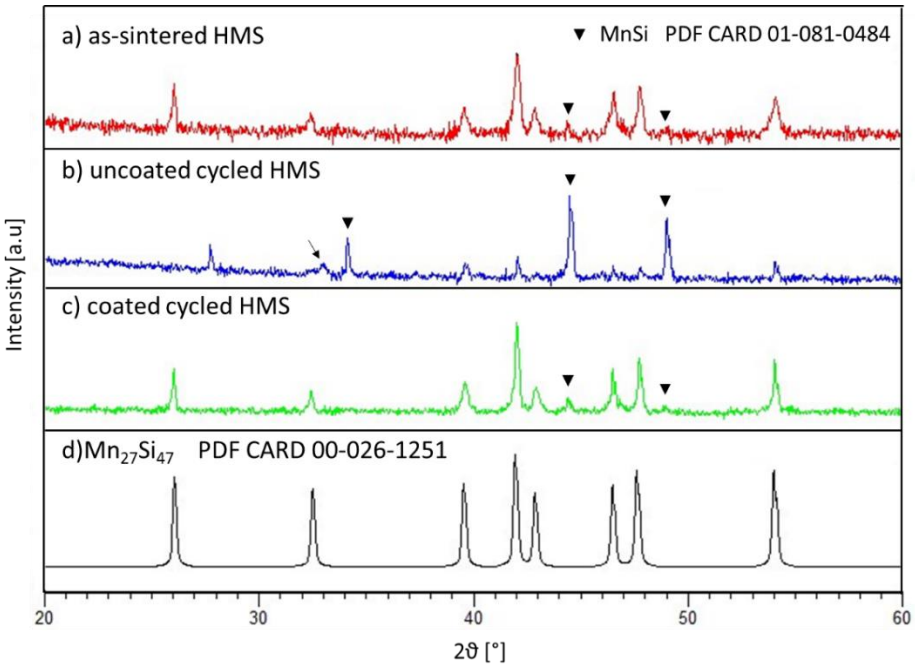

Figure 4.1-2: XRD pattern of (a) as-sintered HMS, (b) uncoated HMS after thermal cycling from room temperature to 600°C, dwelling time 1h, for 10 cycles, (c) glass-ceramic coated HMS (coating removed) after thermal cycling from room temperature to 600°C, dwelling time 1h, for 10 cycles, (d) PDF card (number: 00-026-1251) of $Mn_{27}Si_{47}$. The peak indicated with the black arrow can be attributed to Mn_2O_3 (PDF card number: 01-073-1826).

4.1.2 G11 glass-ceramic coated HMS and self-healing properties of the coating

The G11 glass transition temperature (T_g = 500°C) and coefficient of thermal expansion ($9.04 \cdot 10^{-6}$ $°C^{-1}$ between RT- 400°C) have been already reported in [13,178]. According to previous literature [13], after the deposition treatment carried out at 700°C for 1h under flowing Argon, the G11 glass-ceramic system showed a softening point around 520°C and was characterized by a large quantity of amorphous phase. For this reason, one of the suggested follow ups of the article concerned the investigation of the self-healing property of the residual glassy phase, when heated above its softening point. The self- repair properties of G11 glass-ceramic were evaluated by manually engraving a scratch on its surface with a diamond tip (Figure 4.1-3a) and with several indentations produced on the glass-ceramic coating (Figure 4.1-3c). After the heating of the coating at 600°C for 30 min, under flowing Ar, the complete healing of the scratch occurred (Figure 4.1-3b), all the cracks were healed and indentation marks were not visible (Figure 4.1-3d).

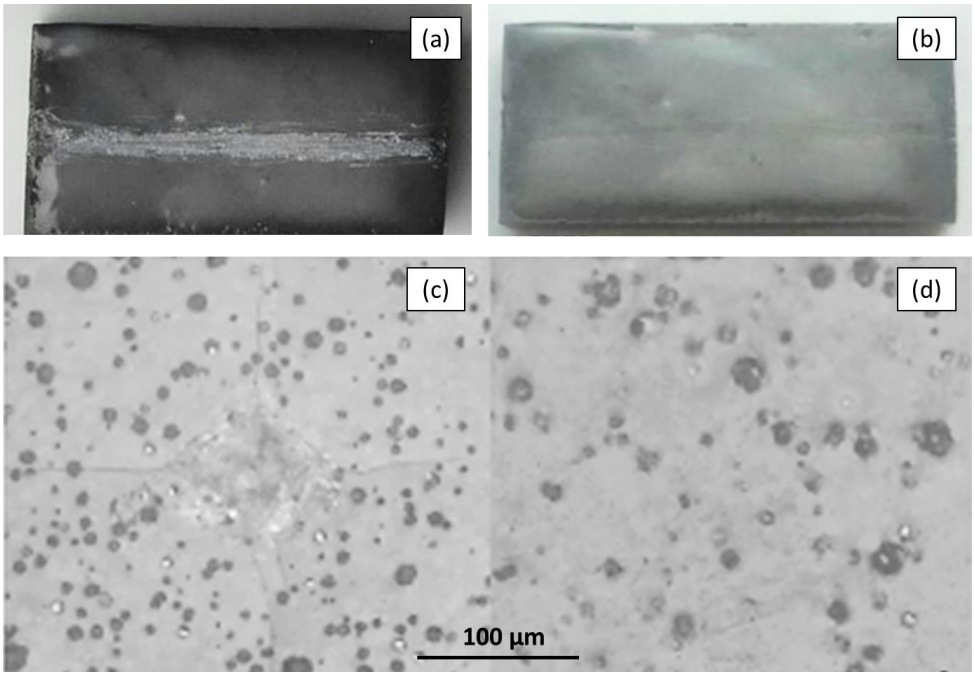

Figure 4.1-3: Healing of (a, b) a scratch on the G11 glass-ceramic coating and (c, d) of an indentation mark and cracks, after thermal treatment at 600°C, for 30min, under flowing Ar

In literature [167], it has been reported that for some glass systems the self-healing ability can be affected by long-term crystallization, which reduces glass viscosity and, consequently, the self- repairing properties. On the contrary, G11 resulted to be stable after the ageing test at 600°C for 500 hrs [13] and after the thermal cycling carried out in this work (see Section 4.1.3), therefore the self-healing ability of the G11 glass-ceramic coating is expected to remain unchanged for long-term use in the thermoelectric devices at least up to 500 hrs.

4.1.3 Characterization after thermal cycling

In Figure 4.1-4, the cross-section of the glass-ceramic coated HMS after the deposition treatment at 700°C, 1h dwelling, under flowing Ar is shown. In the G11 glass-ceramic needle-like shaped crystals are well dispersed in the amorphous phase, no pores or defects are detected at the coating/HMS interface and there is not diffusion between them. In the TE substrate, the MnSi secondary phase, which is represented by brighter areas, was not only dispersed within the main HMS phase, but a sub-micron thick MnSi layer was also present at the interface with the glass-ceramic coating (EDS inset in Figure 4.1-4). As reported in by Ning et al. [13] the MnSi layer did not form when the deposition treatment was carried out in vacuum. Therefore, this MnSi at the interface could be related to the residual oxygen present in the flowing Ar used during the experimental procedure and not to a reaction between HMS and the glass coating.

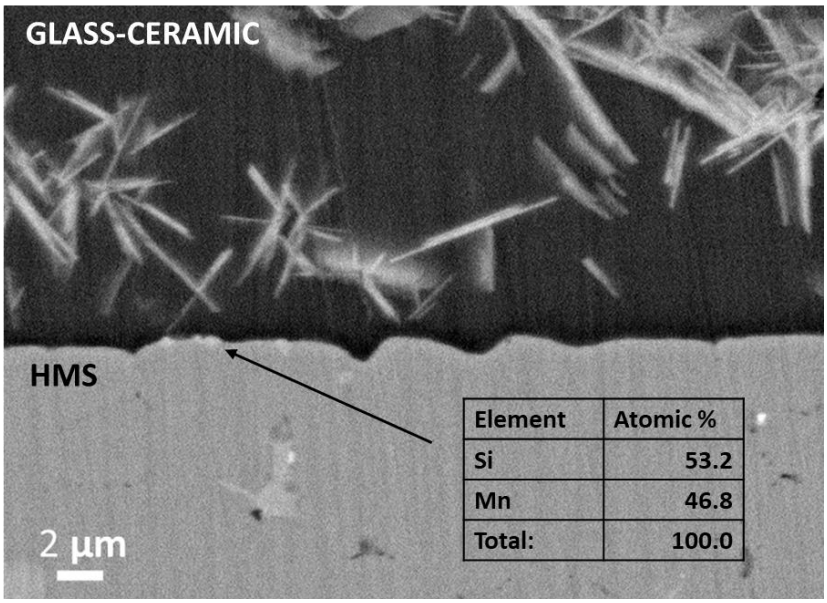

Figure 4.1-4: SEM image of the cross section of G11 glass-ceramic coated HMS (deposited at 700° C, 1h, under Ar flow) and EDS analysis of the area indicated with the arrow

As reported in the previous work [13], the as-deposited G11 glass-ceramic coating has a coefficient of thermal expansion coefficient of $10.7 \cdot 10^{-6}$ °C^{-1} (200-400°C) which is a value slightly lower than that of the HMS substrate ($11.5 \cdot 10^{-6}$ °C^{-1}), thus making the coated HMS thermoelectrics potentially more resistant to thermal cycling thanks to a moderate compression state in the coating. In order to confirm this hypothesis, the resistance of glass-ceramic coated and uncoated HMS specimens was evaluated with oxidation cyclic treatments from room temperature to 600°C in air (10 cycles, 1 h dwelling time for each cycle).

After the thermal cycling, the uncoated HMS was oxidised and completely covered with a white scale. Figure 4.1-5 shows that the formation of an incoherent layer on the surface of the uncoated sample is clearly evident; this 5 µm thick scale

is composed of silica, as confirmed by the EDS analysis (inset of Figure 4.1-6) and was observed on the whole surface of the thermoelectric substrate. The scale was due to the reaction between the higher manganese silicide and oxygen and led to the formation of the silicon deficient layer (MnSi) as shown in Figure 4.1-6. This was already reported after the thermal ageing at 600°C for 500 hrs [13], where the SiO_2 scale was coherent and well adherent to the MnSi, while in the current work, the cycling oxidation tests caused cracks in the silica and the delamination of the layer. The elemental maps of the cross-sectioned uncoated sample after oxidation tests reported in the Figure 4.1-6 demonstrated the presence of a coherent 5 µm thick MnSi layer grown on the $MnSi_{1.74}$ surface.

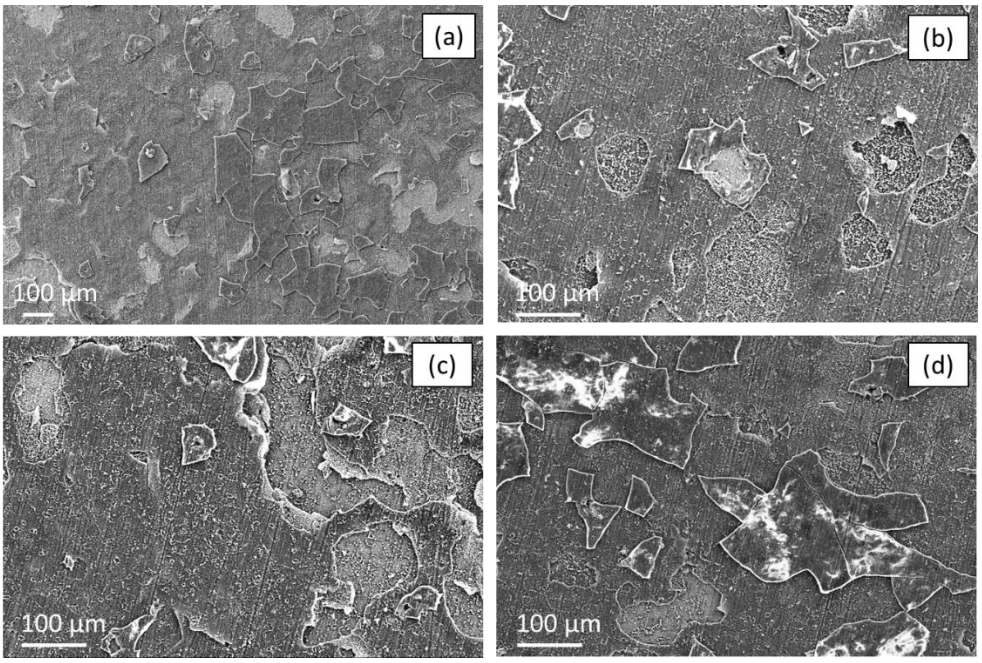

Figure 4.1-5: SEM images of uncoated HMS surface after thermal cycling from room temperature to 600°C, for 10 cycles, dwelling time 1h, in air

The XRD analysis of the uncoated sample surface after cycling oxidation test confirmed that the main phase was MnSi (Figure 4.1-2b) with higher manganese silicide ($MnSi_{1.74}$) present in smaller quantity; it was not possible to detect the SiO_2 scale observed with morphological analysis probably because of the sample preparation process that determined the spallation of the brittle, incoherent and cracked scale. The peak at $2\theta \sim 33°$ could be likely due to the formation of small amount of Mn_2O_3, but the formation of this oxide was not confirmed by SEM and EDS analysis.

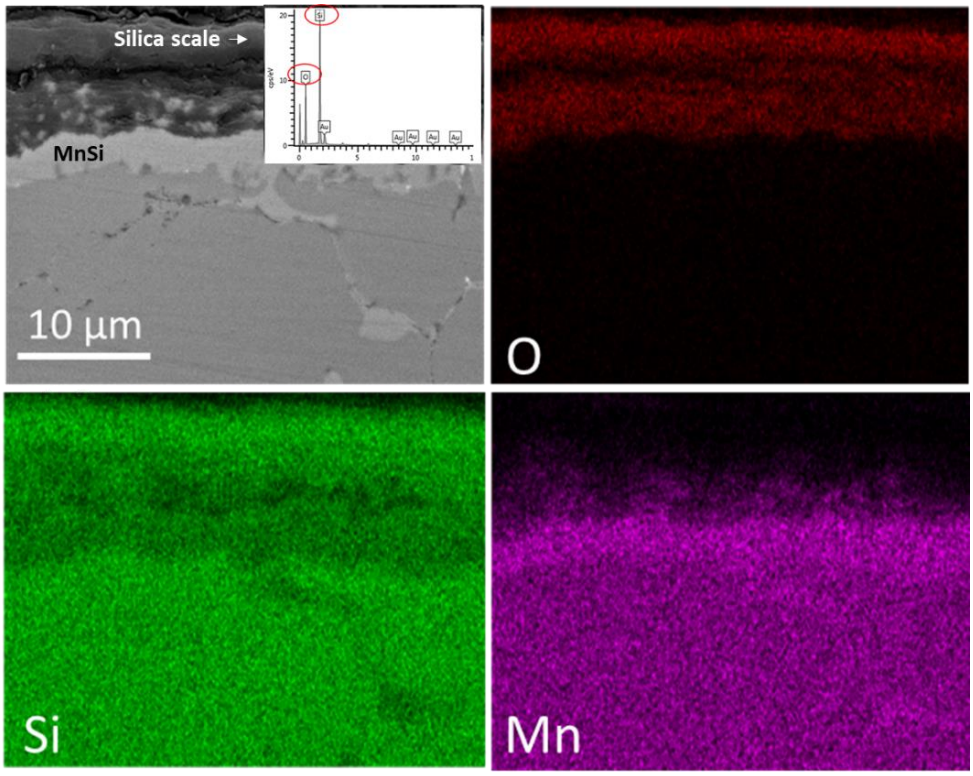

Figure 4.1-6: SEM image of the cross section of uncoated HMS surface after thermal cycling from room temperature to 600°C, for 10 cycles, dwelling time 1h, in air and corresponding elemental maps (EDS)

In Figure 4.1-7, the cross-section of a glass-ceramic coated HMS sample after the cyclic oxidation test is presented. After the thermal cycling, a sound interface can be still observed and no inter-diffusion or reactions between the coating and the substrate are observed. The coating is still well-adherent to the TE substrate, and there are not cracks within the glass-ceramic coating. The EDS elemental map (Figure 4.1-7) and the XRD analysis (Figure 4.1-2c) did not show the presence of a thick continuous MnSi layer at the glass-ceramic/HMS interface as observed in the uncoated HMS. The glass-ceramic coating provides thus a successful protection by inhibiting the oxidation of higher manganese silicide under thermal cycling. The integrity of the coating and of the interface confirmed the excellent CTE matching between HMS and coating, which avoided the formation of dangerous residual stresses within the coated sample.

In addition, the elemental distribution in the EDS map of the glass-ceramic (Figure 4.1-7) showed that the needle-like shaped crystals are barium rich, while the depletion of barium from the glassy phase is clearly evident.

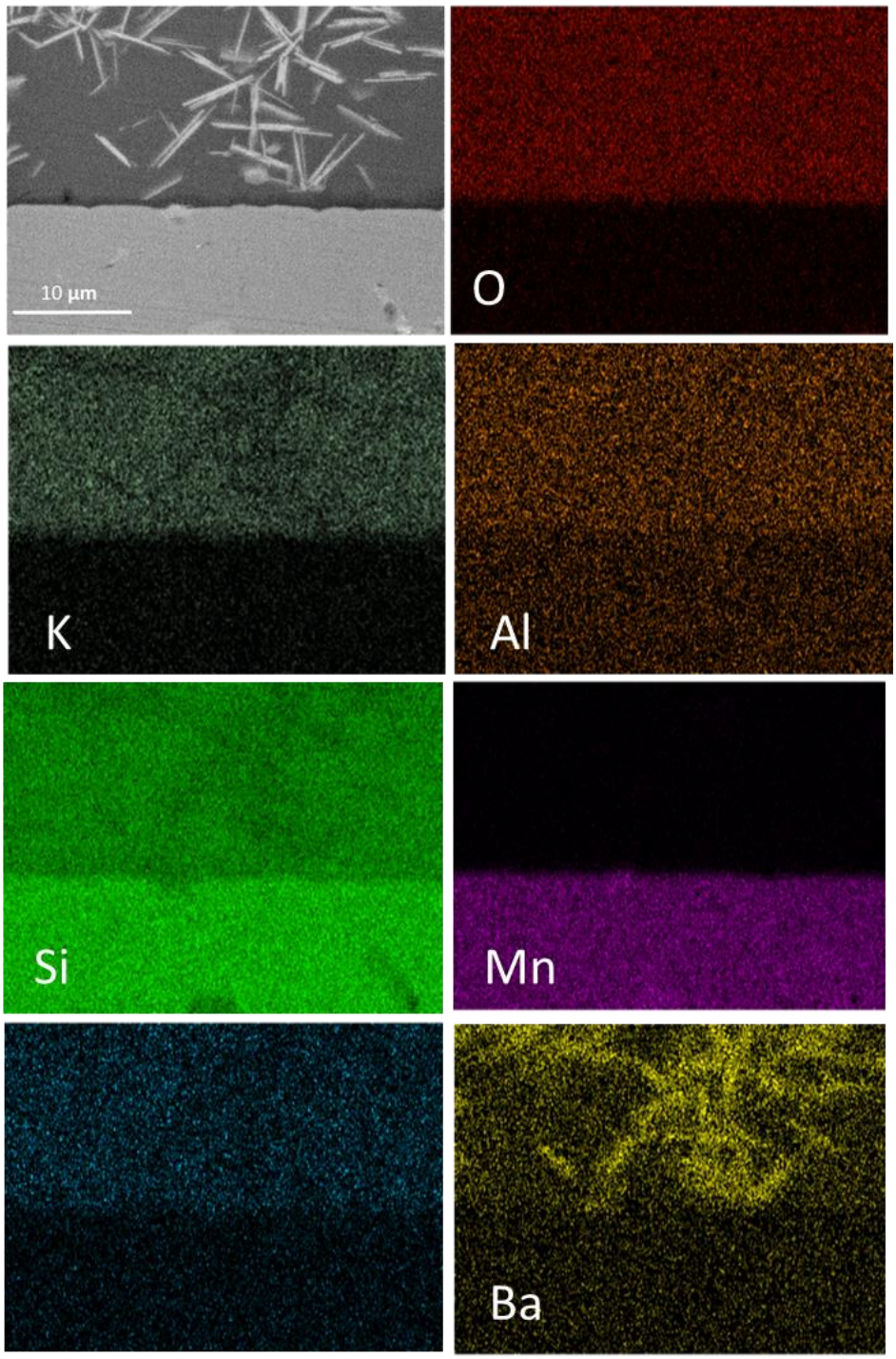

Figure 4.1-7: SEM image of the cross section of G11 glass-ceramic coated HMS after thermal cycling from room temperature to 600°C, dwelling time 1h, for 10 cycles, in air and corresponding elemental maps

In order to evaluate the crystalline phase stability of the glass-ceramic, the XRD analysis was carried out before and after the cyclic oxidation test. The XRD patterns in Figure 4.1-8 showed that the as-deposited and thermally cycled glass-ceramic coated are identical. In addition to the residual glass visible with the morphological characterization, the monoclinic $Ba_2Si_4O_{10}$ was found to be the crystalline phase (PDF card n. 01-071-0797). Nevertheless in previous works [13,178], the main peak

at 2θ ~22.25° was identified as cristobalite; it was found that this peak is almost coincident with the main peak of monoclinic $Ba_2Si_4O_{10}$. The presence of only a minimal concentration of Ba in the residual glassy phase and of a higher quantity in the crystalline phase led to the attribution of barium silicate as the main crystalline phase in the G11 glass-ceramic coating. Furthermore, the formation of $Ba_2Si_4O_{10}$ is in agreement with the study of Petrescu et al. [182], where a similar SiO_2- BaO based- glass system to that used in this work was studied, demonstrating the partial crystallization in $Ba_2Si_4O_{10}$ during an isothermal treatment at 700°C.

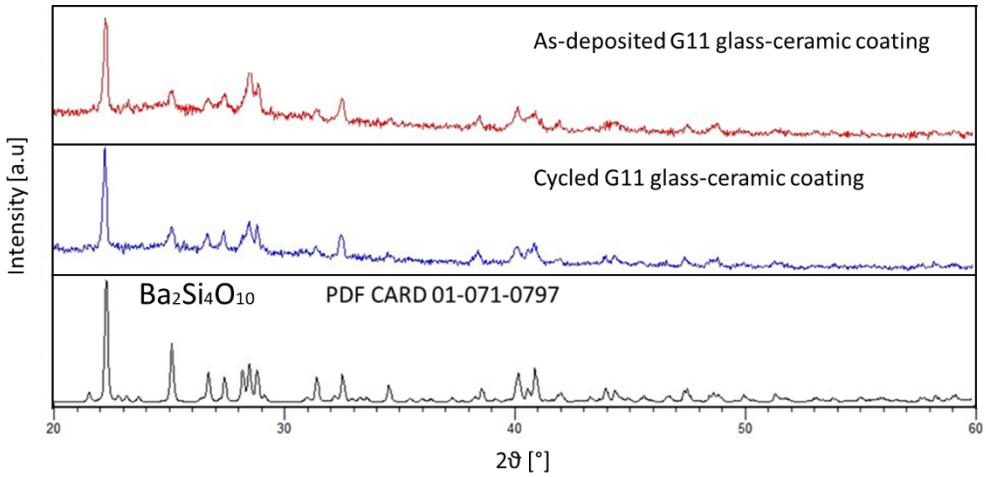

Figure 4.1-8: XRD analysis of the G11 glass-ceramic coating before (red curve) and after (blu curve) the thermal cycling. The black curve represents the PDF card of monoclinic barium silicate

The results of the DSC analysis of the coating material as-cast and after the deposition process (700°C, 1 h, under flowing Ar) are compared in Figure 4.1-9; the reduction of the glass transition temperature (onset) from 500°C to 485°C can be ascribed to the migration of barium from the amorphous glassy phase to the crystalline phase, thus increasing the alkaline oxides/silica ratio in the residual glass.

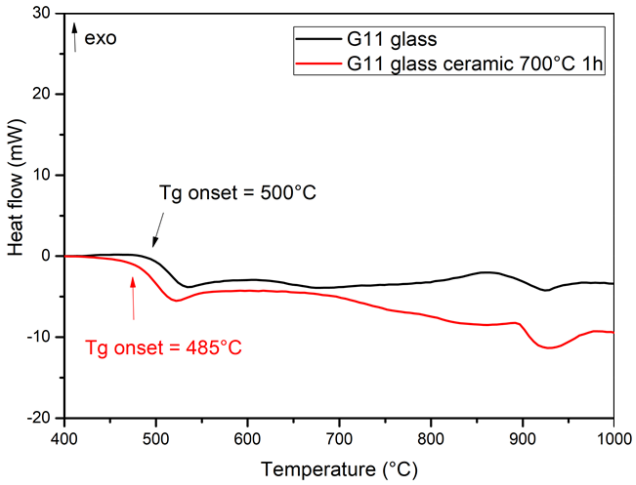

Figure 4.1-9: DSC analysis of the as-casted glass (black curve) and the as-deposited glass-ceramic coating (red curve). The characteristic temperature indicated is: T_g (glass transition temperature).

Figure 4.1-10 compares the values of (a) the Seebeck coefficient S, (b) electrical resistivity ρ, (c) power factor (S^2/ρ) and (d) zT ($S^2T/\rho k$, where T is the absolute temperature and k the thermal conductivity) of the as-sintered, uncoated and coated HMS samples after the thermal cycles. In the Seebeck coefficients (Figure 4.1-10a) of the three samples, significant differences are not visible; however, the values of the coated sample were slightly higher than those of the uncoated HMS in the entire temperature range. The oxidation inhibiting effect of the coating becomes clearer in the electrical resistivity and power factor diagrams (Figure 4.1-10b, c). It can be observed that the coating avoided the increase of the electrical resistivity measured in the uncoated sample after the oxidation treatment if compared to the as-sintered specimen. Furthermore, the coating kept the differences in the power factor values of the as-sintered and coated samples within the error bars, preventing the decrease observed in the uncoated sample. Concerning the figure of merit zT, the results (Figure 4.1-10d) showed that the coated HMS is characterised by an almost unchanged zT compared to the as-sintered specimen; both samples report higher values than those of the uncoated TE, with differences that increase with increasing temperature. The largest differences in the thermoelectric properties verified at high temperature indicate that the coating may result particularly useful for high temperature applications.

Summarising, the G11 silica-based glass-ceramic was used as an effective oxidation resistant coating for higher manganese silicide thermoelectrics. It exhibited excellent thermo-mechanical and chemical compatibility with the substrate. The thermoelectric properties, before and after thermal cycling indicated that the coated HMS samples showed unchanged electrical resistivity, power factor and zT if compared to the as-sintered sample, demonstrating that this glass-ceramic system is a promising candidate for protecting $MnSi_{1.74}$ against oxidation during cyclic working operations.

These findings have important implications for developing reliable and low cost glass-ceramic coatings for HMS-based TE modules. The results presented in this section are significant in at least two major respects:

- a novel approach to coatings for TE substrates, where the self–healing ability of the residual glassy phase could improve the durability of the coated thermoelectric device, also in dynamic operations.
- the possibility to extend the HMS use even up to 550°C-600°C, without any degradation effect.

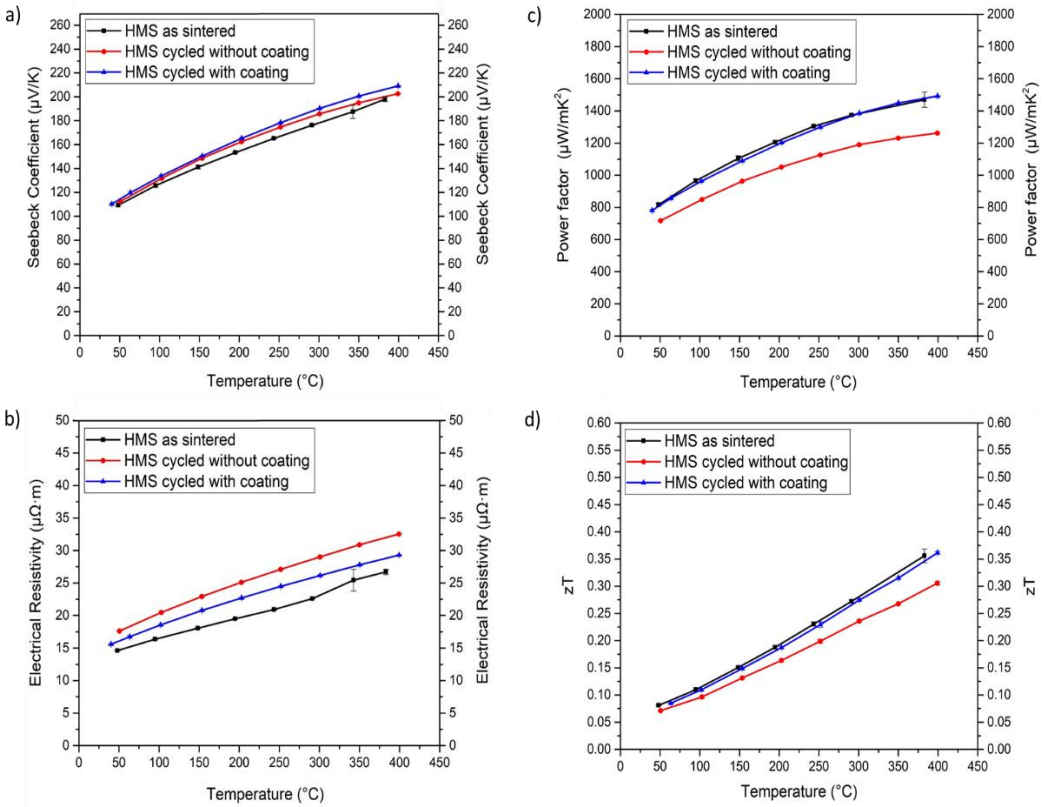

Figure 4.1-10: Temperature dependence of the (a) Seebeck coefficient, (b) electrical resistivity, (c) power factor and (d) zT of the as-sintered HMS (black curve), coated (blu curve) and uncoated HMS (red curve) after thermal cycling from room temperature to 400°C, dwelling time 1h, for 10 cycles

4.2 M glass coated Sb doped $Mg_2(Si,Sn)$

In this section, the results concerning two different approaches aimed to protect the $Mg_2Si_{0.487}Sn_{0.5}Sb_{0.013}$ thermoelectric substrate against the oxidation up to 500°C are evaluated and discussed. The first one is related to the use of glass-ceramic materials completely designed and produced at the Politecnico di Torino. The second approach consists of a hybrid commercial coating produced by Aremco Scientific Company named as Ceramacoat^{TM}512-N.

4.2.1 Sb doped $Mg_2(Si,Sn)$ characterization

The solid-state reaction of the elemental powders produced a single phase solid solution of Mg_2Si and Mg_2Sn with the chemical formula $Mg_2Si_{0.4}Sn_{0.6}$, identified with the PFD card 01-089-4254, as can be demonstrated by the XRD pattern shown in Figure 4.2-1a.

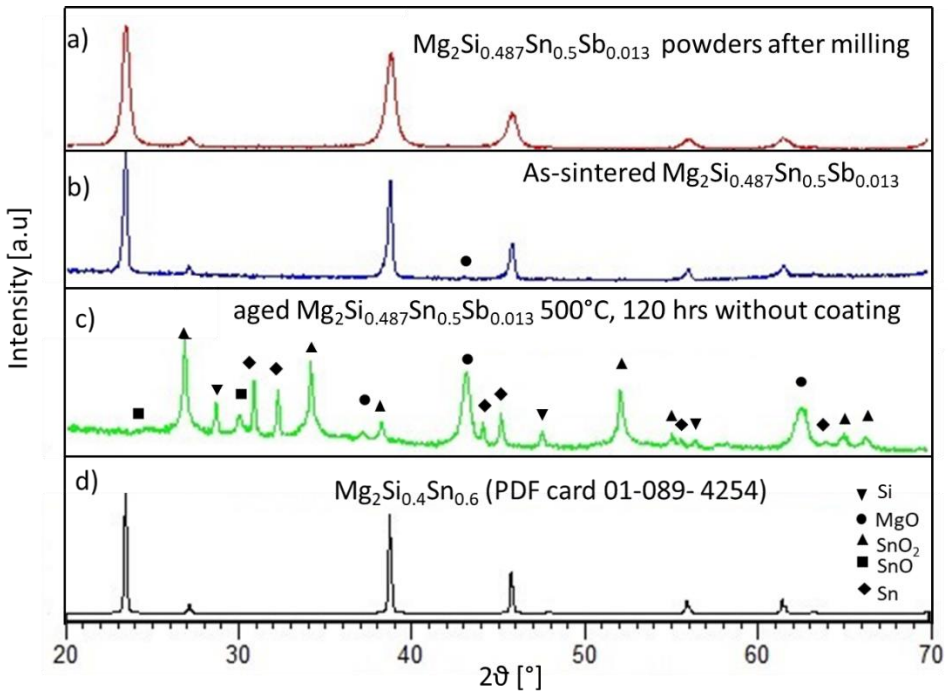

Figure 4.2-1: XRD pattern of $Mg_2Si_{0.487}Sn_{0.5}Sb_{0.013}$ (a) after ball milling, (b) as-sintered, (c) after the oxidation test at 500°C for 120 hrs in air without coating, (d) PDF card (number: 01-089-4254) of $Mg_2Si_{0.4}Sn_{0.6}$

SEM images of the polish surface of an as-sintered Sb doped $Mg_2(Si,Sn)$ produced by SPS with sintering conditions of 720 °C/50 MPa/5 min are presented in Figure 4.2-2a, b; the surface looked really dense, with some porosities homogeneously distributed. In fact, as revealed by XRD analysis in Figure 4.2-1b, after the sintering process at 720°C, no phase separation was visible in the XRD pattern and the peaks correspondent to the single phase became sharper. The peak

around 43°C is related to a little amount of MgO (identified with the PDF card n. 01-075-1525), already identified in previous works [183,184].

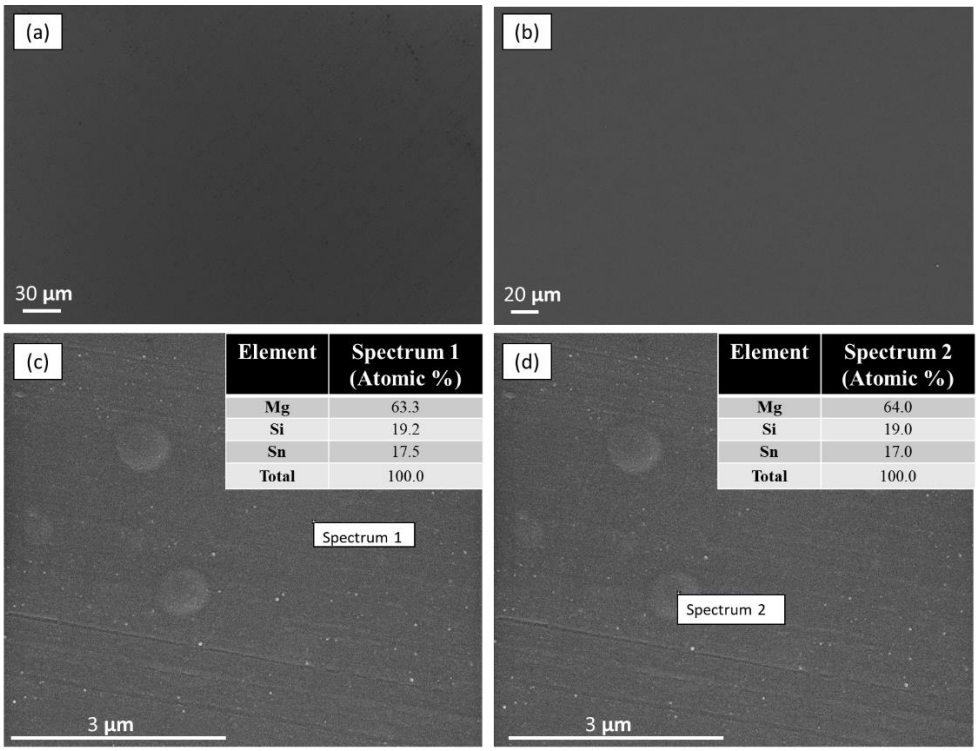

Figure 4.2-2: SEM images (a, b) and EDS analysis (c, d) of a cross- section of as-sintered $Mg_2Si_{0.487}Sn_{0.5}Sb_{0.013}$

The average density of some sintered $Mg_2Si_{0.487}Sn_{0.5}Sb_{0.013}$ pellets, measured using the Archimede's method was 3.00 g/ cm^3 (Table 4.2-1). This higher density respect the theoretical value of the single phase $Mg_2Si_{0.5}Sn_{0.5}$ (2.89 g/ cm^3 [185]) might be related to the impurity of MgO, which has a theoretical density of 3.58 g/ cm^3 [186].

Table 4.2-1: Density of as-sintered $Mg_2Si_{0.487}Sn_{0.5}Sb_{0.013}$ samples

Samples	Density (g/cm^3)
1	2.998
2	3.000
3	3.002
4	2.998
Average	3.000

Dilatometric analysis on the Sb doped $Mg_2(Si,Sn)$ substrate was carried out in order to characterize its thermo-mechanical behaviour and to identify a compatible glass-ceramic coating, thus avoiding the presence of residual stresses at the TE/glass-ceramic coating interface. The dilatometric curve (recorded with a heating rate of 5°C/min) is reported in Figure 4.2-3. The CTE was extrapolated from the

slope of the linear portion of the curves between 50 °C and 300 °C and was found to be $17.6 \cdot 10^{-6}$ K^{-1}.

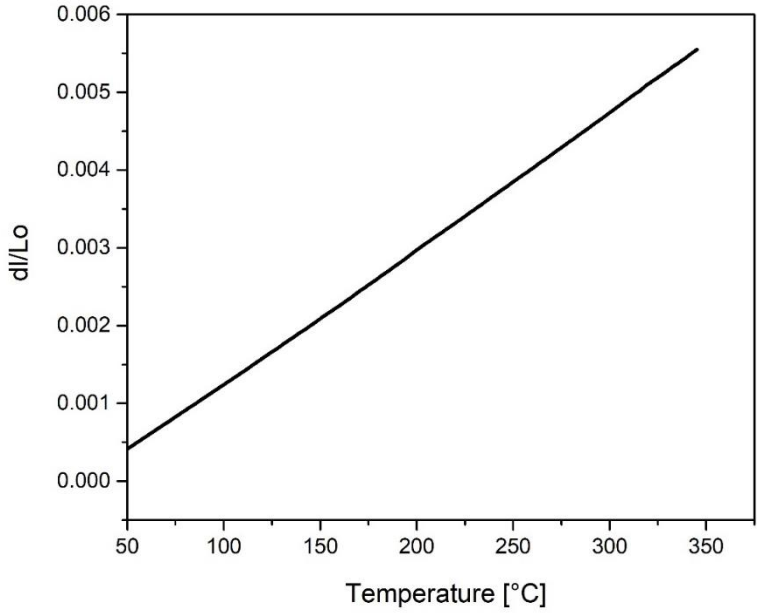

Figure 4.2-3: Dilatometric analysis carried out at 5°C/min on as-sintered $Mg_2Si_{0.487}Sn_{0.5}Sb_{0.013}$

The oxidation test on the thermoelectric substrate performed at 500°C with a dwelling time of 120 hrs in air, in order to verify the behaviour of the Sb doped $Mg_2(Si,Sn)$ in oxidative atmosphere, had a strong effect on the uncoated sample. It was completely oxidised and turned into powder, as it can be observed in Figure 4.2-4. The XRD pattern of the aged $Mg_2Si_{0.487}Sn_{0.5}Sb_{0.013}$ for 120 hrs at 500°C in air without coating (Figure 4.2-1c) showed the decomposition of the thermoelectric substrate into a mixture of compounds: MgO (identified with the PDF card n. 01-075-1525), SnO_2 (detected with the PDF card n. 01-077-0447), SnO (identified with the PDF card n. 01-078-1913), Sn (detected with the PDF card n. 01-089-2761) and Si (identified with the PDF card n. 00-026-1481), as already reported by Skomedal et al.[187].

Figure 4.2-4: $Mg_2Si_{0.487}Sn_{0.5}Sb_{0.013}$ after oxidation test at 500°C for 120 hrs in air without coating

4.2.2 Glass-ceramic and glass-based coatings for Sb doped $Mg_2(Si,Sn)$

In this section the results concerning the glasses and glass-ceramics (referred to as M1 to M5) are presented and discussed in terms of their thermal and thermo-mechanical characterization, their compatibility with the Sb doped $Mg_2(Si,Sn)$ as well as their performances as oxidation protective coatings.

4.2.2.1 Glasses thermal characterization: sintering and crystallization behaviour

In this paragraph, the differential thermal analyses (DTA) results on the as-casted glass powders are shown. Furthermore, these results are also correlated to the hot stage microscopy analyses (HSM) in order to choose the optimal sinter-crystallization thermal treatment, necessary to obtain a suitable densification of the glass-ceramic coatings.

The glass powders from M1 to M5 were characterized by means of DTA, all with a heating rate of 10°C/min and the powders particle size ≤ 38 µm. The DTA curves obtained are reported in Figure 4.2-5.

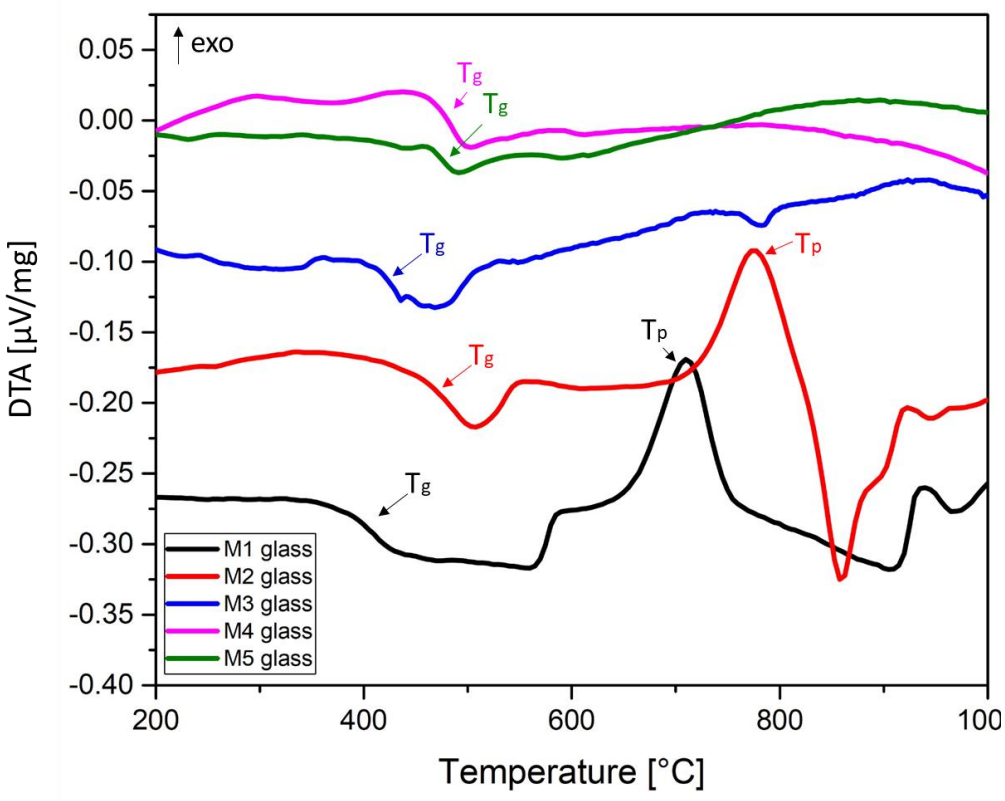

Figure 4.2-5: DTA analyses carried out at 10°C/min of M1 glass (black curve), M2 glass (red curve), M3 glass (blu curve), M4 glass (violet curve) and M5 glass (green curve). The characteristic temperatures indicated are: T_g (glass transition temperature) and T_p (crystallization peak temperature).

The glass transition temperature (T_g), the crystallization peak temperature (T_p) and the melting temperature (T_m) were obtained from these analyses. For all the glasses, the characteristic temperatures were calculated through the use of the Proteus software. A reasonable agreement was found between the values detected by DTA and HSM (as reported later in this chapter). The characteristic temperatures for all the glasses, extrapolated from the DTA curve recorded at 10°C/min are reported in Table 4.2-2. For some glasses, it was not possible to identify some characteristic temperatures. For example, in the DTA of M3 glass only T_g and T_m were identified, while for M4 and M5 glasses both exothermic and endothermic peaks of crystallization and melting respectively were not found, while the decrease of the curves after 900°C was related to the progressive reduction of the viscosity.

Table 4.2-2: Characteristic temperatures and thermal stability of glass powders from M1 to M5, collected at 10°C/min

	Characteristic temperatures (°C)				
	T_g	T_x	$T_x - T_g$	T_p	T_m
M1 glass powders	401	644	243	709	910
M2 glass powders	454	712	258	774	860
M3 glass powders	420	-	-	-	781
M4 glass powders	466	-	-	-	-
M5 glass powders	455	-	-	-	-

The thermal stability of a glass can be defined through the Hruby parameter $K_H = T_x - T_g / T_m - T_x$ [188], where T_x is the temperature corresponding to the onset of the crystallization, and therefore the temperature where the crystallization starts. The thermal stability [188–191] is a parameter which reflects the resistance to devitrification after the formation of the glass [192]. A K_H value above 0.5 indicates a stable glass [188]; a high thermal stability is desirable for this application, because it increases the temperature range in which the viscous flow can act for both sintering and self-healing, before the crystallization occurs during the coating process. $K_H = 0.74$ and $K_H = 1.74$ were calculated for M1 and M2 glasses respectively. In the case of M3, M4 and M5 glasses, it was not possible to detect T_x and T_p by means of the DTA, but a devitrification cannot be excluded and it was further investigated with the XRD analysis, as reported below.

The sintering behaviour of all the five glass compositions were investigated by means of the hot stage microscopy (HSM) and compared to DTA results, in order

to understand the correct order of events during the sinter-crystallization behaviour. Since the crystallization can lead to reduction of the rate of densification by viscous flow, it is important to study the sintering and crystallization mechanisms, in order to design the suitable heat treatment for the production of dense glass-ceramic coatings from glass powders with the sintering-crystallization method. Therefore, it is fundamental to manage the correct order of events, thus avoiding excessive crystallization that may hinder the viscous flow. Most favourable condition consists in reaching firstly the maximum densification (shrinkage) and subsequently inducing the crystals growth and obtain a glass-ceramic. A comparison between DTA and HSM analyses for the five types of glass powders ($\leq 38\mu m$) recorded at 10°C/min is reported in Figures 4.2-6 to 4.2-10. The characteristic temperatures T_g, T_x, and T_p are indicated for each DTA analysis. The hot stage microscopy (HSM) allows to identify the shapes of the sample (reported on the top of each graph) related to some characteristic fixed viscosity points which corresponds to a specific temperature[193]: first shrinkage temperature (T_{FS}), maximum shrinkage temperature (T_{MS}), deformation temperature (DT), sphere temperature (ST), half-sphere temperature (HT), flow temperature (FT). When a sample consisting of compacted powders with a specific distribution of glass particles is sintered, small particles sinter first as explained by Prado et al. [194] and dominate the sintering kinetics as described by the Frenkel model of sintering [195]. When larger pores disappear due to the viscous flow, maximum shrinkage occurs, as previously studied by Mackenzie and Shuttleworth [196].

In the graphs concerning M1 and M2 glasses (Figure 4.2-6 and 4.2-7), it can be noted that the melting temperature detected by DTA and HSM are slightly different; this is probably due to the two different detection methods: while the differential thermal analysis detects the enthalpy variations and phase transitions, the images obtained by means of the hot stage microscopy are dependent on the viscosity and the volume variations of the sample.

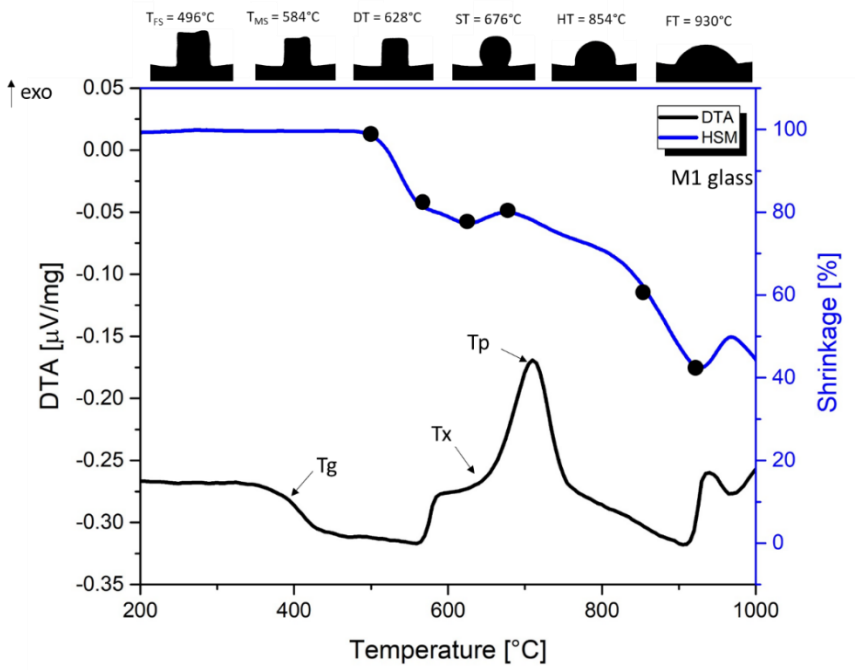

Figure 4.2-6: DTA (black curve) and HSM (blu curve) analyses with characteristic temperatures for M1 glass powders (≤ 38 µm), recorded both at 10°C/min. The characteristic temperatures indicated with the black arrows in the DTA plot are: T_g (glass transition temperature), T_x (onset crystallization temperature) and T_p (crystallization peak temperature).

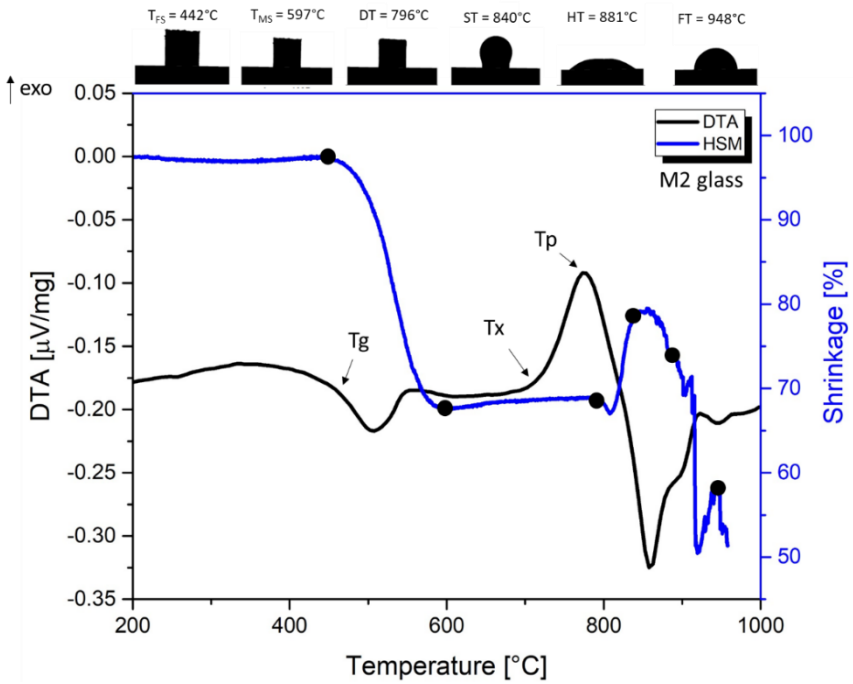

Figure 4.2-7: DTA (black curve) and HSM (blu curve) analyses with characteristic temperatures for M2 glass powders (≤ 38 µm), recorded both at 10°C/min. The characteristic temperatures indicated with the black arrows in the DTA plot are: T_g (glass transition temperature), T_x (onset crystallization temperature) and T_p (crystallization peak temperature).

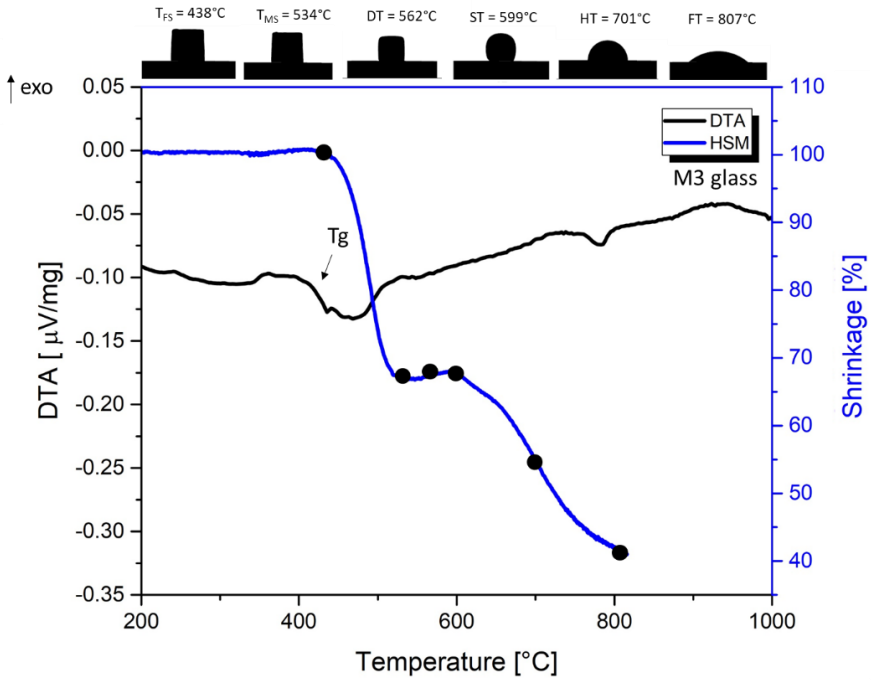

Figure 4.2-8: DTA and HSM analyses with characteristic temperatures for M3 glass powders (≤ 38 µm), recorded both at 10°C/min. The characteristic temperature indicated with the black arrow in the DTA plot is the T_g (glass transition temperature).

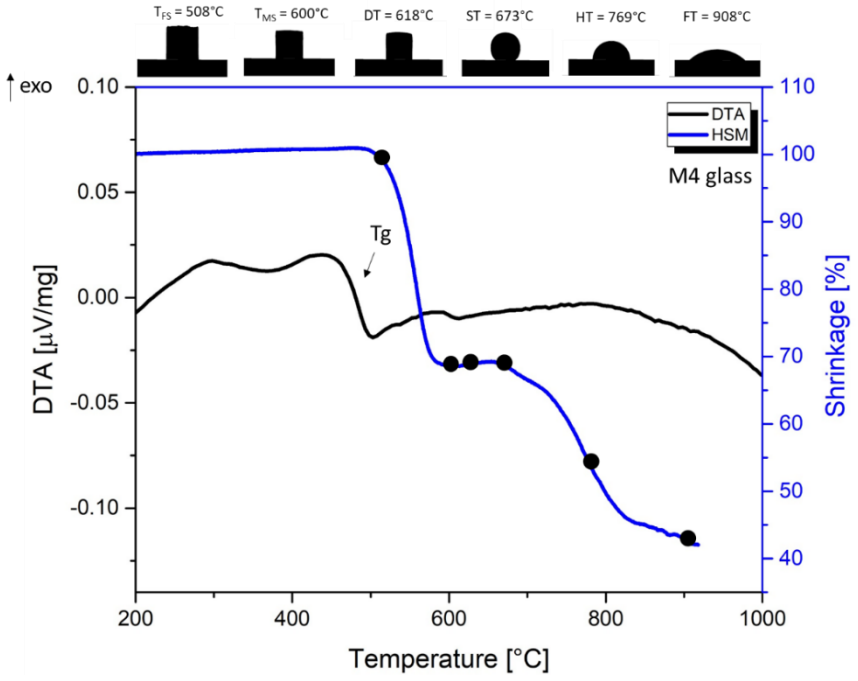

Figure 4.2-9: DTA (black curve) and HSM (blu curve) analyses with characteristic temperatures for M4 glass powders (≤ 38 µm), recorded both at 10°C/min. The characteristic temperature indicated with the black arrow in the DTA plot is the T_g (glass transition temperature).

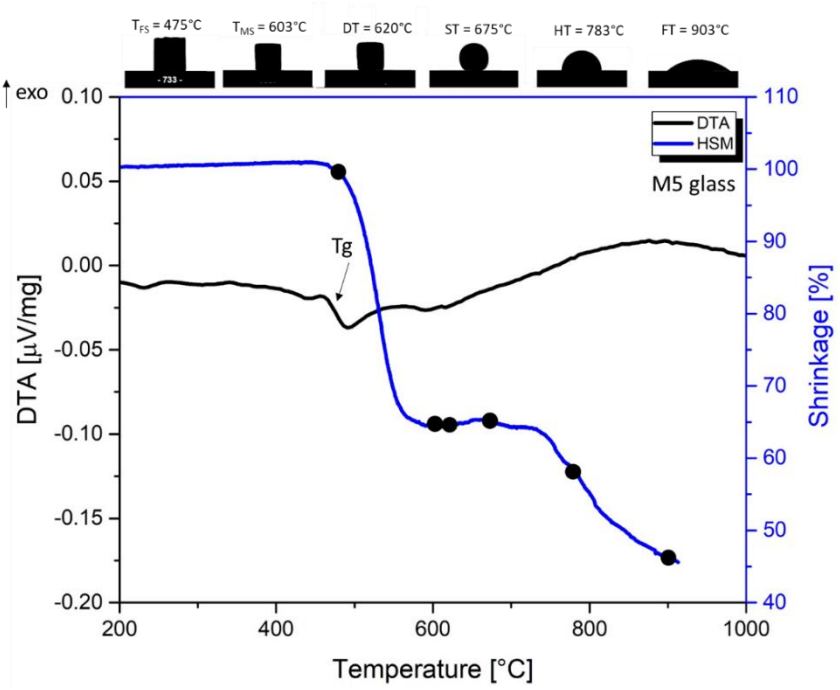

Figure 4.2-10: DTA (black curve) and HSM (blu curve) analyses with characteristic temperatures for M5 glass powders (≤ 38 µm), recorded both at 10°C/min. The characteristic temperature indicated with the black arrow in the DTA plot is the T_g (glass transition temperature).

In all the compositions, the T_g values obtained with DTA and dilatometry of the respective glass are lower than the first shrinkage temperature (T_{fs}) revealed by the HSM analysis, except for the M2 glass, where T_{fs} = 442°C, while the T_g values derived from DTA and dilatometry are 454°C and 467°C respectively. It can be concluded that in this case, the hot stage microscopy provided a slightly inaccurate T_{fs} value.

The method proposed by M. J. Pascual et al. [193] was adopted to predict the viscosity of the glasses at the characteristic temperatures. The data obtained from the HSM curve (Table 4.2-3) can be plotted in Figure 4.2-11, where the viscosity-temperature curves of the studied glasses were obtained fitting the characteristic temperatures and giving a trend line to predict the viscosity of the five systems vs temperature. In all the cases, experimental viscosity points were fitted calculating the constants of the equation $y = ax^b$ and the R-square values (reported in Table 4.2-4), by non-linear regression, fitting all the experimental figures with $\log\eta < 12$ [193]. For each glass composition, the viscosity-temperature behaviour strongly depends on the molar ratio of network former to network modifier oxides [197]. A higher amount of network former oxides (especially SiO_2) determines a shift of the Log η vs T curve to higher temperatures (the black arrow in the Figure 4.2-11 indicates the SiO_2 wt% increase). The slope of the curves depends on the amount and the type of network modifiers included.

Table 4.2-3: Characteristic fixed viscosity points (Tfs, Tms, DT, ST, HT and FT) and related temperatures of glasses from M1 to M5

	M1 glass T (°C)	M2 glass T (°C)	M3 glass T (°C)	M4 glass T (°C)	M5 glass T (°C)	Log η (Poise)
T_{fs}	496	442	438	508	475	9.1
T_{ms}	584	597	534	600	603	7.8
DT	628	796	562	618	620	6.3
ST	676	840	599	673	675	5.4
HT	854	881	701	769	783	4.1
FT	930	948	807	908	903	3.4

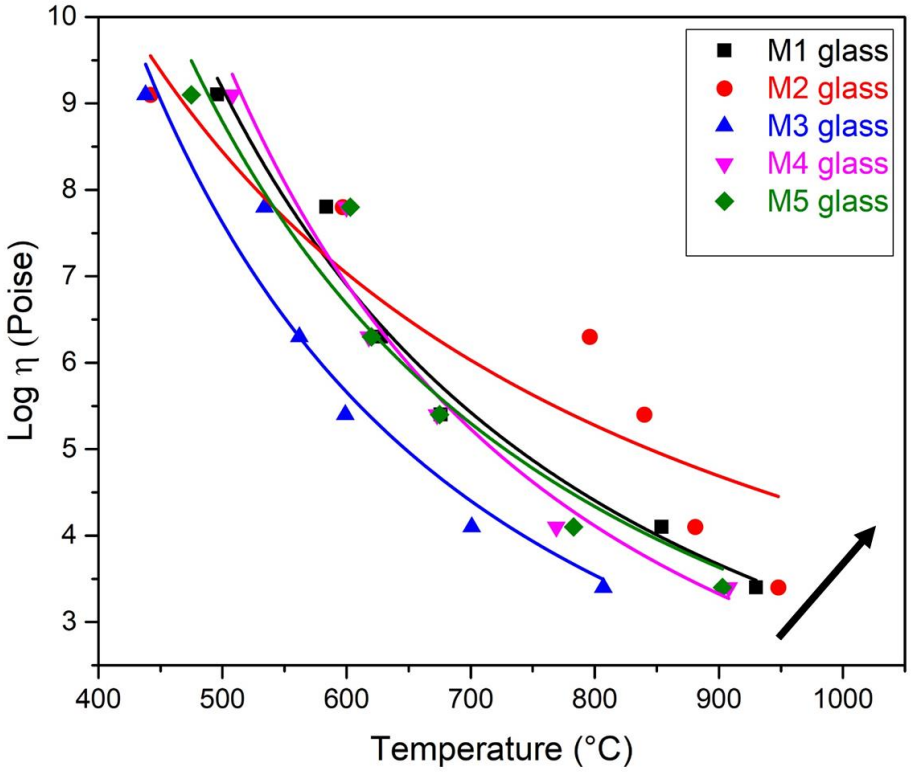

Figure 4.2-11: Viscosity-Temperature curves for M1 glass (black curve), M2 glass (red curve), M3 glass (blu curve), M4 glass (violet curve) and M5 glass (green curve), obtained fitting the characteristic fixed viscosity points and related temperatures. The black arrow in the figure indicates the SiO_2 wt% increase versus

Table 4.2-4: Equations and R-square values obtained through fitting of glasses from M1 to M5

Sample	equation	R-square
M1 glass	$y = 149567x^{-1.561}$	$R^2 = 0.97704$
M2 glass	$y = 4223x^{-1.001}$	$R^2 = 0.85401$
M3 glass	$y = 190599x^{-1.630}$	$R^2 = 0.94894$
M4 glass	$y = 714210x^{-1.805}$	$R^2 = 0.95473$
M5 glass	$y = 100181x^{-1.504}$	$R^2 = 0.92604$

From the graph above we can see that M3 composition has the lower viscosity at 550°C (Log η= 6.5 Poise), thus suggesting the possibility to carry out a lower sintering treatment for its deposition when compared to other compositions and limiting any degradation of the Sb doped $Mg_2(Si,Sn)$.

Concerning M1 and M2 glasses, the evaluation of the HSM results for the representation of the Log η vs T curves, is only feasible up to the beginning of the nucleation and crystallization phenomena, which have a strong influence on the viscosity.

As shown in Figures 4.2-6 to 4.2-10, it is possible to see that the deformation temperature (DT) occurs after the maximum shrinkage (T_{ms}), while a further shrinkage of the sample is likely due to the viscous flow of the glass. In order to evaluate the sintering ability of the glass system, Lara et al.[198,199] proposed the introduction of the S_c parameter, represented by the difference between the onset temperature of crystallization (T_x) and T_{ms}. It is an empirical method to evaluate the glass sintering conditions of the studied compositions. The difference between these two temperatures gives an assessment about the temperatures range and the time available to the system to carry on the sintering by viscous flow, before the crystallization occurs.

The difference between the onset temperature of crystallization (T_x) and T_{ms} was of 60°C in the case of M1 glass and 115° C for M2 glass. The value is quite high and this means that the crystallization and sintering phenomena will be kinetically independent, and consequently the glass-ceramic material should be well densified and without "shrinkage porosity", since only at the end of the densification, the crystallization starts. If on the contrary, the densification extends itself and overlaps with the crystallization, the forecasts are directed towards a dense material of porosity [198]. The data obtained for M1 and M2 glasses confirms that there was no competition between the two phenomena. Since in the case of M3, M4 and M5 glasses the DTA analyses were not detected crystallization peaks, S_c parameter was not calculated.

On the basis of DTA and HSM analyses, the thermal treatment to obtain the glass-ceramic coating was chosen:

- M1, M2: 1h at 650 °C under flowing Ar (heating rate 10°C/min);
- M3: 1 h at 550 °C under flowing Ar (heating rate 10°C/min);
- M4, M5: 1h at 600°C under flowing Ar (heating rate 10°C/min)

4.2.2.2 Glasses thermo-mechanical characterization: dilatometric analyses

Dilatometric analyses were carried out on the bulk glass, in order to characterize the thermo-mechanical behaviour of the five as-cast glasses. The dilatometric curves (recorded with a heating rate of 5 °C/min) are reported in Figure 4.2-12.

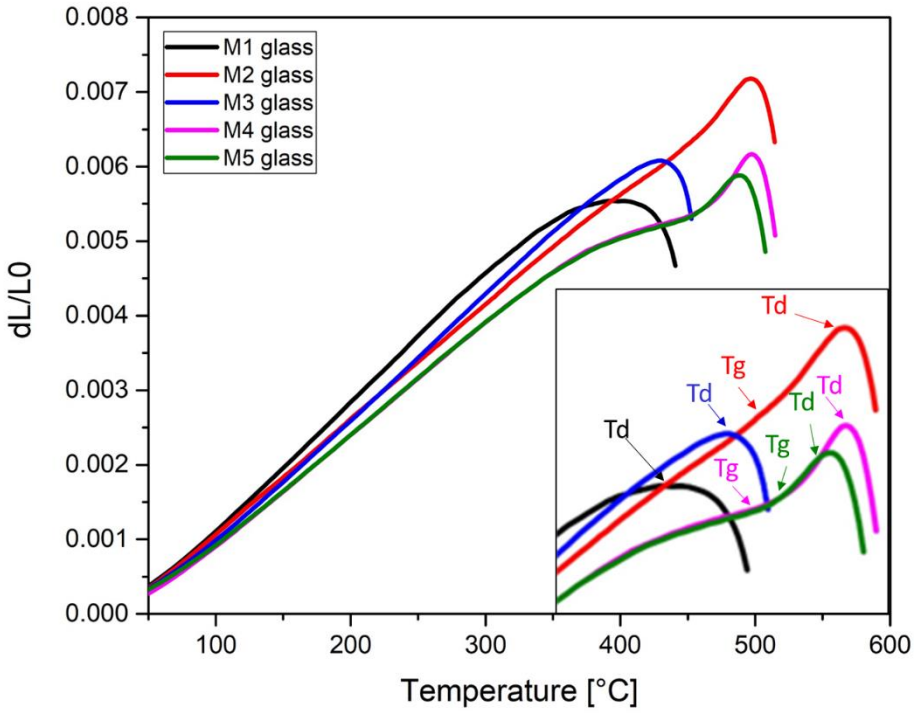

Figure 4.2-12: Dilatometric curves of M1 glass (black curve), M2 glass (red curve), M3 glass (blu curve), M4 glass (violet curve) and M5 glass (green curve), carried out at 5 °C/min. The characteristic temperatures, shown in the in-set and indicated with the arrows, are: T_g (glass transition temperature) and T_d (dilatometric softening point).

The CTEs were extrapolated from the slope of the linear portion of the curves between 150 °C and 300 °C; the CTE values are reported in Table 4.2-5, with other two characteristics temperature of the glass: T_g, measured through the tangent method where the deviation from the linearity of the curve occurs (in some cases it was not possible to detect it), and the dilatometric softening point (T_d) at the peak of the curve. In the same table, for each glass, the simulated values with SciGlass software (Priven-98 model) of CTE and T_g were reported, showing a difference between 0.5- 1.3 for the coefficient of thermal expansion and a difference of 15-

20°C for the glass transition temperature between calculated and experimental values.

Table 4.2-5: Characteristic temperatures and coefficient of thermal expansion of the glasses from M1 to M5, calculated with SciGlass software (Priven-98 model) and experimental measured by means of the dilatometry

	SciGlass calculation		Experimental values		
	CTE(*10^{-6} K^{-1})	T_g (°C)	CTE (*10^{-6} K^{-1}) [150-300°C]	T_g (°C)	T_d (°C)
M1 glass	16.5	416	17	-	401.4
M2 glass	14.6	463.4	15.8	467.9	496.7
M3 glass	14.7	454.6	16.8	-	429
M4 glass	13.4	481.8	14.7	460	496.9
M5 glass	14.1	468.6	14.7	475.8	488.2

4.2.2.3 Glass-ceramic and glass-based coatings characterization: XRD and dilatometry

In this section, the characterisation of the glass-ceramic and the glass-based coatings, obtained from the heat treatment (i. e. coating deposition heat treatment) of M1, M2, M3, M4 and M5 glasses, are presented. The type of crystalline phases formed during the coating process were investigated by means of the XRD analysis. Furthermore, the thermo-mechanical properties were analysed in terms of CTE, that is particularly important for the coating of the thermoelectric substrates.

In order to identify the crystalline phases present in the five compositions, the XRD was carried out on the glass pellets after the heat treatment for the coating process. The results of XRD analyses are presented in Figure 4.2-13. In the M1 glass-ceramic, thermal treated at 650°C for 1h (Figure 4.2-13a), the cubic $Ca_9Al_6O_{18}$ was identified as the main phase (PDF card n. 01-070-0839) and the $KAlSiO_4$ (PDF card n. 00-048-1028) was detected as secondary phase. Furthermore, an amorphous halo was clearly visible, suggesting the presence of a remarkable residual glassy phase. For the M2 glass-ceramic (Figure 4.2-13b), heat treated in the same conditions, the calcium aluminium oxide is still the main phase, but the intensity of the main peak of the potassium aluminium silicate increases considerably. The amorphous halo related to the residual glassy phase seems to be decreased. No clear evidence of crystalline phases was found for M3 heat treated at 550°C for 1h: the XRD pattern was mainly amorphous with some deviation (Figure

4.2- 13c). Finally, no crystalline phases were detected for M4 and M5 compositions thermally treated at 600°C for 1h (Figure 4.2- 13d, e).

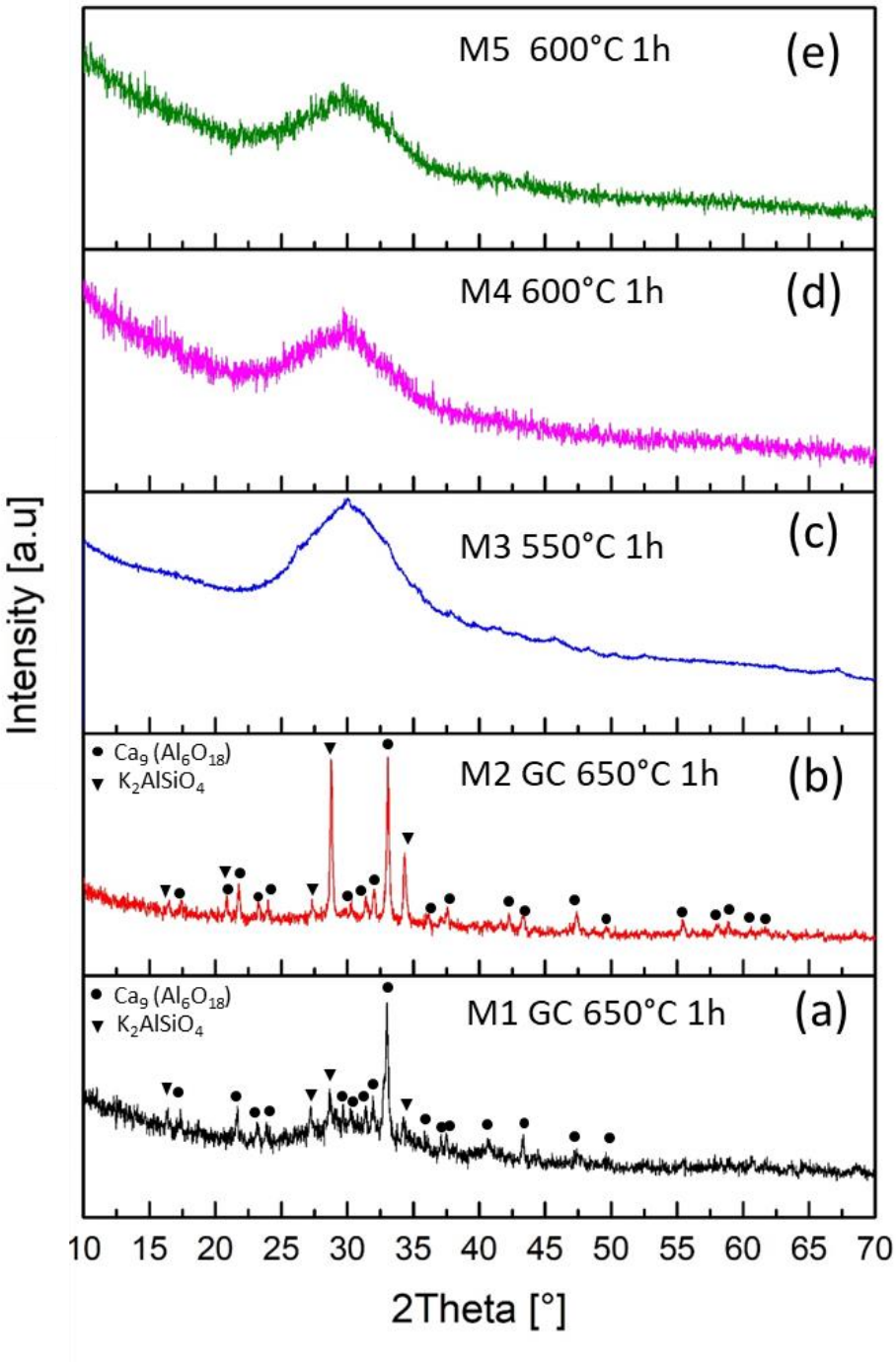

Figure 4.2-13: XRD pattern of (a, b) M1 and M2 glass-ceramic coatings, (c, d, e) M3, M4 and M5 glass-based coatings

Dilatometric analyses were carried out on sintered samples of the five compositions, in order to characterize the thermo-mechanical behaviour especially under the point of view of the CTE of the coating. The pellets were sintered with the chosen coating deposition treatment described in section 4.2.2.1, different from

each composition. The dilatometric curves detected for each sample (recorded with a heating rate of 5 °C/min) are reported in Figure 4.2-14.

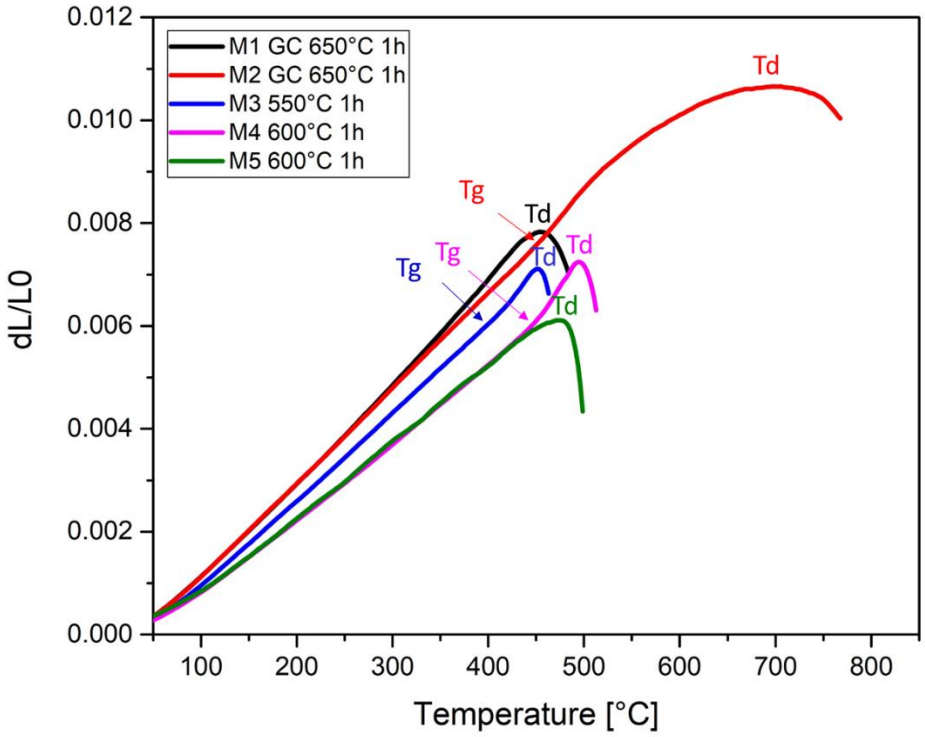

Figure 4.2-14: Dilatometric curves carried out at 5 °C/min of M1 and M2 glass-ceramic coatings (black and red curves), M3, M4 and M5 glass-based coatings (blu, violet and green curves). The characteristic temperatures indicated with the arrows are: T_g (glass transition temperature) and T_d (dilatometric softening point).

The CTE were extrapolated from the slope of the linear portion of the curves between 150 °C and 300 °C. The results of the CTE are reported in Table 4.2-6. In the same table, for each glass-based composition, T_g and T_d are reported (in some cases T_g was not detectable). Since the values of the coefficient of thermal expansion obtained for M1 and M2 glass-ceramics were too high in comparison with the Sb doped $Mg_2(Si,Sn)$ one, these two glass-ceramics were not considered as appropriate coatings for $Mg_2Si_{0.487}Sn_{0.5}Sb_{0.013}$ (which has a CTE= $17.6 \cdot 10^{-6}$ K^{-1}, as reported in section 4.2.1). Therefore, only M3, M4 and M5 compositions were chosen to be deposited on the $Mg_2Si_{0.487}Sn_{0.5}Sb_{0.013}$ thermoelectric.

Table 4.2-6: Characteristic temperatures and coefficient of thermal expansion of the glass-ceramics from M1 to M5

	CTE (*10^{-6} K^{-1}) [150- 300°C]	T_g (°C)	T_d (°C)
M1 GC 650°C 1h	19.2	-	454
M2 GC 650°C 1h	18.5	453	705
M3 550°C 1h	17.0	409	452
M4 600°C 1h	14.9	452	495
M5 600°C 1h	15	-	475

4.2.2.4 M glass-based coated Sb doped $Mg_2(Si,Sn)$: morphological and chemical characterization after deposition treatment

In this section, the results concerning the morphological and chemical analyses on the coated samples are shown and discussed. In the case of the M3 glass-based coating, the results obtained after a thermal ageing at 500°C in air with a dwelling time of 120 hrs are also presented.

Since the results obtained with the dilatometric analyses for M1 and M2 in terms of thermo-mechanical compatibility between glass-ceramic and substrate were not satisfactory (the CTE of M1 and M2 produced was too high compared with the substrate), only M3, M4 and M5 glasses were chosen to be deposit as a slurry paste on the $Mg_2Si_{0.487}Sn_{0.5}Sb_{0.013}$ substrate. After the coating process, at 550°C for 1 h for M3 glass and at 600°C for 1h for M4 and M5 glasses (all of them in flowing Ar), morphological SEM analyses were carries out at the interface and in the bulk of glass-ceramics.

Figure 4.2-15 shows the cross-sections of the M3, M4 and M5 coated $Mg_2Si_{0.487}Sn_{0.5}Sb_{0.013}$. In Figure 4.2-15a, b SEM images of M3 glass coated Sb doped $Mg_2(Si,Sn)$ are shown and it can be seen that the coating is well adherent to the substrate, no pores, cracks or delamination phenomena are visible at the coating/TE interface after the deposition treatment. Furthermore, the M3 coating showed a low amount of closed porosity. No crystalline phases were found, accordingly with the XRD pattern previously reported (Figure 4.2- 13c). Based on the absence of cracks, a good thermo-mechanical compatibility was found between the coating and the thermoelectric substrate, confirming the results obtained with the dilatometric analysis. On the other side, the TE/M4 coating interface shown in Figure 4.2- 15c, d, revealed some delamination phenomena, visible at the interface between the coating and the Sb doped $Mg_2(Si,Sn)$ thermoelectric, probably due to the mismatch between the coefficient of thermal expansion of the M4 glass coating

($14.9 \cdot 10^{-6}$ K^{-1}) and of the TE substrate ($17.6 \cdot 10^{-6}$ K^{-1}). Also in this case, crystalline phases were not detected. Figure 4.2- 15e, f shows the SEM images of the cross-section of the M5 glass coated Sb doped $Mg_2(Si,Sn)$; despite the difference in terms of CTEs between coating and substrate, it can be observed the absence of cracks within the coating, which is well-adherent to the substrate and free of defects. In all the samples, no oxidation/reaction layers are visible at the interface.

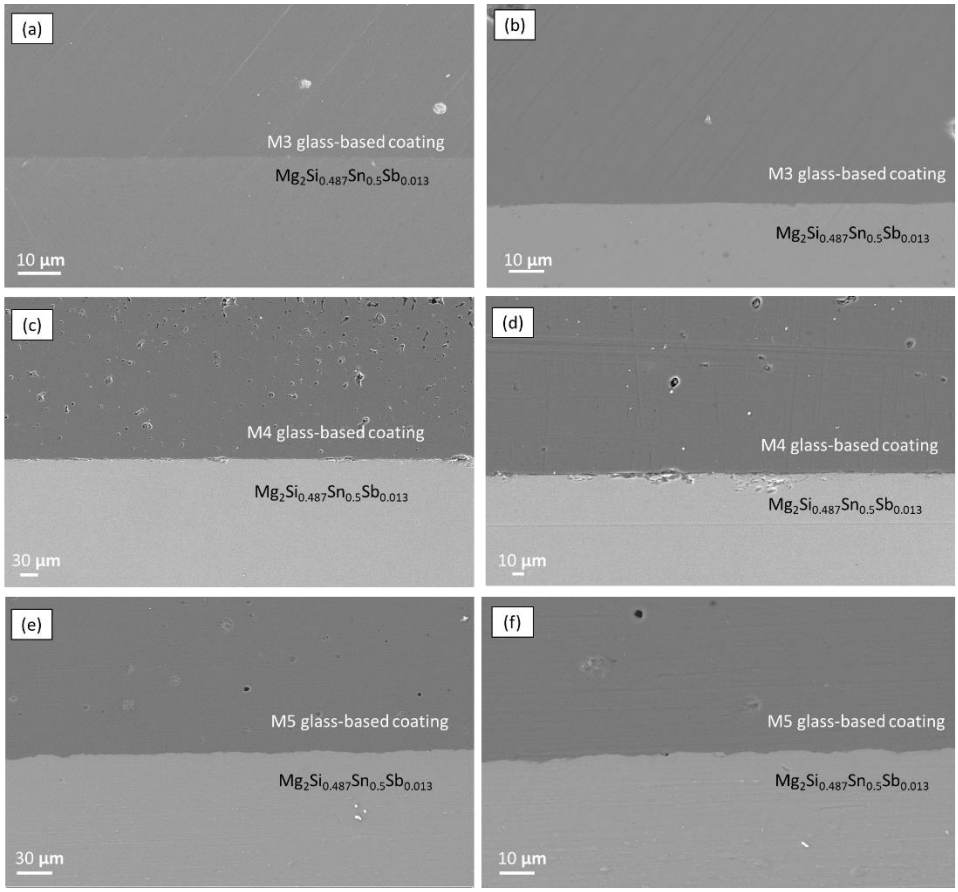

Figure 4.2-15: SEM images of the cross-section of (a, b) M3 glass coated $Mg_2Si_{0.487}Sn_{0.5}Sb_{0.013}$, of (c, d) M4 glass coated $Mg_2Si_{0.487}Sn_{0.5}Sb_{0.013}$ and of (e, f) M5 glass coated $Mg_2Si_{0.487}Sn_{0.5}Sb_{0.013}$, all after deposition heat treatment under flowing Ar.

Based on these results, M3 and M5 glass-based coating were chosen as potential candidates to avoid the degradation of the $Mg_2Si_{0.487}Sn_{0.5}Sb_{0.013}$ during an oxidation test at 500°C for 120 hrs in air.

4.2.2.5 M3 and M5 glasses coated Sb doped $Mg_2(Si,Sn)$ after oxidation test: morphological and chemical characterization

Figure 4.2-16 shows a sample of uncoated $Mg_2Si_{0.487}Sn_{0.5}Sb_{0.013}$ and a sample of M3 glass coated $Mg_2Si_{0.487}Sn_{0.5}Sb_{0.013}$, before and after the ageing test at 500°C for 120 hrs in air. It is clear that the glass coating has an effective role for protecting the thermoelectric substrate in oxidative atmosphere, since without coating it was completely oxidised and turned into powder.

Figure 4.2-16: Uncoated $Mg_2Si_{0.487}Sn_{0.5}Sb_{0.013}$ and M3 glass coated $Mg_2Si_{0.487}Sn_{0.5}Sb_{0.013}$ before and after the oxidation test in oxidative atmosphere at 500°C for 120 hrs.

After the oxidation test at 500°C for 120 hrs, the M3 glass coated $Mg_2Si_{0.487}Sn_{0.5}Sb_{0.013}$ sample was submitted to morphological and chemical analyses by mean of SEM and EDS. Figure 4.2-17 a, b shows that the good compatibility between the glass coating and the Sb doped $Mg_2(Si,Sn)$ substrate was maintained after the long exposure to severe conditions. The interface between the coating and the thermoelectric substrate is characterized by the absence of cracks or delamination phenomena. Two SEM images of the M3 glass coated Sb doped $Mg_2(Si,Sn)$ at higher magnification are reported in Fig. 4.2-17c, d, confirming the optimal adhesion of the coating to the thermoelectric. Figure 4.2-17e shows a SEM image with the related EDS analysis. No diffusion of elements between the substrate and the glass coating was detected. In fact, in the $Mg_2Si_{0.487}Sn_{0.5}Sb_{0.013}$ only Mg, Si and Sn were reported, while in the coating all the chemical elements belonging to the glass composition were found.

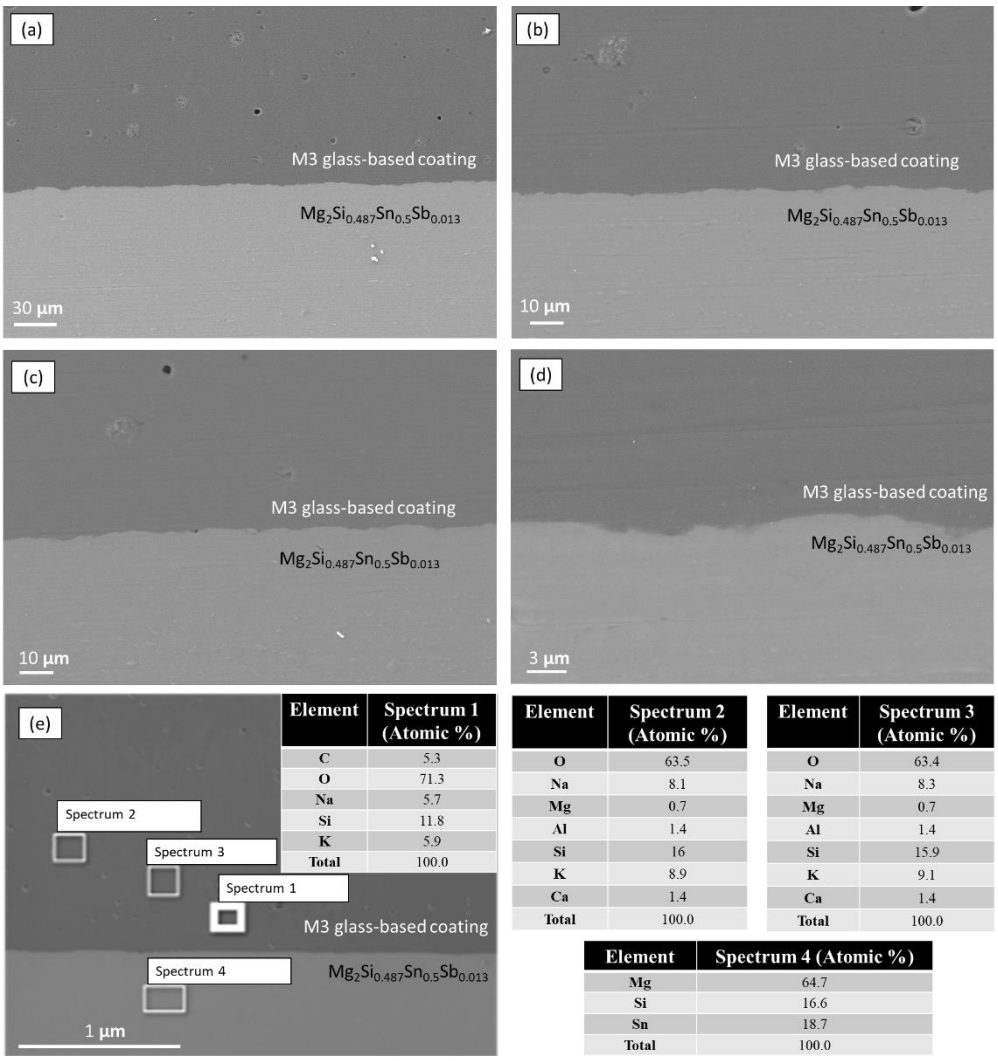

Element	Spectrum 1 (Atomic %)
C	5.3
O	71.3
Na	5.7
Si	11.8
K	5.9
Total	100.0

Element	Spectrum 2 (Atomic %)
O	63.5
Na	8.1
Mg	0.7
Al	1.4
Si	16
K	8.9
Ca	1.4
Total	100.0

Element	Spectrum 3 (Atomic %)
O	63.4
Na	8.3
Mg	0.7
Al	1.4
Si	15.9
K	9.1
Ca	1.4
Total	100.0

Element	Spectrum 4 (Atomic %)
Mg	64.7
Si	16.6
Sn	18.7
Total	100.0

Figure 4.2-17: SEM images and EDS analysis of the cross-section of M3 glass coated $Mg_2Si_{0.487}Sn_{0.5}Sb_{0.013}$ after oxidation test at 500°C for 120 hrs in air

The second material chosen as potential oxidation protective coating for Sb doped $Mg_2(Si,Sn)$ based materials was the M5. Figure 4.2-18 shows a photo of the M5 glass coated $Mg_2Si_{0.487}Sn_{0.5}Sb_{0.013}$ after the deposition heat treatment, before and after the ageing test at 500°C, but after only 8 hours the sample was completely decomposed and therefore it was not possible to carry out the morphological and thermoelectrical characterization. A possible explanation for this might be related to the presence of one or more areas of the substrate not completely covered. In this case the oxygen could be easily gone into contact with the Sb doped $Mg_2(Si,Sn)$ causing the degradation. A possible follow-up for this work could be the optimization of a more uniform and reproducible method of the glass deposition.

In conclusion, the failure of both M4 and M5 glass coatings could be related to the CTEs mismatch between the glass coating and the Sb doped $Mg_2(Si,Sn)$. Comparing the two glass compositions, the former/modifier oxides ratio is quite similar (they differ only slightly in the SiO_2:K_2O ratio) and the glass coatings

obtained after the heat treatment did not crystallize, therefore the CTEs are the same of the parental glasses (~ $15 \cdot 10^{-6}$ K^{-1}), much lower respect that of the Sb doped $Mg_2(Si,Sn)$ which is $17.6 \cdot 10^{-6}$ K^{-1}. This could have led to delamination phenomena, residual stresses and, consequently, presence of cracks.

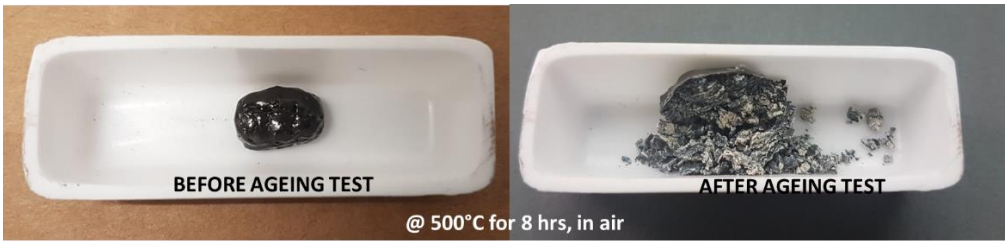

Figure 4.2-18: M5 glass coated $Mg_2Si_{0.487}Sn_{0.5}Sb_{0.013}$ before and after the ageing test in oxidative atmosphere at 500°C. After only 8 hrs the sample was exploded

4.2.2.6 M3 glass coated Sb doped $Mg_2(Si,Sn)$ after oxidation test: XRD and dilatometry

In order to further confirm the effectiveness of the M3 glass-based coating for the protection of $Mg_2Si_{0.487}Sn_{0.5}Sb_{0.013}$, the XRD analysis on coated sample after the oxidation test at 500°C for 120 hrs in air was carried out (after removing of the outer layers to reveal the pristine thermoelectric substrate) and the results are presented in Figure 4.2-19. As can be noted, the single phase $Mg_2Si_{0.4}Sn_{0.6}$ identified with the PFD card 01-089-4254, is the same compared to the as-sintered sample (see Figure 4.2-1b), validating the efficacy of the M3 glass-based coating after the oxidation test; only a slight presence of MgO was found (identified with the PDF card n. 01-075-1525) represented by a peak around 43°, but it was already labelled in the as-sintered $Mg_2Si_{0.487}Sn_{0.5}Sb_{0.013}$ (section 4.2.1).

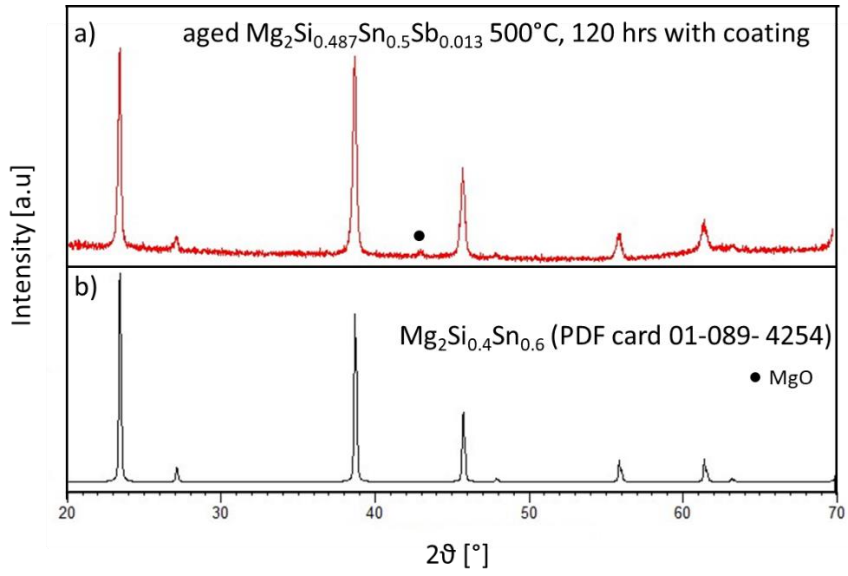

Figure 4.2-19: XRD pattern of (a) aged $Mg_2Si_{0.487}Sn_{0.5}Sb_{0.013}$ at 500°C for 120 hrs in air with coating (removing of the outer layers before doing XRD analysis), (b) PDF card (number: 01-089-4254) of $Mg_2Si_{0.4}Sn_{0.6}$

Furthermore, X-ray diffraction analysis was performed on M3 glass-based coating after the oxidation test to evaluate the thermodynamic stability after the thermal treatment at 500°C for 120 hrs in air (Figure 4.2-20): no crystalline phases were detected after the oxidation test (b curve), as before the oxidation test (a curve) and the amorphous halo linked to the glassy phase seems to be unchanged.

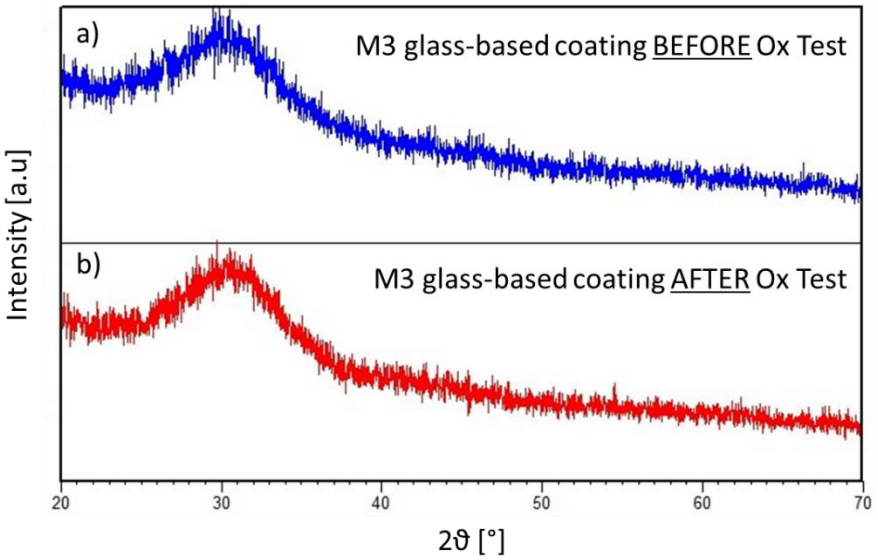

Figure 4.2- 20: XRD pattern of M3 glass-based coating (a) before and (b) after oxidation test at 500°C for 120 hrs in air

Furthermore, the dilatometric curves of M3 glass coating (Figure 4.2-21a) and M3 heat treated at 500°C for 12hrs (Figure 4.2-21b) are very similar and the CTEs, calculated in a temperature range between 150°C and 300°C, are quite similar: $17 \cdot 10^{-6}$ K^{-1} and $16.6 \cdot 10^{-6}$ K^{-1}, respectively (the slight difference probably is due to an experimental error). This further demonstrates the stability of this glass-based system. In addition, both the glass transition temperature and the softening point between and after the oxidation test are almost unchanged.

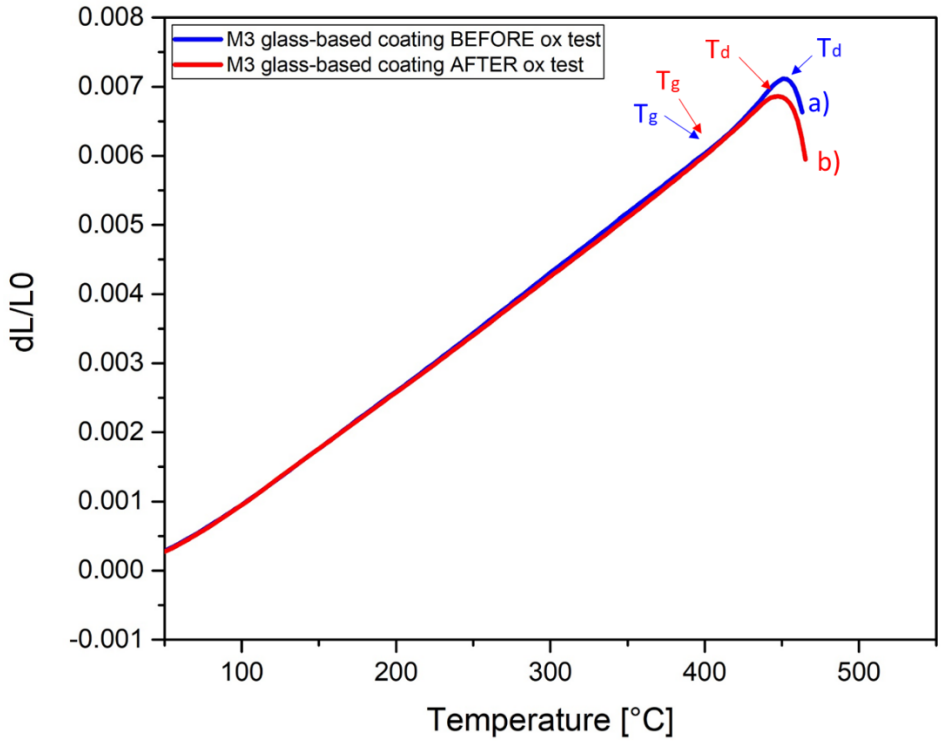

Figure 4.2-21: Dilatometric curves carried out at 5 °C/min of (a) M3 glass-based coating obtained at 550°C for 1h and (b) M3 glass-based coating after the oxidation test at 500°C for 120hrs. The characteristic temperatures indicated with the arrows are: T_g (glass transition temperature) and T_d (dilatometric softening point).

Summarising, a series of new silica-based glass and glass-ceramics were designed as potential coatings and one of them was successfully tested for protecting Sb doped $Mg_2(Si,Sn)$ based materials. The most promising composition is the M3 one. Even if the thermoelectric properties of a coated sample were not carried out yet, the M3 glass-based coating demonstrated to be effective for protecting the $Mg_2Si_{0.487}Sn_{0.5}Sb_{0.013}$ thermoelectric after an ageing at 500°C for 120 hrs, because, after the oxidation test, the coated sample was not oxidised and turned into powder as occurred in the uncoated sample thermally treated in the same conditions. This finding, through preliminary, suggests that the M3 glass-based coating could be a promising candidate for protecting Sb doped $Mg_2(Si,Sn)$ based thermoelectrics against oxidation.

The thermoelectric characterization will be performed, to compare the thermoelectric properties (electrical resistivity, Seebeck coefficient, Power Factor and Figure of Merit) between as-sintered and M3 glass-based coated $Mg_2Si_{0.487}Sn_{0.5}Sb_{0.013}$ after the oxidation test at 500°C for 120 hrs in air.

Very little information was found in literature on glass-based protective coatings for magnesium silicide based thermoelectrics and especially on the Sb doped $Mg_2(Si,Sn)$, which is characterised by a much higher coefficient of thermal expansion (17-17.5· 10^{-6} K^{-1}) than that of pure silicide. The importance and

originality of this section are that it explores a series of glass-based compositions with high CTE and low deposition temperature (550-600°C), with interesting properties as coating material for $Mg_2Si_{0.487}Sn_{0.5}Sb_{0.013}$. The novelty of this research is very significant because it introduces a new approach to the development of protective coatings for Sb doped $Mg_2(Si,Sn)$ and the possibility to optimise glass-based systems which demonstrated excellent thermo-mechanical compatibility with thermoelectric materials, that is a crucial aspect in the manufacturing of reliable and durable thermoelectric modules.

4.2.3 Ceramacoat™ 512-N coated Sb doped $Mg_2(Si,Sn)$

In order to avoid the oxidation of the Sb doped $Mg_2(Si,Sn)$ surface, and consequently the long-term reliability and efficiency of TE modules an alternative route respect the glass-based coating was tested to protect this TE from oxidation. In a previous, a solvent-based commercial hybrid resin was successfully used to protect the same Sb doped $Mg_2(Si,Sn)$ against oxidation at 500°C; the results of this collaborative research with Nanoforce Techology Ltd, Queen Mary University of London, were published in Gucci et al.[174]. In this thesis, the effectiveness of a new hybrid commercial coating labelled as Ceramacoat™512-N (details about its composition and its curing process were reported in the Materials and Method section) was studied.

The cross-section of coated samples (curing in air at different steps at a temperature of 93°C for 4 hrs, at 177°C for 2 hrs, and finally at 260°C for 1h) shows that fillers of different shape are well dispersed in the silicone resin matrix and no pores, cracks or delamination phenomena are detected at the coating/ $Mg_2Si_{0.487}Sn_{0.5}Sb_{0.013}$ interface (Figure 4.2-22). However, the EDS analysis reveals the probable presence of an oxidation layer at the interface, demonstrated with a high atomic% of oxygen which exceeds 60% (Figure 4.2- 22e).

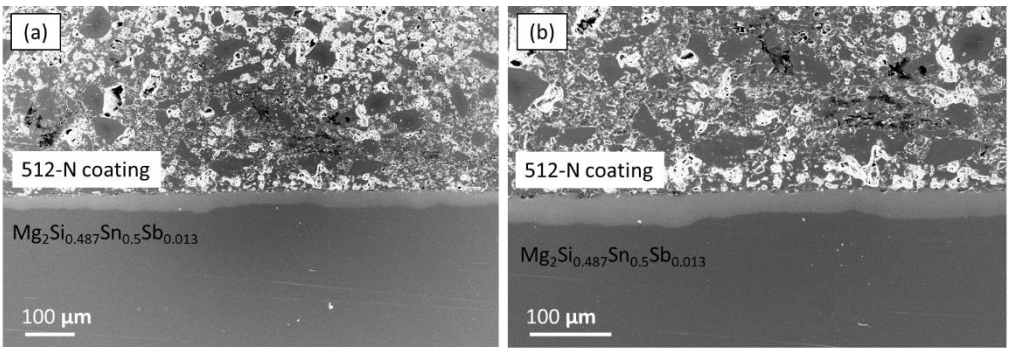

Element	Spectrum 1 (Atomic %)
O	27.8
Mg	45.9
Si	13.0
Sn	13.3
Total	100.00

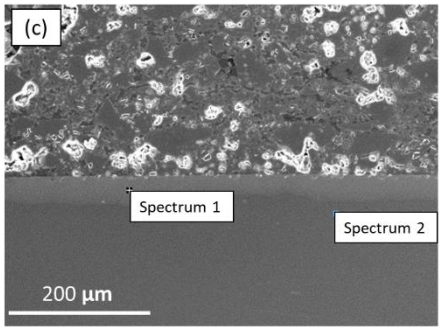

Element	Spectrum 2 (Atomic %)
O	23.3
Mg	49.1
Si	13.5
Sn	14.1
Total	100.0

Element	Spectrum 3 (Atomic %)
C	52.5
O	36.2
Na	2.4
Mg	1.7
Al	0.4
Si	6.2
Cl	0.1
Sn	0.5
Total	100.00

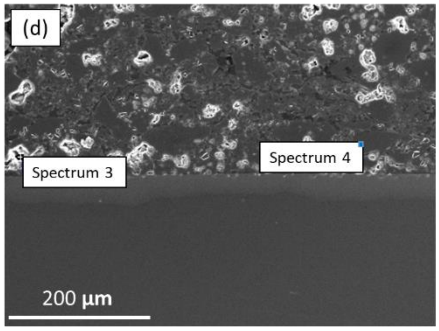

Element	Spectrum 4 (Atomic %)
O	67.6
Al	15.7
Si	16.0
Ti	0.5
Fe	0.2
Total	100.0

Element	Spectrum 5 (Atomic %)
O	65.3
Mg	25.6
Si	4.5
Sn	4.6
Total	100.0

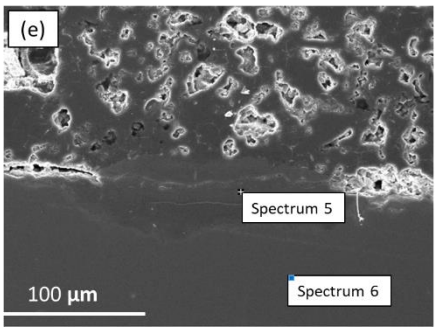

Element	Spectrum 6 (Atomic %)
O	25.2
Mg	47.4
Si	13.6
Sn	13.8
Total	100.0

Figure 4.2-22: SEM images and EDS analysis of the cross-section of Ceramacoat™512-N coated $Mg_2Si_{0.487}Sn_{0.5}Sb_{0.013}$ after curing at different steps of temperature

In order to compare the performance of this coating with the M3 coating, a sample of Ceramacoat™512-N coated $Mg_2Si_{0.487}Sn_{0.5}Sb_{0.013}$ was subjected to a thermal ageing at 500°C for 120 hrs in air, but as it can be seen in Figure 4.3-23, the coated sample was found to be completely decomposed. Therefore, it was not possible to carry out the morphological and electrical characterization. A possible explanation for this might be that the manual method of deposition in this case didn't guarantee the completely coating of the substrate, causing its decomposition when subjected to the oxidation test. Furthermore, the curing of this hybrid coating is very slow, and probably the MgO oxidation layer is produced already at low temperature, as demonstrated by the EDS analysis in Figure 4.2-22e, thus influencing the oxidation resistance of the sample.

Figure 4.2-23: Ceramacoat™ 512-N coated $Mg_2Si_{0.487}Sn_{0.5}Sb_{0.013}$ before and after the ageing test in oxidative atmosphere at 500°C for 120 hrs

4.3 T1 glass-ceramic coated TiO_x

In this section, the results concerning the thermal, thermo-mechanical, chemical and morphological characterization of the T1 glass-ceramic as potential candidate as protective coating for titanium suboxide are discussed. The transformation from T1 glass to T1 glass-ceramic was investigated with two different routes: in the first one, the glass-ceramic was obtained through a bulk crystallization, while in the second one, the T1 glass-ceramic coating was obtained with the sinter-crystallization method (i. e. from pressed glass powder). The glass bulk (first route) and the glass pellet (second route) were submitted to the same heat treatment. A schematic illustration of the two routes is shown in Figure 4.3-1.

Preliminary oxidation tests of T1 glass-ceramic coated TiO_x up to 600°C are in progress and they are not reported in this thesis.

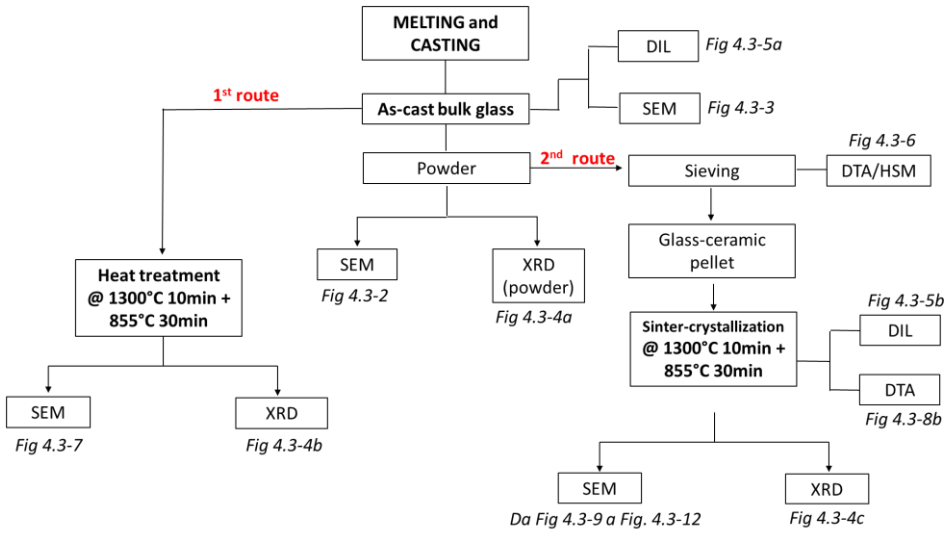

Figure 4.3-1: Schematic illustration of the T1 glass and glass-ceramic characterization

4.3.1 T1 glass characterization: morphological and chemical characterization

In this section, the morphological and chemical characterization of the T1 glass, both as powder and as bulk, is reported.

The as-cast T1 glass looked like an opaque white glass. Figure 4.3-2 shows the T1 glass powder, which is quite irregular in the form and in the size, ranging from 10 to 40 μm.

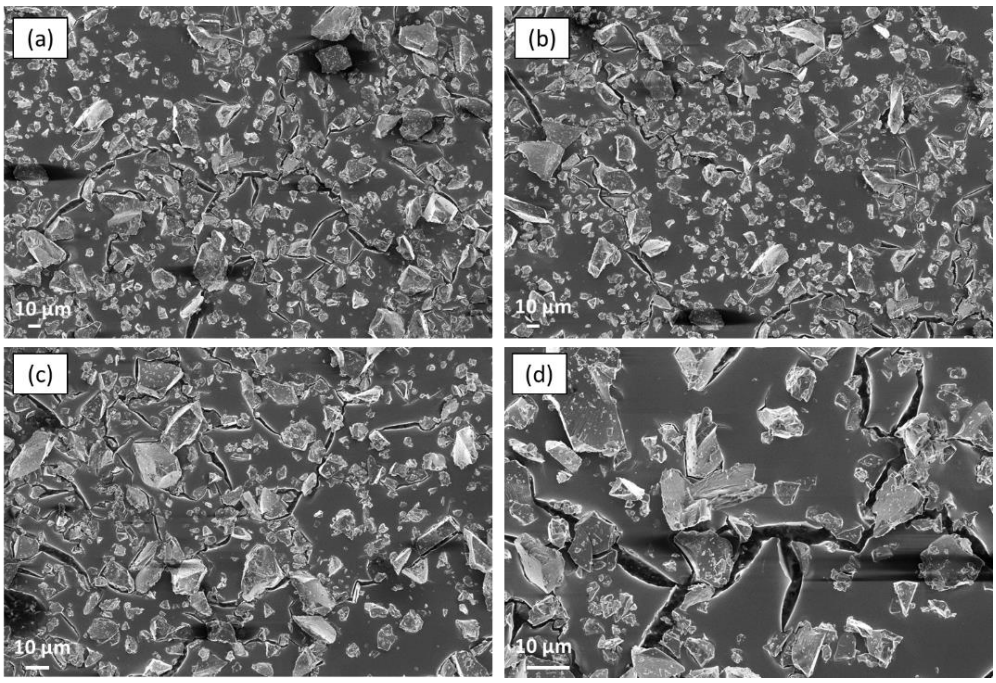

Figure 4.3-2: SEM images of T1 glass powders

Figure 4.3-3 (a, b) shows SEM images of the T1 glass bulk as-cast and polished for the morphological analysis. It can be noted that there are two phases: a dark matrix and a brighter phase which appears as round shaped particles with a size ranging from 200 to 250 nm. The EDS analysis (Figure 4.3-3b) was not able to discriminate the different composition of the two phases and showed the presence of all the elements belonging to the glass composition.

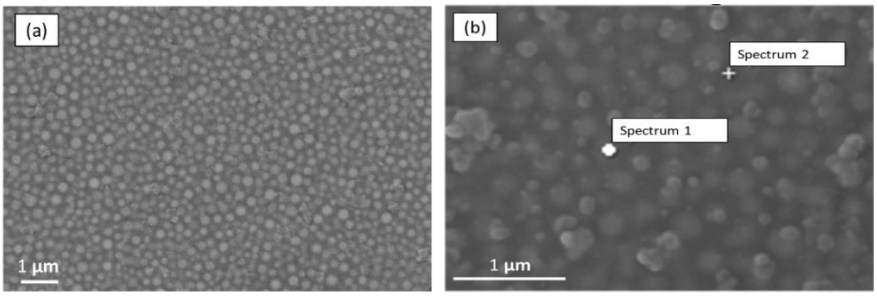

Element	Spectrum 1 (Atomic %)
O	60.9
Na	2.8
Al	10.2
Si	11.1
K	2.5
Ca	2.5
Ti	6.6
Y	3.4
Total:	100.0

Element	Spectrum 2 (Atomic %)
O	60.9
Na	2.8
Al	10.0
Si	10.9
K	2.5
Ca	2.5
Ti	6.7
Y	3.7
Total:	100.0

Figure 4.3-3:(a) SEM image of T1 glass as cast and polished and (b) EDS analysis

The opaque appearance of as-cast T1 is characteristic of phase separated glasses. However, Figure 4.3-4a shows the XRD pattern of T1 as-cast glass where an amorphous halo is visible, but it can be also noted the presence of the main peak of cubic yttrium titanium oxide with stoichiometric formula $Y_2Ti_2O_7$ (PDF card n. 00-042-0413) [200].

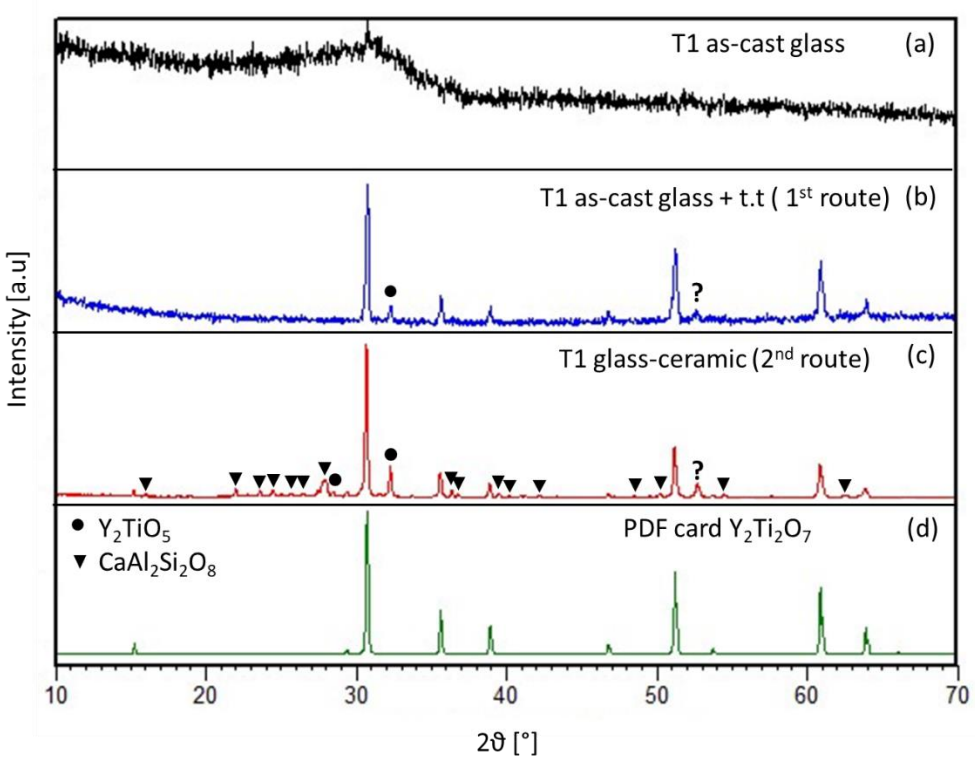

Figure 4.3-4: XRD pattern of (a) T1 as-cast glass, (b) T1 as-cast glass thermally treated at 1300°C for 10 minutes + 855°C for 30 minutes (1st route), (c) T1 glass-ceramic (2nd route) and (d) $Y_2Ti_2O_7$ PDF card n.00-042-0413.

Three different hypotheses were done to explain this microstructure:

(i) the formation of the primary crystal phase during the cooling of the glass melt and the nano-crystals growth in a spherical shape;

(ii) a glass phase separation that led to the formation of spheroids distributed in a homogeneous glassy matrix;

(iii) a glass phase separation caused the formation of Y- and Ti- rich glass droplets in which the primary crystals, yttrium titanate, grew to nanometric sizes.

The XRD results seem to support (i) and (iii) hypotheses, but futher investigation should be carried out with a high resolution trasmission electron microscopy and would be of great help in clarifying the microstructure of the as cast glass.

4.3.2 T1 glass thermo-mechanical characterization: dilatometric analysis

The dilatometric curve (recorded with a heating rate of 5 °C/min) obtained on a little drop of T1 glass is reported in Figure 4.3-5a (black curve).

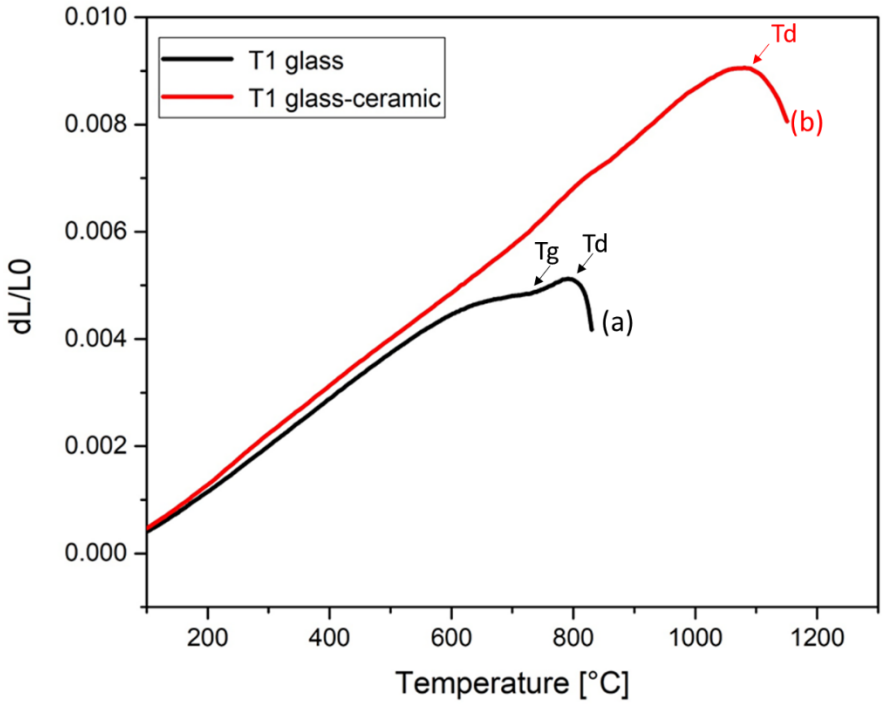

Figure 4.3-5: Dilatometric curves carried out at 5 °C/min of (a) T1 glass and (b) T1 glass-ceramic obtained after curing at 1300°C for 10 minutes+ 855°C for 30 minutes. The characteristic temperatures indicated with the arrows are: T_g (glass transition temperature) and T_d (dilatometric softening point).

The CTE was extrapolated from the slope of the linear portion of the curve between 200 °C and 500 °C and the value is reported in Table 4.3-1, with the T_g, measured with the tangent method where the deviation from the linearity of the curve occurs, and the dilatometric softening point (T_d) at the peak of the curve. In the same table, CTE and T_g calculated with the SciGlass software are reported.

Table 4.3-1: Characteristic temperatures and coefficient of thermal expansion of the T1 glass and T1 glass-ceramic, calculated with SciGlass software and experimental measured

	SciGlass calculation		Experimental values		
	CTE($*10^{-6}$ K^{-1})	T_g (°C)	CTE ($\cdot 10^{-6}$ K^{-1}) [200- 500°C]	T_g (°C)	T_d(°C)
T1 glass	7.1	820	8.6	734	792
T1 glass-ceramic	-	-	9.1	-	1081

4.3.2 Evolution of T1 from glass to glass-ceramic

In this section the transformation of T1 glass to T1 glass-ceramic will be discussed, considering two different routes, as above mentioned.

In the first part of the paragraph, the study of the sintering and the crystallization behaviour are illustrated. The data obtained by DTA and HMS analyses are correlated optimising the sinter-crystallization treatment (2nd route) for an effective oxidation glass-ceramic resistant coating for the titanium suboxide substrate.

The glass powder was characterized by means of the DTA, with a heating rate of 10°C/min and the powders particle size ≤ 38 µm. The DTA curve is shown in Figure 4.3-6 (black curve).

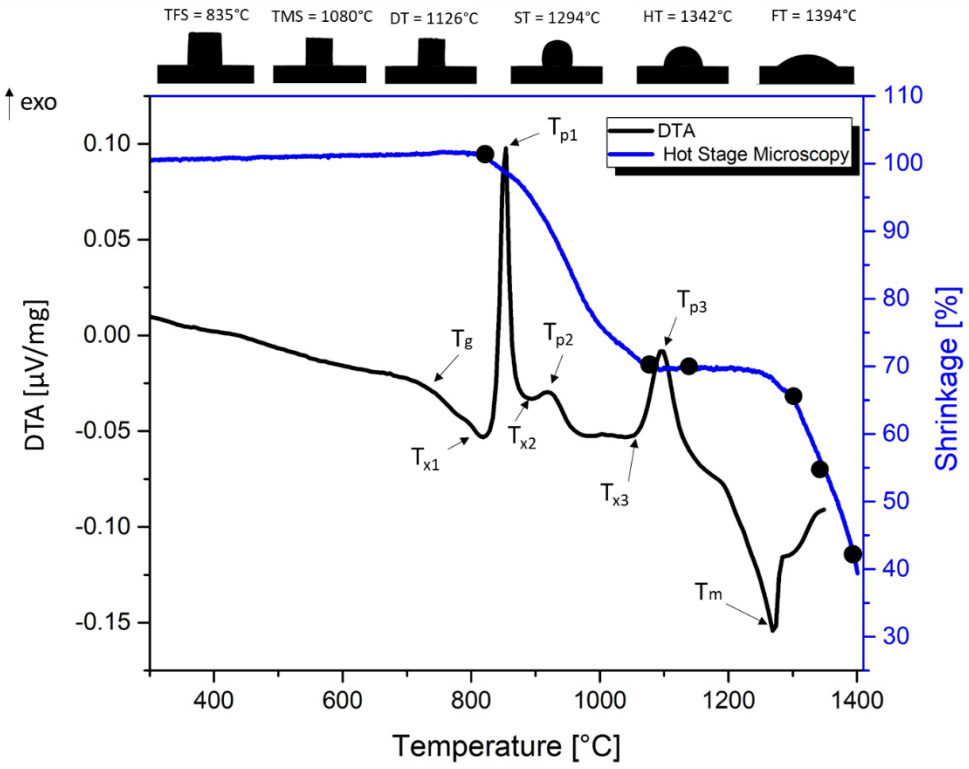

Figure 4.3-6: DTA (black curve) and HSM (blu curve) analyses carried out at 10°C/min on the T1 glass powder. The characteristic temperatures indicated with the black arrows in the DTA plot are: T_g (glass transition temperature), T_x (onset crystallization temperature), T_p (crystallization peak temperature) and T_m (melting temperature).

The glass transition temperature (T_g), three crystallization peaks (T_{p1}, T_{p2}, T_{p3}) and the melting temperature (T_m) are indicated in the graph. The melting temperature detected by DTA can be assumed as the melting of the crystallized phases. However, the melting temperature found with the DTA was lower than that detected with HSM, 1271°C and 1394°C respectively. T_g, as previously explained, was

considered as the onset of the endothermic transition on the left side of the graphs, but in this analysis it was not possible to detect it. The characteristic temperatures for the glass, extrapolated from the DTA curve obtained at 10°C/min are reported in Table 4.3-2.

Table 4.3-2: Characteristic temperatures of T1 glass powders collected at 10°C/min

	Characteristic temperatures (°C)							
	T_g	T_{x1}	T_{p1}	T_{x2}	T_{p2}	T_{x3}	T_{p3}	T_m
T1 glass powders	752	819	852	884	919	1046	1097	1271

The sintering behaviour of T1 glass was investigated by hot stage microscopy (HSM) and was analysed in relation to DTA results, with the aim to study the correct order of events during the sinter-crystallization behaviour. The characteristic figures and the related temperatures obtained by HSM (blu curve) are reported in the Figure 4.3-6 on the top of the graph. Since the coating should protect the thermoelectric substrate from oxidation, it is very important to have a good densification of the glass-ceramic during the coating process. As already discussed above, since the crystallization can reduce the rate of densification by viscous flow, it is desirable to identify the sintering and crystallization mechanisms, in order to identify the suitable heat treatment for the production of glass-ceramic coatings from powders by the sintering-crystallization method. For this reason, all the considerations explained in the 4.2.2.1 paragraph concerning the thermal stability of a glass and the sinter-capability of a glassy system are valid also for T1 glass. The correct order of events should consist in reaching firstly the maximum densification shrinkage and subsequently induce the crystals growth, in order to produce a glass-ceramic. However, as it can be observed in the Figure 4.3-6, the onset of the crystallization in the DTA plot almost overlaps the first shrinkage temperature measure with the hot stage microscopy, so the two phenomena are not as independent as it would be desirable.

The identification of the phase that crystallizes in correspondence to the first peak of crystallization (T_{p1} in Figure 4.3-6) was carried out on T1 glass heat heated at 855°C for 30 minutes and subsequently performing the XRD analysis on the crushed powders. The results (not reported here) indicated the formation of a single phase with stoichiometric formula $Y_2Ti_2O_7$, whose coefficient of thermal expansion is ~8.4 $\cdot 10^{-6}$ K^{-1} in the range 300- 1000°C, very similar to that of the titanium suboxide that is between 7 and 9 $\cdot 10^{-6}$ K^{-1}[201]. For this reason, the thermal treatment chosen for the coating deposition was: 1300°C for 10 minutes and subsequently at 855°C for 30 minutes under flowing Ar. Previously, only H-P. Martin et al. [123] suggested a SiO_2-BaO-CaO based- glass as oxidation resistant coating material for TiO_x, but its effectiveness was proved only up to 500°C.

In order to understand the evolution of the morphology of T1 glass during the coating deposition, the same heat treatment (1300°C for 10 minutes + 855°C for 30 minutes under flowing Ar) was carried out on the as-cast glass bulk (1st route) and on a pellet of uniaxially pressed glass powders (2nd route).

Figure 4.3-7 shows the SEM images of T1 as-cast glass bulk (**1st route**) heat treated at 1300°C for 10 minutes and subsequently at 855°C for 30 minutes, under flowing Ar (1st route). Bright crystals homogeneously dispersed in a glass matrix are clearly visible. They appear with an irregular size and dimension (Figure 4.3-7a, b), homogeneously distributed in the glass matrix, similar to the ones reported in [202,203]. The EDS analysis (Figure 4.3-7c) carried out on the crystals shows higher atomic% of Y and Ti, which indicates the formation of crystalline phases containing these elements, while the compositional analysis performed on the darker matrix (Figure 4.3-7d) reveals higher atomic% for Si, Na, Al, Ca, which compose the glassy phase.

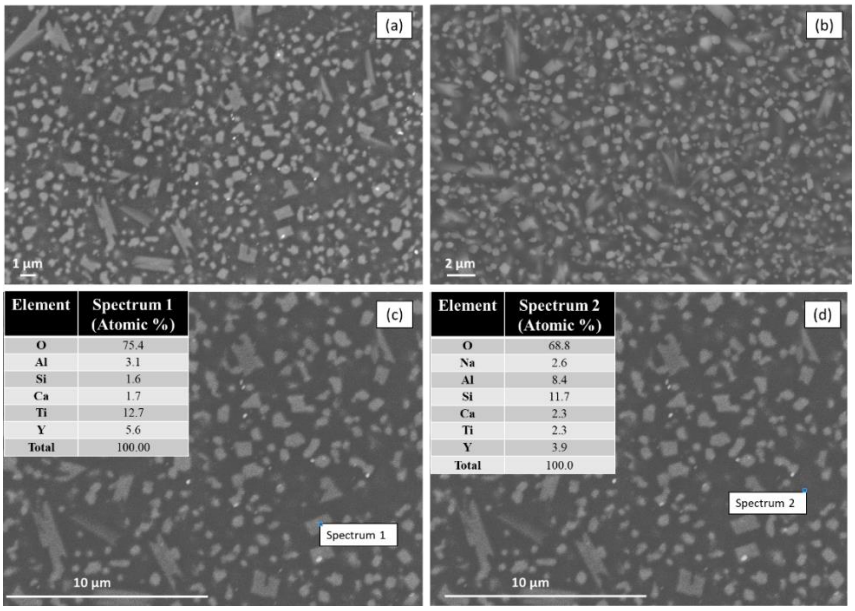

Figure 4.3-7: (a, b) SEM images of T1 glass bulk heat treated at 1300°C for 10 min+ 855°C for 30 min and (c, d) EDS analysis

Furthermore, in the XRD pattern related to the T1 glass bulk after the heat treatment at 1300°C for 10 minutes + 855°C for 30 minutes (Figure 4.3-4b), the amorphous halo due to the glassy phase is considerably decreased, while the peaks related to the primary crystal phase, $Y_2Ti_2O_7$, increased in number and intensity, confirming the EDS analysis previously reported. Furthermore, the indexing of the peak at around 32° is still uncertain. It was tentatively attributed to the hexagonal Y_2TiO_5 (PDF card n. 00-027-0981), but previous studies reported the transformation of the α-orthorhombic yttrium titanium oxide in the ß- hexagonal phase only at 1330°C [204,205]. Therefore, the presence of the hexagonal Y_2TiO_5 in the XRD analysis results should be carefully evaluated in a future work. In addition, it was not possible to identify the phase of the peak around 52.5°.

In the last part of this section, the results concerning the T1 glass-ceramic obtained starting from a pellet of uniaxially pressed glass powder, are presented (**2nd route**).

In order to recognize the crystalline phases present in the T1 glass-ceramic, XRD was carried out on the glass-ceramic pellet (reduced into powder) after the coating deposition heat treatment. This analysis was performed in collaboration with the University of Hertfordshire, Hatfield, UK. The results of XRD analysis are shown in Figure 4.3-4c. The cubic yttrium titanium oxide with stoichiometric formula $Y_2Ti_2O_7$ was identified as the main phase with the PDF card n. 00-042-0413. Furthermore, the calcium aluminum silicate with anorthite crystalline structure and stoichiometric formula $CaAl_2Si_2O_8$ (PDF card n. 01-041-1486) was identified as secondary phase. As mentioned in the previous paragraph, the indexing of the peak around 32° is still under investigation, while the peak at 52.5° could not be identified.

Further experimental activities will be focused on the Rietveld analysis which allows the quantification of the crystalline phase in terms of wt%.

The comparison between the DTA analysis of T1 after the deposition process (1300°C for 10 minutes and subsequently at 855°C for 30 minutes, under flowing Ar) is presented in Figure 4.3-8; the glass transition temperature onset in the glass-ceramic is almost the same of the parent glass (756°C and 752°C respectively), as well as the melting temperature, while crystallization peaks were not detected for the glass-ceramic.

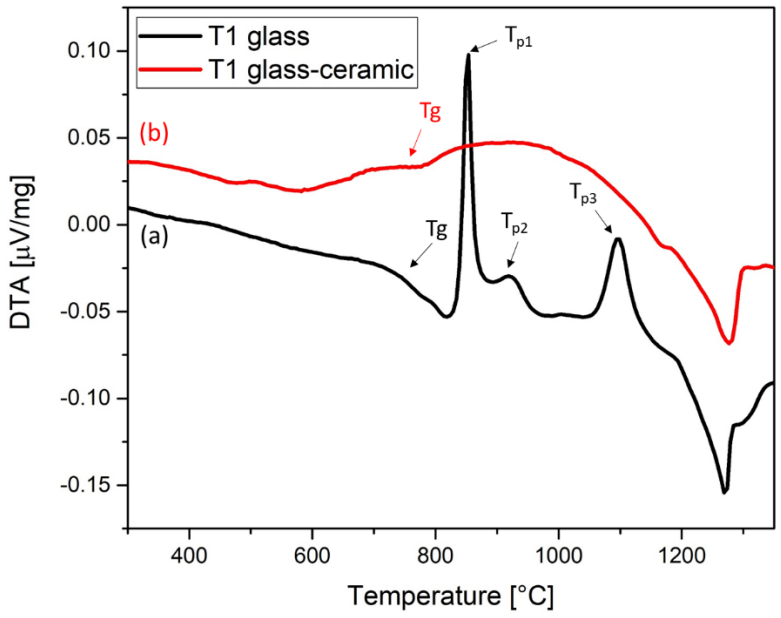

Figure 4.3-8: DTA analysis of (a) as-cast T1 glass and (b) T1 glass-ceramic obtained with a heat treatment at 1300°C for 10 minutes and s at 855°C for 30 minutes, under flowing Ar. The characteristic temperatures indicated with the arrows are: T_g (glass transition temperature) and T_p (crystallization peak temperature).

In addition, thermo-mechanical properties of the glass-ceramic were analysed with particular focus on the CTE, that is a fundamental parameter for the compatibility between coating and the thermoelectric substrates. The dilatometric analysis was carried out on the glass-ceramic (red curve in the Figure 4.3-5b) obtained from uniaxially pressed the glass powders and heat treated at 1300°C for 10 minutes and subsequently at 855°C for 30 minutes, under flowing Ar. The CTE were extrapolated from the slope of the linear portion of the curves between 200 °C and 500 °C. The measured CTE of T1 glass-ceramic, reported in Table 4.3-1, was found to be $9.1 \cdot 10^{-6}$ K^{-1}, very close to the coefficient of thermal expansion of titanium suboxide reported by H- P. Martin et al.[123] (between 7 and $9 \cdot 10^{-6}$ K^{-1}). The dilatometric softening point (T_d) of the glass-ceramic was 1081°C, represented by the peak of the curve recorded during the analysis (Figure 4.3-5b, red curve). It is worth noting that the dilatometric softening point of T1 glass-ceramic, T_d, is considerably increased respect to the T1 glass one (Table 4.3-1). In fact, the process parameters chosen to obtain the T1 coating are advantageous because they allow the increase of the softening temperature of the glass-ceramic, thus extending the working temperature range. Therefore, T1 glass-ceramic coating could be a potential candidate to protect TiO_x modules in oxidative atmosphere up to 600°C.

Since T1 glass-ceramic was found to be thermo-mechanically compatible with the TiO_x substrate, T1 glass was deposited on the titanium suboxide and heat treated at 1300°C for 10 minutes and subsequently at 855°C for 30 minutes to obtain a glass-ceramic protective coating on TiO_x.

In order to study the morphology of the glass-ceramic obtained with the 2nd route, SEM and EDS characterization were carried out on polished cross-sections of the T1 glass-ceramic pellet. Figure 4.3-9 showed two well visible types of crystalline phases. One of them consisted of irregular round-like shaped crystals very similar to those reported for T1 as-cast glass thermally treated at 1300°C for 10 minutes and 855°C for 30 minutes (Figure 4.3-7), while another is represented by needle-like shaped structures not homogeneously distributed. Both of them were immersed in the residual glassy phase. The EDS area reported the elements atomic%, which perfectly corresponded to the calculated atomic% in the glass composition.

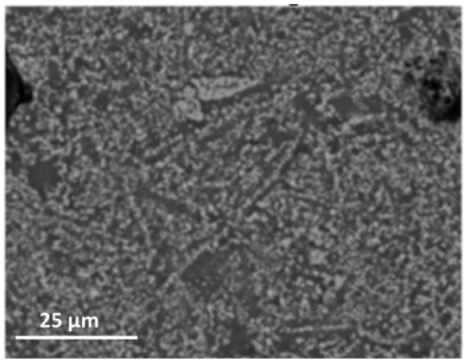

Element	Area (Atomic %)
O	61.3
Na	3.6
Al	9.8
Si	12.3
K	1.1
Ca	2.5
Ti	6.1
Y	3.3
Total	100.00

Figure 4.3-9: SEM image of the cross-section of T1 glass-ceramic (obtained at 1300°C for 10 min+ 855°C for 30 min) and EDS analysis on the all the area

Figure 4.3-10 shows a SEM image of the T1 glass-ceramic and the related EDS elemental maps. As it can be observed, where Ca, Al and Si were detected and formed darker elongated structures in the range 20- 25 μm intersected with each other, K and Na were not present. This confirmed the presence of the $CaAl_2Si_2O_8$ anorthite phase found with the XRD analysis and observed in previous studies [206,207]. Smaller and brighter crystals, homogeneously distributed in all the sample could be ascribed to the main phase identified with XRD, that is the yttrium titanium dioxide ($Y_2Ti_2O_7$). On the other side, K, Na are present in the matrix glassy phase.

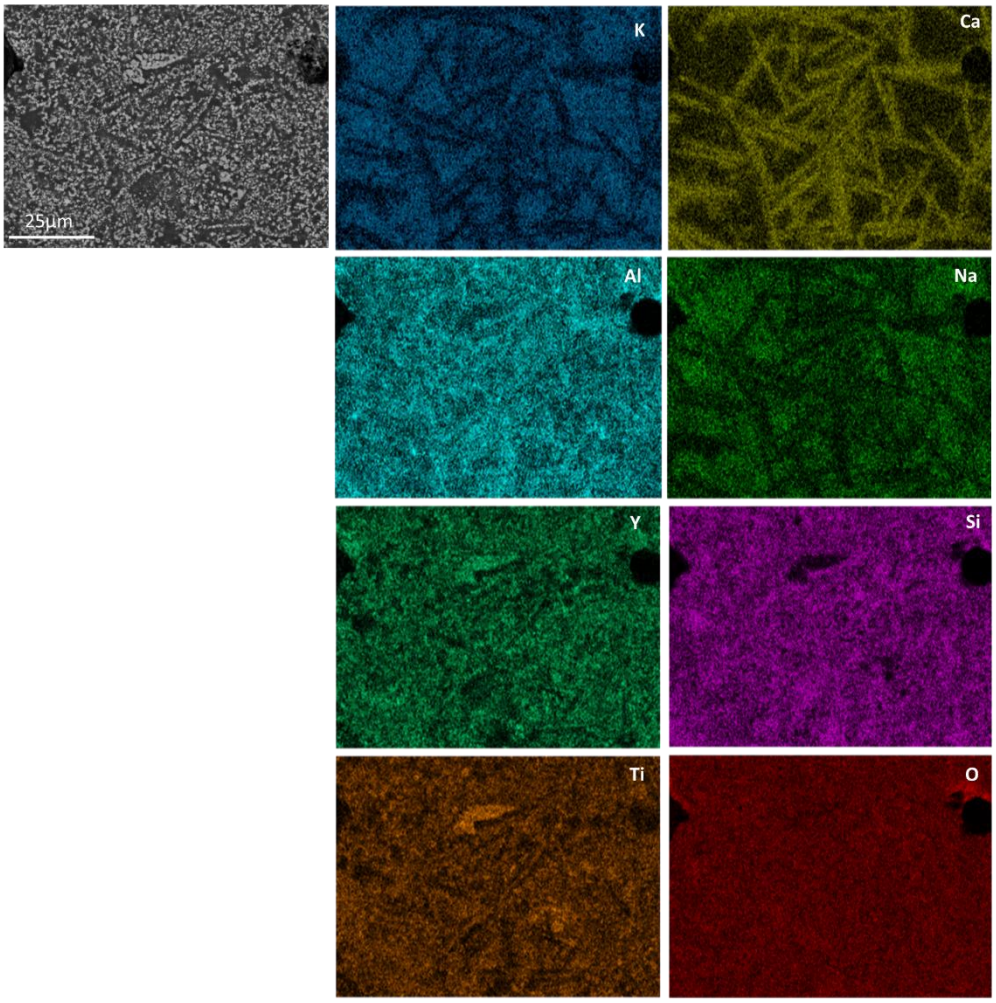

Figure 4.3-10: SEM image of the cross- section of T1 glass-ceramic (obtained at 1300°C for 10 min+ 855°C for 30 min) with the related EDS elemental maps

A SEM image of the cross-section of T1 glass-ceramic at higher magnification and EDS characterization are reported in Figure 4.3-11. The two types of crystalline phases above mentioned are better visible. Furthermore, the EDS area reported the elements atomic% and it corresponded again to the calculated atomic% in the glass composition.

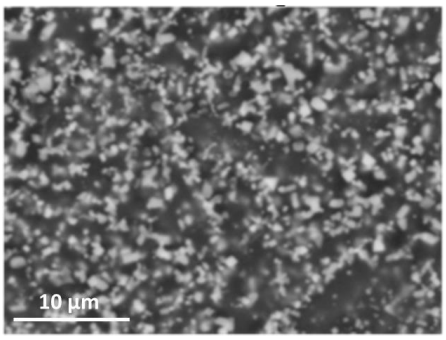

Element	Area (Atomic %)
O	61.4
Na	3.2
Al	10.0
Si	12.6
K	0.9
Ca	2.9
Ti	5.9
Y	3.1
Total	100.00

Figure 4.3-11: SEM image at higher magnification of the cross- section of T1 glass-ceramic (obtained at 1300°C for 10 min+ 855°C for 30 min) and EDS analysis on the all the area

Figure 4.3-12 showed a SEM image at higher magnification of the T1 glass-ceramic and the related EDS elemental maps. The compositional analysis confirmed the presence of needle-like shaped structures consisted of Ca, Al, Si and O, and smaller crystals containing Y and Ti more homogeneously distributed in the residual glassy phase.

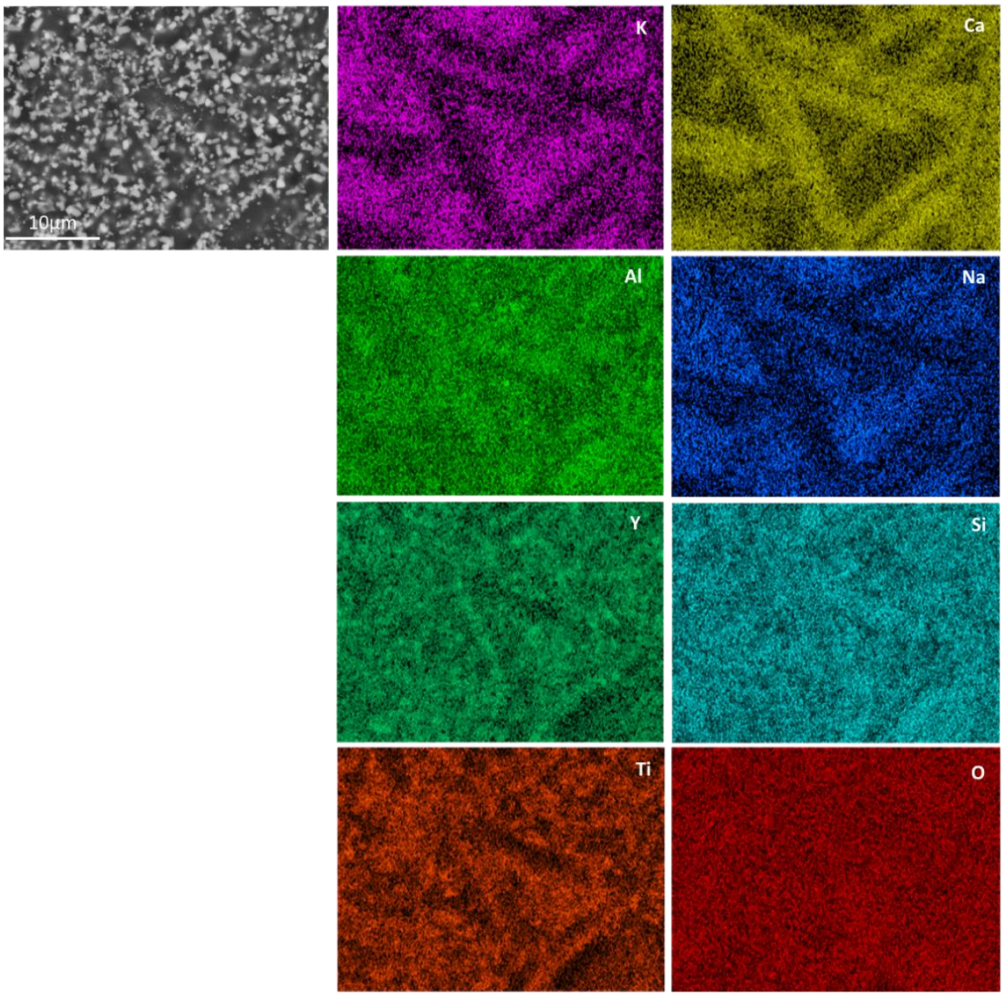

Figure 4.3-12: SEM image at higher magnification of the cross-section of T1 glass-ceramic (obtained at 1300°C for 10 min+ 855°C for 30 min) with the related EDS elemental maps

4.3.5 T1 glass-ceramic coated TiO_x: morphological and chemical characterization after deposition treatment

In this section the performances of the T1 glass-ceramic in terms of adhesion and compatibility at the interface with the titanium suboxide are illustrated and discussed. SEM and EDS analyses were carried out after the coating process, performed at 1300°C for 10 minutes and subsequently at 855°C for 30 minutes, under flowing Ar, in order to investigate the morphology and the differences in chemical composition between the glass phase and the crystalline phases. Fig. 4.3-13 shows the results of these analyses.

Figure 4.3-13a, b shows the SEM images of the cross-section of a T1 glass-ceramic coated TiO_x, and it can be seen that the coating is well-adherent to the substrate, no pores, cracks or delamination phenomena are visible at the coating/TE interface after the deposition treatment. The distribution of the crystalline phases is not homogeneous. As it can be observed, closer to the interface, small lighter grains with size around 1μm and homogeneously distributed are immersed in the darker glassy phase, while further from the T1 glass-ceramic/TiO_x interface, the presence of darker crystalline phases have the tendency to organize themselves in elongated crystals wedged together. The chemical analyses reported in the EDS in Figure 4.3-13c, d, e are in agreement with the XRD patterns presented in section 4.3.4. The main crystalline phase identified as $Y_2Ti_2O_7$ seems to be formed at the interface (spectrum 5) due to the reaction with the TiO_x substrate and to form everywhere in the coating where this crystalline phase is brighter and homogeneously distributed as round shaped crystals (spectrum 1), as it can be noted from the atomic% of Ti and Y. On the other hand, Ca, Al and Si are present in the needle-like shaped crystals in the further area from the interface (spectrums 3 and 4), confirming the $CaAl_2Si_2O_8$ anorthite phase found by XRD analysis. Furthermore, K, Na remained in the glassy phase (spectrum 2).

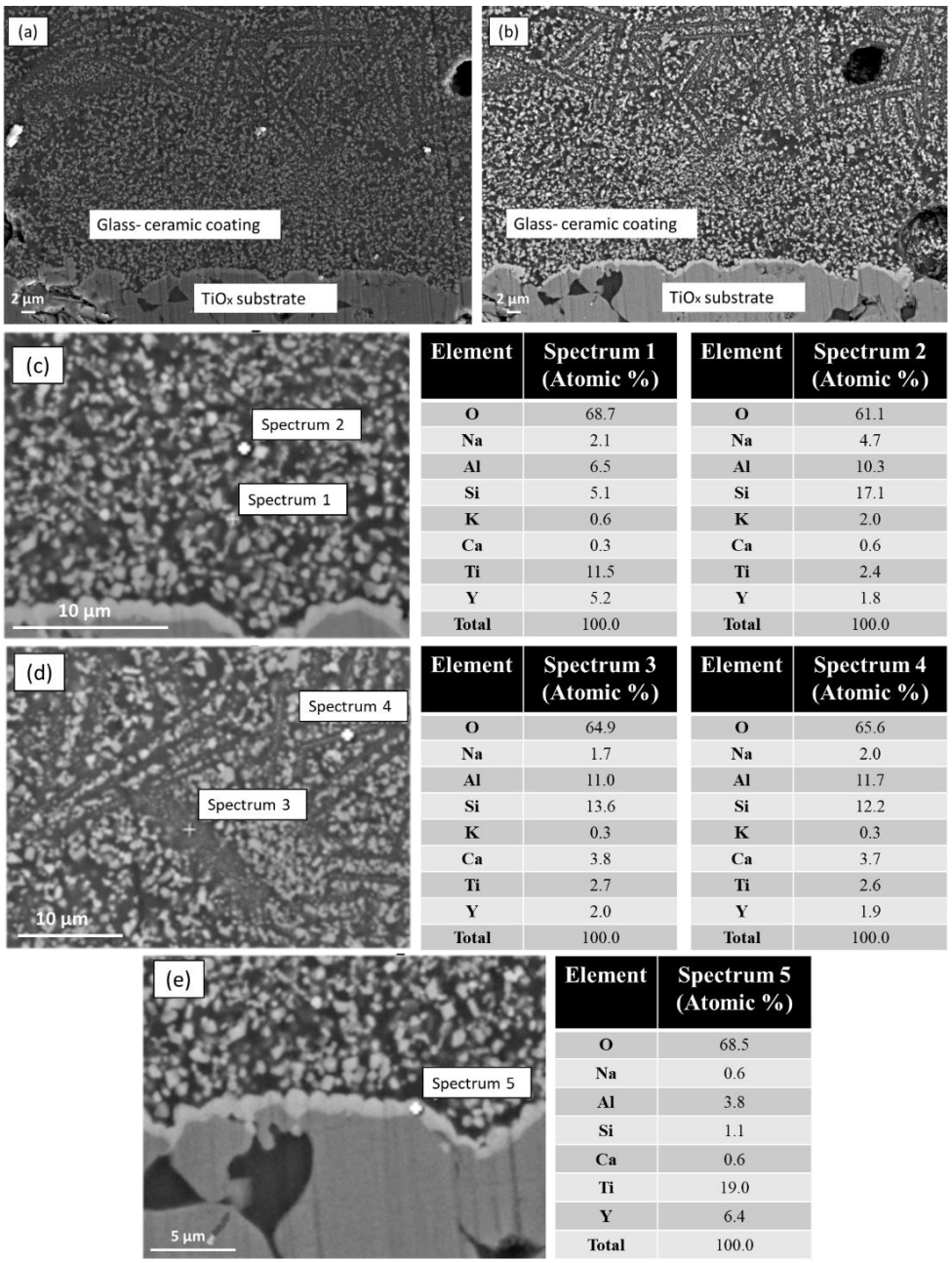

Element	Spectrum 1 (Atomic %)
O	68.7
Na	2.1
Al	6.5
Si	5.1
K	0.6
Ca	0.3
Ti	11.5
Y	5.2
Total	100.0

Element	Spectrum 2 (Atomic %)
O	61.1
Na	4.7
Al	10.3
Si	17.1
K	2.0
Ca	0.6
Ti	2.4
Y	1.8
Total	100.0

Element	Spectrum 3 (Atomic %)
O	64.9
Na	1.7
Al	11.0
Si	13.6
K	0.3
Ca	3.8
Ti	2.7
Y	2.0
Total	100.0

Element	Spectrum 4 (Atomic %)
O	65.6
Na	2.0
Al	11.7
Si	12.2
K	0.3
Ca	3.7
Ti	2.6
Y	1.9
Total	100.0

Element	Spectrum 5 (Atomic %)
O	68.5
Na	0.6
Al	3.8
Si	1.1
Ca	0.6
Ti	19.0
Y	6.4
Total	100.0

Figure 4.3-13: (a, b) SEM images of the cross-section of T1 glass-ceramic (obtained at 1300°C for 10 min+ 855°C for 30 min), respectively in secondary and back scattered electrons and (c, d, e) EDS analysis

A SEM image at the T1 glass-ceramic/TiO_x interface is reported in Figure 4.3-14, together with the related EDS elemental maps. Due to the high level of porosity of the titanium suboxide, the infiltration of the residual glass phase into the substrate was detected: high amount of Si, Na, Al and K were detected in the pores of the substrate. The higher concentration of Y and Ti is evident in the layer at the interface; it is continuous and homogeneous along the investigated region. As mentioned above, the formation of the $Y_2Ti_2O_7$ phase likely occurred at the T1 glass-ceramic/TiO_x interface and it continues to be the main phase in the area closest to the interface, after which the calcium aluminum silicates started to nucleate.

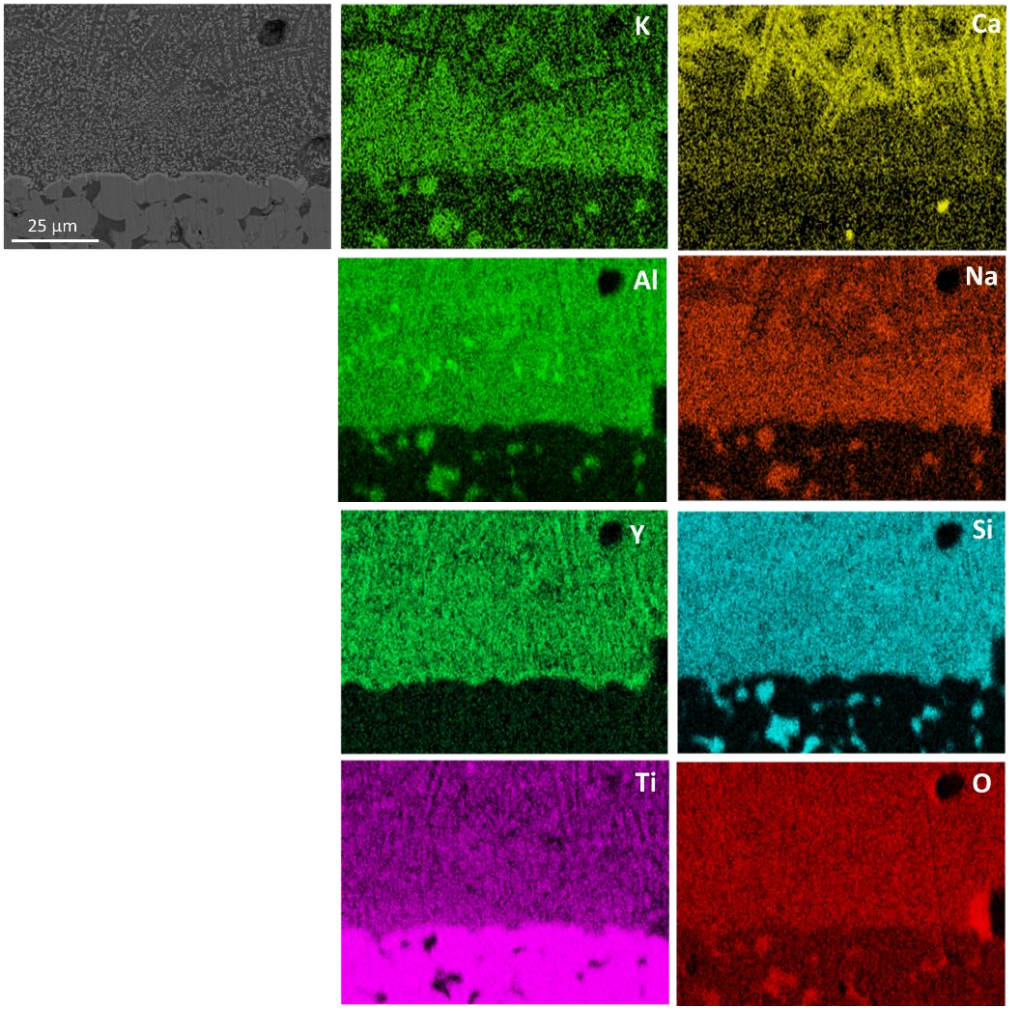

Figure 4.3-14: SEM image at the T1 glass-ceramic/TiO_x interface substrate with the related EDS elemental maps

In order to better understand the composition of the scale formed at the interface, an EDS line-scan was also performed. The results are reported in Figure 4.3-15 and in Figure 4.3-16 respectively. The line-scans related to Si, Na, Al and O show clearly that the presence of these elements slightly increases moving from the substrate (on the left) to the glass-ceramic coating (on the right). Evaluating the trend of the intensities of each chemical element, it can be noted that the line- data concerning Y increases considerably at the interface (zone 1 in Figure 4.3-16), while the Ti slowly decreases, but this is reasonable considering that the substrate is titanium suboxide. After the reaction layer, which is 1-1.5 μm thick, the line scan crosses a dark zone of glassy phase of around 1 μm length (zone 2 in Figure 4.3-16) where an important reduction of Y and Ti intensity peaks can be noted, while the Si, Na e Al intensity increases. Afterwards, Ti and Y intensities increase in correspondence of a smaller round-like shaped crystal (zone 3 in Figure 4.3-16).

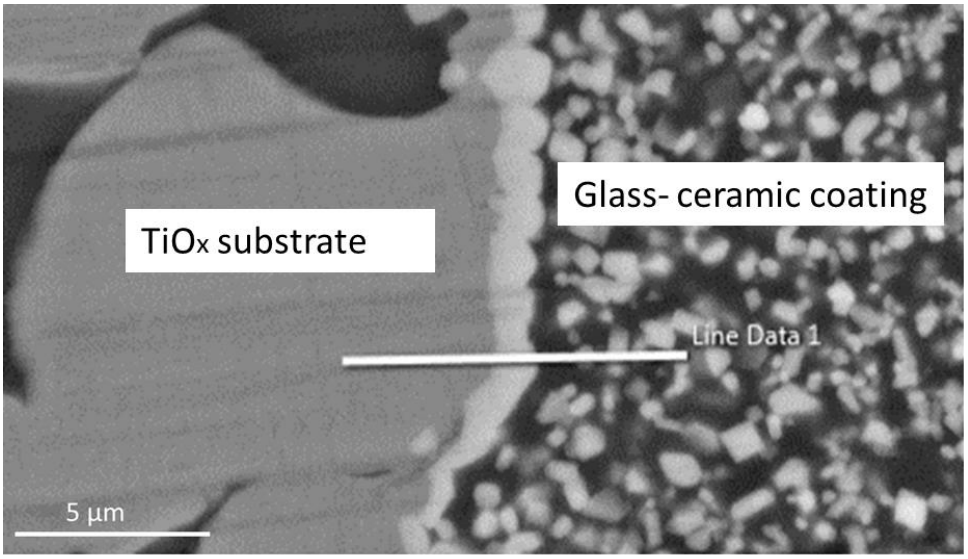

Figure 4.3-15: SEM image collected at the TiO_x/T1 glass-ceramic interface after the coating deposition at 1300°C for 10 min+ 855°C for 30 min, under flowing Ar

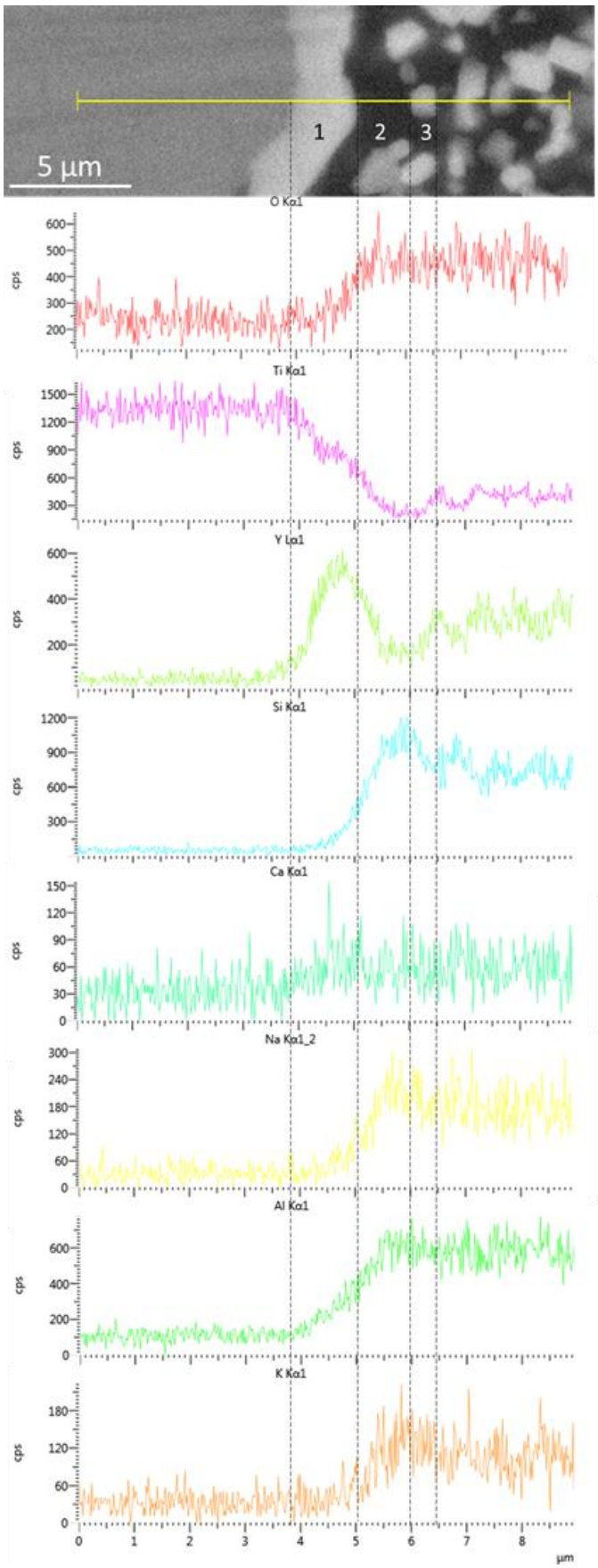

Figure 4.3-16: EDS line-scan results, collected at the TiO_x/T1 glass-ceramic interface after the coating deposition at 1300°C for 10 min+ 855°C for 30 min, under flowing Ar

The purpose of the current study was to characterize and process a silica-based glass-ceramic, specifically designed to protect the TiO_x substrate against oxidation up to 600°C (to be used both as thermoelectric and electrode at high temperatures). Even if results concerning oxidation and thermal cycling tests are in progress, it exhibited excellent thermo-mechanical and chemical compatibility with the TiO_x substrate. After the coating treatment, the obtained glass-ceramic (by sinter-crystallized glass powders) was characterised by the presence of an interesting microstructure due to different crystalline phases, whose complete identification is still in progress. In fact, Rietveld and TEM analysis will be carried out on the glass-ceramic coating in order to better identify the nature and the quantity of the crystalline phases. Even if the study was limited by the lack of information on oxidation test to compare the effects of oxidative atmosphere on a coated/ uncoated sample, these preliminary results are very promising. In fact, these findings constitute an optimal starting point for using T1 glass-ceramic as a promise candidate to protect titanium suboxide during ageing and cyclic working operations.

4.4 Hybrid commercial resins coated Zn doped tetrahedrite

4.4.1 Zn doped THD and resins characterization

The ball milled Zn doped tetrahedrite powders, produced starting from single elements, are shown in the SEM images in Figure 4.4-1a, b; the presence of aggregates of bigger dimensions and other fine powders of smaller size are visible. Furthermore, EDS analysis was carried out (Figure 4.4-1c) showing the presence of the elements Cu, Sb, S, included the Zn doping. In literature, it has been demonstrated that the achievement of the final stoichiometry is progressively obtained during the mechanical alloying by continuous ball milling [208], [209].

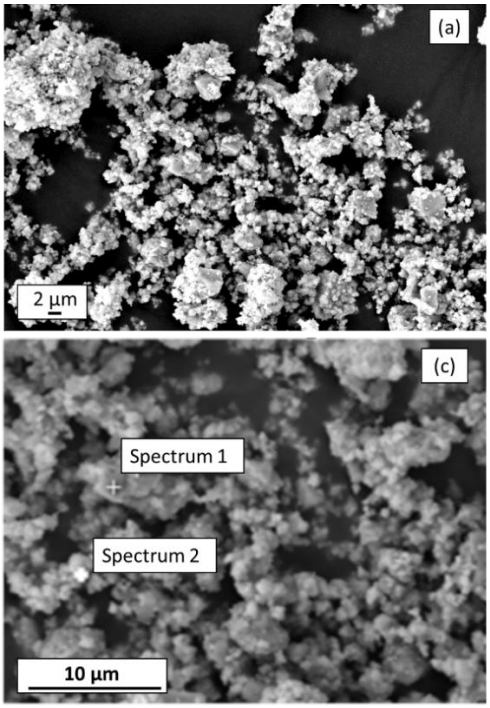

Element	Spectrum 1 (Atomic %)	Spectrum 2 (Atomic %)
S	45.6	34.9
Cu	37.7	48.6
Zn	2.2	6.5
Sb	14.5	10.0
Total:	100.00	100.00

Figure 4.4-1: SEM images of (a, b) Zn doped THD ball milled powders (c) EDS analysis

The XRD pattern reported in Figure 4.4-2a confirmed that the ball milled powders consisted of $Cu_{12}Sb_4S_{13}$ single phase (PDF card n. 00-024-1318).

Figure 4.4-3a illustrated a SEM image of the polished surface of an as-sintered Zn doped THD obtained by SPS with sintering conditions 400 °C/50 MPa/5 min, that looked really dense without contrast of the phases. In fact, as revealed by XRD analysis in Figure 4.4-2b, the famatinite (Cu_3SbS_4) second phase (PDF card n. 01-071-0555) was present in the as-sintered sample only in a very small quantity, while the $Cu_{12}Sb_4S_{13}$ continued to be the main phase. Figure 4.4-3b, c, d shows the fracture surface of Zn doped tetrahedrite, where it is interesting to notice the

presence of tiny grains with narrow size distribution (around few hundreds of nanometers).

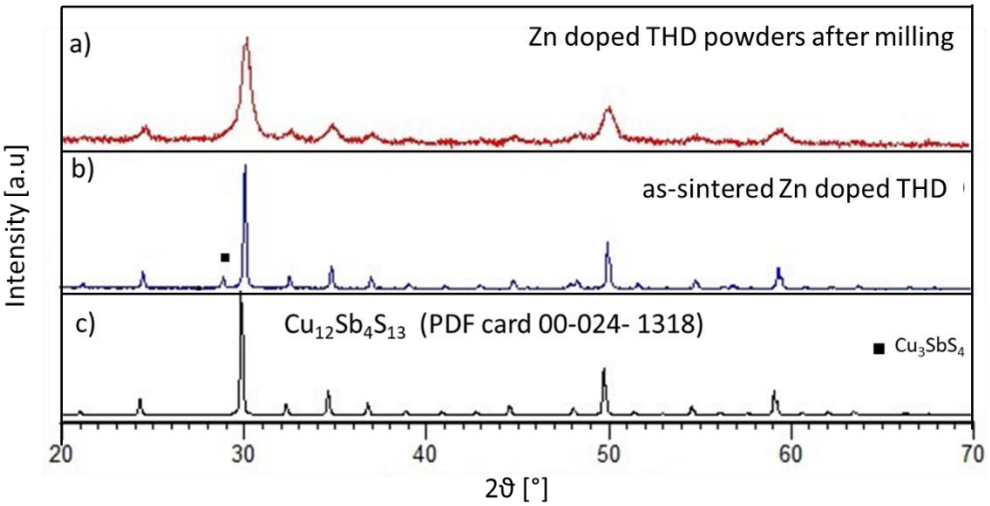

Figure 4.4-2: XRD pattern of (a) Zn doped THD powders after ball milling, (b) as-sintered Zn doped THD, (c) PDF card (number: 00-024-1318) of $Cu_{12}Sb_4S_{13}$

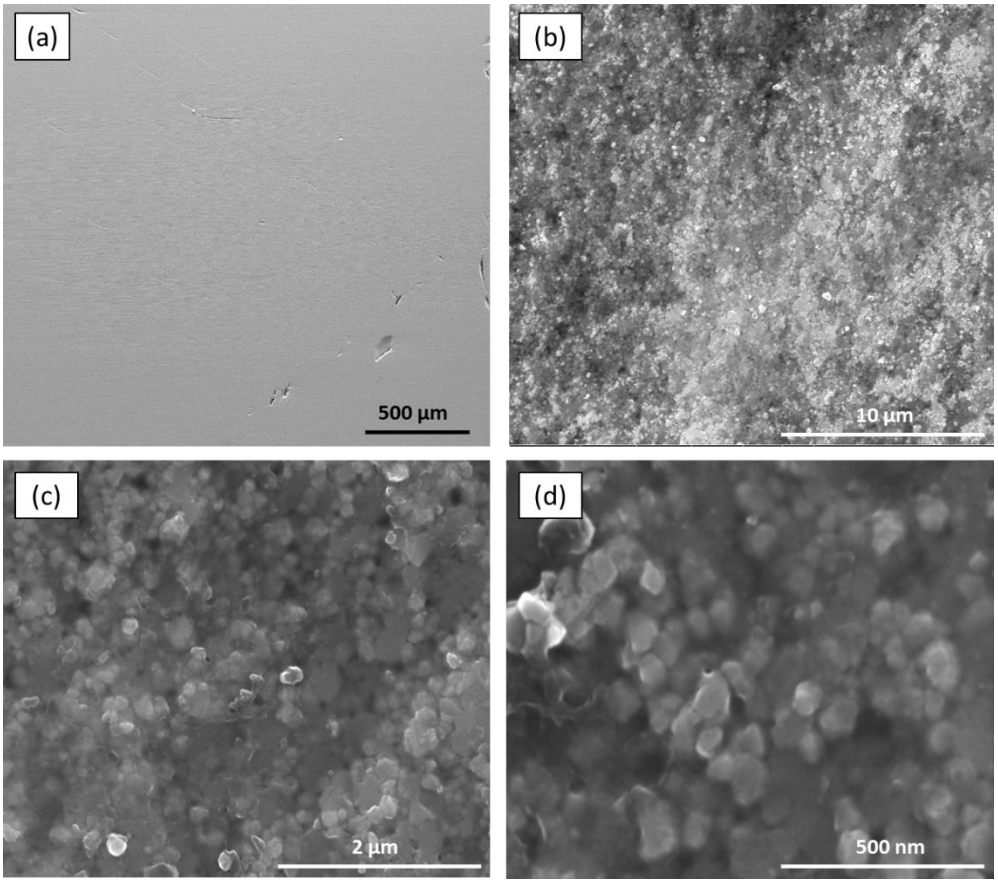

Figure 4.4-3: SEM images of (a) polished surface and (b, c, d) fracture surfaces of Zn doped THD samples sintered by SPS

The density of some sintered Zn doped THD pellets was measured with the Archimede's method (Table 4.4-1) resulting to have an average of 4.86 g/cm^3, which results in a high relative density of 97% if compared with the theoretical value (4.99 g/cm^3) [192].

Table 4.4-1: Density of sintered Zn doped THD samples

Samples	Density (g/cm^3)
1	4.888
2	4.896
3	4.800
4	4.919
5	4.806
Average	**4.861**

As previously reported [136,137,140,208,210], the oxidation of the surface of this thermoelectric substrate degrades the power generation and decreases the reliability and efficiency of TE modules mainly due to the production of Sb_2O_3, Cu_3SbS_4 and Cu_2S . In order to inhibit the degradation of the thermoelectric properties, the effectiveness of the CP4040 water-based and the CP4040-S1 solvent-based resins were tested. Figure 4.4-4 shows the two resins deposited on soda-lime glasses after curing at 250°C for 45minutes (Figure 4.4-4a) and after an ageing treatment with a dwell of 4hrs at 590°C (Figure 4.4-4b), which is the nominal temperature resistance indicated in the data sheet supplied by AREMCO. Despite after ageing the presence of some cracks on both hybrid coatings is evident, the coatings continue to be well adherent to the substrate, as after the curing.

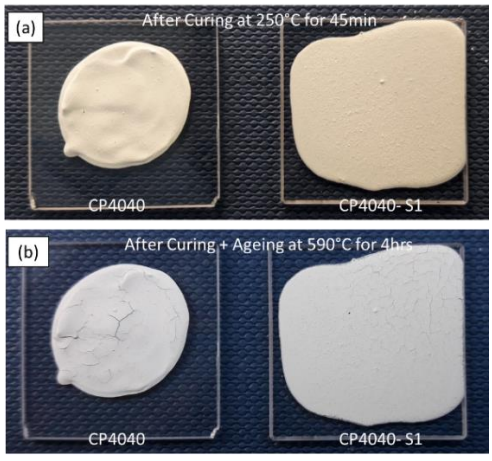

Figure 4.4-4: Images of water- and solvent-based resins (a) after curing at 250°C for 45min and (b) after curing and subsequently ageing at 590°C for 4 hrs

The XRD pattern of the water-based resin (CP4040) after curing in Figure 4.4-5 shows the presence of TiO_2 as main phase (PDF card n. 01-088-1172) and some secondary phases such as SiO_2 (PDF card n. 01-081-0068 and PDF card n. 01-078-1255), ZnO (PDF card n. 01-079-0205) and $Fe_3Si_{0.66}$ (PDF card n. 01-089-5975) all visible in smaller quantities. XRD analysis of the solvent-based resin (CP4040- S1) after curing in Figure 4.4-6 contains very similar crystalline phases if compared with CP4040, but with a new one that is aluminium silicate hydrate (PDF card n. 00-038-0449). In general, XRD pattern of the CP4040 coating carried out after curing at 250°C for 45 min and after the subsequently ageing at 580°C for 4hrs does not report any significant differences, while in the case of CP4040- S1 hybrid resin a couple of new peaks (indicated with the black arrow in Figure 4.4-6) not labelled were present after the ageing at 580°C for 4hrs.

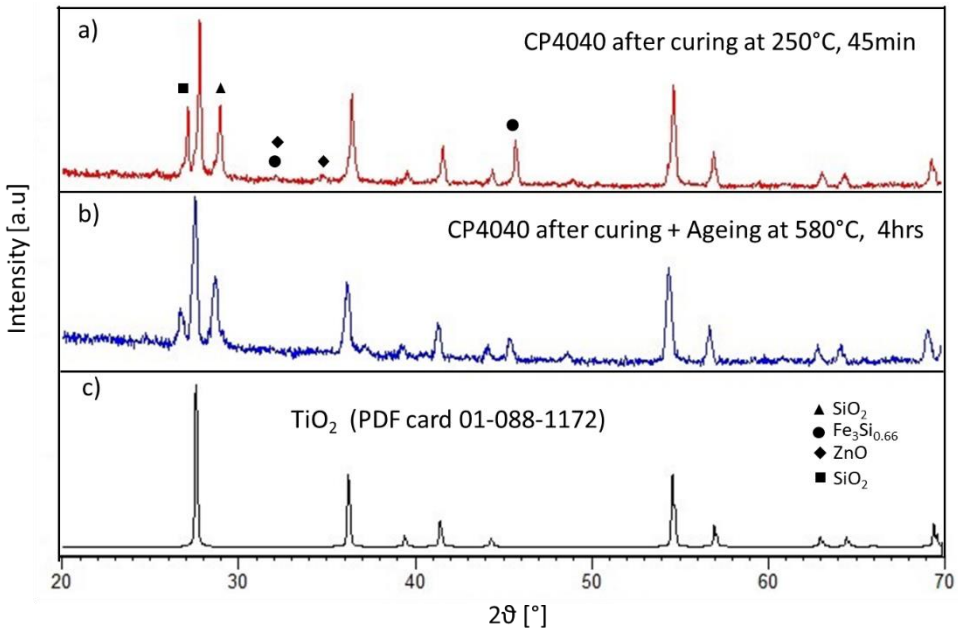

Figure 4.4-5: XRD pattern of (a) CP4040 after curing at 250°C for 45 min, (b) CP4040 after curing and ageing at 580°C for 4 h (c) PDF card (number: 01-088-1172) of Ti_2O

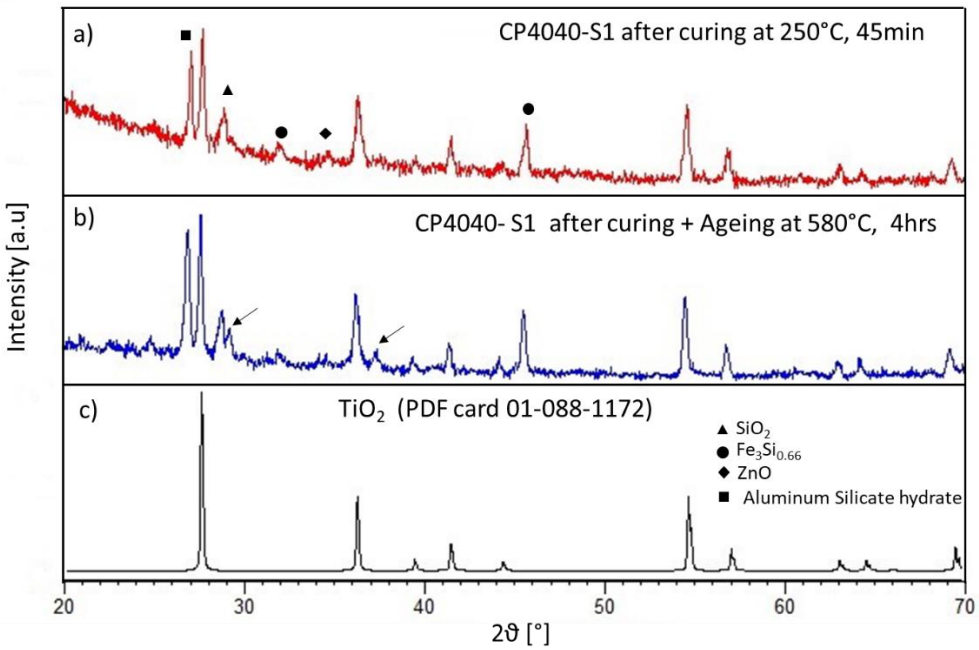

Figure 4.4-6: XRD pattern of (a) CP4040- S1 after curing at 250°C for 45 min, (b) CP4040-S1 after curing and ageing at 580°C for 4 h (c) PDF card (number: 01-088-1172) of Ti_2O

Figure 4.4-7 illustrates a photo of the water-based resin coated Zn doped THD (on the left) and the solvent-based resin coated Zn doped THD (on the right).

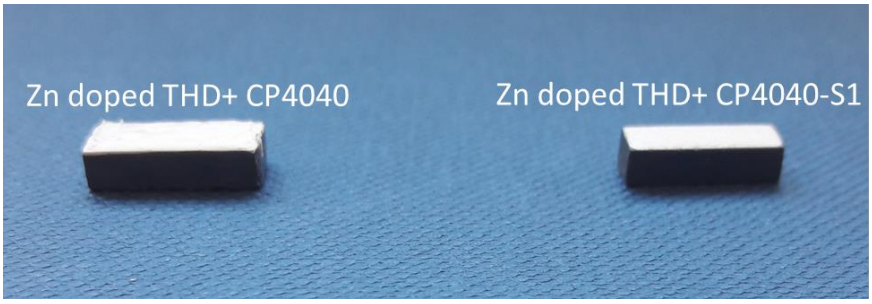

Figure 4.4-7: Photo of the water-based resin coated Zn doped THD (on the left) and the solvent-based resin coated Zn doped THD (on the right) after curing at 250°C for 45 min

The cross-sections of both samples after curing at 250°C for 45 min (Figure 4.4-8a, b) shows crystals of different shape well dispersed in the silicone resin matrixes, and no pores, cracks or other defects are visible at the coating/Zn doped THD interface. The EDS analysis (Figure 4.4-8c, d) reveals the presence of different elements in both hybrid coatings, while in the Zn doped THD substrate Cu, S, Sb and sometimes Zn are detectable. The presence of Cr in some EDS analysis is due to the metallization of the surface need for the morphological characterization.

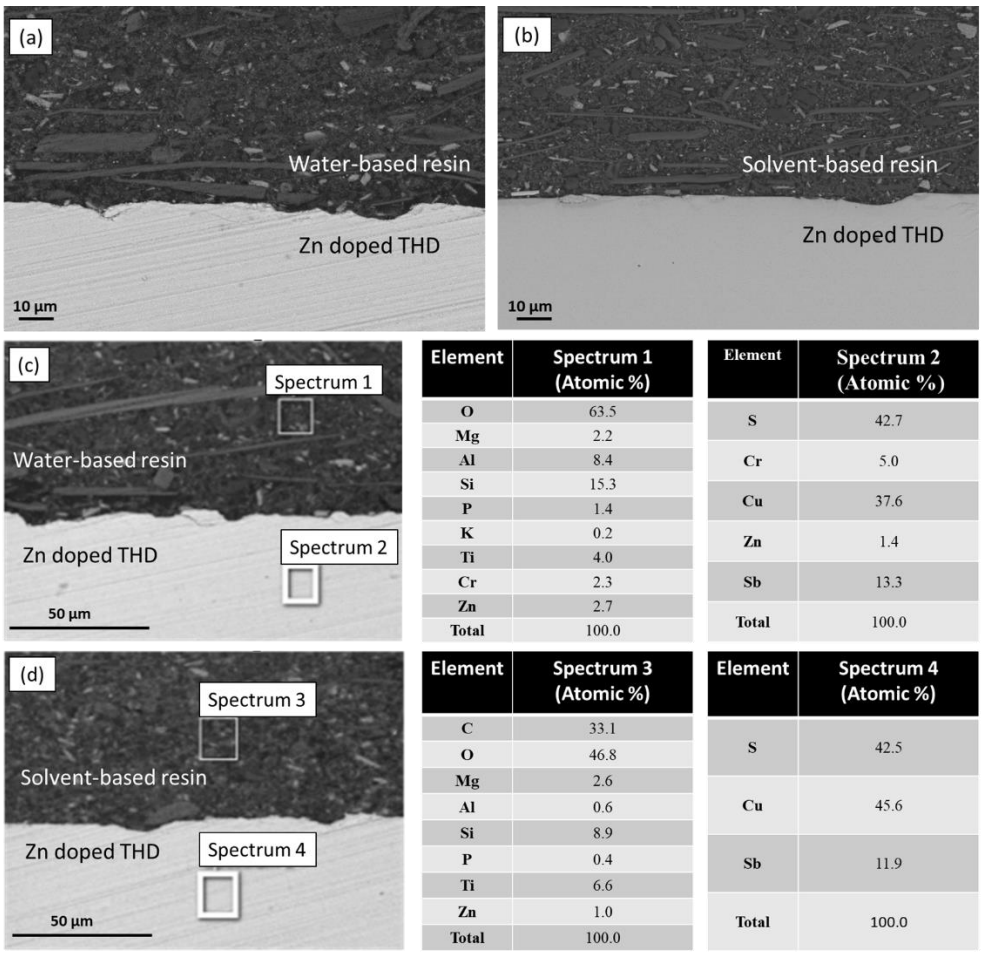

Element	Spectrum 1 (Atomic %)
O	63.5
Mg	2.2
Al	8.4
Si	15.3
P	1.4
K	0.2
Ti	4.0
Cr	2.3
Zn	2.7
Total	100.0

Element	Spectrum 2 (Atomic %)
S	42.7
Cr	5.0
Cu	37.6
Zn	1.4
Sb	13.3
Total	100.0

Element	Spectrum 3 (Atomic %)
C	33.1
O	46.8
Mg	2.6
Al	0.6
Si	8.9
P	0.4
Ti	6.6
Zn	1.0
Total	100.0

Element	Spectrum 4 (Atomic %)
S	42.5
Cu	45.6
Sb	11.9
Total	100.0

Figure 4.4-8: SEM images and EDS analysis of the cross-section of (a, c) water-based resin coated Zn doped THD and (b, d) solvent-based resin coated Zn doped THD after curing at 250°C for 45 min

After these preliminary tests, the water-based resin has been chosen as oxidation protective coating for Zn doped tetrahedrite because of its simplicity to deposit (the solvent-based resin had a viscosity too low if compared with CP4040, and too many depositions were need to cover completely the samples).

Two different aging tests were performed on the coated samples:

- at a temperature of 350°C for 48 hrs with a heating rate of 1.2° C/min.
- at a temperature of 400°C for 120 hrs with a heating rate of 1.2° C/min.

The choice of oxidation temperatures was guided by previous literature [140,210] and the potential operating temperatures of the materials. The tests would provide an initial benchmark for the testing of hybrid coatings.

4.4.2 Thermal ageing at 350°C for 48hrs

As it can be observed in the SEM images and EDS analysis in Figure 4.4-9a, b after the ageing at 350°C for 48hrs in air the Zn doped tetrahedrite without coating appeared completely oxidized. SEM images of the cross-section of uncoated Zn doped THD in Figure 4.4-9c, d shows the presence of an inhomogeneous layer (around 3- 5 µm) on the whole surface of the thermoelectric substrate. The point indicated with the black arrow can be attributed to the antimony oxide, but it was not possible to carry out EDS analysis because of the spallation of the brittle scale.

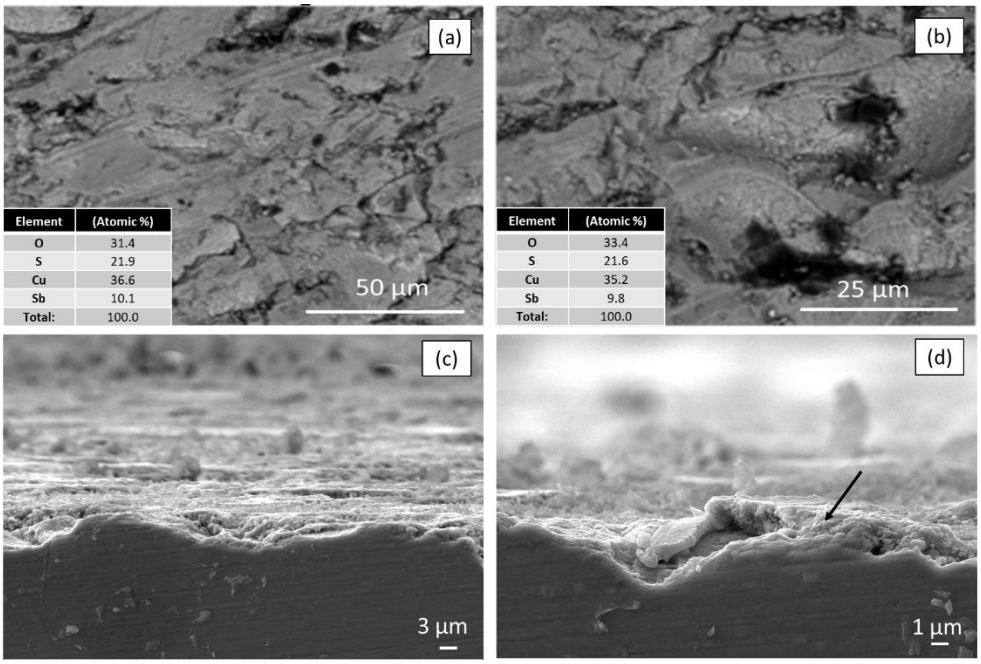

Figure 4.4-9: SEM images and EDS analysis of top view (a, b) and SEM images of the cross-section (c, d) of aged Zn doped THD 350°C 48hrs without coating

The XRD analysis of the uncoated sample surface after ageing (Figure 4.4-10a) shows that the main phase was Sb_2O_3 (PDF card n. 00-043- 1071), confirming the morphological analysis (SEM), with the presence of $Cu_{12}Sb_4S_{13,}$ Cu_3SbS_4 and Cu_2S (PDF card n. 01-072-1071) as secondary phases, as previously discussed by Chetty et al. and Harish et al.[208,210].

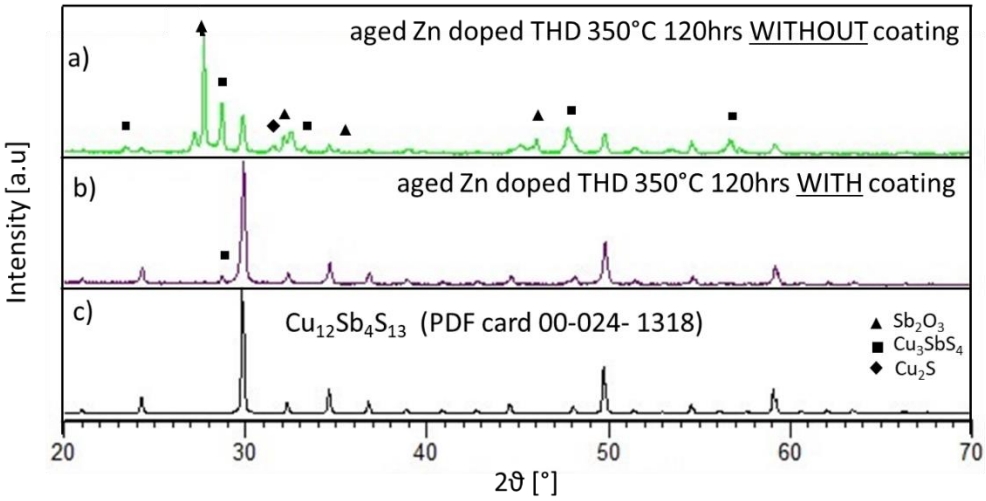

Figure 4.4-10: XRD pattern of (a) aged Zn doped THD at 350°C for 48h without coating, (b) aged Zn doped THD at 350°C for 48h with coating and (c) PDF card (number: 00-024-1318) of $Cu_{12}Sb_4S_{13}$

As shown in the cross-section image of the water-based coated Zn doped THD after ageing at 350°C for 48 hrs (Figure 4.4-11a, b) the coating is still well-adherent to the substrate and there is no evidence of cracks within the coating and the Zn doped tetrahedrite. As can be observed in the SEM image, the absence of the formation of oxidation layers at the coating/ Zn doped THD interface makes evident the effective protection of the hybrid coating, which as demonstrated by the EDS analysis (Figure 4.4-11c, d) seems not be subjected to compositional changing after the ageing at these conditions.

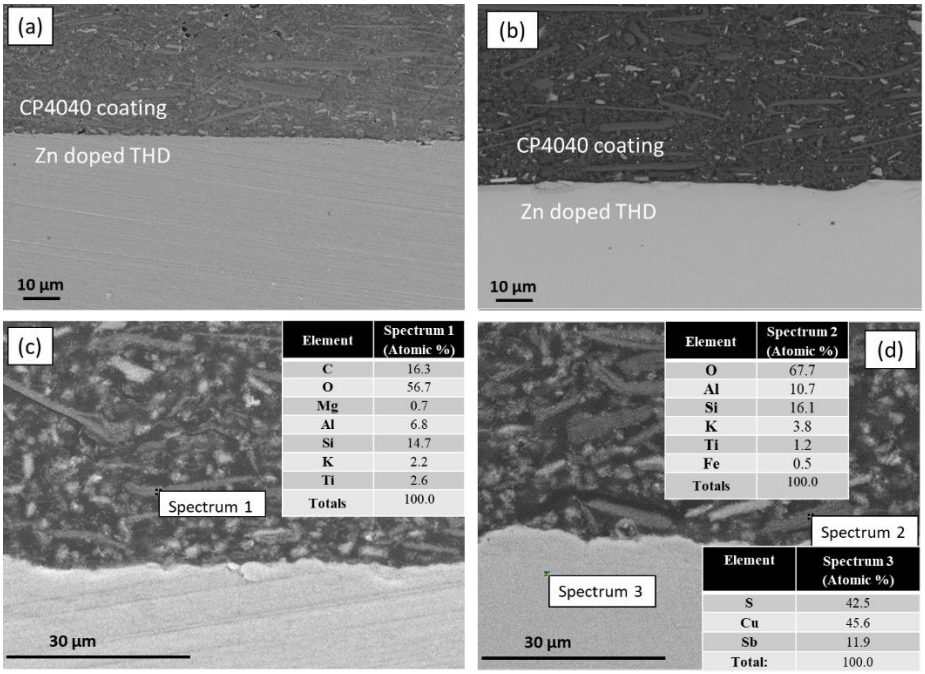

Element	Spectrum 1 (Atomic %)
C	16.3
O	56.7
Mg	0.7
Al	6.8
Si	14.7
K	2.2
Ti	2.6
Totals	100.0

Element	Spectrum 2 (Atomic %)
O	67.7
Al	10.7
Si	16.1
K	3.8
Ti	1.2
Fe	0.5
Totals	100.0

Element	Spectrum 3 (Atomic %)
S	42.5
Cu	45.6
Sb	11.9
Total:	100.0

Figure 4.4-11: SEM images (a, b) and EDS analysis (c, d) of the cross-section of water-based resin coated Zn doped THD after ageing at 350°C, dwelling time 48 hrs, in air

XRD analysis in Figure 4.4-10b shows that after the ageing at 350°C for 48 hrs in air there were no apparent changes in the Zn doped THD if compared to as-sintered sample, confirming that the hybrid coating provided an effective protection, inhibiting the oxidation of Zn doped THD under thermal ageing.

Concerning the thermoelectric properties, the comparison between the as-sintered, the uncoated and coated samples is shown in Figure 4.4-12. The Seebeck coefficients of the three samples did not show remarkable differences, but the values of the aged Zn doped THD with coating were slightly higher than those without coating, at least starting from 150°C. The coating is able to avoid the increase in electrical resistivity observed in the uncoated sample, as it maintains the original chemical composition. Consequently, the power factor of the uncoated sample decreases, while the coated sample maintains a similar value.

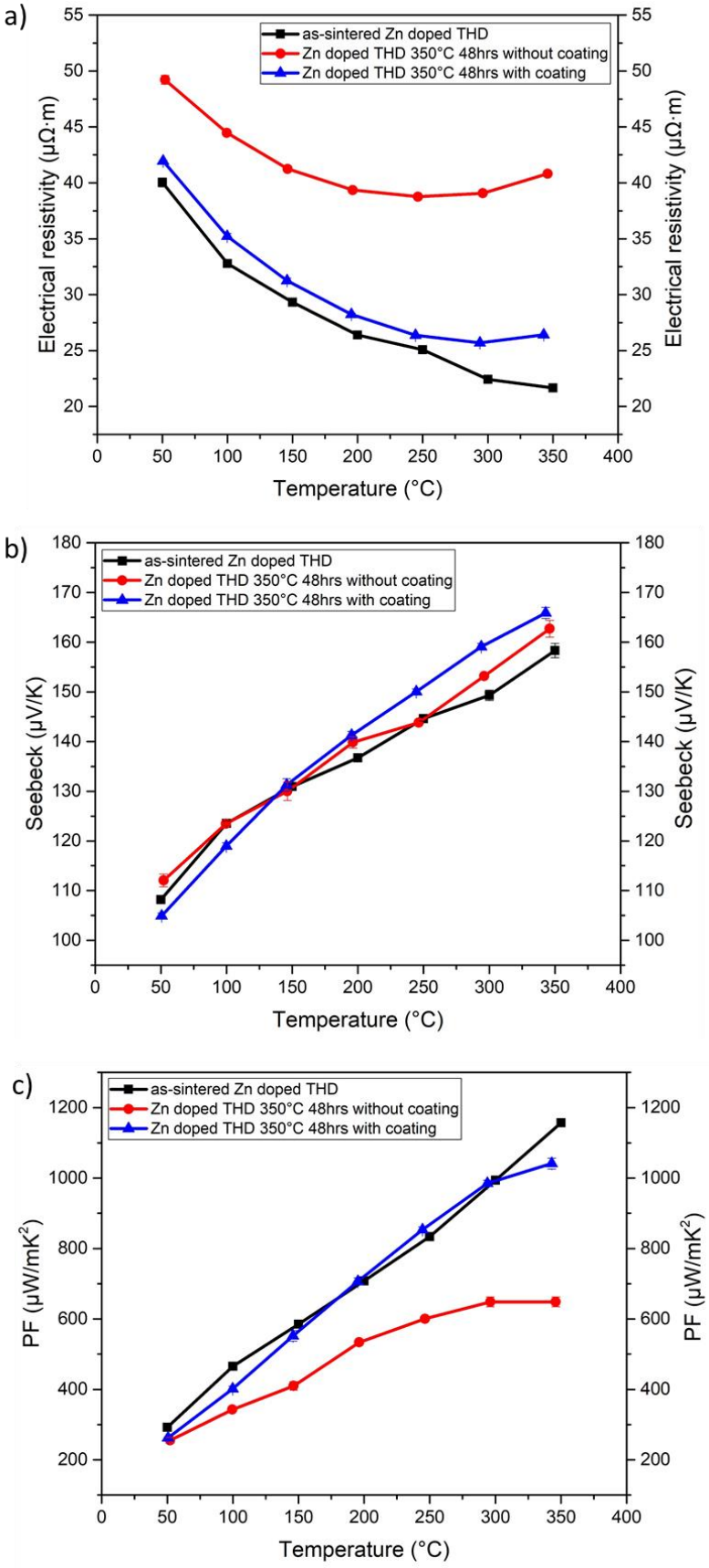

Figure 4.4-12: Temperature dependence of the (a) electrical resistivity, (b) Seebeck coefficient, (c) power factor of the as-sintered Zn doped THD (black curve), coated (blu curve) and uncoated Zn doped THD (red curve) after thermal ageing at 350°C, dwelling time 48hrs, in air

4.4.3 Thermal ageing at 400°C for 120hrs

After the ageing at 400°C for 120 hrs in air, SEM images of the cross-section of uncoated Zn doped THD in Figure 4.4-13 shows, as in the previously cited thermal ageing at 350°C for 48 hrs, the presence of an inhomogeneous layer (around 5 µm) on the whole surface of the thermoelectric substrate. As can be observed in the EDS analysis in Figure 4.4-13c, d, the Sb/O ratio within the interface could attribute the presence of antimony oxide at the Zn doped THD/embedding resin interface.

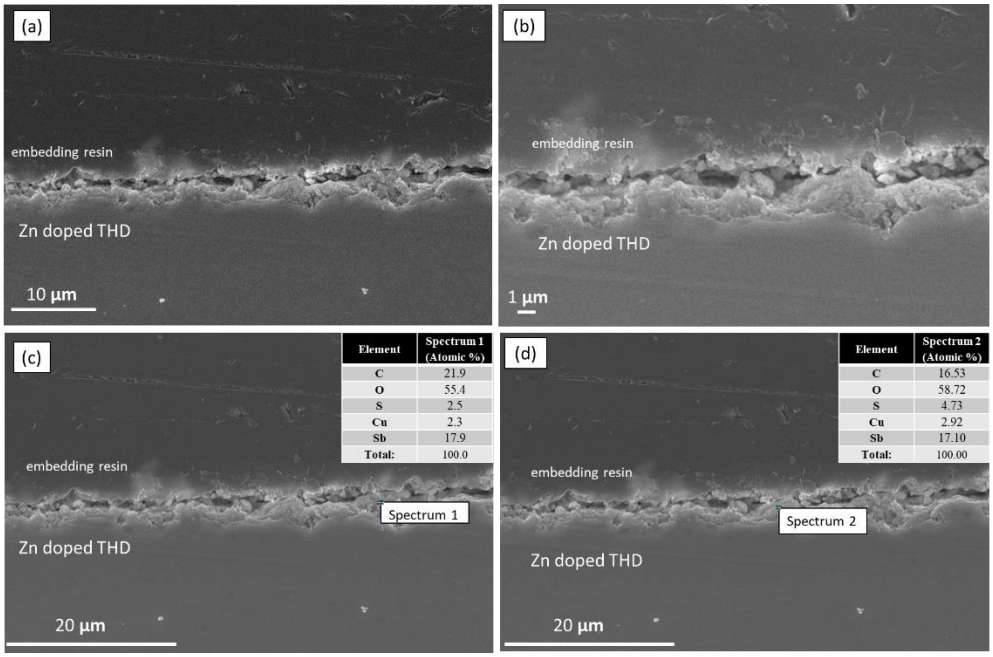

Figure 4.4-13: SEM images (a, b) and EDS analysis (c, d) of the cross-section of aged Zn doped Zn doped THD 400°C 120 hrs without coating

The XRD analysis of the uncoated sample surface after ageing (Figure 4.4-14a) shows that the main phases are represented by the orthorhombic antimony oxide which is present as Sb_2O_3 (PDF card n. 03-065-2426) and Sb_2O_4 (PDF card n. 01-071-0564) confirming the morphological analysis, with the presence of $Cu_{12}Sb_4S_{13}$, Cu_2S (PDF card n. 01-072-1071) and CuS (PDF card n. 01-079-2321) as secondary phases.

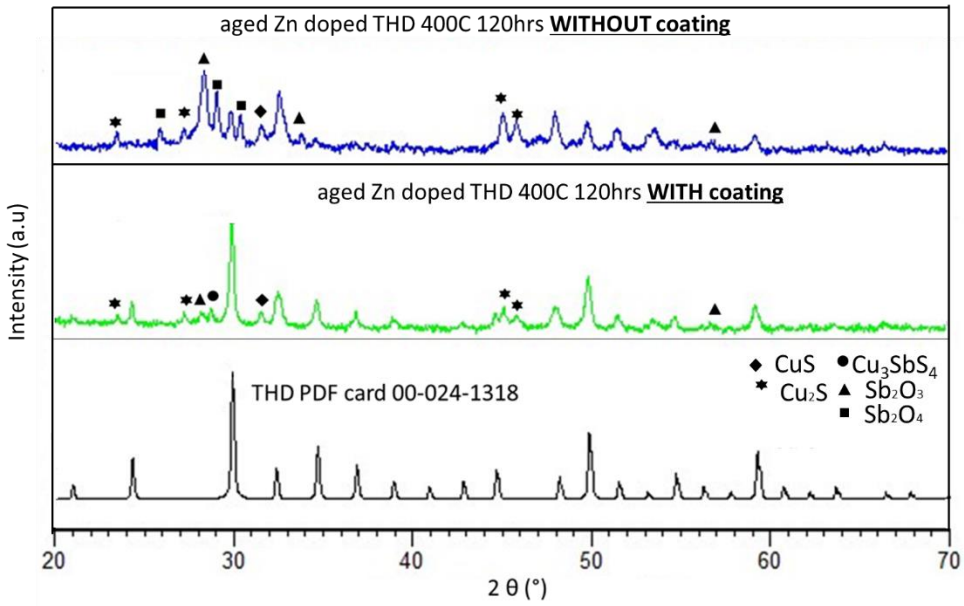

Figure 4.4-14: XRD pattern of (a) aged Zn doped THD at 400°C for 120 hrs without coating, (b) aged Zn doped THD at 400°C for 120 hrs with coating and (c) PDF card (number: 00-024-1318) of $Cu_{12}Sb_4S_{13}$

The SEM image of the cross-section of the water-based coated Zn doped THD after ageing at 400°C for 120 hrs (Figure 4.4-15 a) showed the absence of cracks within the coating, which is well-adhered to the thermoelectric substrate. Nevertheless, the evidence for the formation of a 20- 25 µm thick oxidation layer was found (Figure 4.4-15c, d) at the coating/Zn doped THD interface.

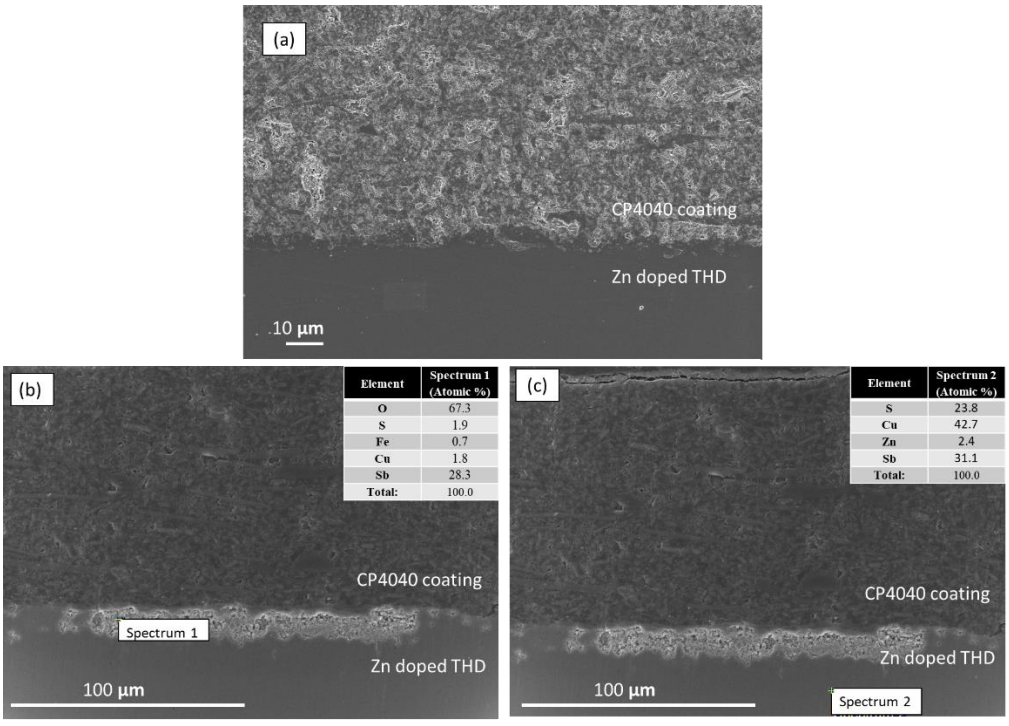

Figure 4.4-15: SEM images (a, b) and EDS analysis (c, d) of the cross-section of aged Zn doped THD 400°C 120 hrs with coating

XRD analysis of the aged Zn doped THD with coating (Figure 4.4-14 b) reported the effectiveness of the CP4040 hybrid coating because the main phase remained the $Cu_{12}Sb_4S_{13}$ with Cu_3SbS_4 as secondary phase (like the as-sintered sample in Figure 4.4- 2 b), but confirmed also the presence of oxidation layers of antimony oxide (Sb_2O_3) with the other phase Cu_2S.

Concerning the thermoelectric properties, the comparison between the as-sintered, the uncoated and coated samples was carried out and shown in Figure 4.4-16. The Seebeck coefficients of the aged Zn doped THD without coating (Figure 4.4-16b) were slightly lower than those as-sintered and with coating, which did not show any differences. The formation of second phases in the uncoated sample observed in the XRD analysis and in the SEM images probably reduces the carrier concentration, and therefore can led to a higher resistivity. On the other side, the coating is able to avoid the increase in electrical resistivity observed in the uncoated sample (Figure 4.4-16a). Consequently, the power factor of the uncoated sample decreases, while the coated sample maintains a similar value to as-sintered one. As can be seen in the graph of the temperature dependence of the Power Factor (Figure 4.4-16c), the maximum value reached in the as-sintered sample is around 700 $\mu W/mK^2$, that is little lower than the maximum value previously reported after the thermal ageing at 350°C for 48 hrs (section 4.4.2) around 1100 $\mu W/mK^2$. This difference in the thermoelectric properties is probably due to the different ball mill machines used during the powders preparation and certainly it will need further processing parameter optimization to reach the same or better properties respect the previously ones.

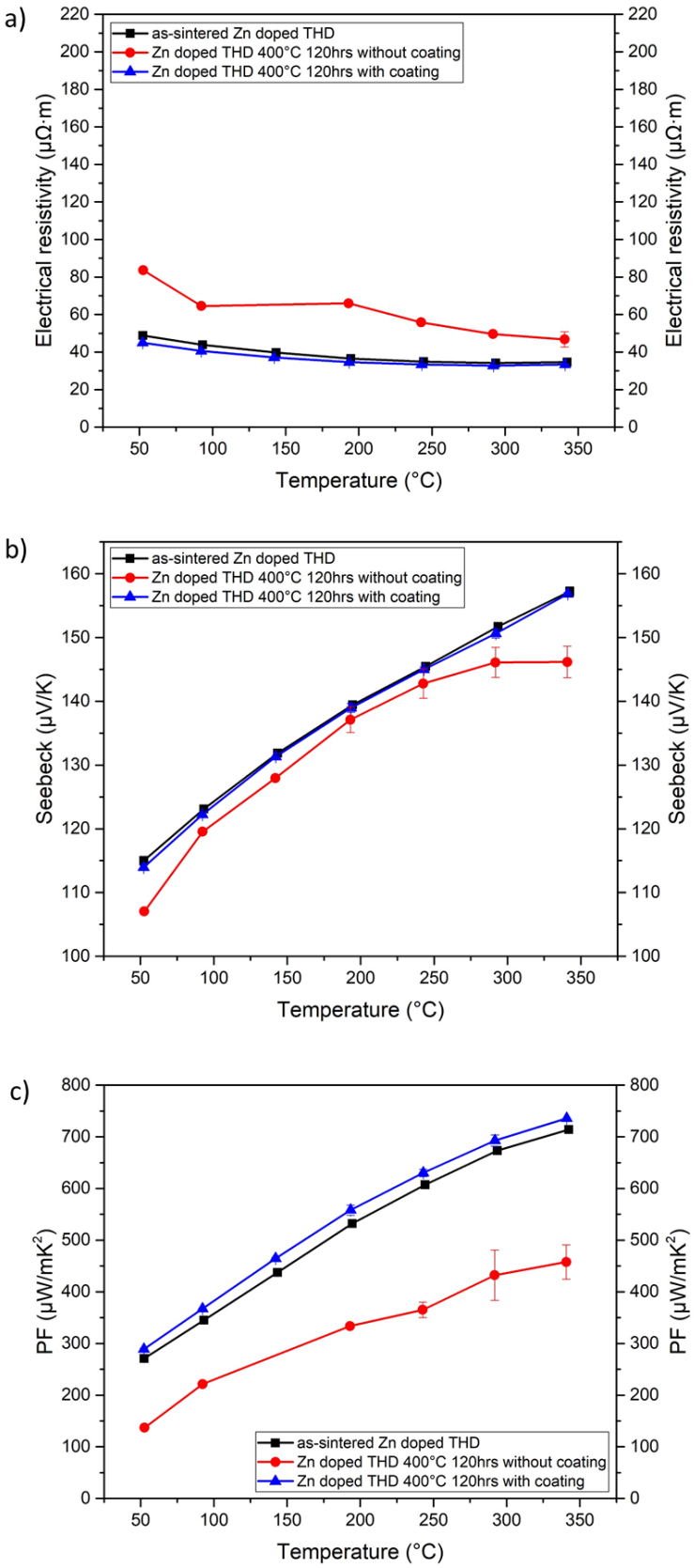

Figure 4.4-16: Temperature dependence of the (a) electrical resistivity, (b) Seebeck coefficient, (c) power factor of the as-sintered Zn doped THD (black curve), coated (blu curve) and uncoated Zn doped THD (red curve) after thermal ageing at 400°C, dwelling time 120hrs, in air

Summarising, the effectiveness of a hybrid commercial coating as an alternative oxidation protective coating technology for thermoelectric material, and in particular for Zn doped tetrahedrite substrates, was successfully assessed.

The water-based hybrid resin proved to be effective at providing a barrier coating to avoid the oxidation. The values concerning the power factor did not decrease in the coated sample, demonstrating that it is a promising candidate for protecting Zn doped THD in presence of oxidative atmosphere up to 400°C.

These results have important implications for employing of commercial hybrid coatings for tetrahedrite based TE modules. The findings presented in this section are relevant because they represent a novel approach to coatings for TE substrates, never tested and studied in literature before.

Chapter 5

Conclusions and future perspectives

In this PhD thesis, new oxidation protective coatings for different thermoelectric substrates have been developed. Their effectiveness was assessed as coatings for different thermoelectrics: higher manganese silicide (HSM), magnesium silicide based material (Sb doped $Mg_2(Si,Sn)$, $Mg_2Si_{0.487}Sn_{0.5}Sb_{0.013}$, zinc doped tetrahedrite (Zn doped THD) and titanium suboxide (TiO_x).

A higher manganese silicide thermoelectric, produced by spark plasma sintering at Nanoforce Technology Ltd, was successfully coated with a silica-based glass-ceramic (G11), in order to be used at temperatures higher than 500°C.

In the G11 glass-ceramic coating, needle-like shaped crystals of $Ba_2Si_4O_{10}$ were well-dispersed in the amorphous matrix, and no defects or pores were visible at the coating/HMS interface. The as-deposited G11 glass-ceramic was a CTE of $10.7 \cdot 10^{-6}$ °C^{-1} (200-400°C) a value slightly lower than that of the HMS substrate ($11.5 \cdot 10^{-6}$ °C^{-1}) thus leading to a moderate compression state in the coating and potentially more resistant to thermal cycling.

G11 glass-ceramic coated and uncoated HMS were submitted to thermal cycling from room temperature to 600°C in air (10 cycles, 1h dwelling time for each cycle). The formation of a 5 μm thick silica layer was observed on the whole surface of the uncoated thermoelectric, due to the reaction between HMS and oxygen, which determined the formation of a Si-deficient layer (MnSi). The XRD analysis of the uncoated sample surface after cycling oxidation test confirmed that the main phase was MnSi with higher manganese silicide ($MnSi_{1.74}$) present in smaller quantity. On the other hand, the cross-sections of a glass-ceramic coated HMS sample after the cyclic oxidation test, showed a sound interface, without inter-diffusion and reaction between the coating and the substrate. The coating was still well-adherent to the TE substrate, and there were no cracks within the glass-ceramic coating. The EDS elemental map and the XRD analysis did not show a continuous

MnSi layer at the glass-ceramic/HMS interface as in the case of uncoated HMS. XRD patterns confirmed that the as-deposited and thermally cycled glass-ceramic coated HMS were identical. The glass-ceramic coating provides thus a successful protection inhibiting the oxidation of higher manganese silicide under thermal cycling. Concerning the thermoelectric properties, uncoated cycled HMS samples showed a higher electrical resistivity and a significantly reduced power factor in comparison with the coated one. The coated cycled HMS samples showed unchanged electrical resistivity, power factor and zT compared to the as-sintered sample (zT around 0.35), indicating that the integrity of the coating and of the interface verified the excellent CTE matching between HMS and coating, thus demonstrating that the use of this glass-ceramic coating is an efficient oxidation protective system during cyclic working conditions.

Furthermore, the residual amorphous phase may add self-healing properties to the coating during cyclic working conditions. For this reason, during the PhD work the self-repair ability of this glass-ceramic system was demonstrated, evidencing the closure of pre-induced scratches/ cracks during heating at temperature above its softening point, which confirms its ability to enhance the reliability and durability of the coated thermoelectric system.

The results concerning the higher manganese silicide thermoelectric obtained during this PhD thesis have important implications for the development of reliable and low-cost glass ceramic coatings for HMS-based TE devices. In fact, the findings presented in this section are relevant in the thermoelectricity field because they represent a new approach to coatings for TE substrates, in which the self-healing ability of the residual glass phase could improve the durability of the coated thermoelectric module, even in dynamic operations.

In the literature very little was found concerning glass-based coating for the magnesium silicide and in particular for Sb doped $Mg_2(Si,Sn)$ based materials. The novelty of this part of the thesis consists in the designing of five glass-based compositions with low deposition temperature (550-600°C) and high coefficient of thermal expansion (17-17.5 $\cdot 10^{-6}$ K^{-1}) similar to that of the thermoelectric substrate. In fact, the development of glass-based coating thermo-mechanically compatible with the $Mg_2Si_{0.487}Sn_{0.5}Sb_{0.013}$ plays a key role in the manufacturing of reliable, efficient and durable TE devices.

Two different approaches were studied and discussed, in order to protect Sb doped $Mg_2(Si,Sn)$ based materials against oxidation up to 500°C. The first method focused on the development of a novel glass-based coating. A series of five glasses were designed (labelled from M1 to M5), produced and characterized in order to identify the most suitable to protect the TE substrate. Differential thermal analyses and hot stage microscopy were carried out in order to study the crystallization and the sintering glasses behaviour, respectively. Dilatometric analyses were performed in order to measure the coefficient of thermal expansion of the glasses, which resulted slightly higher compared to the values calculated with the SciGlass software. On the basis of the thermal analyses, the heat treatments to obtain the correspondent

glass-ceramic coatings were chosen. Only the M3 glass-based coating had a CTE of $17 \cdot 10^{-6}$ °C^{-1} (150-300°C), very close to that of the substrate; it was selected as the most promising solution and it was chosen for the oxidation tests at 500°C for 120 hrs in air. The morphological characterization of the M3 glass coated $Mg_2Si_{0.487}Sn_{0.5}Sb_{0.013}$ showed that the good compatibility between the coating and the thermoelectric substrate was maintained after the long exposure to severe conditions. The interface between the glass-based coating and the Sb doped $Mg_2(Si,Sn)$ was characterized by the absence of cracks or delamination phenomena and no diffusion of elements was detected. XRD analysis on the coated sample after the oxidation test at 500°C for 120 hrs in air was the same compared to the as-sintered thermoelectric, demonstrating the efficacy in the protection of the Sb doped $Mg_2(Si,Sn)$ substrate. Dilatometry and XRD analysis on the glass-based coating after the oxidation test confirmed the thermo-mechanical and the thermodynamic stability, respectively. Electric properties will be carried out in the near future to compare the electric performances of an as-sintered Sb doped $Mg_2(Si,Sn)$ with a coated sample after oxidation test at 500°C for 120 hrs, in order to further validate the efficiency of this glass-based system.
The second approach to protect the $Mg_2Si_{0.487}Sn_{0.5}Sb_{0.013}$ thermoelectric consisted in utilizing a hybrid commercial coating produced by Aremco Scientific Company, named as Ceramacoat^{TM}512-N. After the oxidation test at 500°C for 120 hrs in air the sample of Ceramacoat™512-N coated $Mg_2Si_{0.487}Sn_{0.5}Sb_{0.013}$ was found to be completely decomposed, concluding that it could be necessary to optimize a different deposition method to obtain a more uniform coating in order to avoid the formation of oxidation layers at the interface.

A new silica-based glass-ceramic, indicated as T1, was designed, produced and characterized as a potential oxidation resistant coating for TiOx substrate up to 600°C. Differential thermal analyses and hot stage microscopy were performed aimed to study the crystallization and the sintering glasses behaviour, respectively. Dilatometric analyses were performed in order to measure the coefficient of thermal expansion of the glass, resulted slightly higher ($8.6 \cdot 10^{-6}$ °C^{-1} measured in the range 200-500°C) compared to the calculated value with the SciGlass software ($7.1 \cdot 10^{-6}$ °C^{-1}). The value of the experimentally measured CTE of T1 glass-ceramic is $9.1 \cdot 10^{-6}$ K^{-1}, very close to the coefficient of thermal expansion of titanium suboxide (between 7 and $9 \cdot 10^{-6}$ K-1). Furthermore, the substantial increase of the dilatometric softening point of the glass-ceramic (T_d =1081°C), with respect to the T1 parent glass one (T_d =792°C) represents an interesting aspect of this glass-ceramic system, because it could be an advantage in terms of the coating operational temperature range. The morphological analysis of the T1 glass-ceramic coated TiO_x revealed that the coating was well-adherent to the substrate, without the presence of cracks, pores or delamination phenomena at the interface. The study of the complex microstructure carried out with XRD analysis, EDS elemental maps and EDS line-scan led to find the presence of different crystalline phases in the glass-ceramic coating. The main phase was identified as smaller and brighter crystals of $Y_2Ti_2O_7$, while darker needle-like shaped crystals were ascribed to the $CaAl_2Si_2O_8$ anorthite

phase. The T1 glass-ceramic coating could be considered a potential candidate to protect TiO_x modules in oxidative atmosphere up to 600°C, due to the optimal thermo-mechanical compatibility with the substrate and the possibility to use TiO_x above 400°C in air without any degradation effect. The oxidation tests will be performed at IKTS in the next few months.

Since glass-ceramic coatings would have required a deposition temperature too high for zinc doped tetrahedrite ($Cu_{11.5}Zn_{0.5}Sb_4S_{13}$), two commercial hybrid resins with low curing temperature and with nominal temperature resistance up to 590°C, were chosen as potential protective resistance coatings.

After preliminary tests, the water-based silicone resin was successfully identified as a potential candidate to avoid oxidation of the Zn doped tetrahedrite. Compositional changes in both the Zn doped THD substrate and the hybrid coating are evaluated and discussed with respect to the morphological, chemical and electrical properties of the uncoated and coated Zn doped THD before and after ageing at 350 and 400°C in air.

The first thermal ageing at 350°C for 48hrs induced in the uncoated Zn doped THD the formation of an inhomogeneous layer (3- 5 μm thick) on the whole surface, detected as antimony oxide by means the XRD analysis, which detected the presence of other secondary phases reported in literature such as Cu_3SbS_4 and Cu_2S. On the contrary, in the coated Zn doped THD after ageing, the coating was still well-adherent to the substrate as in the as-deposited sample, without oxidation layers and evidence of cracks within the coating and the Zn doped THD. This made evident the effective protection of the hybrid coating, which as demonstrated by the EDS analysis, seems not be subjected to compositional changing after the ageing at these conditions. Furthermore, XRD analysis showed that after the ageing at 350°C for 48 hrs in air there were no apparent changes in the Zn doped THD if compared to as-sintered sample. Concerning the electrical properties, the Seebeck coefficients of the three samples did not show remarkable differences. The coating is able to avoid the increase in electrical resistivity observed in the uncoated sample, as it maintains the original chemical composition. Consequently, the power factor of the uncoated sample decreases, while the coated sample maintains a similar value.
After the second thermal ageing, carried out at 400°C for 120 hrs, the uncoated Zn doped THD was characterized again by an oxidation layer on the whole surface of the thermoelectric substrate. On the other hand, the SEM analysis on the coated Zn doped THD after ageing showed the absence of cracks within the coating, which was well-adhered to the thermoelectric substrate. However, the evidence for the formation of a 20- 25 μm thick oxidation layer was found at the coating/Zn doped THD interface. In spite of XRD analysis of the aged Zn doped THD with coating reported the effectiveness of the CP4040 hybrid coating because the main phase remained the $Cu_{12}Sb_4S_{13}$ with Cu_3SbS_4 as secondary phase, XRD pattern confirmed also the presence of a small amount of antimony oxide (Sb_2O_3). The Seebeck coefficients of the aged Zn doped THD without coating were lower than those as-sintered and with coating, which did not show any differences. The formation of

second phases in the uncoated sample observed in the XRD analysis and in the SEM images probably reduced the carrier concentration, and this can lead to a higher resistivity. However, the coating is able to avoid the increase in electrical resistivity observed in the uncoated sample. Consequently, the power factor of the uncoated sample decreases, while the coated sample maintains a similar value to as-sintered one. Summarising, the effectiveness of a hybrid commercial coating as an alternative oxidation protective coating for thermoelectric material, and in particular for Zn doped tetrahedrite substrates, was successfully demonstrated.

The results presented in this section are relevant because they represent a novel and easier approach to coatings for TE substrates. Further studies will be focused on the optimization of the deposition technique in order to obtain thinner and more uniform coatings.

In this PhD thesis critical issues related to the oxidation of thermoelectric substrates and the degradation of their electrical performances were studied. The design and the development of new glass and glass-ceramics as oxidation protective coatings were the main focus of this research. In this context, this PhD thesis represents a valuable contribution to the integration of advanced engineering ceramics for energy conversion systems and research findings have important implications for developing durable and reliable TE modules.

Future experimental work in the topics presented in this thesis may address to the following issues:

a) Upscaling of low cost coating deposition and module assembly:

- In some cases, the manual deposition carried out in this work did not lead to a uniform and reproducible thickness of the glass/ glass-ceramic coating. The future perspectives in this context are related to implement a viable and versatile method, for example electrophoretic deposition (EPD), to deposit the coatings produced during this PhD work in order to be used at industrial scale.

b) Joining and integration techniques:

- New investigations are needed to ensure an appropriate and reliable joining and assembly packaging technology in order to develop a TE module design which can adapt to thermal gradients without damage even over long periods of time.

Dissemination of the results

- G. Viola, F. D'Isanto, A. E. Mahmoud, M.J. Reece, G., F. Smeacetto, M. Salvo, The effect of processing conditions on phase and microstructure of CaGeO3 ceramics, Ceram. Int. 43 (2017) 12035-12043; doi:10.1016/j.ceramint.2017.06.056

- G. Viola, F. D'Isanto, V. Koval, G. Cempura, H. Yan, F. Smeacetto, M. Salvo, Orthoenstatite to forsterite phase transformation in magnesium germanate ceramics, Ceram. Int. 45 (2019) 7878-7884; doi:10.1016/j.ceramint.2019.01.098

- M. Salvo, F. Smeacetto, F. D'Isanto, G. Viola, P. Demitri, F. Gucci, M.J. Reece, Glass-ceramic oxidation protection of higher manganese silicide thermoelectrics, J. Eur. Ceram. Soc. 39 (2019) 66-71; doi:10.1016/j.jeurceramsoc.2018.01.007

- F. Gucci, F. D'Isanto, R. Zhang, M. J. Reece, F. Smeacetto, M. Salvo, Oxidation Protective Hybrid Coating for Thermoelectric Materials, Materials 12 (2019) 573; doi: 10.3390/ma12040573

- F. D'Isanto, F. Smeacetto, M.J. Reece, K. Chen, M. Salvo. Oxidation protective glass coating for magnesium silicide based- thermoelectrics; submitted to Ceram. Int.

- F. D'Isanto, F. Smeacetto, H-P. Martin, A. Chrysanthou, M. Salvo. A new oxidation resistant glass-ceramic coating for TiOx; to be submitted to J. Eur. Ceram. Soc.

- F. D'Isanto, M. Salvo, F. Smeacetto, G. Viola, F. Gucci, M.J. Reece, Glass-ceramic oxidation protective coatings for higher manganese silicide thermoelectrics of higher manganese silicide thermoelectrics, 37th International Conference on Thermoelectrics- 16th European Conference on Thermoelectrics (2017), Caen (France); poster presentation

- M. Salvo, F. Smeacetto, F. D'Isanto, G. Viola, P. Demitri, F. Gucci, M. J. Reece, Ceramics for Energy - 2nd International Forum on Ceramics and Inorganic Materials (2017), Faenza (Italy); oral presentation

- F. D'Isanto, M. Salvo, F. Smeacetto, F. Gucci, K. Chen, M.J. Reece, Glass-ceramic oxidation protective coatings for manganese- and magnesium-based thermoelectric silicides, 43rd International Conference & Exposition on Advanced Ceramics and Composites (2018), Daytona Beach (Florida, USA); oral presentation

- F. D'Isanto, M. Salvo, F. Smeacetto, F. Gucci, R. Zhang, K. Chen, M.J. Reece, CoACH Industrial Workshop – Advanced Materials for High Growth Industries (2018) Torino (Italy); poster presentation

- F. D'Isanto, M. Salvo, F. Smeacetto, F. Gucci, R. Zhang, K. Chen, M.J. Reece, Innovative oxidation protective coatings for thermoelectric materials, 16th ECerS Conference (2019), Torino (Italy); oral presentation

- F. D'Isanto, M. Salvo and F. Smeacetto, Ytterbium disilicate-based glass-ceramic as joining material for ceramics and CMCs protective coatings for thermoelectric materials, 10th International on High Temperature Ceramic Matrix Composites (2019), Bordeaux (France); oral presentation
(SPIN-OFF ACTIVITY)

- M. Salvo, F. Smeacetto, F. D'Isanto, Le mille vite del vetro (2019), Murano Venezia (Italy), oral presentation

- F. D'Isanto, M. Salvo, F. Smeacetto, NIS colloquium Theoretical and experimental approaches to thermoelectrics for waste heat harvesting (2020) Torino (Italy); oral presentation

References

[1] A. Zecca, L. Chiari, Fossil-fuel constraints on global warming, Energy Policy. 38 (2010) 1–3. https://doi.org/10.1016/j.enpol.2009.06.068.

[2] OECD Green Growth Studies: Energy, 2011. https://doi.org/10.1787/9789264115118-en.

[3] M.Z. Jacobson, Review of solutions to global warming, air pollution, and energy security, Energy Environ. Sci. 2 (2009) 148–173. https://doi.org/10.1039/b809990c.

[4] B. Knopf, P. Nahmmacher, E. Schmid, The European renewable energy target for 2030 - An impact assessment of the electricity sector, Energy Policy. 85 (2015) 50–60. https://doi.org/10.1016/j.enpol.2015.05.010.

[5] S. Twaha, J. Zhu, Y. Yan, B. Li, A comprehensive review of thermoelectric technology: Materials, applications, modelling and performance improvement, Renew. Sustain. Energy Rev. 65 (2016) 698–726. https://doi.org/10.1016/j.rser.2016.07.034.

[6] R. Zevenhoven, A. Beyene, The relative contribution of waste heat from power plants to global warming, Energy. 36 (2011) 3754–3762. https://doi.org/10.1016/J.ENERGY.2010.10.010.

[7] G.J. Snyder, E.S. Toberer, Complex thermoelectric materials, Nat. Mater. 7 (2008) 105–114. https://doi.org/10.1038/nmat2090.

[8] D.M. Rowe, CRC Handbook of Thermoelectrics, 1995.

[9] Waste Heat Recovery: Technology and Opportunities in U.S. Industry, U.S. Dep. Energy, Ind. Technol. Progr. (2008). https://www1.eere.energy.gov/manufacturing/intensiveprocesses/pdfs/waste_heat_recovery.pdf (accessed on Feb 12, 2020).

[10] J.W. Fairbanks, Automotive Thermoelectric Generators and HVAC, 2012 Anu. Merit Rev. DOE Veh. Technol. Progr. Hydrog. Fuel Cells Progr. (2012). https://doi.org/papers3://publication/uuid/18985935-CA12-4E52-9B86-2476B4BFB1AE.

[11] C. Bode, J. Friedrichs, R. Somdalen, J. Köhler, K.-D. Büchter, C. Falter, U. Kling, P. Ziolkowski, K. Zabrocki, E. Müller, D. Kožulović, Potential of Future Thermoelectric Energy Recuperation for Aviation, in: Proc. ASME 2016 Int. Mech. Eng. Congr. Expo. ASME IMECE 2016 Novemb. 11-17, 2016, Pheonix, AZ, USA, 2016. https://doi.org/10.1115/imece2016-66650.

[12] J.C. Bass, R.L. Farley, Examples of power from waste heat for gas fields, in:

Proc16th Int. Conf. Thermoelectr. ICT, 1997: pp. 547–550. https://doi.org/10.1109/ict.1997.667588.

[13] H. Ning, M.J. Reece, F. Smeacetto, M. Salvo, Oxidation protective glass–ceramic coating for higher manganese silicide thermoelectrics, J. Mater. Sci. 51 (2016) 9484–9489. https://doi.org/10.1007/s10853-016-0192-1.

[14] G. Pastorino, Alessandro Volta and his role in thermoelectricity, J. Thermoelectr. 1 (2009) 7–10.

[15] U. Lachish, Thermoelectric Effect Peltier Seebeck and Thomson, Guma Sci. (2016) 1–11. https://doi.org/10.13140/EG.2.1.2722.3443.

[16] T. J. Seebeck, Magnetic polarization of metals and minerals, Abhandlungen Der Dtsch. Akad. Der Wissenschaften Zu Berlin. 265 (1822) 289–346.

[17] E. Velmre, Thomas Johann Seebeck (1770- 1831), in: Proc. Est. Acad. Sci. Eng, 2007: pp. 276–282. http://www.kirj.ee/public/Engineering/2007/issue_4/eng-2007-4-2.pdf.

[18] J. Zheng, Recent advances on thermoelectric materials, Front. Phys. China. 3 (2008) 269–279. https://doi.org/10.1007/s11467-008-0028-9.

[19] K. Koumoto, I. Terasaki, R. Funahashi, Complex Oxide Materials for Potential Thermoelectric Applications, MRS Bull. 31 (2006) 206–210. https://doi.org/10.1557/mrs2006.46.

[20] S. Kasap, Thermoelectric Effects in Metals: Thermocouples, An E-Booklet, 2001. (2001) 1–11. http://www.kasap.usask.ca/samples/ Thermoelectric-Seebeck.pdf.

[21] W.Thomson, On the dynamical theory of heat: with numerical results deduced from Mr. Joule's equivalent of a thermal unit and Messr. Regnault's observation on steam., Trans." R. Soc. Edinburgh Earth Sci. 3 (1851) 91–98.

[22] X. C. Tong, Advanced Materials for Thermal Managment of Electronic Packaging, 2011.

[23] D. Beretta, N. Neophytou, J.M. Hodges, M.G. Kanatzidis, D. Narducci, M. Martin- Gonzalez, M. Beekman, B. Balke, G. Cerretti, W. Tremel, A. Zevalkink, A.I. Hofmann, C. Müller, B. Dörling, M. Campoy-Quiles, M. Caironi, Thermoelectrics: From history, a window to the future, Mater. Sci. Eng. R Reports. 138 (2019) 210–255. https://doi.org/10.1016/j.mser.2018.09.001.

[24] A. Polozine, S. Sirotinskaya, L. Schaeffer, History of development of thermoelectric materials for electric power generation and criteria of their quality, Mater. Res. 17 (2014) 1260–1267. https://doi.org/10.1590/1516-1439.272214.

[25] J.G. Stockholm, Applications in thermoelectricity, in: Mater. Today Proc.,

Elsevier Ltd, 2018: pp. 10257–10276. https://doi.org/10.1016/j.matpr.2017.12.273.

[26] L. D. Hicks and M. S. Dresselhaus, Effect of quantum-well structures on the thermoelectric figure of merit, Phys. Rev. B. 47 (1993) 12727.

[27] R. Stobart, M.A. Wijewardane, Z. Yang, Comprehensive analysis of thermoelectric generation systems for automotive applications, Appl. Therm. Eng. 112 (2017) 1433–1444. https://doi.org/10.1016/j.applthermaleng.2016.09.121.

[28] J.P. Longtin, L. Zuo, D. Hwang, G. Fu, M. Tewolde, Y. Chen, S. Sampath, Fabrication of thermoelectric devices using thermal spray: Application to vehicle exhaust systems, J. Therm. Spray Technol. 22 (2013) 577–587. https://doi.org/10.1007/s11666-013-9903-1.

[29] K. Matsubara, Development of a high efficient thermoelectric stack for a waste exhaust heat recovery of vehicles, in: Twenty-First Int. Conf. Thermoelectr. 2002. Proc. ICT '02., 2002: pp. 418–423. https://doi.org/10.1109/ICT.2002.1190350.

[30] X. Zhang, L.D. Zhao, Thermoelectric materials: Energy conversion between heat and electricity, J. Mater. 1 (2015) 92–105. https://doi.org/10.1016/j.jmat.2015.01.001.

[31] S. LeBlanc, Thermoelectric generators: Linking material properties and systems engineering for waste heat recovery applications, Sustain. Mater. Technol. 1 (2014) 26–35. https://doi.org/10.1016/j.susmat.2014.11.002.

[32] J. Yang, F.R. Stabler, Automotive applications of thermoelectric materials, J. Electron. Mater. 38 (2009) 1245–1251. https://doi.org/10.1007/s11664-009-0680-z.

[33] R. Zevenhoven, A. Beyene, The relative contribution of waste heat from power plants to global warming, Energy. 36 (2011) 3754–3762. https://doi.org/https://doi.org/10.1016/j.energy.2010.10.010.

[34] D.K. Aswal, R. Basu, A. Singh, Key issues in development of thermoelectric power generators: High figure-of-merit materials and their highly conducting interfaces with metallic interconnects, Energy Convers. Manag. 114 (2016) 50–67. https://doi.org/10.1016/j.enconman.2016.01.065.

[35] M.S. El-Genk, H.H. Saber, Performance analysis of cascaded thermoelectric converters for advanced radioisotope power systems, Energy Convers. Manag. 46 (2005) 1083–1105. https://doi.org/https://doi.org/10.1016/j.enconman.2004.06.019.

[36] T. Hendricks, Engineering Scoping Study of Thermoelectric Generator Systems for Industrial Waste Heat Recovery, U.S Dep. Energy, Ind. Technol. Progr. (2006).

[37] J. Fairbanks, Vehicular Thermoelectrics: The New Green Technology, in: DEER Conf., 2010.

[38] J. LaGrandeur, D. Crane, A. Eder, Vehicle Fuel Economy Improvement through Thermoelectric Waste Heat Recovery, in: DEER Conf., IEEE, 2005. https://doi.org/10.1109/RAMS.2012.6175475.

[39] T.J. Hendricks, N.K. Karri, T.P. Hogan, C.J. Cauchy, New perspectives in thermoelectric energy recovery system design optimization, J. Electron. Mater. 42 (2013) 1725–1736. https://doi.org/10.1007/s11664-012-2406-x.

[40] G. Schierning, R. Chavez, R. Schmechel, B. Balke, G. Rogl, P. Rogl, Concepts for medium-high to high temperature thermoelectric heat-to-electricity conversion: a review of selected materials and basic considerations of module design, Transl. Mater. Res. 2 (2015) 025001. https://doi.org/10.1088/2053-1613/2/2/025001.

[41] A. Chen, P.K. Wright, Medical applications of thermoelectrics, in: Modul. Syst. Appl. Thermoelectr., 2012: pp. 26-1-26–22. https://doi.org/10.1201/b11892.

[42] P.M. Kumar, V.J. Babu, A. Subramanian, A. Bandla, N. Thakor, S. Ramakrishna, H. Wei, The Design of a Thermoelectric Generator and Its Medical Applications, Designs. 3 (2019) 22. https://doi.org/10.3390/designs3020022.

[43] S.B. Riffat, X. Ma, Thermoelectrics: A review of present and potential applications, Appl. Therm. Eng. 23 (2003) 913–935. https://doi.org/10.1016/S1359-4311(03)00012-7.

[44] D. Enescu, Thermoelectric Energy Harvesting: Basic Principles and Applications, in: Green Energy Adv., 2019. https://doi.org/http://dx.doi.org/10.5772/57353.

[45] Z.L.W. Ya Yang, Zong-Hong Lin, Techien Hou, Fang Zhang, Nanowire-composite based flexible thermoelectric nanogenerators and self-powered temperature sensors, Nano Res. 5 (2012) 888–895.

[46] Multi-Mission Radioisotope Thermoelectric Generator (MMRTG), Natl. Aeronaut. Sp. Adm. (2013). https://mars.nasa.gov/internal_resources/788/ (accessed February 16, 2020).

[47] Advanced Thermoelectric Technology: Powering Spacecraft and Instruments to Explore the Solar System, NASA Sci. (2018). https://science.nasa.gov/technology/technology-stories/advanced-thermoelectric-technology (accessed February 16, 2020).

[48] Y. Zhou, S. Paul, S. Bhunia, Harvesting wasted heat in a microprocessor using thermoelectric generators: Modeling, analysis and measurement, Proc. -Design, Autom. Test Eur. DATE. (2008) 98–103. https://doi.org/10.1109/DATE.2008.4484669.

[49] D. Kraemer, B. Poudel, H.-P. Feng, J.C. Caylor, B. Yu, X. Yan, Y. Ma, X. Wang, D. Wang, A. Muto, K. McEnaney, M. Chiesa, Z. Ren, G. Chen, High-performance flat-panel solar thermoelectric generators with high thermal concentration, Nat. Mater. 10 (2011) 532. https://doi.org/10.1038/nmat3013.

[50] P. Sundarraj, D. Maity, S.S. Roy, R.A. Taylor, Recent advances in thermoelectric materials and solar thermoelectric generators – a critical review, RSC Adv. 4 (2014) 46860–46874. https://doi.org/10.1039/C4RA05322B.

[51] W. He, J. Zhou, J. Hou, C. Chen, J. Ji, Theoretical and experimental investigation on a thermoelectric cooling and heating system driven by solar, Appl. Energy. 107 (2013) 89–97. https://doi.org/https://doi.org/10.1016/j.apenergy.2013.01.055.

[52] J. LaGrandeur, D. Crane, S. Hung, B. Mazar, A. Eder, Automotive Waste Heat Conversion to Electric Power using Skutterudite, TAGS, PbTe and BiTe, in: 2006 25th Int. Conf. Thermoelectr., 2006: pp. 343–348. https://doi.org/10.1109/ICT.2006.331220.

[53] Q.E. Hussain, D.R. Brigham, C.W. Maranville, Thermoelectric Exhaust Heat Recovery for Hybrid Vehicles, SAE Int. J. Engines. (2009). https://doi.org/https://doi.org/10.4271/2009-01-1327.

[54] N. Espinosa, M. Lazard, L. Aixala, H. Scherrer, Modeling a Thermoelectric Generator Applied to Diesel Automotive Heat Recovery, J. Electron. Mater. 39 (2010) 1446–1455. https://doi.org/10.1007/s11664-010-1305-2.

[55] M. Mori, Y. Takeshi, S. Mitsumasa, M. Takatoshi, T. Shunji, H. Tomohide, Simulation of Fuel Economy Effectiveness of Exhaust Heat Recovery System Using Thermoelectric Generator in a Series Hybrid, SAE Int. J. Mater. Manuf. 4 (2011) 1268–1276. https://doi.org/https://doi.org/10.4271/2011-01-1335.

[56] M.A. Karri, E.F. Thacher, B.T. Helenbrook, Exhaust energy conversion by thermoelectric generator: Two case studies, Energy Convers. Manag. 52 (2011)1596–1611. https://doi.org/https://doi.org/10.1016/j.enconman.2010.10.013.

[57] A.S. Kushch, J.C. Bass, S. Ghamaty, N.B. Elsner, R.A. Bergstrand, D. Furrow, M. Melvin, Thermoelectric Development at Hi-Z Technology *, in: Proc. 20th Int. Conf. Thermoelectr. Beijing, China, 2001: pp. 422–430.

[58] A. Nemś, S. Mikołaj, N. Magdalena, M. Tomasz, Analysis of car waste heat recovery system utilizing thermoelectric generator, Autobusy. 6 (2018) 619–626. https://doi.org/10.24136/atest.2018.144.

[59] G.S. Nolas, J. Sharp, J. Goldsmid, Thermoelectrics: Basic Principles and New Materials Developments, Springer, 2001.

[60] D.M. Rowe, Thermoelectrics handbook: macro to nano, 2005.

[61] W. He, G. Zhang, X. Zhang, J. Ji, G. Li, X. Zhao, Recent development and application of thermoelectric generator and cooler, Appl. Energy. 143 (2015) 1–25. https://doi.org/10.1016/j.apenergy.2014.12.075.

[62] G.J. Snyder, T.S. Ursell, Thermoelectric efficiency and compatibility, Phys. Rev. Lett. 91 (2003) 148301/1-148301/4. https://doi.org/10.1103/PhysRevLett.91.148301.

[63] G.J. Snyder, Application of the compatibility factor to the design of segmented and cascaded thermoelectric generators, Appl. Phys. Lett. 84 (2004) 2436–2438. https://doi.org/10.1063/1.1689396.

[64] Z.G. Chen, G. Hana, L. Yanga, L. Cheng, J. Zou, Nanostructured thermoelectric materials: Current research and future challenge, Prog. Nat. Sci. Mater. Int. 22 (2012) 535–549. https://doi.org/10.1016/j.pnsc.2012.11.011.

[65] J.R. Sootsman, D.Y. Chung, M.G. Kanatzidis, New and old concepts in thermoelectric materials, Angew. Chemie - Int. Ed. 48 (2009) 8616–8639. https://doi.org/10.1002/anie.200900598.

[66] M.H. Elsheikh, D.A. Shnawah, M.F.M. Sabri, S.B.M. Said, M.H. Haji, M.B. Ali Bashir, M. Mohamad, A review on thermoelectric renewable energy: Principle parameters that affect their performance, Renew. Sustain. Energy Rev. 30 (2014) 337–355. https://doi.org/10.1016/j.rser.2013.10.027.

[67] A.W. Van Herwaarden, P.M. Sarro, Thermal sensors based on the seebeck effect, Sensors and Actuators. 10 (1986) 321–346.

[68] A. Bulusu, D.G. Walker, Review of electronic transport models for thermoelectric materials, Superlattices Microstruct. 44 (2008) 1–36. https://doi.org/10.1016/j.spmi.2008.02.008.

[69] T.C. Harman, P.J. Taylor, M.P. Walsh, B.E. LaForge, Quantum dot superlattice thermoelectric materials and devices, Science (80-.). 297 (2002) 2229–2232. https://doi.org/10.1126/science.1072886.

[70] V. Damodara Das, P. Gopal Ganesan, Thickness and temperature effects on thermoelectric power and electrical resistivity of (Bi0.25Sb0.75)2Te3 thin films, Mater. Chem. Phys. 57 (1998) 57–66.

[71] A. V Dmitriev, I.P. Zvyagin, Current trends in the physics of thermoelectric materials, Physics-Uspekhi. 53 (2010) 789–803. https://doi.org/10.3367/ufne.0180.201008b.0821.

[72] C. Wan, Y. Wang, N. Wang, K. Koumoto, Low-thermal-conductivity (MS)1+x(TiS2)2 (M = Pb, Bi, Sn) misfit layer compounds for bulk thermoelectric materials, Materials (Basel). 3 (2010) 2606–2617. https://doi.org/10.3390/ma3042606.

[73] Z. Tian, S. Lee, G. Chen, A Comprehensive Review of Heat Transfer in Thermoelectric Materials and Devices, Annu. Rev. Heat Transf. (2014) 1–64. https://doi.org/10.1615/AnnualRevHeatTransfer.2014006932.

[74] G. Pennelli, Review of nanostructured devices for thermoelectric applications, Beilstein J. Nanotechnol. 5 (2014) 1268–1284. https://doi.org/10.3762/bjnano.5.141.

[75] H.J. Goldsmid, G.S. Nolas, A review of the new thermoelectric materials, in: Proc. ICT2001 20 Int. Conf. Thermoelectr. Cat No01TH8589, 2001: pp. 1–6. https://doi.org/10.1109/ICT.2001.979602.

[76] M.S. Dresselhaus, G. Chen, M.Y. Tang, R. Yang, H. Lee, D. Wang, Z. Ren, J.P. Fleurial, P. Gogna, New directions for low-dimensional thermoelectric materials, Adv. Mater. 19 (2007) 1043–1053. https://doi.org/10.1002/adma.200600527.

[77] S. Hebert, D. Berthebaud, R. Daou, Y. Breard, D. Pelloquin, E. Guilmeau, F. Gascoin, O. Lebedev, A. Maignan, Searching for new thermoelectric materials: some examples among oxides, sulfides and selenides, J. Physics-Condensed Matter. 28 (2015) 23. https://doi.org/10.1088/0953-8984/28/1/013001.

[78] M.W. Gaultois, T.D. Sparks, C.K.H. Borg, R. Seshadri, W.D. Bonificio, D.R. Clarke, Data-driven review of thermoelectric materials: Performance and resource onsiderations, Chem. Mater. 25 (2013) 2911–2920. https://doi.org/10.1021/cm400893e.

[79] B.C. Sales, D. Mandrus, B.C. Chakoumakos, V. Keppens, J.R. Thompson, Filled skutterudite antimonides: Electron crystals and phonon glasses, Phys. Rev. B. 56 (1997) 15081–15089.

[80] M. Kubouchi, K. Hayashi, Y. Miyazaki, Thermoelectric and magnetic properties of Yb2MgSi2 prepared by spark plasma sintering method, Appl. Phys. A Mater. Sci. Process. 122 (2016) 1–6. https://doi.org/10.1007/s00339-016-0300-8.

[81] M. Saleemi, A. Famengo, S. Fiameni, S. Boldrini, S. Battiston, M. Johnsson, M. Muhammed, M.S. Toprak, Thermoelectric performance of higher manganese silicide nanocomposites, J. Alloys Compd. 619 (2015) 31–37. https://doi.org/10.1016/j.jallcom.2014.09.016.

[82] I. Terasaki, Y. Sasago, K. Uchinokura, Large thermoelectric power in NaCo2O4 single crystals, Phys. Rev. B - Condens. Matter Mater. Phys. 56 (1997) R12685–R12687. https://doi.org/10.1103/PhysRevB.56.R12685.

[83] X.Y. Huang, Y. Miyazaki, K. Yubuta, Y. Oide, T. Kajitani, The thermoelectric properties of [Ca2CoO3]0.62[CoO2] textured ceramics, in: Int. Conf. Thermoelectr. ICT, Proc., 2006: pp. 89–91. https://doi.org/10.1109/ICT.2006.331287.

[84] M. Backhaus-Ricoult, J.R. Rustad, D. Vargheese, I. Dutta, K. Work, Levers for thermoelectric properties in titania-based ceramics, J. Electron. Mater. 41 (2012) 1636–1647. https://doi.org/10.1007/s11664-012-2019-4.

[85] M. Hamid Elsheikh, D.A. Shnawah, M.F.M. Sabri, S.B.M. Said, M. Haji Hassan, M.B. Ali Bashir, M. Mohamad, A review on thermoelectric renewable energy: Principle parameters that affect their performance, Renew. Sustain. Energy Rev. (2014). https://doi.org/10.1016/j.rser.2013.10.027.

[86] M.A. Kamarudin, S.R. Sahamir, R.S. Datta, B.D. Long, M.F. Mohd Sabri, S. Mohd Said, A review on the fabrication of polymer-based thermoelectric materials and fabrication methods, Sci. World J. 2013 (2013). https://doi.org/10.1155/2013/713640.

[87] Y. Gelbstein, J. Tunbridge, R. Dixon, M.J. Reece, H. Ning, R. Gilchrist, R. Summers, I. Agote, M.A. Lagos, K. Simpson, C. Rouaud, P. Feulner, S. Rivera, R. Torrecillas, M. Husband, J. Crossley, I. Robinson, Physical, mechanical, and structural properties of highly efficient nanostructured n- and p-silicides for practical thermoelectric applications, J. Electron. Mater. 43 (2014) 1703–1711. https://doi.org/10.1007/s11664-013-2848-9.

[88] G. Skomedal, L. Holmgren, H. Middleton, I.S. Eremin, G.N. Isachenko, M. Jaegle, K. Tarantik, N. Vlachos, M. Manoli, T. Kyratsi, D. Berthebaud, N.Y. Dao Truong, F. Gascoin, Design, assembly and characterization of silicide-based thermoelectric modules, Energy Convers. Manag. 110 (2016) 13–21. https://doi.org/10.1016/j.enconman.2015.11.068.

[89] A. Nozariasbmarz, A. Agarwal, Z.A. Coutant, M.J. Hall, J. Liu, R. Liu, A. Malhotra, P. Norouzzadeh, M.C. Öztürk, V.P. Ramesh, Y. Sargolzaeiaval, F. Suarez, D. Vashaee, Thermoelectric silicides: A review, Jpn. J. Appl. Phys. 56 (2017). https://doi.org/10.7567/JJAP.56.05DA04.

[90] W. Luo, H. Li, Y. Yan, Z. Lin, X. Tang, Q. Zhang, C. Uher, Rapid synthesis of high thermoelectric performance higher manganese silicide with in-situ formed nano-phase of MnSi, Intermetallics. 19 (2011) 404–408. https://doi.org/https://doi.org/10.1016/j.intermet.2010.11.008.

[91] Y. Sadia, L. Dinnerman, Y. Gelbstein, Mechanical alloying and spark plasma sintering of higher manganese silicides for thermoelectric applications, J. Electron. Mater. 42 (2013) 1926–1931. https://doi.org/10.1007/s11664-013-2476-4.

[92] T.B. Massalski, H. Okamoto, P.R. Subramanian, L. Kacprzak, Binary alloy phase diagrams, 2nd Edition, 1990.

[93] R. Zhao, F. Guo, Y. Shu, X. Zhang, Q. Lu, J. Zhang, Improvement of Thermoelectric Properties Via Combination of Nanostructurization and Elemental Doping, Jom. 66 (2014) 2298–2308. https://doi.org/10.1007/s11837-014-1148-z.

[94] L. Akselrud, R. Cardoso Gil, M. Wagner-Reetz, Y. Grin, Disorder in the composite crystal structure of the manganese “disilicide” MnSi1.73 from powder X-ray diffraction data, Acta Crystallogr. Sect. B Struct. Sci. Cryst. Eng. Mater. 71 (2015) 707–712. https://doi.org/10.1107/S2052520615019757.

[95] Y. Miyazaki, D. Igarashi, K. Hayashi, T. Kajitani, K. Yubuta, Modulated crystal structure of chimney-ladder higher manganese silicides MnSiγ (γ∼1.74), Phys. Rev. B - Condens. Matter Mater. Phys. 78 (2008) 1–8. https://doi.org/10.1103/PhysRevB.78.214104.

[96] S. Okada, T. Shishido, Y. Ishizawa, M. Ogawa, K. Kudou, T. Fukuda, T. Lundström, Crystal growth by molten metal flux method and properties of manganese silicides, J. Alloys Compd. 317–318 (2001) 315–319. https://doi.org/https://doi.org/10.1016/S0925-8388(00)01363-3.

[97] R. Funahashi, Y. Matsumura, H. Tanaka, T. Takeuchi, W. Norimatsu, E. Combe, R.O. Suzuki, Y. Wang, C. Wan, S. Katsuyama, M.K. and K. Koumoto, Thermoelectric properties of n-type Mn3−xCrxSi4Al2 in air, J. Appl. Phys. 112 (2012).

[98] R. Funahashi, Y. Matsumura, T. Barbier, T. Takeuchi, R.O. Suzuki, S. Katsuyama, A. Yamamoto, H. Takazawa, E. Combe, Durability of Silicide-Based Thermoelectric Modules at High Temperatures in Air, J. Electron. Mater. 44 (2015) 2946–2952. https://doi.org/10.1007/s11664-015-3784-7.

[99] S. Ghodke, R. Sobota, D. Berthebaud, P. Pichon, C. Navone, Effect of Re Substitution on the Phase Stability of Complex MnSiγ, J. Electron. Mater. 48 (2019) 5827–5834. https://doi.org/10.1007/s11664-019-07363-8.

[100] A. Allam, C. Angelo, J. Zalesak, M. Record, On the stability of the Higher Manganese Silicides, J. Alloys Compd. 512 (2012) 278–281. https://doi.org/10.1016/j.jallcom.2011.09.081.

[101] R.G. Morris, R.D. Redin, G.C. Danielson, Semiconducting properties of Mg2Si single crystals, Phys. Rev. 109 (1958) 1909–1915. https://doi.org/10.1103/PhysRev.109.1909.

[102] J.I. Tani, H. Kido, Thermoelectric properties of Bi-doped Mg2Si semiconductors, Phys. B Condens. Matter. 364 (2005) 218–224. https://doi.org/10.1016/j.physb.2005.04.017.

[103] C. Liu, W.; Tang, X.F.; Li, H.; Yin, K.; Sharp, J.; Zhou, X.Y.; Uher, Enhanced thermoelectric properties of n-type Mg2.16(Si0.4Sn0.6)1-ySby due to nano-sized Sn-rich precipitates and an optimized electron concentration, J. Mater. Chem. 22 (2012) 13653–13661.

[104] V.K. Zaitsev, M.I. Fedorov, E.A. Gurieva, I.S. Eremin, P.P. Konstantinov, A.Y. Samunin, M. V. Vedernikov, Highly effective Mg2 Si1-x Snx thermoelectrics, Phys. Rev. B - Condens. Matter Mater. Phys. 74 (2006) 2–

6. https://doi.org/10.1103/PhysRevB.74.045207.

[105] W. Liu, Q. Zhang, K. Yin, H. Chi, X. Zhou, X. Tang, C. Uher, High figure of merit and thermoelectric properties of Bi-doped Mg 2Si0.4Sn0.6 solid solutions, J. Solid State Chem. 203 (2013) 333–339. https://doi.org/10.1016/j.jssc.2013.04.041.

[106] L. Chen, G. Jiang, Y. Chen, Z. Du, X. Zhao, T. Zhu, J. He, T.M. Tritt, Miscibility gap and thermoelectric properties of ecofriendly $Mg_2Si_{1-x}Sn_x$ $(0.1 \leq x \leq 0.8)$ solid solutions by flux method, J. Mater. Res. 26 (2011) 3038–3043. https://doi.org/10.1557/jmr.2011.385.

[107] S.W. You, D.K. Shin, I.H. Kim, The effects of Sb on the thermoelectric properties of Mg2Si1-xGex prepared by using solid-state synthesis, J. Korean Phys. Soc. 64 (2014) 1346–1350. https://doi.org/10.3938/jkps.64.1346.

[108] A.U. Khan, N. Vlachos, T. Kyratsi, High thermoelectric figure of merit of Mg2Si0.55Sn0.4Ge0.05 materials doped with Bi and Sb, Scr. Mater. 69 (2013) 606–609.

[109] P. Gao, I. Berkun, R.D. Schmidt, M.F. Luzenski, X. Lu, P. Bordon Sarac, E.D. Case, T.P. Hogan, Transport and Mechanical Properties of High-ZT Mg2.08Si0.4−x Sn0.6Sb x Thermoelectric Materials, J. Electron. Mater. 43 (2014) 1790–1803. https://doi.org/10.1007/s11664-013-2865-8.

[110] C. Liu, S. Lu, Y. Fu, H. Zhang, Flammability and the oxidation kinetics of the magnesium alloys AZ31, WE43, and ZE10, Corros. Sci. 100 (2015) 177–185. https://doi.org/https://doi.org/10.1016/j.corsci.2015.07.020.

[111] F. Czerwinski, Oxidation characteristics of magnesium alloys, Jom. 64 (2012) 1477–1483. https://doi.org/10.1007/s11837-012-0477-z.

[112] G. Skomedal, N.R. Kristiansen, M. Engvoll, H. Middleton, Methods for Enhancing the Thermal Durability of High-Temperature Thermoelectric Materials, J. Electron. Mater. 43 (2014) 1946–1951. https://doi.org/10.1007/s11664-013-2917-0.

[113] J. Bourgeois, J. Tobola, B. Wiendlocha, L. Chaput, P. Zwolenski, D. Berthebaud, F. Gascoin, Q. Recour, H. Scherrer, Study of electron, phonon and crystal stability versus thermoelectric properties in Mg2x (x= Si, Sn) compounds and their alloys, Funct. Mater. Lett. 06 (2013) 1340005. https://doi.org/10.1142/S1793604713400055.

[114] M. Søndergaard, M. Christensen, K.A. Borup, H. Yin, B.B. Iversen, Thermal stability and thermoelectric properties of Mg2Si0.4Sn0.6 and Mg2Si0.6Sn0.4, J. Mater. Sci. 48 (2013) 2002–2008. https://doi.org/10.1007/s10853-012-6967-0.

[115] G. Skomedal, A. Burkov, A. Samunin, R. Haugsrud, H. Middleton, High temperature oxidation of Mg2(Si-Sn), Corros. Sci. 111 (2016) 325–333.

https://doi.org/https://doi.org/10.1016/j.corsci.2016.05.016.

[116] I. Tsuyumoto, H. Uchikawa, Nonstoichiometric orthorhombic titanium oxide, TiO2−δ and its thermochromic properties, Mater. Res. Bull. 39 (2004) 1737–1744. https://doi.org/10.1016/j.materresbull.2004.04.037.

[117] S. Andersson, B. Collén, U. Kuylenstierna, A. Magnéli, Phase Analysis Studies on the Titanium- Oxigen System, Acta Chem. Scand. 11 (1957) 1641–1652.

[118] S. Harada, K. Tanaka, H. Inui, Thermoelectric properties and crystallographic shear structures in titanium oxides of the Magnèli phases, J. Appl. Phys. 108 (2010) 83703. https://doi.org/10.1063/1.3498801.

[119] J.B. M. Backhaus-Ricoult, J. Rustad, L. Moore, C. Smith, Semiconducting large bandgap oxides as potential thermoelectric materials for high-temperature power generation?, Appl. Phys. A. 116 (2014) 433–470.

[120] S. Conze, A. Poenicke, H.-P. Martin, A. Rost, I. Kinski, J. Schilm, A. Michaelis, Manufacturing Processes for TiO x -Based Thermoelectric Modules: from Suboxide Synthesis to Module Testing, J. Electron. Mater. 43 (2014) 3765–3771. https://doi.org/10.1007/s11664-014-3128-z.

[121] B. Feng, H.-P. Martin, F.-D. Börner, W. Lippmann, M. Schreier, K. Vogel, A. Lenk, I. Veremchuk, M. Dannowski, C. Richter, P. Pfeiffer, G. Zikoridse, H. Lichte, J. Grin, A. Hurtado, A. Michaelis, Manufacture and Testing of Thermoelectric Modules Consisting of B x C and TiO x Elements, Adv. Eng. Mater. 16 (2014) 1252–1263. https://doi.org/10.1002/adem.201400183.

[122] J. Schilm, A. Pönicke, M. Kluge, I. Sichert, H.-P. Martin, A. Michaelis, TiOx Based Thermoelectric Modules – Manufacturing, Properties and Operational Behavior, Mater. Today Proc. 2 (2015) 770–779. https://doi.org/10.1016/j.matpr.2015.05.097.

[123] H.-P. Martin, A. Pönicke, M. Kluge, I. Sichert, A. Rost, S. Conze, K. Wätzig, J. Schilm, A. Michaelis, TiOx -Based Thermoelectric Modules: Manufacturing, Properties, and Operational Behavior, J. Electron. Mater. 45 (2016) 1570–1575. https://doi.org/10.1007/s11664-015-4115-8.

[124] K. Hoang, S.D. Mahanti, J.R. Salvador, M.G. Kanatzidis, Atomic Ordering and Gap Formation in Ag-Sb-Based Ternary Chalcogenides, Phys. Rev. Lett. 99 (2007) 156403. https://doi.org/10.1103/PhysRevLett.99.156403.

[125] K. Ramasamy, H. Sims, W.H. Butler, A. Gupta, Selective Nanocrystal Synthesis and Calculated Electronic Structure of All Four Phases of Copper–Antimony–Sulfide, Chem. Mater. 26 (2014) 2891–2899. https://doi.org/10.1021/cm5005642.

[126] M.L. Jeanloz, R. & Johnson, A note on the bonding, optical spectrum and composition of tetrahedrite, Phys. Chem. Miner. 11 (1984) 52.

[127] B. Du, K. Chen, H. Yan, M.J. Reece, Efficacy of lone-pair electrons to engender ultralow thermal conductivity, Scr. Mater. 111 (2016) 49–53. https://doi.org/10.1016/j.scriptamat.2015.05.031.

[128] K. Suekuni, K. Tsuruta, T. Ariga, M. Koyano, Thermoelectric Properties of Mineral Tetrahedrites Cu10Tr2Sb4S13 with Low Thermal Conductivity, Appl. Phys. Express. 5 (2012) 51201. https://doi.org/10.1143/apex.5.051201.

[129] X. Lu, D.T. Morelli, Y. Wang, W. Lai, Y. Xia, V. Ozolins, Phase Stability, Crystal Structure, and Thermoelectric Properties of Cu12Sb4S13-xSex Solid Solutions, Chem. Mater. 28 (2016) 1781–1786. https://doi.org/10.1021/acs.chemmater.5b04796.

[130] J. van Embden, Y. Tachibana, Synthesis and characterisation of famatinite copper antimony sulfide nanocrystals, J. Mater. Chem. 22 (2012) 11466–11469. https://doi.org/10.1039/C2JM32094K.

[131] B. Du, R. Zhang, K. Chen, A. Mahajan, M.J. Reece, The impact of lone-pair electrons on the lattice thermal conductivity of the thermoelectric compound CuSbS2, J. Mater. Chem. A. 5 (2017) 3249–3259. https://doi.org/10.1039/C6TA10420G.

[132] K. Chen, B. Du, N. Bonini, C. Weber, H. Yan, M.J. Reece, Theory-Guided Synthesis of an Eco-Friendly and Low-Cost Copper Based Sulfide Thermoelectric Material, J. Phys. Chem. C. 120 (2016) 27135–27140. https://doi.org/10.1021/acs.jpcc.6b09379.

[133] K. Chen, C. Di Paola, B. Du, R. Zhang, S. Laricchia, N. Bonini, C. Weber, I. Abrahams, H. Yan, M. Reece, Enhanced thermoelectric performance of Sn-doped Cu3SbS4, J. Mater. Chem. C. 6 (2018) 8546–8552. https://doi.org/10.1039/c8tc02481b.

[134] B. Du, R. Zhang, M. Liu, K. Chen, H. Zhang, M.J. Reece, Crystal structure and improved thermoelectric performance of iron stabilized cubic Cu3SbS3 compound, J. Mater. Chem. C. 7 (2019) 394–404. https://doi.org/10.1039/C8TC05301D.

[135] X. Lu, D.T. Morelli, Y. Xia, F. Zhou, V. Ozolins, H. Chi, X. Zhou, C. Uher, High Performance Thermoelectricity in Earth-Abundant Compounds Based on Natural Mineral Tetrahedrites, Adv. Energy Mater. 3 (2013) 342–348. https://doi.org/10.1002/aenm.201200650.

[136] M.H. Braga, J.A. Ferreira, C. Lopes, L.F. Malheiros, Phase Transitions in the Cu-Sb-S System, Mater. Sci. Forum. 587–588 (2008) 435–439. https://doi.org/10.4028/www.scientific.net/MSF.587-588.435.

[137] T. Barbier, P. Lemoine, S. Gascoin, O.I. Lebedev, A. Kaltzoglou, P. Vaqueiro, A. V. Powell, R.I. Smith, E. Guilmeau, Structural stability of the synthetic thermoelectric ternary and nickel-substituted tetrahedrite phases, J. Alloys Compd. 634 (2015) 253–262.

https://doi.org/10.1016/j.jallcom.2015.02.045.

[138] R. Chetty, A. Bali, R.C. Mallik, Tetrahedrites as thermoelectric materials: An overview, J. Mater. Chem. C. 3 (2015) 12364–12378. https://doi.org/10.1039/c5tc02537k.

[139] J. Pi, S. Kwak, S. Kim, G. Lee, I. Kim, Thermal Stability and Mechanical Properties of Thermoelectric Tetrahedrite Cu 12 Sb 4 S 13, J. Electron. Mater. 48 (2019) 1991–1997. https://doi.org/10.1007/s11664-018-06883-z.

[140] A.P. Gonçalves, E.B. Lopes, M.F. Montemor, J. Monnier, B. Lenoir, Oxidation Studies of Cu12Sb3.9Bi0.1S10Se3 Tetrahedrite, J. Electron. Mater. 47 (2018) 2880–2889. https://doi.org/10.1007/s11664-018-6141-9.

[141] W. Park, M.T. Barako, A.M. Marconnet, M. Asheghi, K.E. Goodson, Effect of thermal cycling on commercial thermoelectric modules, in: Intersoc. Conf. Therm. Thermomechanical Phenom. Electron. Syst. ITHERM, 2012: pp. 107–112. https://doi.org/10.1109/ITHERM.2012.6231420.

[142] H. Dong, X. Li, Y. Tang, J. Zou, X. Huang, Y. Zhou, W. Jiang, G.J. Zhang, L. Chen, Fabrication and thermal aging behavior of skutterudites with silica-based composite protective coatings, J. Alloys Compd. 527 (2012) 247–251. https://doi.org/10.1016/j.jallcom.2012.02.116.

[143] S.H. Park, Y. Kim, C.Y. Yoo, Oxidation suppression characteristics of the YSZ coating on Mg2Si thermoelectric legs, Ceram. Int. 42 (2016) 10279–10288. https://doi.org/10.1016/j.ceramint.2016.03.161.

[144] Kelly C.E., The MHW converter (RTG), in: Proc. 10th Intersoc. Energy Convers. Eng. Conf. Am. Inst. Chem. Eng. New York, 1975: pp. 880–886.

[145] G.J.S. J. Sakamoto, T. Caillat, J.-P. Fleurial, Method of suppressing sublimation in advanced thermoelectric devices, U.S. Patent No. 7480984 B1, 2009.

[146] M.S. El-Genk, H.H. Saber, T. Caillat, J. Sakamoto, Tests results and performance comparisons of coated and un-coated skutterudite based segmented unicouples, Energy Convers. Manag. 47 (2006) 174–200. https://doi.org/10.1016/j.enconman.2005.03.023.

[147] H.H. Saber, M.S. El-Genk, T. Caillat, Tests results of skutterudite based thermoelectric unicouples, Energy Convers. Manag. 48 (2007) 555–567. https://doi.org/10.1016/j.enconman.2006.06.008.

[148] G.S. J. Sakamoto, T. Calliat, J. Fleurial, Coating Thermoelectric Devices to Suppress Sublimation, NASA's Jet Propulsion Laboratory, NASA Tech Briefs. (2007) 5–6.

[149] H.H. Saber, M.S. El-Genk, Effects of metallic coatings on the performance of skutterudite-based segmented unicouples, Energy Convers. Manag. 48

(2007) 1383–1400. https://doi.org/10.1016/j.enconman.2006.04.024.

[150] M. Kambe, T. Jinushi, Z. Ishijima, Encapsulated thermoelectric modules for advanced thermoelectric systems, J. Electron. Mater. 43 (2014) 1959–1965. https://doi.org/10.1007/s11664-013-2926-z.

[151] J.R. Salvador, J.Y. Cho, Z. Ye, J.E. Moczygemba, A.J. Thompson, J.W. Sharp, J.D. König, R. Maloney, T. Thompson, J. Sakamoto, H. Wang, A.A. Wereszczak, G.P. Meisner, Thermal to electrical energy conversion of skutterudite-based thermoelectric modules, J. Electron. Mater. 42 (2013) 1389–1399. https://doi.org/10.1007/s11664-012-2261-9.

[152] M. Kambe, T. Jinushi, Z. Ishijima, Encapsulated Thermoelectric Modules and Compliant Pads for Advanced Thermoelectric Systems, J. Electron. Mater. 39 (2010) 1418–1421. https://doi.org/10.1007/s11664-010-1315-0.

[153] J.S. Sakamoto, G.J. Snyder, T. Calliat, J.-P. Fleurial, S.M. Jones, J.-A. Palk, System and method for suppressing sublimation using opacified aerogel, U.S. Patent No. 7461512 B2, 2008.

[154] T. Caillat, J. Sakamoto, A. Jewell, J. Cheng, J. Paik, F. Gascoin, J. Snyder, R. Blair, C.-K. Huang, J.-P. Fleurial, Advanced Radioisotope Power Systems Technology development at JPL, in: Proc. 24th Int. Conf. Thermoelectr. Clemson, SC, USA, 2005.

[155] W.D. J. Sakamoto, T. Caillat, J.-P. Fleurial, S. Jones, J.-A. Paik, Improving thermoelectric technology performance and durability with aerogel, Jet Propulsion Laboratory, National Aeronautics and Space Administration, JPL Technical Report Server, Pasadena, CA, USA, 2005.

[156] Y.S. Park, T. Thompson, Y. Kim, J.R. Salvador, J.S. Sakamoto, Protective enamel coating for n- and p-type skutterudite thermoelectric materials, J. Mater. Sci. 50 (2015) 1500–1512. https://doi.org/10.1007/s10853-014-8711-4.

[157] J. García-Cañadas, A. V. Powell, A. Kaltzoglou, P. Vaqueiro, G. Min, Fabrication and evaluation of a skutterudite-based thermoelectric module for high-temperature applications, J. Electron. Mater. 42 (2013) 1369–1374. https://doi.org/10.1007/s11664-012-2241-0.

[158] K. Zawadzka, E. Godlewska, K. Mars, M. Nocun, Oxidation Resistant Coatings for CoSb3, in: AIP Conf. Proc., 2012: pp. 231–234. https://doi.org/10.1063/1.4731539.

[159] E. Godlewska, K. Zawadzka, K. Mars, R. Mania, K. Wojciechowski, A. Opoka, Protective properties of magnetron-sputtered Cr-Si layers on CoSb 3, Oxid. Met. 74 (2010) 205–213. https://doi.org/10.1007/s11085-010-9209-3.

[160] H. Dong, X. Li, X. Huang, Y. Zhou, W. Jiang, L. Chen, Improved oxidation resistance of thermoelectric skutterudites coated with composite glass,

Ceram. Int. 39 (2013) 4551–4557. https://doi.org/10.1016/j.ceramint.2012.11.051.

[161] J. Tani, M. Takahashi, H. Kido, Fabrication of oxidation-resistant β-FeSi2 film on Mg2Si by RF magnetron-sputtering deposition, J. Alloys Compd. 488 (2009) 346–349. https://doi.org/10.1016/j.jallcom.2009.08.128.

[162] S. Battiston, S. Boldrini, S. Fiameni, A. Famengo, M. Fabrizio, S. Barison, Multilayered thin films for oxidation protection of Mg2Si thermoelectric material at middle-high temperatures, Thin Solid Films. 526 (2012) 150–154. https://doi.org/10.1016/j.tsf.2012.10.114.

[163] L. Zhang, X. Chen, Y. Tang, L. Shi, G.J. Snyder, J.B. Goodenough, J. Zhou, Thermal stability of Mg 2 Si 0.4 Sn 0.6 in inert gases and atomic-layer-deposited Al 2 O 3 thin film as a protective coating, J. Mater. Chem. A. 4 (2016) 17726–17731. https://doi.org/10.1039/C6TA07611D.

[164] M. Ferraris, V. Casalegno, F. Smeacetto, Glass as a joining material for ceramic matrix composites : 25 years of research at Politecnico di Torino, (2020) 1–8. https://doi.org/10.1111/ijag.15032.

[165] M.K. Mahapatra, K. Lu, Glass-based seals for solid oxide fuel and electrolyzer cells - A review, Mater. Sci. Eng. R Reports. 67 (2010) 65–85. https://doi.org/10.1016/j.mser.2009.12.002.

[166] W. Höland, G. Beall, Glass-ceramic technology, 2002

[167] R.N. Singh, Sealing Technology for Solid Oxide Fuel Cells (SOFC), Int. J. Appl. Ceram. Technol. 4 (2007) 134–144. https://doi.org/10.1111/j.1744-7402.2007.02128.x.

[168] R.N. Singh, Self-repairable glass seals for solid oxide fuel cells, J. Mater. Res. 27 (2012) 2055–2061. https://doi.org/DOI: 10.1557/jmr.2012.188.

[169] R. Chen, L. Goto, T. Tu, T. Hirai, High-temperature oxidation behavior of PbTe and oxidation-resistive glass coating, in: XVI ICT '97. Proc. ICT'97. 16th Int. Conf. Thermoelectr. (Cat. No.97TH8291), 1997: pp. 251–254. https://doi.org/10.1109/ICT.1997.667101.

[170] M.A. Stefan, K. Schierle-Arndt, G. Huber, J.S. Blackburn, I.W. Jones, F. Stackpool, S. Heavens, Thermoelectric material coated with a protective layer. US 2012/00244332 A1, 2012.

[171] P. Nieroda, K. Mars, J. Nieroda, J. Leszczyński, M. Król, E. Drożdż, P. Jeleń, M. Sitarz, A. Koleżyński, New high temperature amorphous protective coatings for Mg 2 Si thermoelectric material, Ceram. Int. 45 (2019) 10230–10235. https://doi.org/10.1016/j.ceramint.2019.02.075.

[172] K. Zawadzka, E. Godlewska, K. Mars, M. Nocun, A. Kryshtal, A. Czyrska-Filemonowicz, Enhancement of oxidation resistance of

CoSb3thermoelectric material by glass coating, Mater. Des. 119 (2017) 65–75. https://doi.org/10.1016/j.matdes.2017.01.055.

[173] M. Salvo, F. Smeacetto, F. D'Isanto, G. Viola, P. Demitri, F. Gucci, M.J. Reece, Glass-ceramic oxidation protection of higher manganese silicide thermoelectrics, J. Eur. Ceram. Soc. 39 (2019) 66–71. https://doi.org/10.1016/J.JEURCERAMSOC.2018.01.007.

[174] F. Gucci, F. D'Isanto, R. Zhang, M. Reece, F. Smeacetto, M. Salvo, Oxidation Protective Hybrid Coating for Thermoelectric Materials, Materials (Basel). 12 (2019) 573. https://doi.org/10.3390/ma12040573.

[175] V. Mamedov, Spark plasma sintering as advanced PM sintering method, Powder Metall. 45 (2002) 322–328. https://doi.org/10.1179/003258902225007041.

[176] S. Grasso, Y. Sakka, G. Maizza, Electric current activated/assisted sintering (ECAS): a review of patents 1906–2008, Sci. Technol. Adv. Mater. 10 (2009) 053001. https://doi.org/10.1088/1468-6996/10/5/053001.

[177] O. Guillon, J. Gonzalez-Julian, B. Dargatz, T. Kessel, G. Schierning, J. R??thel, M. Herrmann, Field-assisted sintering technology/spark plasma sintering: Mechanisms, materials, and technology developments, Adv. Eng. Mater. 16 (2014) 830–849. https://doi.org/10.1002/adem.201300409.

[178] F. Smeacetto, M. Salvo, A. Ventrella, S. Rizzo, M. Ferraris, Durable Glass-Ceramic Coatings for Foam Glass, Int. J. Appl. Glas. Sci. 3 (2012) 69–74. https://doi.org/10.1111/j.2041-1294.2011.00071.x.

[179] S. Datta, S. Das, A New High Temperature Resistant Glass – Ceramic Coating for Gas Turbine A new high temperature resistant glass – ceramic coating for gas turbine engine components, Bull. Mater. Sci. 28 (2005) 689–696. https://doi.org/10.1007/BF02708539.

[180] Arun K. Varshneya, Fundamentals of inorganic glasses, 2012.

[181] D.Y. Nhi Truong, H. Kleinke, F. Gascoin, Preparation of pure Higher Manganese Silicides through wet ball milling and reactive sintering with enhanced thermoelectric properties, Intermetallics. 66 (2015) 127–132. https://doi.org/10.1016/j.intermet.2015.07.002.

[182] S. Petrescu, M. Malki, M. Constantinescu, E.M. Anghel, I. Atkinson, R. State, M. Zaharescu, Vitreous and glass-ceramics materials in the SiO 2-Al 2O 3-MeO-M 2O type system, J. Optoelectron. Adv. Mater. 14 (2012) 603–612.

[183] B. Du, F. Gucci, H. Porwal, S. Grasso, A. Mahajan, M.J. Reece, Flash spark plasma sintering of magnesium silicide stannide with improved thermoelectric properties, J. Mater. Chem. C. 5 (2017) 1514–1521. https://doi.org/10.1039/C6TC05197A.

[184] W. Liu, X. Tang, H. Li, J. Sharp, X. Zhou, C. Uher, Optimized Thermoelectric Properties of Sb-Doped Mg 2(1+ z) Si 0.5– y Sn 0.5 Sb y through Adjustment of the Mg Content, Chem. Mater. 23 (2011) 5256–5263. https://doi.org/10.1021/cm202445d.

[185] H. Ning, D. Mastrorillo, S. Grasso, B. Du, T. Mori, C. Hu, Y. Xu, K. Simpson, M.J. Reece, Enhanced thermoelectric performance of porous magnesium tin silicide prepared using pressure-less spark plasma sintering, J. Mater. Chem. A. 3 (2015) 17426–17432. https://doi.org/10.1039/c5ta03473f.

[186] Y. Zhang, A. Song, D. Ma, X. Zhang, M. Ma, R. Liu, Sintering characteristics and grain growth behavior of MgO nanopowders by spark plasma sintering, J. Alloys Compd. 608 (2014) 304–310. https://doi.org/http://dx.doi.org/10.1016/j.jallcom.2014.04.148.

[187] G. Skomedal, A. Burkov, A. Samunin, R. Haugsrud, H. Middleton, High temperature oxidation of Mg 2 (Si-Sn), Corros. Sci. 111 (2016) 325–333. https://doi.org/10.1016/j.corsci.2016.05.016.

[188] A. Hrubý, Evaluation of glass-forming tendency by means of DTA, Czechoslov. J. Phys. 22 (1972) 1187–1193. https://doi.org/10.1007/BF01690134.

[189] S. Kumar, K. Singh, Glass transition, thermal stability and glass-forming tendency of Se90−xTe5Sn5Inx multi-component chalcogenide glasses, Thermochim. Acta. 528 (2012) 32–37. https://doi.org/10.1016/j.tca.2011.11.005.

[190] A. Dietzel, Glass structure and glass properties, J. Glas. Ber. 22 (1968) 41.

[191] M. Saad, M. Poulain, Glass Forming Ability Criterion, Mater. Sci. Forum. 19–20 (1987) 11–18. https://doi.org/10.4028/www.scientific.net/MSF.19-20.11.

[192] M.L.F. Nascimento, L.A. Souza, E.B. Ferreira, E.D. Zanotto, Can glass stability parameters infer glass forming ability?, J. Non. Cryst. Solids. 351 (2005) 3296–3308. https://doi.org/10.1016/j.jnoncrysol.2005.08.013.

[193] M.J. Pascual, A. Durán, M.O. Prado, A new method for determining fixed viscosity points of glasses, Phys. Chem. Glas. 46 (2005) 512–520.

[194] M. Oscar Prado, E. Dutra Zanotto, R. Müller, Model for sintering polydispersed glass particles, J. Non. Cryst. Solids. 279 (2001) 169–178. https://doi.org/10.1016/S0022-3093(00)00399-9.

[195] J. Frenkel, Viscous flow of crystalline bodies under the action of surface tension, J. Physics, USSR. 9 (1945) 385. http://ci.nii.ac.jp/naid/10012829642/en/ (accessed February 6, 2020).

[196] J.K Mackenzie and R. Shuttleworth, A Phenomenological Theory of Sintering, Proc. Phys. Soc. Sect. B. 62 (1949) 833–852.

[197] A. Hülsenberg, Dagmar, Harnisch, Alf, Bismarck, Microstructuring of Glasses, 2008.

[198] C. Lara, M.J. Pascual, A. Durán, Glass-forming ability, sinterability and thermal properties in the systems RO–BaO–SiO2 (R=Mg, Zn), J. Non. Cryst. Solids. 348 (2004) 149–155. https://doi.org/10.1016/j.jnoncrysol.2004.08.140.

[199] C. Lara, M. Pascual, M. Prado, A. Duran, Sintering of glasses in the system RO–Al2O3–BaO–SiO2 (R=Ca, Mg, Zn) studied by hot-stage microscopy, Solid State Ionics. 170 (2004) 201–208. https://doi.org/10.1016/j.ssi.2004.03.009.

[200] S.T. Nguyen, T. Nakayama, H. Suematsu, T. Suzuki, M. Takeda, K. Niihara, Low thermal conductivity Y2Ti2O7 as a candidate material for thermal/environmental barrier coatings, Ceram. Int. 42 (2016) 11314–11323. https://doi.org/10.1016/j.ceramint.2016.04.052.

[201] J.K. Gill, O.P. Pandey, K. Singh, Role of sintering temperature on thermal, electrical and structural properties of Y2Ti2O7 pyrochlores, Int. J. Hydrogen Energy. 36 (2011) 14943–14947. https://doi.org/10.1016/j.ijhydene.2011.02.138.

[202] T. Wei, Y. Zhang, L. Kong, Y.J. Kim, A. Xu, I. Karatchevtseva, N. Scales, D.J. Gregg, Hot isostatically pressed Y2Ti2O7 and Gd2Ti2O7 pyrochlore glass-ceramics as potential waste forms for actinide immobilization, J. Eur. Ceram. Soc. 39 (2019) 1546–1554. https://doi.org/10.1016/j.jeurceramsoc.2018.11.012.

[203] L. Kong, Y. Zhang, I. Karatchevtseva, Preparation of Y2Ti2O7 pyrochlore glass-ceramics as potential waste forms for actinides: The effects of processing conditions, J. Nucl. Mater. 494 (2017) 29–36. https://doi.org/10.1016/j.jnucmat.2017.07.004.

[204] N. Mizutani, Y. Tajima, M. Kato, Phase Relations in the System Y2O3-TiO2, J. Am. Ceram. Soc. 59 (1976) 168–168. https://doi.org/10.1111/j.1151-2916.1976.tb09459.x.

[205] W. Gong, D. Li, Z. Chen, F. Zheng, Y. Liu, Y. Du, B. Huang, Phase equilibria of the TiO2 - Y2 O3 system, Calphad Comput. Coupling Phase Diagrams Thermochem. 33 (2009) 624–627. https://doi.org/10.1016/j.calphad.2009.06.005.

[206] V. Fuertes, M.J. Cabrera, J. Seores, D. Muñoz, J.F. Fernández, E. Enríquez, Enhanced wear resistance of engineered glass-ceramic by nanostructured self-lubrication, Mater. Des. 168 (2019) 107623. https://doi.org/10.1016/j.matdes.2019.107623.

[207] J. Partyka, M. Leśniak, Raman and infrared spectroscopy study on structure and microstructure of glass–ceramic materials from SiO2–Al2O3–Na2O–K2O–CaO system modified by variable molar ratio of SiO2/Al2O3, Spectrochim. Acta Part A Mol. Biomol. Spectrosc. 152 (2016) 82–91. https://doi.org/10.1016/j.saa.2015.07.045.

[208] S. Harish, D. Sivaprahasam, M. Battabyal, R. Gopalan, Phase stability and thermoelectric properties of Cu10.5Zn1.5Sb4S13 tetrahedrite, J. Alloys Compd. 667 (2016) 323–328. https://doi.org/10.1016/j.jallcom.2016.01.094.

[209] S. Battiston, C. Fanciulli, S. Fiameni, A. Famengo, S. Fasolin, M. Fabrizio, One step synthesis and sintering of Ni and Zn substituted tetrahedrite as thermoelectric material, J. Alloys Compd. 702 (2017) 75–83. https://doi.org/10.1016/j.jallcom.2017.01.187.

[210] R. Chetty, A. Bali, R.C. Mallik, Tetrahedrites as thermoelectric materials: an overview, J. Mater. Chem. C. 3 (2015) 12364–12378. https://doi.org/10.1039/C5TC02537K.